Degradable Fluorene-based Polymers for Highly Selective Sorting of Semiconducting Single-walled Carbon Nanotubes

Inauguraldissertation

zur

Erlangung der Würde eines Doktors der Philosophie

vorgelegt der

Philosophisch-Naturwissenschaftlichen Fakultät

der Universität Basel

von

Liang Xu

Basel, 2021

Genehmigt von der Philosophisch-Naturwissenschaftlichen Fakultät

auf Antrag von

Prof. Dr. Marcel Mayor

Prof. Dr. Christof Sparr

Prof. Dr. Alex Adronov

Basel, 15.12.2020

Prof. Dr. Martin Spiess

Dekan

Dedicated to:

My family

ACKNOWLEDGMENTS

First and foremost, I would like to express my sincere gratitude to *Prof. Dr. Marcel Mayor* for offering me the opportunity to work in his research group, for giving me such an interesting project, and for the continuous support during my whole PhD study with his patience, enthusiasm, knowledge, and experience.

I would also like to thank *Prof. Dr. Christof Sparr* for being my second supervisor and offering me support and opinions, and to thank *Prof. Dr. Alex Adronov* for being the external expert in my Doctoral Committee.

My special thanks goes to *Dr. Michal Valášek* for his support, advices, and guidance during my PhD study. I benefited a lot from his professional background and experience as a chemist. He is not only a colleague, but also a true friend outside the scientific world.

Sincere thanks as well goes to *Dr. Frank Hennrich*, who has been providing me fabulous carbon nanotube samples for my project and always ready to offer helps and opinions.

Furthermore, deep thanks to my former colleague *Dr. Jasmin Santoro* and current colleagues *Nico Balzer* of FG Mayor, as well *Tingting Ruan* of FG Ruben at INT in Karlsruhe. Thank you guys, for the support, accompany, and for being my best buddies. I would also like to thank all the current and former members of FG Mayor in Basel, especially *Dr. Rajesh Mannancherry*, *Dr. Erich Henrik Peters*, *Alfredo Di Silvestro* and *Florian Degen*. I appreciate for your help, both scientific and personal. Additionally, I would like to thank my lovely colleagues at INT, *Dr. Concepción Molina-Jirón*, *Dr. Eufemio Moreno-Pineda*, *Dr. Svetlana Klyatskaya*, *Dr. Asato Mizuno*, *Dr. Senthil Kumar Kuppusamy*, *Shirin Shakouri*, *Nithin Suryadevara*, *Sören Schlittenhardt*, *Sai Prasanna Kumar Panguluri*, and *Hagen Sparrenberger*. Together, we built a cheerful and comfortable atmosphere on the third floor of lab-wing at INT.

I am grateful to *Prof. Dr. Daniel Häussinger* for the 2D NMR measurements, *Dr. Han Li* for helping me to understand more about carbon nanotubes, *Dr. Sergei Lebedkin* for the technical support on Raman and PLE spectroscopy, *Dr. Joachim Bürck* for his guidance to the concept of circular dichroism as well the measurements, *Dr. Frank Biedermann* for allowing me to use the CD spectroscopy, *Dr. Leonardo Velasco Estrada* for performing the XPS measurements, *Dr.*

Elaheh Sedghamiz and *Montserrat Penaloza-Amion* for the theoretical calculation, and *Dr. Di Wang* for the SEM images.

I thank *Familie Glantz* for providing me such a wonderful accommodation during my PhD and for treating me like their family member. I also thank *Rodina Valášek* for the hospitality and the wonderful time we spent together.

Finally, I would like to thank my family for the full support, especially my mother, who has always been the lighthouse in my life. Last but not least, I thank *Jiaojiao* for her trust and love.

TABLE OF CONTENTS

1 Introduction and background

1.1 Carbon and carbon allotropes

Carbon, a chemical element with the atomic number six, is one of the most ancient and abundant elements in the universe since the Big Bang. It has four outer shell electrons which can hybridize into sp^3-, sp^2- and sp-orbitals and form covalent bonds with itself or other elements in diverse ways. Three-dimensional (3D) carbon allotropes are well-known for a long period due to their early discover in nature, such as graphite, amorphous carbon and diamond. In 1985, H. W. Kroto, R. F. Curl and R. E. Smalley reported the discovery of fullerene C_{60} during the vaporization of graphite by laser irradiation, which is a spherical zero-dimensional (0D) allotrope of carbon.[1] Later in 1991, Iijima discovered one-dimensional (1D) tubular carbon nanotubes with the method similar to that used for fullerene.[2] Graphene, the two-dimensional (2D) carbon allotrope was finally isolated by Geim and Novoselov by mechanical exfoliation of graphite in 2004,[3] which builds up carbon materials of all other dimensionalities, as shown in Figure 1.1.

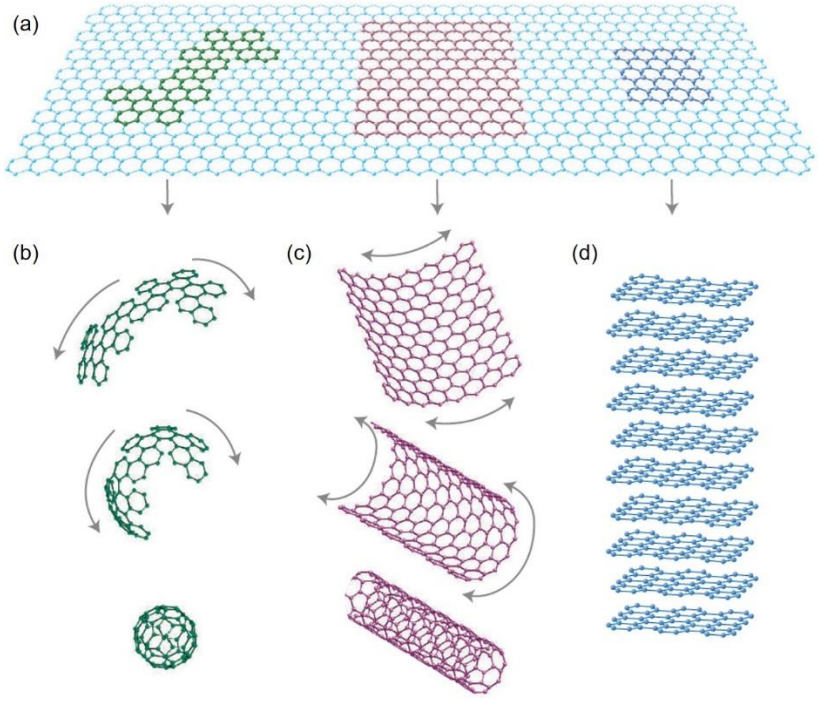

Figure 1.1. Illustrated construction of 0D fullerene (b), 1D carbon nanotube (c), and 3D graphite (d) from 2D graphene (a).[4]

Each of these discoveries represents a revolutionary event at their time notably in fields of physics, chemistry, material science and nanotechnology. Despite of the numerous publications and efforts from the researchers all over the world, the carbon materials still surprise with new properties. One of the recent examples was published in 2018 by Cao *et al*. They reported the realization of intrinsic unconventional superconductivity between two sheets of graphene that are twisted relative to each other by a small angle of about 1.1°.[5]

1.2 Carbon nanotubes

Carbon nanotubes (CNTs) are cylindrical one-dimensional (1D) sp^2 hybridized carbon allotropes with diameters in the range of one to several nanometers. Based on the number of walls inside a single tube, CNTs can be categorized mainly into single-walled carbon nanotubes (SWCNTs) and multi-walled carbon nanotubes (MWCNTs). Ever since the discovery of CNTs in the early 1990s by Sumio Iijima,[2] the number of CNT-related publications has been rapidly increasing, particularly in the field of chemistry, material science, and physics (Figure 1.2). The unique and outstanding properties of CNTs have made them an extraordinary candidate for electronic devices,[6] thin film transistors[7] and solar cells.[8] Indeed, CNTs have become one of the most intensively studied carbon materials in the last two decades.

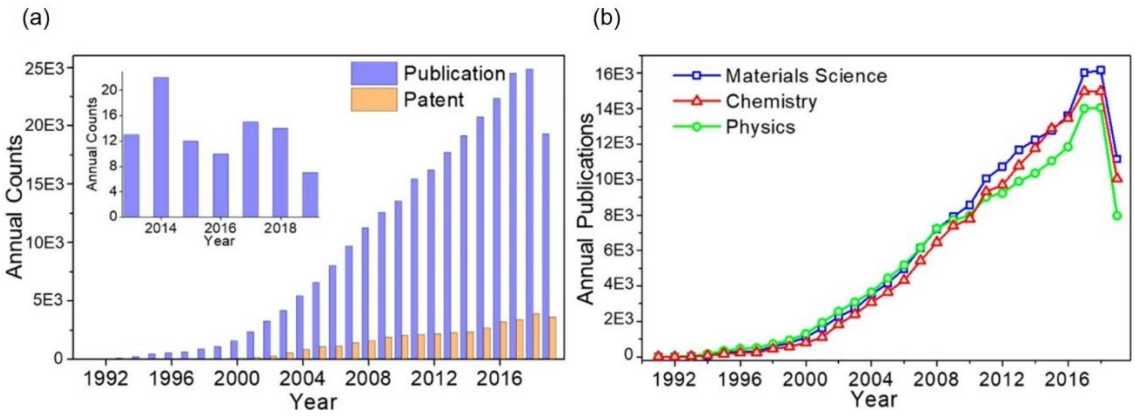

Figure 1.2. (a) Number of journal publications and patents about CNTs from year 1991 to 2019. Inset shows the CNTs related publications in *Science* and *Nature* in the last 7 years; (b) Number of journal publications about CNTs in the fields of Chemistry, Material Science and Physics from year 1991 to 2019.[9]

1.3 Single-walled carbon nanotubes

1.3.1 The geometry of SWCNTs

A single-walled carbon nanotube (SWCNT) can be thought of as a graphene sheet rolled up into a seamless cylinder with a certain direction of chiral angle. The geometrical structure of a SWCNT depends on how the graphene sheet is cut and rolled up, which can be described with the chiral vector C_h, defined as $C_h = na_1 + ma_2$, where a_1 and a_2 are two primitive lattice vectors with length $a = \sqrt{3}a_{c-c}$ and $a_{c-c} = 1.42$ Å. The chiral index (n,m) is a pair of integers with $0 \leq m \leq n$.[10] The length of this chiral vector is defined as $|C_h| = a\sqrt{n^2 + nm + m^2}$. Figure 1.3 shows the chiral vector of (4,2) SWCNT as an example on a typical hexagonal lattice of graphene.

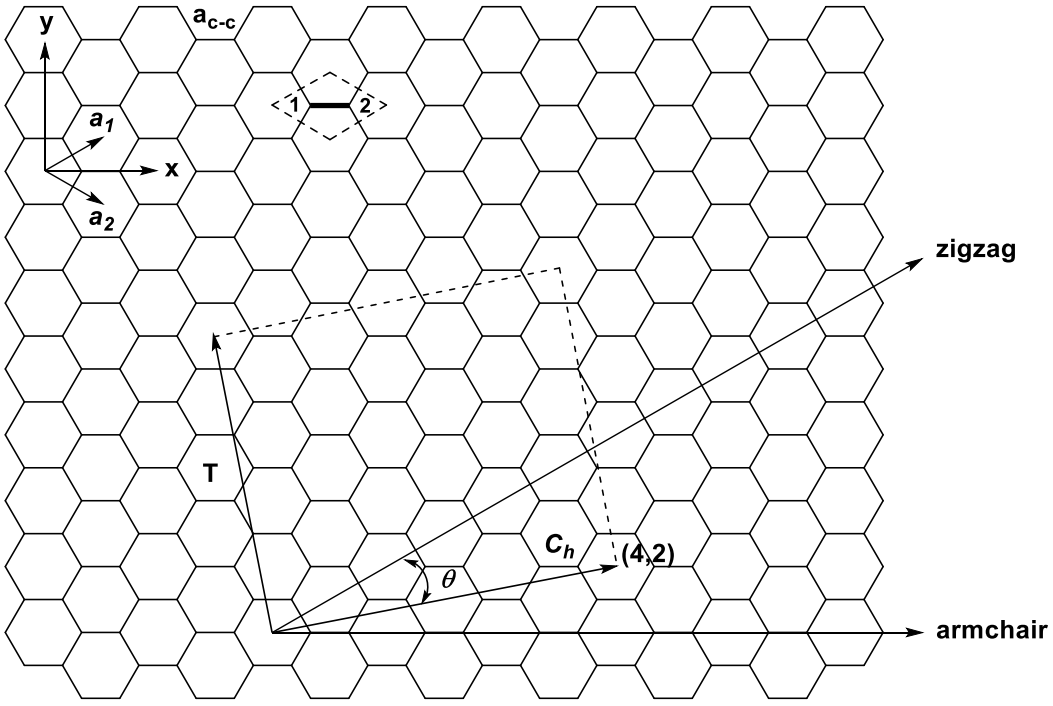

Figure 1.3. A typical hexagonal lattice of graphene with its unit cell as a dashed rhombus and a projection of (4,2) nanotube unit cell as a rectangle. The unit cell of (4,2) nanotube is defined by the chiral vector C_h and the translational vector T along the tube axis. a_1 and a_2 are the primitive lattice vectors and θ is the chiral angle.

The chiral index (n,m) of a SWCNT decides its electronic type, which is either metallic or semiconducting. The nanotubes whose indices are such that *n*-*m* equals 0 or is a multiple of 3 are

metallic, while all others are semiconducting. Theoretically, the family of SWCNTs has 1/3 of metallic SWCNTs (m-SWCNTs) and 2/3 of semiconducting SWCNTs (s-SWCNTs). The diameter *d* of a SWCNT can be calculated from the chiral index (n,m) using the following formulas $d = |C_h|/\pi = a\sqrt{(n^2 + nm + m^2)}/\pi$, where $a = 1.42 \times \sqrt{3}$ Å corresponding to the lattice constant of the graphene sheet. The chiral angle θ is defined as the angle between the chiral vector C_h and the zigzag direction, which can be calculated from the equation $\theta = \arctan[\sqrt{3}m/(2n + m)]$.[11] Armchair SWCNTs are metallic and achiral with $\theta = 30°$, while the zigzag SWCNTs are also achiral but can be both metallic and semiconducting with $\theta = 0°$. All other tubes in-between with $0 < \theta < 30°$ are chiral. Figure 1.4 shows the structure of a (5,5) armchair, a (9,0) zigzag and a (6,4) chiral nanotube with similar diameter as an example. The geometrical difference of those three nanotubes can be seen from the orientation of hexagonal carbon rings.

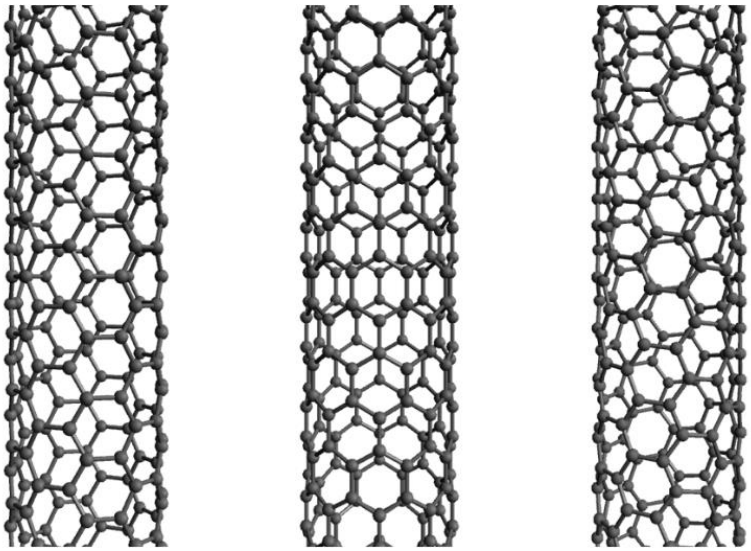

Figure 1.4. Sidewall structure of a (5,5) armchair SWCNT (left), a (9,0) zigzag SWCNT (middle) and a (6,4) chiral SWCNT (right).

1.3.2 The handedness of SWCNTs

In Figure 1.3, the unit cell of (4,2) SWCNT has been defined by the chiral vector C_h and the translational vector T on a graphene lattice layer as an example. The translational vector T can be defined as $T = t_1 a_1 + t_2 a_2$ with $t_1 = (2m + n)/d_R$ and $t_2 = -(2n + m)/d_R$, while d_R is the

greatest common divisor of $(2n + m)$ and $(2m + n)$. The length of vector T is $|T| = \sqrt{3}|C_h|/d_R$. In general, by prolongation of such defined area along the translational vector T and rolling up along the chiral vector C_h, a SWCNT can be obtained with a certain (n,m) index. However, there are two opposite rolling directions to let the sidewalls close up into a seamless tube, i.e. either rolling from the front of the layer to the back or from the back to the front. To note, achiral nanotubes such as zigzag ($\theta = 0°$) and armchair ($\theta = 30°$) nanotubes obtain two identical tubes after such operation, while each chiral nanotube ($0 < \theta < 30°$) with the same chiral angle and diameter can exist as two mirror-imaged enantiomers with the opposite handedness. Similar to the small chiral structures, such enantiomers are named as a left-handed and a right-handed SWCNT.[12] According to the IUPAC nomenclature, the helical structure of chiral SWCNTs can be either left-handed (*M*) or right-handed (*P*), as shown in Figure 1.5.[13,14] The mirror image of chiral indices (n,m) is also defined as (n+m,-m) and is commonly used for referring the mirror enantiomers.[15,16] Without further indication, each chiral (n,m) SWCNT exists as a racemic mixture, containing equal amount of left- and right-handed enantiomer.

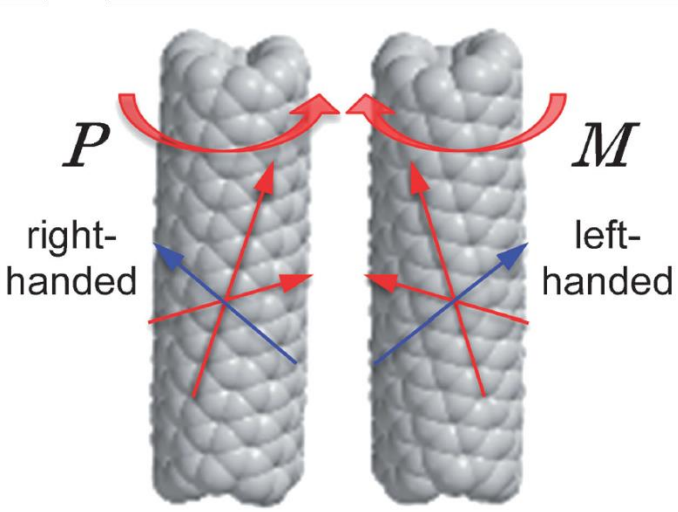

Figure 1.5. Definition of *M*- and *P*-configuration of (8,3) SWCNT as a model, proposed by Komatsu *et al*.[14] Red and blue arrows indicate the zigzag lines.

1.4 Electronic structure of SWCNTs

As described before, since carbon nanotubes can be considered as a sheet of graphene rolled up into a seamless cylinder with certain chiral index and angle, the electronic band structure and properties of carbon nanotubes can be calculated simply from that of 2D graphene using tight binding (TB) approximation (see details below).

1.4.1 Band structure of graphene

In the structure of a graphene lattice, each carbon has four valence electrons. Three of those build tight sp^2 bonds (σ bonds) with neighboring carbons and the fourth electron in p_z orbital from each carbon atom contributes to the π bond which plays an important role in the conduction phenomenon. In real space, each unit cell of the graphene lattice contains two carbon atoms as denoted by 1 and 2 in Figure 1.3. In reciprocal space or *k*-space (Figure 1.6) the unit cell of graphene is a hexagon, which is well known as 1st Brillouin zone. The primitive reciprocal lattice vector b_1 and b_2 have the length $4\pi/\sqrt{3}a$, where *a* is the length of the primitive vector. The middle point of the Brillouin zone is Γ and the corners are the alternating K, K´ points, also called Dirac points.

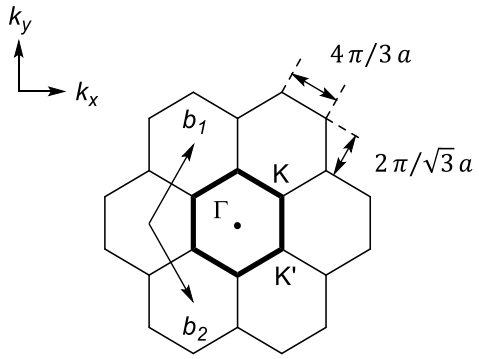

Figure 1.6. Reciprocal graphene lattice with k_x and k_y coordinates. b_1 and b_2 are the primitive lattice vector in reciprocal space. The highlighted hexagonal is the 1st Brillouin zone with middle point Γ and corner points K and K´.

The electronic structure of graphene depends on the interactions between orbitals within the lattice. Under the nearest-neighbor TB approximation, only the two p_z orbitals from carbon 1 and 2 in the unit cell which interact into π band and π* band, will be taken into consideration. The

calculation starts with the linear combination of well localized wave functions ϕ_1 and ϕ_2 of those two p_z atomic orbitals, gives a total function as: $\phi = c_1\phi_1 + c_2\phi_2$, where c_1 and c_2 are two constants. The final energy dispersion relation of π electrons is given by the equation: $E_{2D}(k_x, k_y) = \pm\gamma_0[1 + 4\cos\left(\frac{\sqrt{3}ak_x}{2}\right) \cdot cos\frac{ak_y}{2} + 4cos^2(\frac{ak_y}{2})]^{\frac{1}{2}}$, where k_x and k_y are the two components of wave vector k in reciprocal lattice, ± sign indicates the conduction band (π^* band) and valence band (π band), γ_0 is the nearest neighbor hopping energy with a value of approximately 2.7-3.0 eV.[17,18]

By plotting this function into 3D energy spectrum, one can obtain the visualized electronic dispersion or band structure of graphene, as shown in Figure 1.7(a). The valence (π) and conduction (π^*) band are located below and above the Fermi level, respectively. They meet each other at six Dirac points (K and K´) of each Brillouin zone, which leads to zero bandgap. Near to these points, the energy dispersion relation is near linear. Thus, pairs of symmetric Dirac cones are often used to demonstrate the band structure near Dirac points. An overview of the energy dispersion relation of π^* band by viewing from the top is also given in Figure 1.7(b) with equi-energy contour lines. The energy dispersion becomes quite clear with this map, which helps to understand the band structure of nanotubes later. To note, two neighboring saddle points (M) share one contour line, which means the energy stays the same along each nearest equi-energy M-M line.

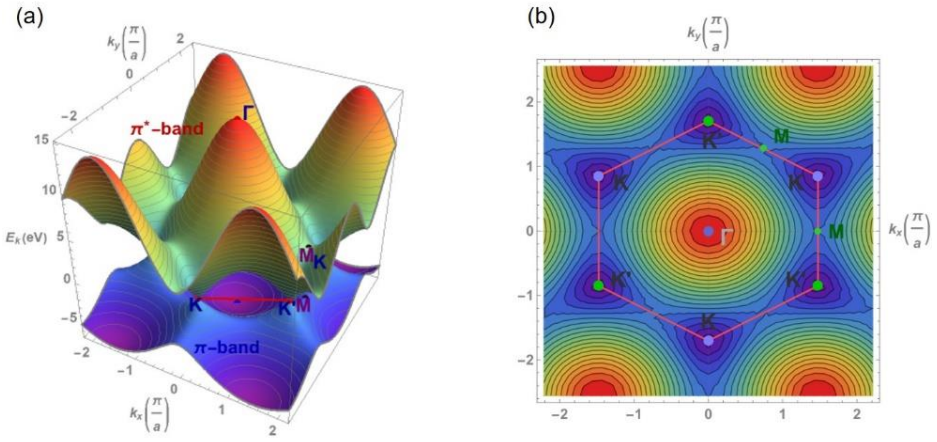

Figure 1.7. (a) Band structure of graphene under TB approximation. The upper part is antibonding π^* band with positive sign and the lower part is bonding π band with negative sign. The hexagon in the middle is the 1st Brillouin zone with Γ, K and K´ points as well the saddle points M; (b) 2D energy dispersion relation of π^* band. The contour lines indicate the energy level in the Brillouin zone. The spectrum is created with WOLFRAM Demonstrations Project, contributed by Vladimir Gavryushin (Vilnius University, Lithuania).

The first Brillouin zone and the critical points Γ, K and K´ are quite valuable for the derivation of the nanotube band structure. In Figure 1.8, the detailed band structure within the first Brillouin zone is illustrated, as well the energy dispersion along the high-symmetry directions in the zone. The conduction band and valence band meet each other on the Fermi energy level which equals 0 eV. The corresponding density of electronic states (DOS) is also given.

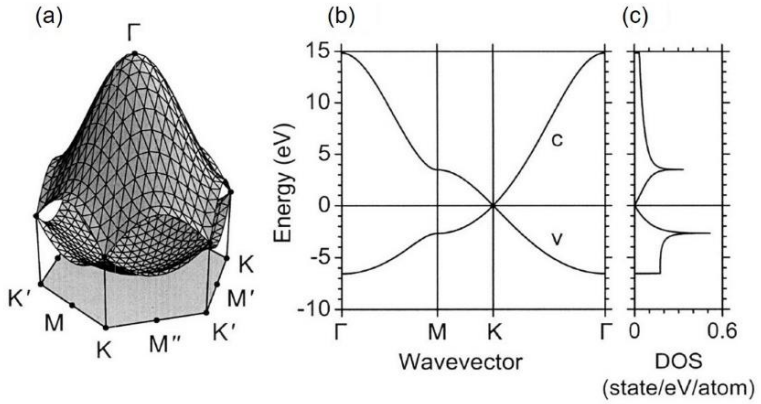

Figure 1.8. (a) The TB electronic dispersion relations for the π and π^* bands of graphene within the first Brillouin zone; (b) energy dispersion profile along the high-symmetry directions with *c* and *v* referring to conduction band and valence band respectively; (c) the corresponding density of electronic states (DOS).[19]

1.4.2 Cutting lines and first Brillouin zone of SWCNTs

The unit cell of a SWCNT in real space has been defined as a rectangle with chiral vector C_h and translational vector T. In reciprocal space of a nanotube, the lattice vectors related to C_h and T are K_1 and K_2 with magnitudes $|K_1| = 2/d$ and $|K_2| = 2\pi/|T|$, respectively. In real space, by rolling the unit cell along the chiral vector, a seamless tube can be obtained. However, due to rolled-up structure, the wave function of the unit cell has to obey the periodic boundary conditions along the circumference of the nanotube. As a consequence, the wave vector component along the circumference becomes quantized with discrete values and creates a set of equi-distant parallel lines called as cutting lines, whereas the other component along the nanotube axis can be assumed continuous. The distant or spacing between two adjacent cutting lines is $|K_1| = 2/d$. And the number of quantized states or cutting lines equals to the number of hexagons within the nanotube unit cell, and can be calculated by dividing the area of nanotube unit cell with the area of graphene unit cell in real space, resulting in the number of hexagons as $N = 2(n^2 + nm + m^2)/d_R$.[20] Thus,

the unit cell of 1D SWCNT in reciprocal space has been considered as a line with length $|\mathrm{K}_2| = 2\pi/|\mathrm{T}|$, just like 2D graphene layer has 2D unit cell in reciprocal space. The allowed wave vector *k* is continuous and lies on the cutting lines with the boundary of their length. The periodicity of this vector results from the translational symmetry of the SWCNT.[19]

The energy band structure of SWCNT can be obtained by superimposing the cutting lines on the first Brillouin zone of graphene in reciprocal space. So that the first Brillouin zone of a SWCNT becomes a set of *N* parallel segments bordered by cutting lines which are related to the chiral index (n,m) of this nanotube. The resulting electronic band structure of SWCNT can be described as $E_\mu(k) = E_{2D}(\mu\mathrm{K}_1 + k\frac{\mathrm{K}_2}{|\mathrm{K}_2|})$, where quantum number μ = -*N*/2+1, -*N*/2+2, …, 0, 1, …, *N*/2 and $-\frac{\pi}{|\mathrm{T}|} < k < \frac{\pi}{|\mathrm{T}|}$. Figure 1.9 shows the extended first Brillouin zone (gray rectangle) of an armchair nanotube (5,5) and a zigzag nanotube (5,0) centered at Γ point in graphene reciprocal space as examples. Those two nanotubes have the same number of cutting lines but different spacing, length and orientation. Each set of cutting lines locates in a rectangle highlight in gray. By crossing the 2D energy dispersion relation or 2D band structure of graphene in Figure 1.7 with the cutting lines of a given nanotube, we obtain two sets of *N* energy dispersion curves for π band and π^* band, which corresponds to $E_\mu(k)$.

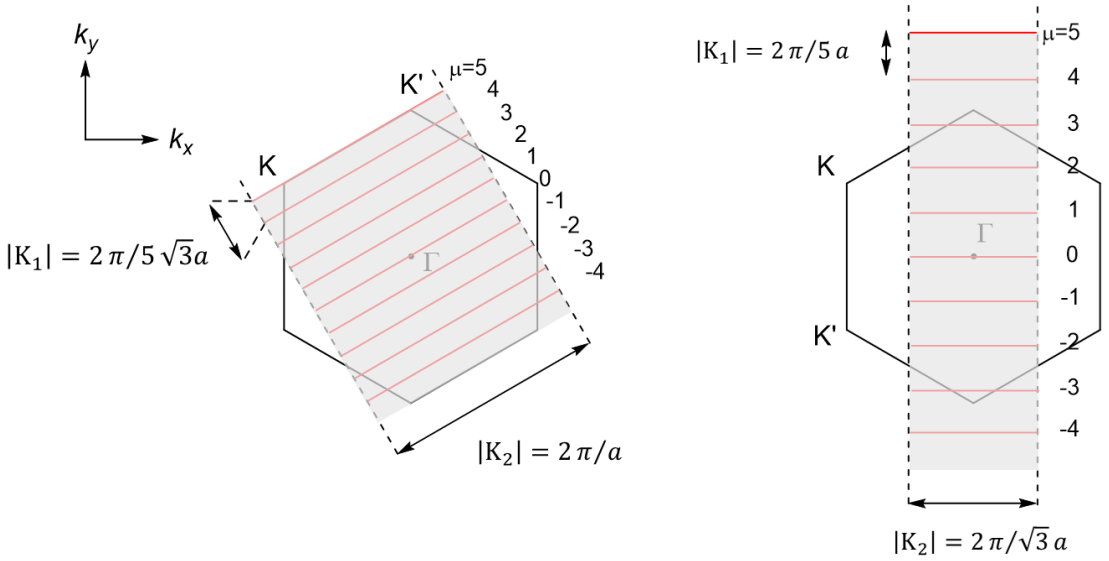

Figure 1.9. Extended first Brillouin zone of an armchair (5,5) SWCNT (left) and a zigzag (5,0) SWCNT (right) with cutting lines in rectangles (colored in gray) in reciprocal space of graphene, centered at Γ point.

The cutting lines are labelled with quantum number μ. The length and spacing of the cutting lines are also given.

To note, the cutting lines of (5,5) nanotube locate almost all inside the first Brillouin of graphene reciprocal lattice, whereas (5,0) nanotube has cutting lines in neighboring Brillouin zones. In the case of (5,0) nanotube, three of the cutting lines cross two Brillouin zones and two of the cutting lines, which are closet to the K-points, even cross three Brillouin zones. Since the *k* vector is 1D and continuous in the reciprocal space, the obtained energy dispersion relations of those multi-zone cutting lines are still meaningful. However, with the increasing number of cutting lines, more Brillouin zone need to be taken into consideration when collecting all the energy dispersion relations along the cutting lines.

If we calculate the area of the rectangle where all the cutting lines and sections locate, the area is as same as the area of one Brillouin zone. It indicates that the extended first Brillouin zone of a random (n,m) SWCNT can fit into the first Brillouin zone of graphene in reciprocal space. In other words, one Brillouin zone can hold all cutting lines of a nanotube inside the area with a fully reduced representation described by Samsonidze *et al*.[20] In Figure 1.10, the cutting lines of a chiral (4,2) SWCNT are extended in K_1 direction in graphene reciprocal space over several Brillouin zones, whereas in a fully reduced representation, all cutting lines are placed into the first Brillouin zone of graphene.

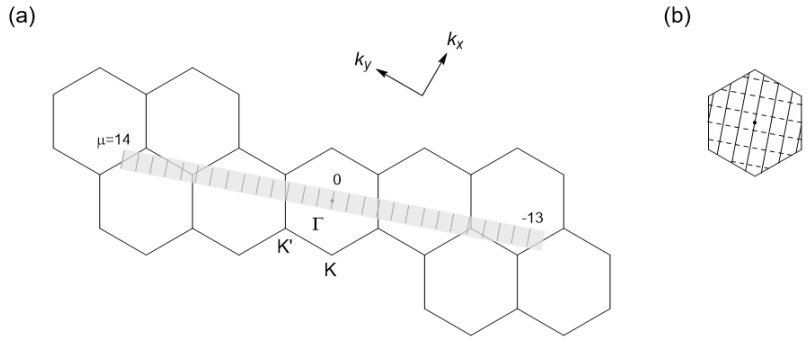

Figure 1.10. (a) Extended first Brillouin zone of a chiral (4,2) SWCNT with cutting lines in a rectangle (colored in gray) in reciprocal space of graphene; (b) The fully reduced representation of the cutting lines within the first Brillouin zone of graphene. The solid line segments are the cutting lines, while the dashed line segments represent the borders of the rectangle.[20]

Each solid line in Figure 1.10(b) consists of several cutting lines and reaches the edge of the first Brillouin zone of graphene, where the critical points K, K´ and M locate. This is of great

importance when evaluating the 1D band structure of a SWCNT. For a better understanding of the benefit of this representation, we superimpose those cutting lines on the 3D band structure of graphene within the first Brillouin zone as shown in Figure 1.11. Each solid curve is a cutting line with dots indicating the boundaries. In this diagram, the obtained energy dispersion along each cutting line of (4,2) nanotube becomes quite visible and easy to evaluate.

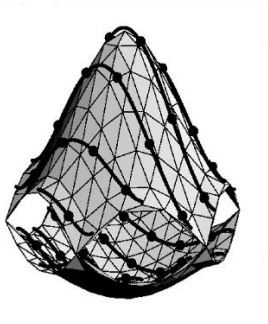

Figure 1.11. 3D band structure of graphene within the first Brillouin zone under TB approximation. Solid curves represent the cutting lines of (4,2) SWCNT and the dots indicate the boundaries of each cutting line.[20]

1.4.3 1D band structure and density of electronic states of SWCNTs

As introduced already, the energy dispersion along each cutting line can be derived by superimposing the cutting line on the 3D band structure of graphene within the first Brillouin zone. If we follow the zone-folding method, which was developed by Saito, Dresselhaus and *et al.*,[18] and plot all the dispersion relations into one diagram, we obtain the 1D Brillouin zone also known as 1D band structure of a SWCNT.

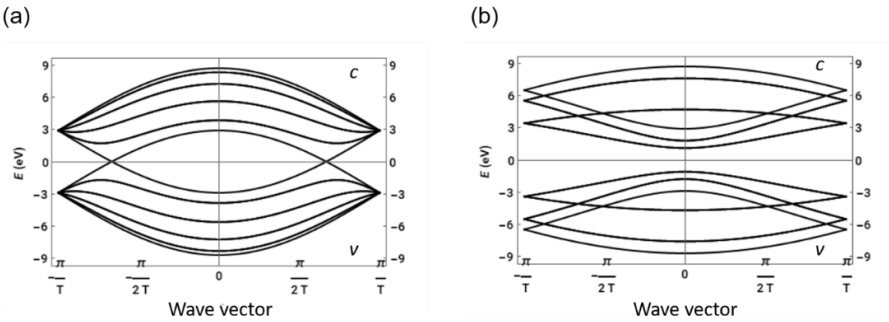

Figure 1.12. 1D band structure of (a) armchair (5,5) SWCNT (metallic) and (b) zigzag (5,0) SWCNT (semiconducting). *c* denotes the conduction band and *v* denotes the valence band. The diagrams are created with WOLFRAM Demonstrations Project, contributed by Jessica Alfonsi (University of Padova, Italy).

Figure 1.12 shows the 1D band structure of (5,5) and (5,0) SWCNTs. The upper halves with $E > 0$ belong to the conduction bands while the lower halves with $E < 0$ belong to the valence bands. Each cutting line gives one dispersion relation in the conduction band as well in the valence band. The dispersion relations of (5,5) nanotube meet each other at two K points and lead to zero bandgap, which means (5,5) armchair nanotube is metallic. The cutting lines of zigzag (5,0) nanotubes don't cross any K points so that it's a semiconducting nanotube with a non-zero bandgap. It is worth noting that not all the cutting lines from (5,0) nanotube give a curve in its 1D Brillouin zone. The reason for that is the degeneracy of the quantized states with the same energy. Here, the cutting lines with μ of ±1, ±2, ±3 and ±4 are degenerate, resulting only six dispersion curves in the conduction and valence band. The two lowest dispersion curves in Figure 1.12(b) are from the cutting lines with μ = ±3 and μ = ±4, which are the nearest cutting lines to K points. The resulting energy bandgap of approximately 2 eV and the following transition bands are of great importance to the absorption behavior and other phenomenon of such SWCNT, because these energy levels lie in the visible region. Since the cutting lines in the vicinity of K points are critical for predicting the electronic properties of a SWCNT, we can thus emphasize the shape of the Dirac cones and the relative positions of the nearest cutting lines instead of all of them in one complete Brillouin zone.

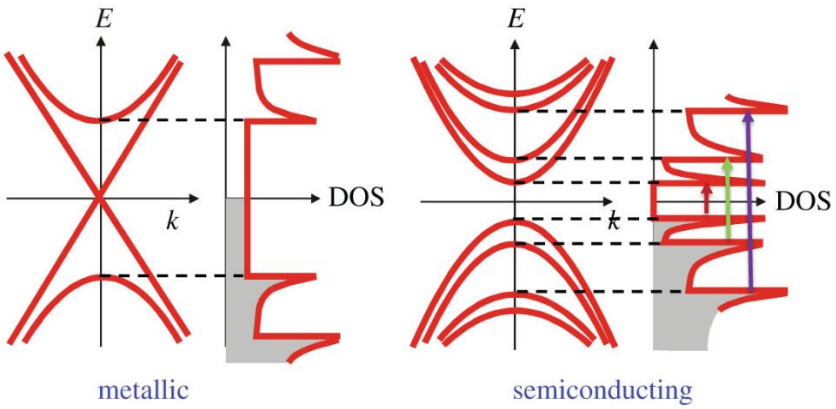

Figure 1.13. Simplified 1D band structure of m- and s-SWCNT with corresponding DOS.[21]

The 1D band structure of a SWCNT can be interpreted into the density of electronic states (DOS), which describes the number of each possible electronic states in the system. Figure 1.13 shows the typical DOS of m- and s-SWCNTs with corresponding simplified band structures. Each dispersion relation (also called subband) with a saddle point gives a spike in the DOS, which is called van Hove singularity (VHS). The VHSs are symmetric at Fermi level just like the band structure. The DOS of metallic nanotubes is continuous because of the overlap of conduction and valence band. The open bandgap in the DOS of semiconducting nanotubes is defined by the distance between two VHSs nearest to Fermi level. The transition energy can be calculated as $E_g = \gamma_0(2a_{c-c}/d)$ by applying the TB approximation, where γ_0 = 2.9 eV is the nearest neighbor C-C interaction energy, $a_{c-c} = 1.42$ Å is the nearest neighbor C-C distance and d is the tube diameter. Metallic nanotubes don't have real bandgap and the energy interval between two nearest VHSs to Fermi level is $3E_g$.[22]

1.5 Optical properties and characterization methods of SWCNTs

Optical properties of SWCNTs with chiral indices (n,m) can be investigated by various optical spectroscopies as a single-chirality species or as a mixture of more chiralities. The obtained spectroscopic results can be explained with the help of theoretical calculations and predictions. In this chapter, basic optical properties will be introduced and discussed including the relevant characterization methods such as absorption, photoluminescence excitation, Raman and circular dichroism spectroscopies.

The optical processes of SWCNTs in correlation with the spectroscopies start with the interaction with light, more specifically with the electron-photon interaction. In SWCNTs, the optical transition happens in the visible region between the valence band (π band) and conduction band (π^* band). When an electron from a valence subband absorbs a photon with certain energy and excites into a conduction subband, general selection rules corresponding to the polarization of the light must be followed: (a) For light polarized parallel to the SWCNT axis, only transitions between valence and conduction subbands with the same quantum number μ value ($\mu \rightarrow \mu$), i.e. from the same cutting line with no angular momentum difference, are allowed; (b) For light polarized perpendicular to the SWCNT axis, only transitions between valence subbands μ and conduction subbands $\mu \pm 1$, i.e. from the neighboring cutting lines with angular momentum difference, are allowed.[23]

1.5.1 Absorption spectroscopy

For s-SWCNTs, when the energy of light reaches the minimal value required for optical transition (E_g), the electrons can be excited from the highest occupied valence subband to the lowest empty conduction subband. With increasing energy of light, interband transitions of higher orders occur following the selection rules. Generally, VHSs in the DOS profile represent the density of local electronic states. So, when the excitation energy for the sample reaches the gap between two VHSs from valence and conduction bands, a significantly enhanced absorption of light can be observed. Due to this reason, we discuss the absorption behavior of SWCNTs based on the VHSs in the DOS instead of the 1D band structure with dispersion curves. A typical DOS profile of s-SWCNTs with E_{ii} transition bands is given in Figure 1.14.

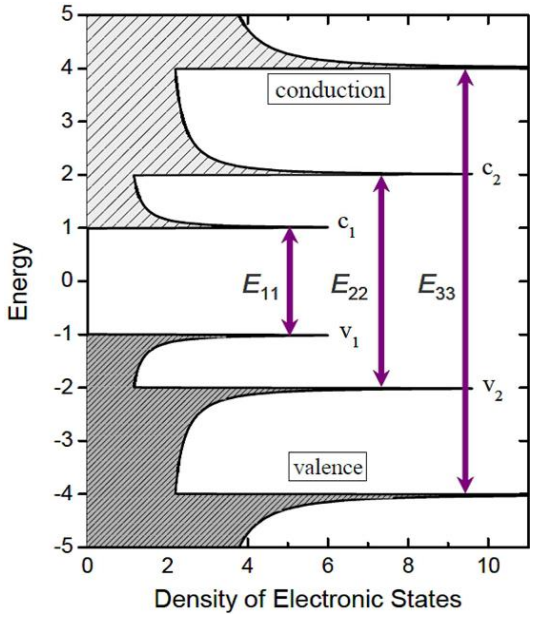

Figure 1.14. A typical DOS profile of s-SWCNTs. The VHSs are labelled as c_i and v_i, with c and v denoting the conduction and valence band respectively. The index i indicates the VHS number counting from the Fermi level. The transition energy between VHSs with the same index is defined as E_{ii}, such as E_{11}, E_{22} and E_{33} which are presented with arrow in the figure.[24]

In this transition process, the incident light having random polarization directions propagates towards the sample while the individual nanotubes are considered to be randomly orientated. Under these circumstances, the optical transition is dominated by the absorption of light polarized parallel to the tube axis, which leads to the transition between v_1 and c_1, v_2 and c_2, etc. The corresponding transition energies are E_{11}, E_{22} and *et al*. The cross transitions with energy (E_{ij}) are suppressed by the depolarization effect and thus extremely weak.[25] In the case of m-SWCNTs, the energy of E_{11} is $3E_g$ which means is three times higher than E_{11} of s-SWCNTs.

In 1999, Kataura *et al*. published the famous Kataura plot and thus established guidelines for the optical characterization of carbon nanotubes.[26] Later in 2003, Weisman *et al*. predicted the first (E_{11}) and second (E_{22}) van Hove optical transitions for s-SWCNTs with a certain diameter between 0.48-2.5 nm. With the help of the direct bandgap photoluminescence (PL), they presented an empirical Kataura plot of both experimental and predicted optical transition energies E_{ii} as a function of nanotube diameter, as shown in Figure 1.15.[27]

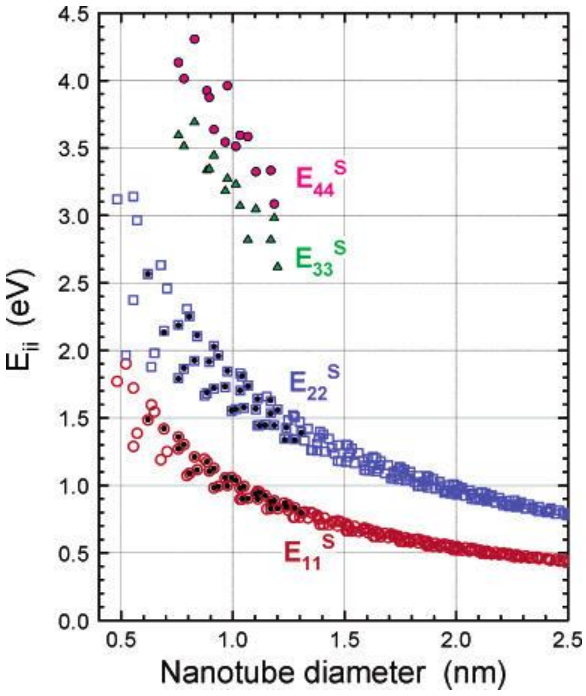

Figure 1.15. Empirical Kataura plot: optical transition energies vs diameter for s-SWCNTs. The filled symbols represent experimental data and the empty symbols represent predicted data of E_{11} and E_{22}, respectively. *S* denotes semiconducting.[27]

From this empirical Kataura plot, one can clearly see that the transition energy E_{ii} between symmetric VHSs is decreasing with increasing diameter, which correlates with the bandgap energy equation. Small diameter SWCNTs absorb mainly in the UV-Vis region (above 1.6 eV) while large diameter SWCNTs absorb in the near-infrared (NIR) region. The four optical transition energies E_{ii} of SWCNTs with chiral index (n,m) separate well from each other which simplifies the determination of a single chiral entity in complex mixture. And this is indeed how we assign the optical transition bands of different SWCNTs in our samples, since we mainly process samples that contain diverse chiralities.

As-produced SWCNTs exist both as thick bundles due to their high surface energy and strong van der Waals force, and as a mixture of nanotube species with various diameters and lengths, resulting broad absorption bands when they are dispersed before purification. The purification and sorting processes help to disperse the SWCNTs in a way that the tubes are mainly present as individual entities instead of bundles, which causes the broad peaks to split into several sharp peaks that belongs to different nanotube species. For example, the dashed curve in Figure 1.16 represents the absorption spectrum of an as-produced sample (laser-ablation-grown) in a co-surfactant

solution. The broad peak in S_{22} region (E_{22} for s-SWCNTs) comes from the bundles in the raw material. The peaks in M_{11} (E_{11} for m-SWCNTs) region indicate that this sample contains as well several metallic species. After the sorting process according to the electronic type, the raw sample has been separated into enriched m- and s-SWCNTs as shown with blue and red curves. The peaks in S_{22} and S_{33} region for s-SWCNTs become sharper due to the well dispersion of individual nanotubes, and the flatness in M_{11} region proves the total separation of m-SWCNTs.

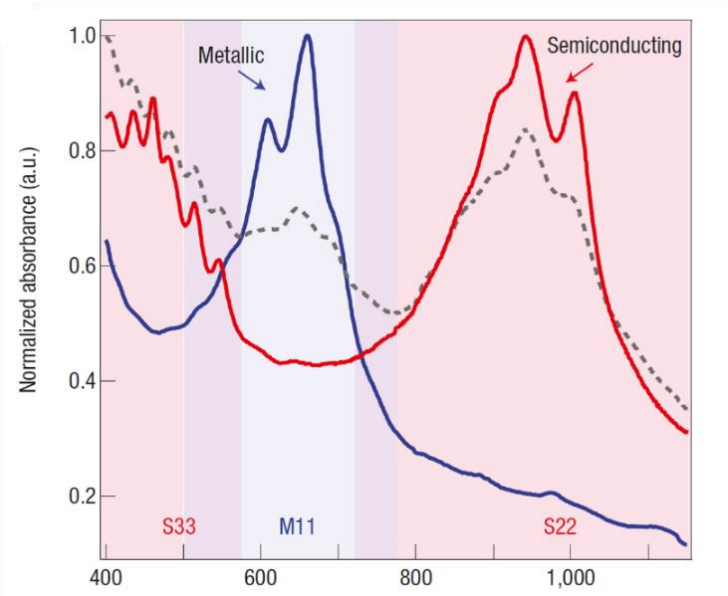

Figure 1.16. Absorption spectra of laser-ablation-grown SWCNTs separated in a co-surfactant solution. The absorption spectrum of the sample before the separation is given as a dashed curve. The spectra of separated m- and s-SWCNTs are shown as blue and red curves, respectively. S_{22}, S_{33} denote the E_{22} and E_{33} transition bands for s-SWCNTs. M_{11} denotes the E_{11} transition bands for m-SWCNTs.[28]

1.5.2 Photoluminescence excitation spectroscopy (PLE)

During the excitation process, an electron jumps from the valence band to the conduction band and leaves a positive charge behind. This electrostatically bound two particle system (electron-hole) is called an exciton. Photoluminescence (PL) occurs when an electron-hole pair recombines after allowed relaxation and emits a photon (radiative). In s-SWCNTs, PL is mostly expected when the nanotubes absorb light at E_{22} transition band and emit at E_{11} band, as illustrated in Figure 1.17. In the case of m-SWCNTs, electrons decay non-radiatively.

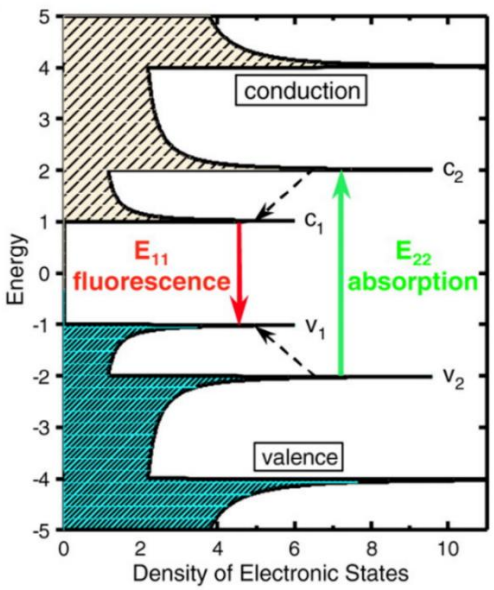

Figure 1.17. A DOS profile of s-SWCNTs. The green arrow denotes the absorption at E_{22} band and the red arrow denotes the fluorescence at E_{11} band. Dashed arrows indicates the non-radiative relaxation of electron and hole before emission.[29]

The characteristic wavelength range for E_{22} and E_{11} bands of as-produced s-SWCNTs are between 500-950 nm and 950-1700 nm, respectively. For example, when a (7,5) SWCNT excites at 645 nm and emits at 1024 nm, a characteristic spot appears in the 2D-PLE map (y as excitation axis, x as emission axis). Thus, by performing PLE spectroscopy and with the guidance of an empirical Kataura plot, it is possible to assign or identify all bright spots in a PLE map corresponding to the individual chirality of SWCNT. For instance in Figure 1.18, the PLE map of poly(9,9-di-n-dodecylfluorenyl-2,7-diyl) (PODOF) wrapped SWCNTs shows the presence of multiple nanotube species in this sample with a different concentration that corresponds to the signal intensity. The spots are well separated from each other in this 2D map, which makes the assignment easy.

PLE measurement can be carried out in various solvents. However, a good PLE map requires a well dispersed sample in the solvent with as less aggregate or bundles as possible. Moreover, there are several factors that can quench the PLE signal e.g. inter-tube energy transition due to aggregations, interaction of s-SWCNTs with m-SWCNTs, solvent and concentration effects.[30–33] However, there are also methods for brightening the PL of nanotubes, such as incorporation of sp^3 defects to the nanotube structure after chemical functionalization e.g. with aryl diazonium salts.[34]

Besides the absorption and emission at E_{22} and E_{11}, other minor but interesting features e.g. transverse $E_{12,21}$ excitations, G-and G´-phonon-coupled PLE satellites can also be observed.[35] In general, more structural information about the SWCNT can be obtained from PLE than from absorption spectroscopy.

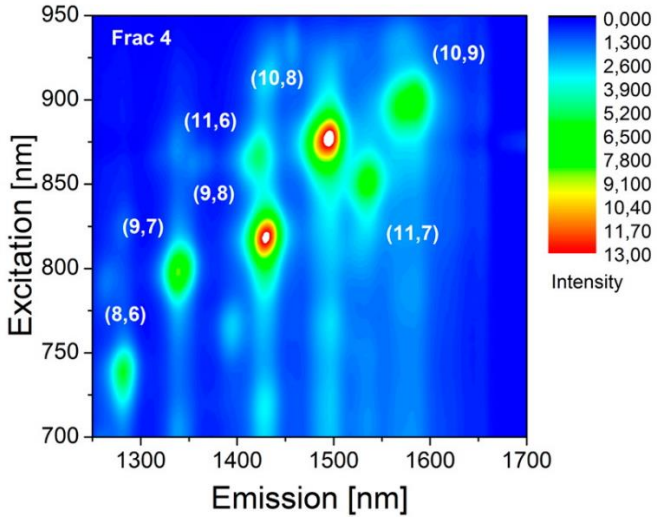

Figure 1.18. A PLE map of PODOF wrapped SWCNTs. Chiral indices (n,m) are assigned to each spots on the map.[36]

1.5.3 Raman spectroscopy

Raman spectroscopy is one of the most powerful methods for the characterization of SWCNTs, which requires only minimal sample preparation and still provides valuable structural information about m- and s-SWCNTs. Raman scattering describes the inelastic scattering of light. When the incident light gets scattered in carbon nanotubes, only small fraction of the scattered light can be scattered inelastically, leading to an energy loss or gain due to the emission or absorption of a phonon from carbon nanotubes.[37] Raman spectra of SWCNTs contain several characteristic peak modes such as G'-band, G-band, D-band and radial breathing mode (RBM). A typical Raman spectrum of SWCNTs is given in Figure 1.19 with above mentioned modes.

The G band (or graphite band) is located at ~ 1580 cm^{-1} and is commonly associated with the sp^2 hybridized carbon atoms in the nanotube wall. For SWCNTs, the G-band is split into two components, G^+ and G^-. The G^+ peak has higher intensity and results from the vibrations of carbon atoms along the nanotube axis, while the G^- peak with much lower intensity denotes the vibrations

of carbon atoms along the nanotube circumference. As for m-SWCNTs, their G band shows a asymmetric feature of Breit-Wigner-Fano (BWF) line shape.[38] The D band is at ~1300 cm^{-1} and originates from the structural defects in the nanotube structure. Therefore, the ratio of G/D is commonly used to evaluate the structural quality and purity of carbon nanotubes. Defects can be either brought to the nanotubes during the production or introduced afterwards by covalent functionalization.[39] The G' band is the second overtone of the defect induced D band, also called as 2D.[37,40]

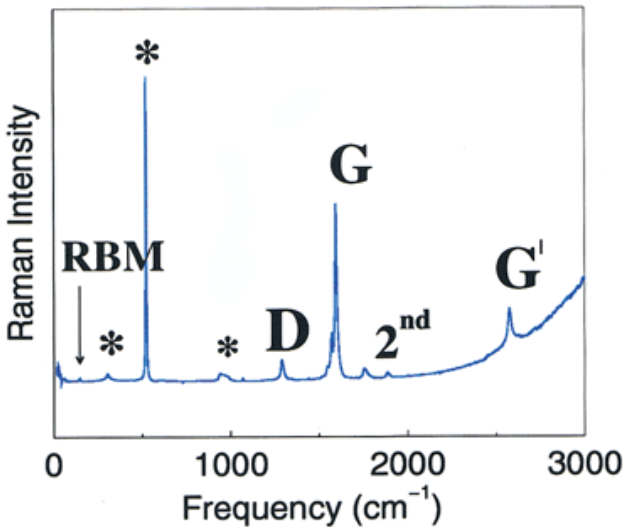

Figure 1.19. Raman spectrum from a single nanotube using excitation wavelength of 785 nm with characteristic G'-band, G-band, D-band and RBM mode. The symbol * denotes the signal from Si/SiO_2 substrate.[40]

Radial breathing mode (RBM) corresponds to the vibration of the nanotubes in radial direction (expansion-contraction). The peaks are located in the low frequency region between 150 cm^{-1} and 300 cm^{-1}. The position of the RBM peaks corresponds to the individual chiralities of nanotube and can be determined by the relation with the tube diameter: $\omega_{RBM} = A/d + B$, where A and B are empirically determined parameters related to the nanotube environment.[41,42] It is worth noting that, only the nanotubes which have S_{22} (for s-SWCNTs) or M_{11} (for m-SWCNTs) transition energy close to the laser energy can be observed in the RBM. Therefore, the excitation wavelength has to be chosen carefully according to the average diameter of the nanotubes within the sample in order to keep a good interpretation of the RBM.

Beside the chirality assignment, the RBM is also a strong tool to evaluate a highly enriched s-SWCNTs sample. Figure 1.20 shows the Raman spectra (RBM) of SDBS and PFO dispersed SWCNT samples. From the black line, it is quite obvious that PFO has a selectivity towards (7,5) nanotube and more importantly, the metallic nanotubes are totally removed.

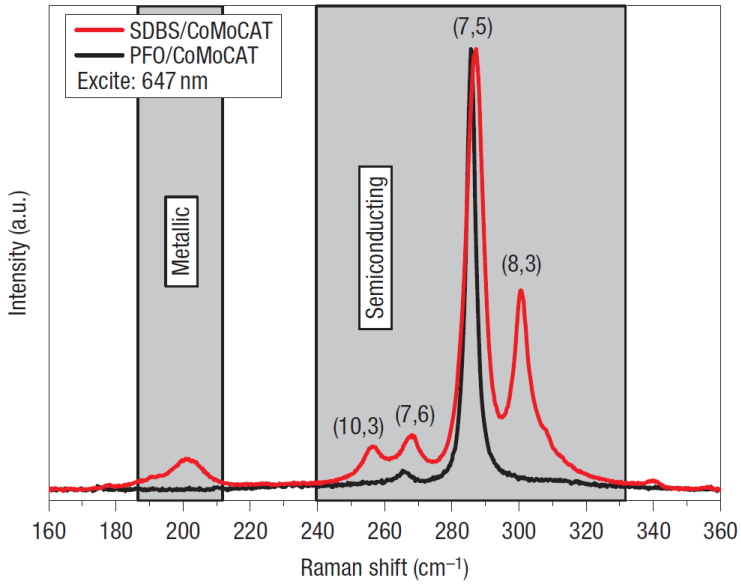

Figure 1.20. Raman spectra (RBM region) of SDBS dispersed (red line) and PFO dispersed (black line) CoMoCAT SWCNTs with excitation wavelength of 647 nm.[43] SDBS refers to sodium dodecylbenzene sulfonate and PFO refers to poly(9,9-dioctylfluorenyl-2,7-diyl).

The sample preparation for Raman spectroscopy is rather quick and easy. Unlike for absorption and PLE spectroscopy which requires well dispersed nanotube samples in solution, only a little amount of solid nanotubes is needed for Raman spectroscopy.

1.5.4 Circular dichroism spectroscopy

Circular dichroism (CD) spectroscopy is an absorption spectroscopic method based on the differential absorption of left-handed circularly polarized light (LCP) and right-handed circularly polarized light (RCP). The electric field vector of circularly polarized light rotates around the propagation direction axis while for linearly polarized light, the electric field vector oscillates in one plane (Figure 1.21).

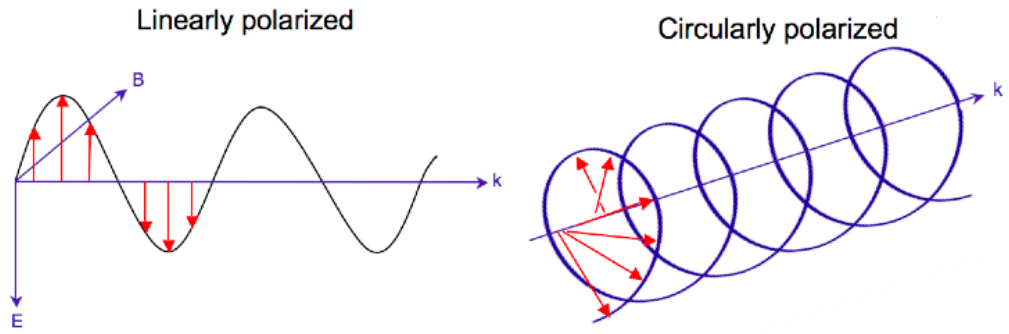

Figure 1.21. A demonstration of linearly polarized light (left) and circularly polarized light (right).[44]

Optically active molecules or materials preferentially absorb one direction of the circularly polarized light. The resulting difference in absorption (ΔA) of LCP and RCP leads to a CD spectrum with non-zero value: $\Delta A(\lambda) = A(\lambda)_{LCP} - A(\lambda)_{RCP}$, where λ is the wavelength. The measurements are normally carried out in UV-Vis region, but can be extended into NIR region. The sign of the CD signals is either positive or negative, depending on whether LCP is absorbed more or less than RCP. CD signals are commonly recorded in ellipticity (θ) which correlates with the difference in absorption as: $\Delta A = \theta/32.982$, where ellipticity θ has the unit of millidegree (mdeg).[45]

Chiral SWCNTs have chiral angle between 0-30° (Figure 1.3) and each of them consists of left-handed and right-handed mirror enantiomers in equal amount (racemate). Once one of the enantiomers is partially or fully separated from the other, the sample shows optical activity. Thus, CD spectrum with a non-zero value is observed from an optically enriched sample with an enantiomer excess (*ee*) or from an enantiomeric pure SWCNT sample.

CD spectra of SWCNTs have been theoretically calculated by Sánchez-Castillo *et al*. using a dipole approximation and first-principles studies.[46,47] However, the calculated results could not correlate well with the experimental results. Later, Saito *et al*. comprehensively calculated CD spectra of SWCNTs by the tight binding method as a function of the wavelength.[48] In their calculation, they considered the optical absorption of SWCNTs for the circular polarized light with propagation direction parallel and perpendicular to the nanotubes axis separately. Due to the time reversal symmetry between K and K' points in the Brillouin zone, the absorption probability of a SWCNT for LCP and RCP at those points cancel each other and leads to a zero CD value. However, after taking the phase factor of light ($\tau = T/\lambda$) into consideration, the quenching of K and K' points

does not occur, which results in non-zero CD values. Their numerical calculations show that (1) the sign of the CD values for a nanotube of one handedness alternates at each E_{ii} van Hove singularity; (2) the signs of the CD values at each E_{ii} are opposite for left- and right-handed enantiomers. The experimental results fully agree with the calculated spectra, especially the E_{ii} transitions are equal.

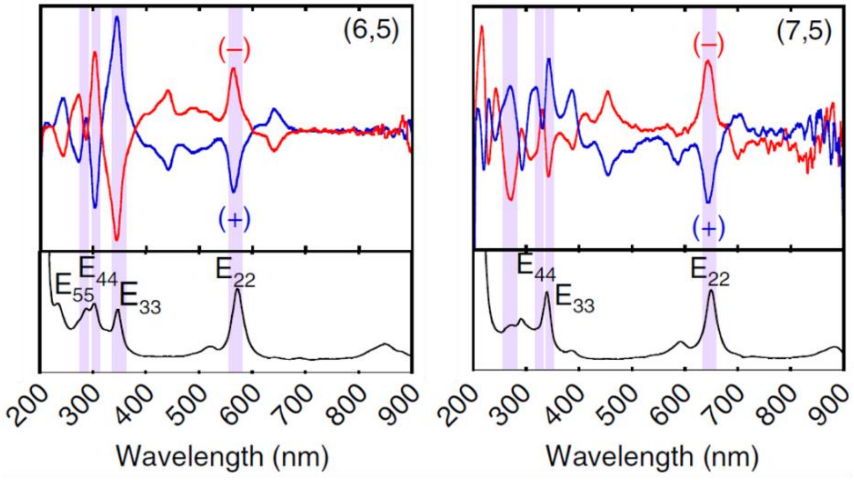

Figure 1.22. Experimental CD spectra and absorption spectra of (6,5) and (7,5) enantiomers.[49]

Later, Saito and Kataura *et al*. separated 12 different single chirality enantiomers using gel column chromatography. Due to the high enantiomeric purity of obtained SWCNTs, the samples show strong CD intensity and characteristic features.[49] Figure 1.22 demonstrates the CD spectra of (6,5) and (7,5) single chirality enantiomers from their work. In the spectra, (+) and (-) signs denote to the enantiomers with negative and positive E_{22} CD peaks, respectively. Both enantiomers exhibit typical mirror images of CD spectra as well the alternating signs of CD peaks at E_{11}, E_{22} and E_{33}. Each E_{ii} peak corresponds to a peak in absorption spectrum, which simplifies the assignment. The relative enantiomeric purity of the enantiomers can be determined by normalized CD intensity: $CD_{norm} = (CD_{raw}/L_{CD})/(A_{E22}/L_{abs})$, where CD_{norm} and CD_{raw} are the CD intensity of the E_{22} transition peak after and before normalization, A_{E22} is the absorbance at E_{22}, L_{CD} and L_{abs} are the optical path lengths (cm) of the cell used for the CD and absorption analysis.[50]

Interestingly, during their experiments they found out that the separated enantiomers of some nanotube species behaved differently than the others, for instance (6,5) nanotubes required higher concentration of sodium deoxycholate (DOC) for the (-)-enantiomers than for the (+)-enantiomers, whereas (7,5) required higher concentration of DOC for the (+)-enantiomers instead of (-)-

enantiomers. Also, the separation order of (+)- and (-)-enantiomers for (6,5) and (7,5) SWCNTs was reversed. These experimental phenomena can be explained by theoretical calculation as given in Figure 1.23.

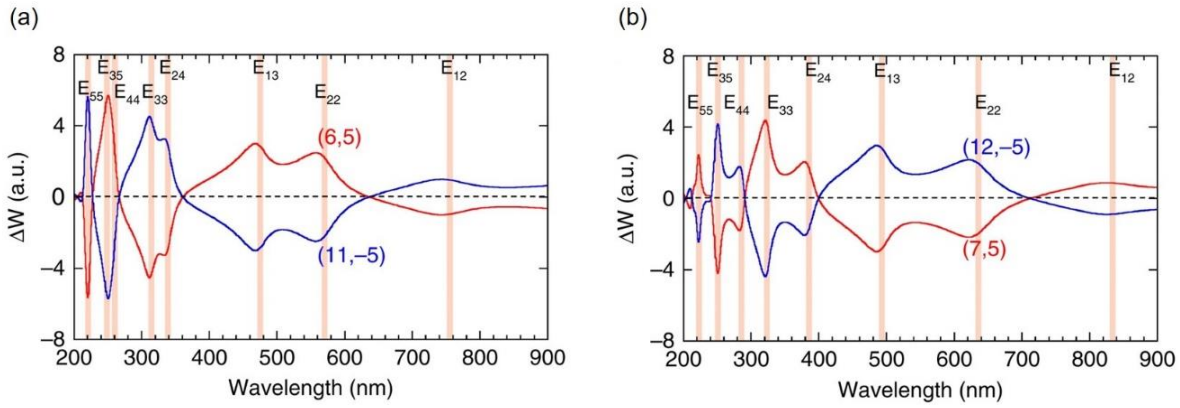

Figure 1.23. Calculated CD signals with the difference of absorption probability ΔW as a function of wavelength. (a) (6,5) and (11,-5) enantiomers; (b) (7,5) and (12,-5) enantiomers. E_{ii} and E_{ij} transitions are highlighted as orange lines.[49]

From the calculated CD spectra, left-handed (or right-handed) (6,5) and (7,5) SWCNTs have opposite sign for each E_{ii} and E_{ij} transition peaks, which means they response reversely towards circular polarized light even though they have the same handedness. This phenomenon originates from the different types of carbon nanotubes that they are categorized to, either type 1 or type 2 (Figure 1.24).[19]

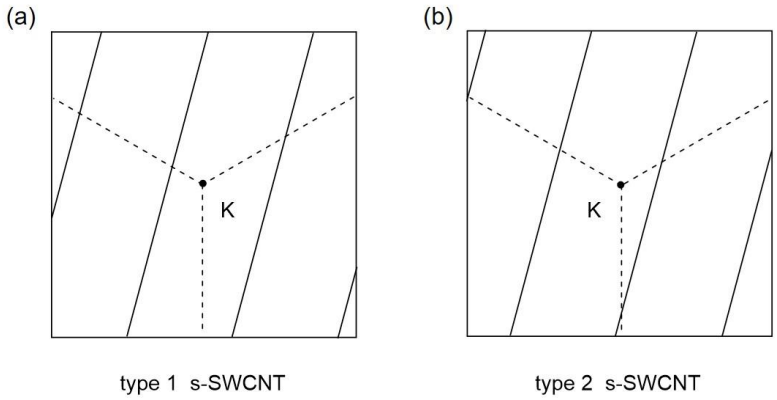

Figure 1.24. Cutting lines for type 1 (a) and type 2 (b) s-SWCNTs in the reciprocal space of graphene. The cutting lines are numbered according to the distance to the K point, from the closest to the farthest.

Type 1 and type 2 SWCNTs are both semiconducting and have none of the cutting line crosses the K point in the reciprocal space of graphene. Type 1 and type 2 SWCNTs have $mod(n-m,3)$

of 1 and 2 respectively, where $mod(x, y)$ is the remainder of the division of x by y. The number of the cutting line corresponds to the E_{ii} van Hove transitions. From Figure 1.24 one can see that E_{ii} transitions of type 1 and type 2 nanotubes occur at the opposite position in regard to the K point, resulting in the opposite dipole moments around the K point and opposite signs of E_{ii} transition peak. Metallic nanotubes have $mod(n - m, 3) = 0$ and cutting lines are crossing the K point.

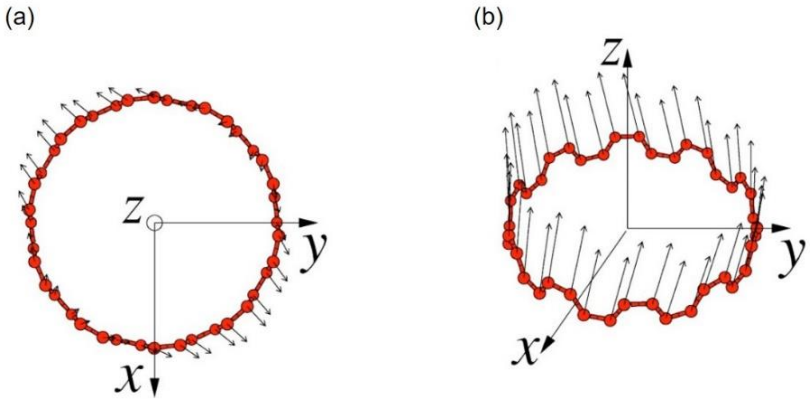

Figure 1.25. Views of atomic dipole vectors for a (10,10) carbon nanotube from the top (a) and from the side (b). The arrows in (a) denote the x and y components of the dipole vector for each carbon atom while the arrows in (b) denote to the z component.[51]

In general, CD measurements are carried out in solution. Thus, absorption of circularly polarized light by randomly oriented SWCNTs in the sample follows the dipole selection rule. Despite of the propagating direction of light towards each single nanotube, the overall polarization vector of the light for each carbon atom of the nanotube surface is different from one another. The sum of the x and y components of the dipole vectors from each carbon atom contribute to the polarization of light perpendicular to the tube axis, which allows the E_{ij} cross transitions. And the sum of the z components contributes to the polarization of light parallel to the tube axis, which allows the E_{ii} transitions (Figure 1.25).[51]

1.6 Production of SWCNTs

The research focus on SWCNTs is growing rapidly, thus SWCNTs with high structural purity and large quantity are demanded. In this chapter, organic synthetic approach and the most important techniques for the production of SWCNTs in bulk will be discussed. Details of the commercially available HiPco, PLV and CoMoCAT SWCNTs, which are commonly used as raw material for nanotube research, will also be presented.

1.6.1 Organic synthesis of SWCNTs

Organic synthetic approach or bottom-up synthesis has always been considered promising towards SWCNTs with the desired chirality. The idea of this approach is to first synthesize a precursor or template, from which a carbon nanotube would then extend by the addition of corresponding building blocks or grow with a continuous feed of carbon source under certain conditions. Due to the total control over the synthesis and growth, the resulting SWCNTs are expected to be defect-free and ultra-pure.

Numerous ring-shaped and cap-shaped aromatic hydrocarbons have been synthesized as a template or building blocks for the construction of SWCNTs.[52] However, due to the low solubility and low processability of the large aromatic hydrocarbons, less progress in templated organic synthesis of SWCNTs has been reported except a few small models. Later, several methods have been developed for growing SWCNTs from such aromatic hydrocarbon templates in combination with CVD.[52]

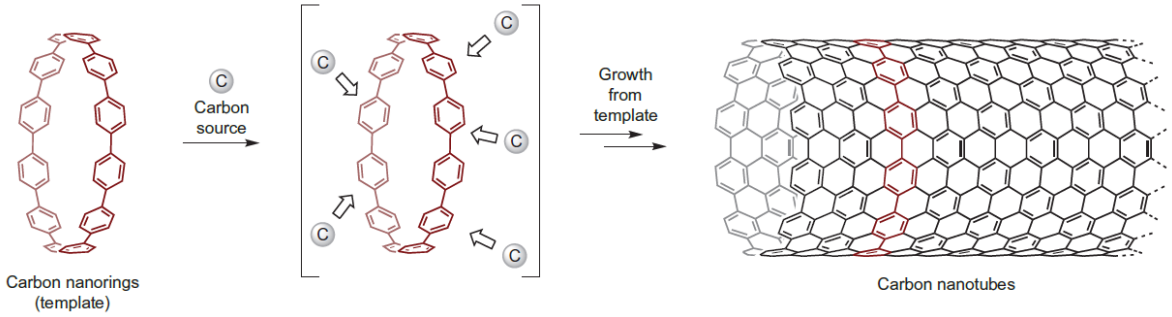

Figure 1.26. General strategy for CNT growth using a carbon nanoring [12]CPP as a template.[53]

A representative example using the template synthesis of CNTs was demonstrated by Itami *et al*. in 2013.[53] They first synthesized a series of cycloparaphenylenes (CPPs) such as [12]CPP (Figure 1.26) to use these nanorings as templates to initiate the growth of SWCNTs under a flow of ethanol as carbon source at 500 °C. The large majority of the obtained CNTs were between 1.3-1.7 nm in diameter, which is close to that of [12]CPP (1.7 nm), however the chirality control during the growth was lost possibly due to the thermal decomposition of CPPs at high temperature.

Another example was later presented by Fasel *et al*. in 2014.[54] They proposed a two-step synthesis of SWCNTs starting with the precursor $C_{96}H_{54}$ as shown in Figure 1.27. The precursor P1 was synthesized by multi-step organic synthesis. Finally, a singly capped ultra-short (6,6) SWCNT S1 (approximately 4-5 Å) was obtained by intramolecular cyclodehydrogenation (CDH) of P1 which was later deposited on a Pt (111) surface and annealed. The subsequent epitaxial elongation of (6,6) SWCNT seed S1 via surface-catalyzed C2 incorporation was carried out by CVD with ethanol as a carbon feedstock. This method was successful, but the yield of obtained SWCNTs was rather low and hard to quantify.

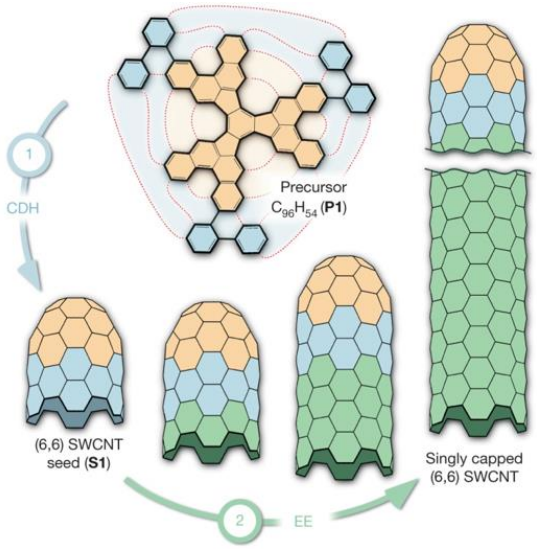

Figure 1.27. Two-step bottom-up synthesis of SWCNTs: (1) formation of seed S1 via cyclodehydrogenation (CDH) of precursor P1; (2) growth via epitaxial elongation (EE).[54]

1.6.2 Techniques for production of SWCNTs in bulk

The arc-discharge carbon plasma method for the production of carbon nanotubes was first introduced by Iijima *et al*. in 1991 and was initially used to produce fullerenes.[2] In this method, a pair of graphite electrodes are held at short distance and a direct or alternating current is generated under an inert gas atmosphere (helium or argon). The evaporated graphite is deposited on the chamber walls or electrodes. MWCNTs can be produced by arc discharge without any metal catalyst.[55] While for achieving SWCNTs, metal catalysts need to be coated on the graphite electrodes, such as Ni, Fe and Co.[56–58] The obtained SWCNTs have a good quality, varying lengths, and little defects. However, the addition of metal catalysts during the process brings also significant impurities such as catalyst particles and amorphous carbon materials.

The principally similar laser ablation method was first developed by Smalley *et al*. in 1995.[59] In this process, a pulsed laser vaporizes a graphite target which consists of raw natural graphite doped with catalyst nanoparticles (such as Ni and Co) in a high-temperature reactor under an inert gas atmosphere.[60,61] The nanotubes produced by laser ablation are purer (up to about 90% pure) than those produced in the arc process,[62] and are primarily SWCNTs with a narrow diameter distribution. The main drawback of the laser ablation is that this procedure requires high-purity graphite rods and great requirement of laser powers.[63]

Chemical vapor deposition (CVD) is one of the most popular methods for the production of SWCNTs. During a CVD process, a carbon feedstock in the form of hydrocarbon such as ethanol is thermally decomposed and flows through a substrate containing metal catalyst particles (such as Fe, Co, Ni etc.). The growth of the nanotube is then generated on the surface of the catalyst particles. By optimizing the catalyst composition, a carbon feedstock and other reaction conditions, high purity and high performance SWCNTs can be obtained.[64–67]

The high pressure CO disproportionation process (HiPco) is another method of gas-phase catalytic production of SWCNTs from carbon monoxide.[68] In this procedure, $Fe(CO)_5$ acts as catalyst precursor and CO gas as a carbon feedstock. The iron atoms obtained from the thermal decomposition of $Fe(CO)_5$ condensed into iron clusters. The nucleation and growth of SWCNTs then occur on these clusters. The dominant impurities from this method are the carbon coated iron nanoparticles, thus the as-produced raw material commonly requires a purification process with acid to remove the metal impurities.[69]

1.6.3 Commercially available SWCNTs

HiPco® SWCNTs are produced by high pressure CO disproportionation process and commercially available as a raw power. The purchased raw tubes are commonly treated with concentrated HCl solution, neutralized with NaOH solution, rinsed with water and annealed before further experiments. The HiPco tubes have a distribution of diameter from 0.8 nm to 1.2 nm, which indicates the existence of various chiralities.[69] Semiconducting and metallic SWCNTs are both obtained in as-produced raw material. However, s-SWCNTs enriched samples are also commercially available with m-SWCNTs content less than 5 wt%. HiPco SWCNTs are intensively used for various post-sorting techniques because of the numerous nanotube chiralities.

PLV SWCNTs are synthesized by pulsed laser vaporization method catalyzed by a mixture of Co and Ni.[70] The samples contain 90% of SWCNTs and less amorphous carbon. Such tubes have a diameter range between 1.2 nm and 1.5 nm. For building of carbon based electronic devices such as transistors, large-diameter SWCNTs are of great advantage.[71]

CoMoCAT® SWCNTs are produced by catalytic CVD method using a flow of carbon monoxide as a carbon source and a Co-Mo bimetallic catalyst.[72] CoMoCAT samples have an average diameter of 0.8 nm and a quite narrow distribution of diameter (0.7-0.9 nm).[73] The main chiralities in a CoMoCAT sample are (6,5) and (7,5), which are near armchair SWCNTs.[74] The high content of (6,5) and (7,5) nanotubes makes CoMoCAT SWCNTs as perfect starting material for single chirality enrichment of nanotubes.

To note, all those commercially available as-produced samples are mixtures of m-SWCNTs and s-SWCNTs. For the application of SWCNTs, purification and sorting processes are of great necessity.

1.7 Application of SWCNTs

SWCNTs have a wide range of emerging electronic and optical applications due to their small size, processability in solution, chemical stability, and variable optoelectronic properties depending on the electronic type (metallic, semiconducting) and chirality.[75] Metallic SWCNTs are found useful in conductive films and transparent electrodes because of the high intrinsic electrical conductivity.[76–79] Of particular interest are the semiconducting SWCNTs owing to their high charge carrier mobility, high current-carrying capability and small intrinsic capacitance.[6,80,81] These characteristic features of s-SWCNTs have made them promising for a large number of applications, such as field-effect transistors (FET),[82–84] thin films,[85–87] optoelectronic devices,[88–90] chemical sensors,[91,92] and next-generation computing.[93,94]

Among all the applications of s-SWCNTs that have been mentioned above, FETs have attracted the most attention because their tremendous potential as most basic components for building future nano-size electronics and devices. Carbon nanotube field effect transistors (CNTFETs) are FETs based on a single carbon nanotube or an array of carbon nanotubes as the channel material instead of conventional silicon. CNTFETs have been developed since 1998 and significant progress has been made recently.[95,96]

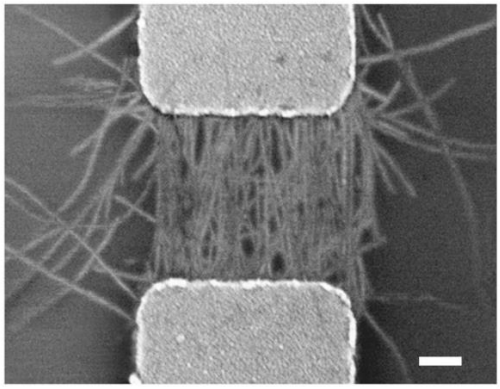

Figure 1.28. SEM image of a high-density, short channel transistor made of PODOF-wrapped s-SWCNTs, deposited by dielectrophoresis (DEP).[36]

In 2016, Hennrich *et al*. demonstrated short-channel transistors comprising densely aligned s-SWCNTs, as shown in Figure 1.28.[36] The highly enriched s-SWCNTs were prepared by combining PODOF-polymer wrapping with size-exclusion chromatography, resulting length sorted s-SWCNTs with a purity >99.7%. Their transistors have a hole mobility of up to

297 $cm^2V^{-1}s^{-1}$ and an On/Off ratio as high as 2×10^8, which is the best performance reported so far for CNT-based transistors.

Enantiomerically pure SWCNTs have been achieved and developed since a decade, the methods for the separation will be discussed in the next chapter. Left- and right-handed SWCNTs are optically active, which makes them potential candidates for electrochemical and chiral sensing.[9,75] Recently, Shi *et al*. presented a new electrochemical sensor for chiral discrimination based on the left- and right-handed enantiomers of enriched (6,5) chirality.[97] The glass carbon electrodes which were modified with left- or right-handed (6,5) nanotube on the surface can distinguish the enantioselectivity of analytes by different peak current response observed in differential pulse voltammogram (DPV) (Figure 1.29).

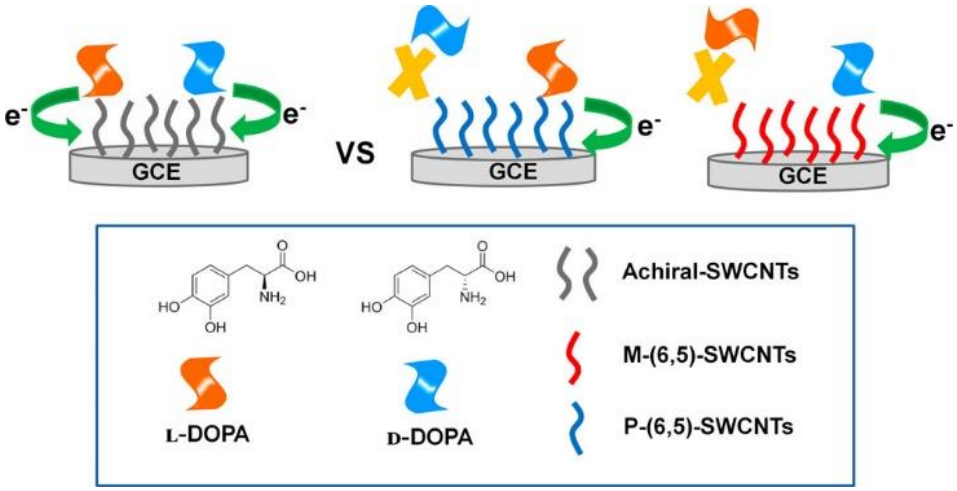

Figure 1.29. A schematic illustration of chiral discrimination between L-DOPA and D-DOPA analyte enantiomers by glass carbon electrodes (GCE) modified with (*M*) left- and (*R*) right-handed (6,5) SWCNTs.[97]

The application of SWCNTs in technologies still remains in the stage of research and there is a long way upon us before we can actually have SWCNT-based "products" on the market. However, with no doubts, carbon nanotubes are one of the key components in the nanotechnology of the foreseeable future.

1.8 Purification and sorting of as-produced SWCNTs

Most of the aforementioned applications of SWCNTs require a high purity of s-SWCNTs since the presence of m-SWCNTs brings drawback to the device performance.[76,98,99] Moreover, chirality-enriched s-SWCNTs are of great interest and demand for making devices with precisely controllable bandgap and optoelectronic properties. However, in the commercially available as-produced SWCNTs, semiconducting and metallic species coexist all the time. Besides that, SWCNTs prefer to exist as bundles due to their strong inter-tube van der Waals interaction. Hence, post-processing purification/sorting of SWCNTs according to their electronic type and chirality becomes an emerging topic in carbon nanotube research.

In general, the purification or sorting methods for SWCNTs involve the functionalization of the nanotube sidewalls, i.e. covalent and non-covalent functionalization in order to disperse these carbon materials for further purification. Covalent sidewall functionalization brings defects to the SWCNTs and alters the intrinsic properties such as solubility, bandgap and photoluminescence quantum yield.[100–103], whereas non-covalent approaches preserve the intrinsic properties of SWCNTs, thus are more commonly preferred. The general idea of non-covalent functionalization is to modify the hydrophobic sidewall of SWCNTs with the help of dispersant, so that the nanotubes can be dispersed individually in liquid medium for further purification and sorting process.

Over the last decade, various techniques have been developed for sorting SWCNTs according to their electronic type and chirality in water or organic solvents.[9,104,105] In this chapter, the most reported and successful sorting techniques will be introduced containing: 1) density gradient ultracentrifugation; 2) gel column chromatography; 3) aqueous two-phase extraction; 4) sorting by small aromatic molecules; and 5) sorting by conjugated polymers. The methods for sorting of SWCNTs according to their handedness will be discussed in the end of this chapter.

1.8.1 Density gradient ultracentrifugation (DGU)

DGU is originally used for the isolation and separation of biomolecules from biological fluids. The process involves the centrifugation of a sample through a centrifugation medium of graded density. Due to the elevated centrifugal force, the components within the sample move through the

medium faster or slower based on their buoyant density. Inspired by this methodology, Hersam *et al*. first demonstrated the sorting of DNA-wrapped SWCNTs by DGU with selective diameter and electronic type.[28,106] The buoyant density of each SWCNT species was controlled using structure-discriminating surfactants. Under high centrifugal force, the SWCNTs were then separated into different layers in the density gradient medium, as shown in Figure 1.30.

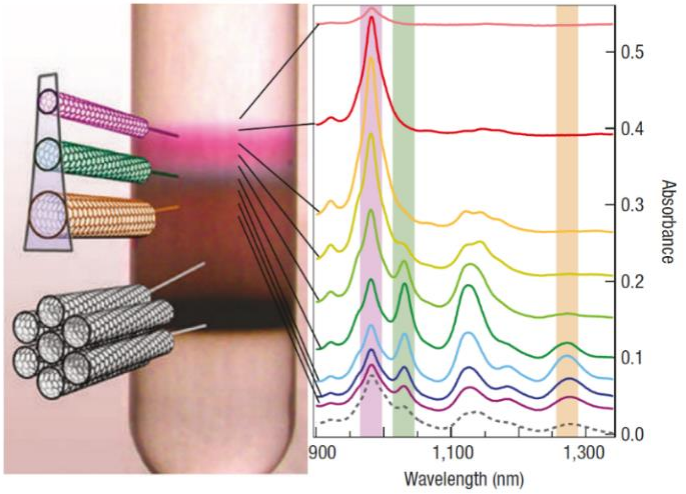

Figure 1.30. Photograph of the centrifugation tube and absorption spectra of several layers of SWCNTs after sorting by DGU.[28]

The different colors from the layers indicate nanotube species with different diameters, resulting bandgap-dependent absorption of the visible light. Moreover, the density of the separated SWCNTs was found to increase with an increasing diameter, so that the first layer contains nanotubes with the smallest diameter while bundles and aggregates were found in the lowest layer due to their much higher density. Later, they succeeded to enrich small diameter (0.7-1.1 nm) s-SWCNTs with purity of approximately 99% and nearly single-chirality of (6,5) SWCNTs with an orthogonal iterative DGU strategy.[107] By using a tailored nonlinear DGU, Weisman *et al*. separated ten different (n,m) species out of a raw HiPco material, which proved that DGU method is readily scalable for commercial purposes.[108] The disadvantages of DGU method are the time-consuming centrifugation, expensive instrumentation, and a multi-step processing.

1.8.2 Gel column chromatography

In chemistry, column chromatography is a method used to separate a compound from a mixture based on differential adsorption of individual compounds to the stationary phase. For sorting of SWCNTs, similar principle is applied and the separation depends on the selective interaction of the surfactant dispersed SWCNT species with the gel medium. Electronic type (m/s) separation can be simply achieved with column chromatography in an agarose gel medium because s-SWCNTs interact stronger with the gel beads and allow m-SWCNTs to elute out of the column first.[109] Furthermore, by the use of different dispersants, by tuning the stationary as well the mobile phase, s-SWCNTs can be sorted by their diameter and chirality.

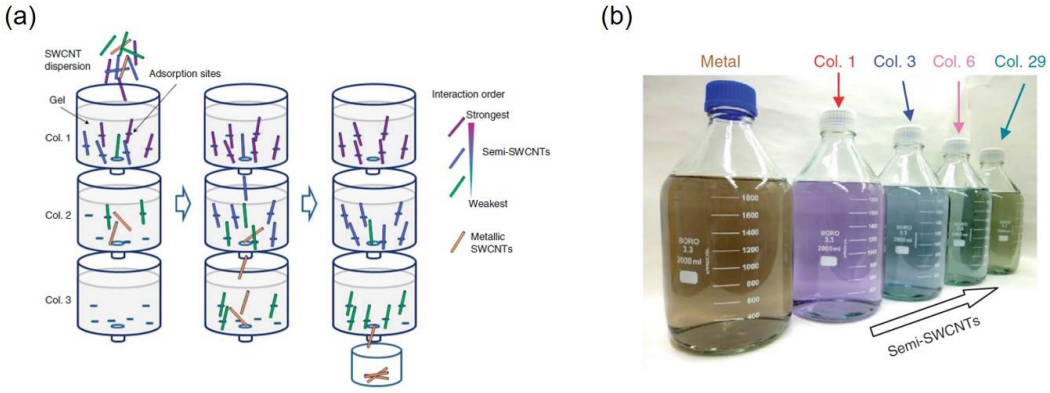

Figure 1.31. Schematic diagram of multicolumn gel chromatography procedure (a) and the color differences of each fraction are the indication of diverse chiral indices of SWCNTs.[110]

In 2011, Kataura *et al*. reported the successful separation of thirteen (n,m) SWCNT species using a multicolumn gel chromatography method (Figure 1.31).[110] In their work, allyl dextran-based size-exclusion gel was applied as a stationary phase and sodium dodecyl sulfate (SDS) aqueous solution (2-5 wt%) as a mobile phase. The chirality-dependent separation was believed to originate from different curvature of the nanotubes and different degree of SDS coverage, resulting a higher or lower interaction strength with the gel. Since there was only one surfactant used for the separation, the purity of the separated samples can be further improved by simply repeating the process. Sorted fractions with single-chirality purity up to 94% and large scale up to 2 liters (~0.8 μg/mL) are suitable for industrial applications.

Due to the high yield and the ability of both electronic type and chirality separation, gel column chromatography has become one of the most applied method for sorting of s-SWCNTs. However, the challenge of sorting s-SWCNTs with the larger diameters still remains.

1.8.3 Aqueous two-phase extraction (ATPE)

Aqueous two-phase systems have been developed and used in biological applications for many years.[111] One of the most commonly used aqueous two-phase systems is the PEG-dextran system, which consists of the more hydrophobic polyethylene glycol (PEG, Figure 1.32) solution and the more hydrophilic dextran solution. The phase separation between these two solutions is accomplished due to their immiscibility upon mixing.

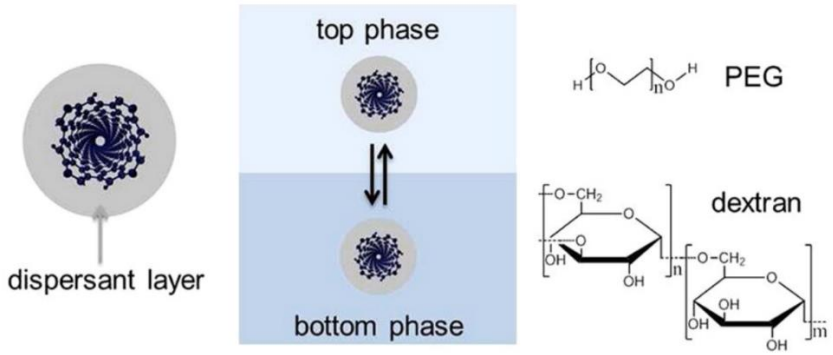

Figure 1.32. Schematic illustration of a PEG-dextran two-phase system for spontaneous partition of SWCNTs. Top phase is PEG-rich and bottom phase is dextran-rich.[112]

Based on this PEG-dextran system, Zheng *et al*. first established the ATPE approach for an effective separation of m-SWCNTs and s-SWCNTs in 2013.[112] In their work, surfactant-encapsulated SWCNTs spontaneously partitioned between the PEG- and the dextran-rich phases according to their electronic structure (Figure 1.32). Thermodynamic analysis suggested that the selective extraction is based on the different hydrophilicity of SWCNTs. Later on, Zheng *et al*. extended the ATPE method to the separation of DNA-SWCNT hybrids.[113] Fifteen single-chirality nanotube species were separated from as-produced carbon nanotube mixture by varying the salt and polymer additives. The hydration energy of each DNA-SWCNT hybrid was found sensitive to the spatial distribution of hydrophilic groups, resulting the DNA assisted ATPE method highly sequence-dependent. Moreover, high purity (10,10), (9,9) and (8,8) m-SWCNTs were successfully enriched by Fagan *et al*. with ATPE utilizing a simple gradient of two co-surfactants.[114] The use

of pH to modulate CNT partitioning in the ATPE process was published by Flavel *et al*. to isolated eleven nanotube species in the diameter range of 0.69-0.91 nm including both s- and m-SWCNTs.[115]

In comparison to DGU and gel column chromatography, ATPE has an obvious advantage of sorting m-SWCNT species. However, the fully removal of the salts and dispersant impurities after sorting remains a challenge for water soluble surfactant-based methods.[105]

1.8.4 SWCNTs sorting by small aromatic molecules

Small aromatic molecules with conjugated π-systems have been used for dispersing of SWCNTs in organic solvents or water via their π-π stacking or van der Waals interaction with CNTs, e.g. fluorophore and dye molecules,[116] pyrene, porphyrin, and their derivatives.[117–119] Aromatic molecules such as oligoacene and porphyrin derivatives are capable of selectively extracting s-SWCNTs.[120–123] Representative examples are the porphyrin derivatives. In 2004, Sun *et al*. first reported the separation of s-SWCNTs from an arc-discharge nanotube sample by long alkyl chain-derivatized porphyrin molecules.[124] The sidewall functionalization of s-SWCNTs was evidenced by significant broadening of porphyrin signals in ^{1}H NMR spectrum and visualized by high-resolution TEM. Later, Komatsu *et al*. even achieved the handedness separation of s-SWCNTs with chiral nano-tweezers based on diporphyrins.[125] The main drawbacks of using small aromatic molecules for SWCNTs sorting are the low purity of obtained semiconducting samples and the multiple purification steps required to get rid of an excess of small aromatic molecules which tend to remain bound on the aromatic CNT surface.

1.8.5 SWCNTs sorting by conjugated polymers

Sorting of SWCNTs by conjugated polymers has emerged as one of the most promising method due to their high selectivity, tunable structure and simple processability.[90,126–128] Polymers with tailor-made structures selectively interact with SWCNTs based on their electronic type and chirality. In this chapter we will focus on the most commonly used fluorene-based and carbazole based polymers, as well as at the end on easily removable polymers. Moreover, the postulated mechanisms for the polymer sorting of s-SWCNTs will be detailed.

1.8.5.1 Fluorene-based polymers

In 2007, Nicholas *et al*. first demonstrated the selective dispersion of s-SWCNTs by using fluorene-based aromatic polymers in toluene.[43] They found out that the conjugated polymer dispersed s-SWCNTs show improvement in purity and resolution of the absorption spectra when compared to the water-soluble surfactants dispersed s-SWCNTs. Moreover, they discovered that the changes in the polymer backbone led to the dramatic difference in selection of nanotubes species. Inspired by this work, various fluorene-based polymers were later synthesized and used for the sorting of SWCNTs.

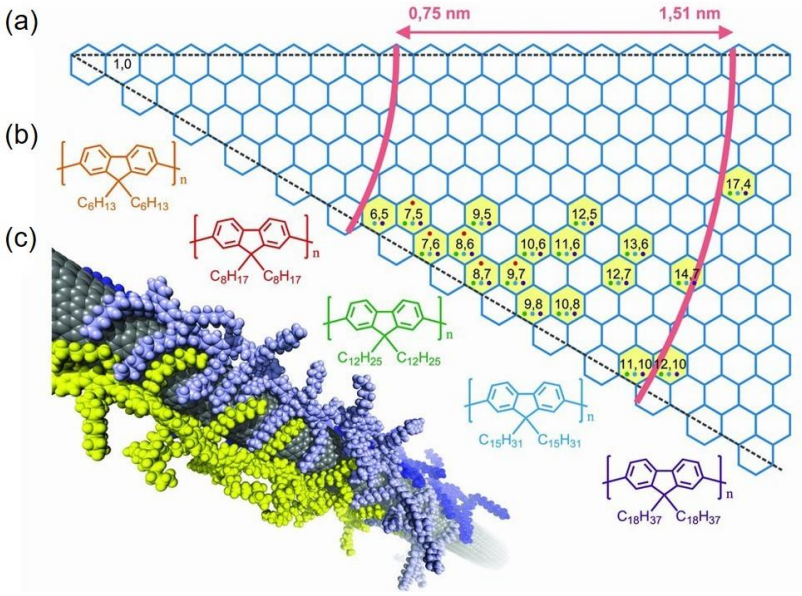

Figure 1.33. (a) Chirality map of SWCNTs selected by polyfluorenes bearing different alkyl chains. The color of each dot in hexagons corresponds to a polyfluorene derivative; (b) Structure of polyfluorene derivatives; (c) Simulated wrapping structure of polyfluorene chains on a nanotube sidewall.[129]

Simply by tuning the length of the alkyl chains on monomeric backbone, such polyfluorenes (PFs) can extract s-SWCNTs with different diameters and chiralities as shown in Figure 1.33.[129] In general, longer alkyl chains enable to disperse s-SWCNTs with a higher concentration but a less specific chirality selection. Molecular dynamics simulations revealed that the long alkyl chains provide the polymers a much stronger and firmly binding to the nanotube sidewalls, which allow more nanotube species to be wrapped. Diameter and chirality control of nanotubes can be realized by embedding other aromatic subunits into the polymer backbone structure. Moreover, subunits with extra functionalities can bring interesting features to the polymers and their performance.

Figure 1.34 highlights several representative fluorene-based copolymers which have been reported for SWCNT sorting.

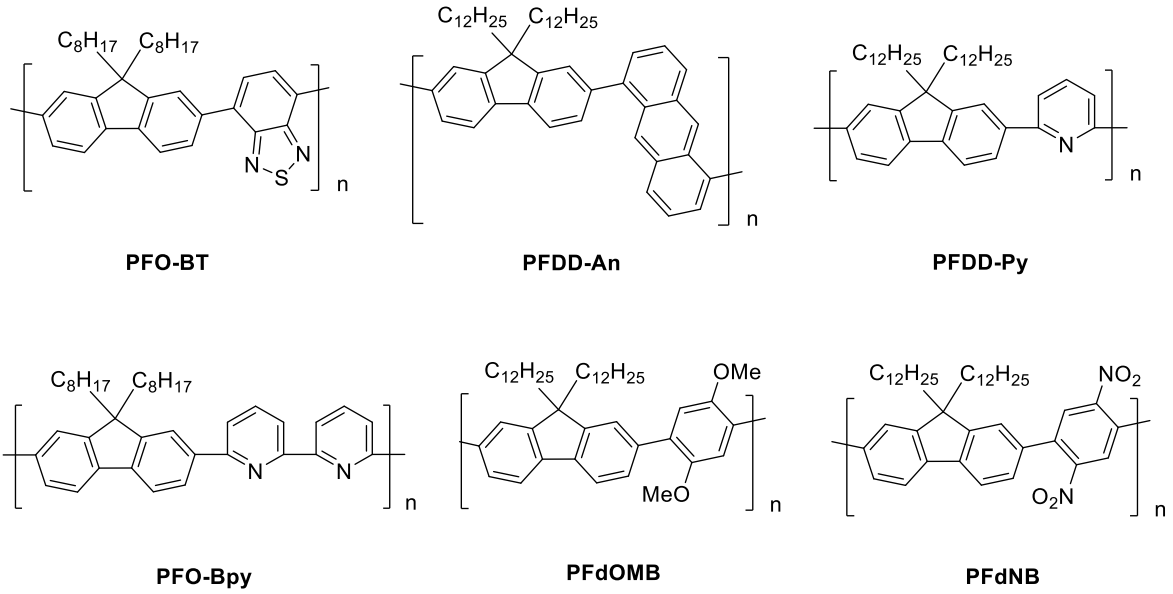

Figure 1.34. Synthetic conjugated fluorene-based copolymers used for selective sorting of SWCNT.

In 2011, Iijima *et al*. reported the ability of PFO-BT (F8BT) to selectively disperse (15,4) SWCNTs with high purity from arc-discharge raw nanotubes.[130] In the same year, Mayor *et al*. synthesized several fluorene-based copolymers with naphthalene, anthracene, and anthraquinone subunits for selective dispersing of HiPco SWCNTs in toluene.[131] Among those polymers, they found out that poly(9,9-didodecylfluorene-2,7-diyl-*alt*-anthracene-1,5-diyl) (PFDD-An) exhibits a strong preference towards s-SWCNTs with a diameter ≥ 0.95 nm. This diameter preference is attributed to the anthracene subunit. Later, they investigated the dispersing properties of a family of pyridine-containing copolymers.[132] In their work, poly(9,9-didodecylfluorene-2,7-diyl-*alt*-pyridine-2,6-diyl) (PFDD-Py) favors the s-SWCNTs with a diameter > 1 nm from as-produced PLV nanotubes. For the understanding of this wrapping mechanism, they developed a hybrid coarse-grained model combining density functional theory (DFT) and geometry-based calculations, which revealed the close relation between dihedral angles (α,β) of the polymer backbone and the tube diameter (Figure 1.35). By embedding bipyridine (Bpy) into the PFO backbone, Nakashima *et al*. enriched (6,5) SWCNTs up to 97% in *m*-xylene and *p*-xylene with poly[(9,9-dioctylfluorenyl-2,7-diyl)-*alt*-*co*-(6,6´-{2,2´-bipyridine})] (PFO-Bpy) from raw

CoMoCAT SWCNTs.[133] This is so far the highest single-chirality CNT purity which has been achieved by conjugated polymers.

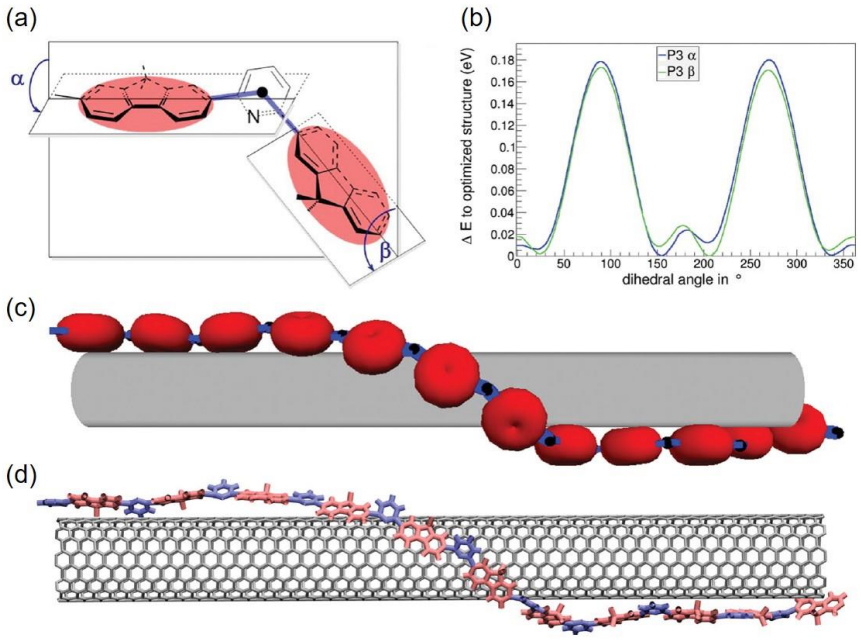

Figure 1.35. (a) Structure of polymer PFDD-Py with α and β denoting the dihedral angles between pyridine- and fluorene subunits; (b) Energy profile of the dihedral angles α and β obtained by DFT calculations in vacuum; (c) Example solution calculated for PFDD-Py with a nanotube cylinder (1.2 nm). Red balls represent the fluorene subunits and the black dots indicate the pyridine subunits. (d) Molecular model of calculated solution (c). The alkyl chains in the backbone structure are simplified as methyl groups.[132]

In 2015, Adronov *et al*. synthesized one pair of fluorene-based copolymers containing phenyl subunits with either methoxy (PFdOMB) or nitro groups (PFdNB), as drawn in Figure 1.34.[134] The electron-donating methoxy groups allow the copolymer PFdOMB to preferentially interact with s-SWCNTs, whereas the electron-withdrawing nitro groups enable the copolymer PFdNB to enrich m-SWCNTs. This work encourages the further exploration of tailor-made polymers with specific functionalities for a selective sorting of SWCNTs.

1.8.5.2 Carbazole-based polymers

Carbazole-based polymers belong to the second largest family of polymers which have been synthesized for the purpose of dispersing and sorting of SWCNTs. The carbazole backbone contains a nitrogen atom in the middle of the structure which can be functionalized with an alkyl

chain. Besides that, the extra electron pair on the nitrogen makes the carbazole π-system more electron rich than the fluorene π-system. Due to such differences, carbazole-based polymers show a quite different performance and selectivity towards s-SWCNTs in comparison with the polymers derived from fluorene.

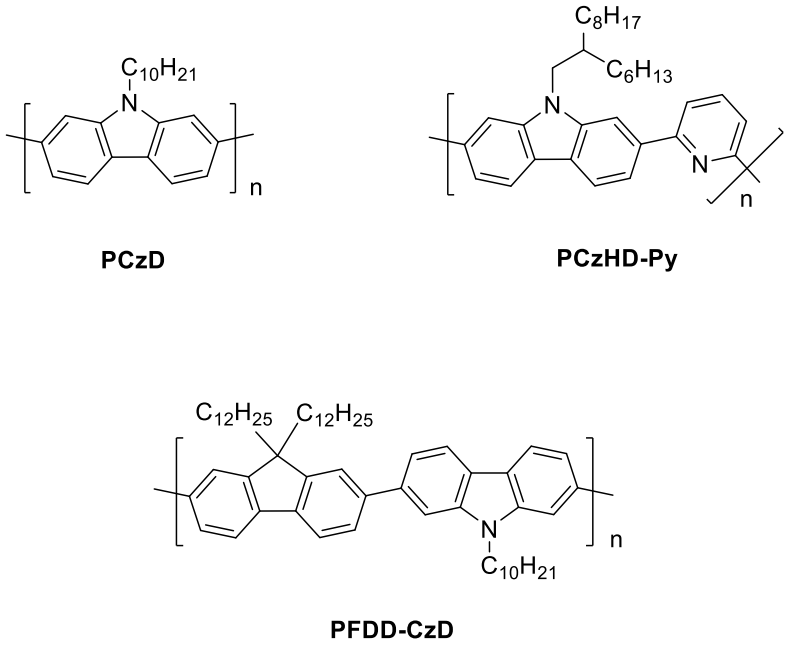

Figure 1.36. Carbazole-based polymers synthesized and reported by Mayor *et al*. for a selective dispersion of s-SWCNTs.[132,135,136]

Mayor *et al*. has pioneered studies of carbazole-based polymers for a selective dispersing and sorting of s-SWCNTs.[132,135,136]. Figure 1.36 shows three polymers which have been synthesized and demonstrated in the early studies. In 2010, they reported that poly(*N*-decyl-2,7-carbazole) (PCzD) can exclusively disperse s-SWCNTs of (n-m) ≥ 2 in toluene, while PFO disperses mainly near armchair species with (n-m) ≤ 2.[135] These experimental results were supported by molecular dynamic (MD) simulations with a decamer of PCzD and PFO as a shorter polymeric model for a selective wrapping of (10,2) and (7,6) SWCNTs. Later, they introduced a branched alkyl chain to the nitrogen atom of carbazole backbone and found out that the dispersing efficiency increased by a factor of 2.[136] Variation of the connection of the carbazole monomers (2,7-linked or 3,6-linked) gives the corresponding homo-polycarbazoles with a diverse conformation. However, the low molecular weight and solubility of obtained polymers hinder their performance. In the further studies, pyridine-containing copolymer poly[*N*-(2-hexyl)decylcarbazole-2,7-diyl-*alt*-pyridine-

2,6-diyl] (PCzHD-Py) with a complementary structure of PFDD-Py shows no obvious tendency to prefer the large diameter s-SWCNTs, as reported for PFDD-Py.[132] A mixed copolymer poly(9,9-didodecylfluorene-2,7-diyl-*alt*-*N*-decylcarbazole-2,7-diyl) (PFDD-CzD) extracts s-SWCNTs efficiently and with a wide range of chiral angles.[136] The excellent performance of this copolymer is a result of combined selectivity of polyfluorene and polycarbazole towards SWCNTs with $(n\text{-}m) \leq 2$ and $(n\text{-}m) \geq 2$.

1.8.5.3 Removable polymers

As discussed before, high purity s-SWCNTs samples have been achieved by wrapping with various conjugated polymers. Although those polymer-wrapped s-SWCNTs can be directly integrated into devices such as FETs, the residual polymer chains along the sidewalls of SWCNTs limit the performance of such devices due to the hindered charge transport and increased tunneling barrier between the neighboring SWCNTs.[71,126,137–139] To solve this problem, various removable polymers have been synthesized and used for SWCNTs sorting in order to get sorted and dispersant-free s-SWCNTs for various applications. Among those, fluorene-based removable polymers are of great interest because of their high efficiency in selective dispersion of s-SWCNTs. In general, these polymers contain degradable groups or can undergo polymer conformational changes, which could then desorb from SWCNTs and being removed.

In 2011, Mayor and co-works designed and synthesized photocleavable polymers based on fluorene backbone and *o*-nitrobenzylether, which was one of the first study involving the precipitation of solubilized s-SWCNTs (Figure 1.37a).[140] Photoirradiation of the polymer induces the cleavage of the polymer backbone and release sorted SWCNTs. In the same year, Chan-Park *et al*. reported a new class of copolymers containing fluorene and disilane subunits in the backbone structure for SWCNTs sorting (Figure 1.37b). In that case, the wrapped nanotubes have been treated with hydrofluoric acid (HF) solution to break the disilane bond in the polymer and thus release sorted tubes.[139] Later, Adronov *et al*. presented a novel conformationally switchable fluorene-based copolymer with tetrathiafulvalene (TTFV) subunits (Figure 1.37c).[141] These copolymers show a strong interaction towards small diameter s-SWCNTs and desorbs from the nanotubes upon protonation.

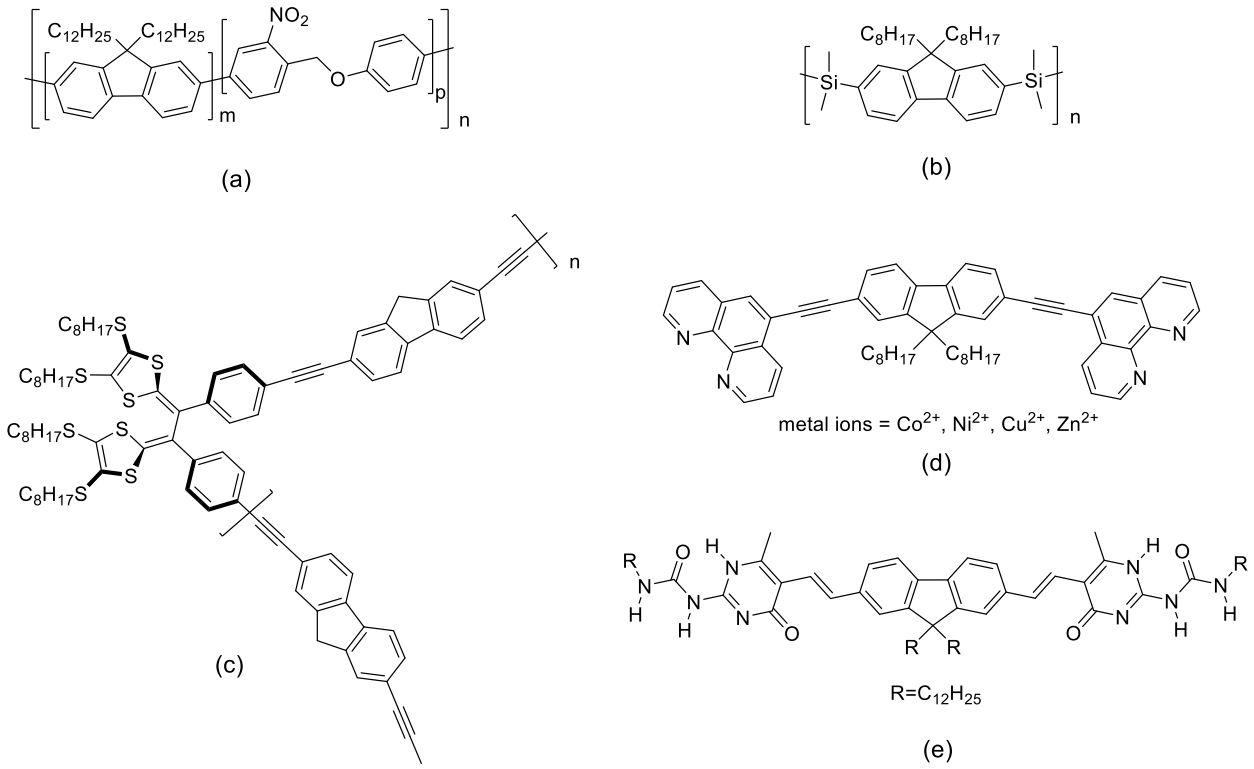

Figure 1.37. Fluorene-based removable polymers for s-SWCNTs sorting.[139–143]

A new strategy of an efficient extraction of highly pure s-SWCNTs with non-covalent polymers was developed later by Toshimitsu and Nakashima.[142] They designed and synthesized metal-coordination polymers consisting of fluorene-bridged bis(phenanthroline) ligands with different metal ions (Figure 1.37d). The sedimentation of m-SWCNTs was achieved by the addition of toluene to the benzonitrile solution which contains all the dispersed SWCNTs and the removal of the coordination polymer from the sorted s-SWCNTs was done by the acid treatment. The monomers can be reused after base treatment. Following this non-covalent approach, Bao *et al*. synthesized a 2-ureido-6[1*H*]-pyrimidinone (UPy)-based H-bonded supramolecular polymer for the isolation of dispersant-free s-SWCNTs (Figure 1.37e).[143] The monomer contains fluorene subunits with long alkyl chains to ensure the polymer solubility as well the sorting efficiency towards s-SWCNTs. The terminal UPy groups enable not only the polymerization of the monomers via non-covalent H-bond formation, but also the subsequent depolymerization upon hydrogen bond disruption with an acid. The electron mobility of the SWCNT transistors after removal of the dispersants could increase by 94 and 24% for HiPco and AD SWCNTs,

respectively.[137] By introducing chain stoppers into the Upy-based system, the polymer conformation was controlled and the effect on nanotube sorting was studied.[144]

In the case of aforementioned non-covalently bonded supramolecular polymers, the cleavage of the polymers was complete but the molecular weights of such polymers were relatively low which limited their sorting performance and yield towards s-SWCNTs. Thus, desired polymers should have high molecular weight for sorting and can depolymerize into monomeric units in order to fully release the nanotubes. Furthermore, this kind of supramolecular polymers is difficult to synthesize. One of the proper candidates is the family of imine-based conjugated polymers.

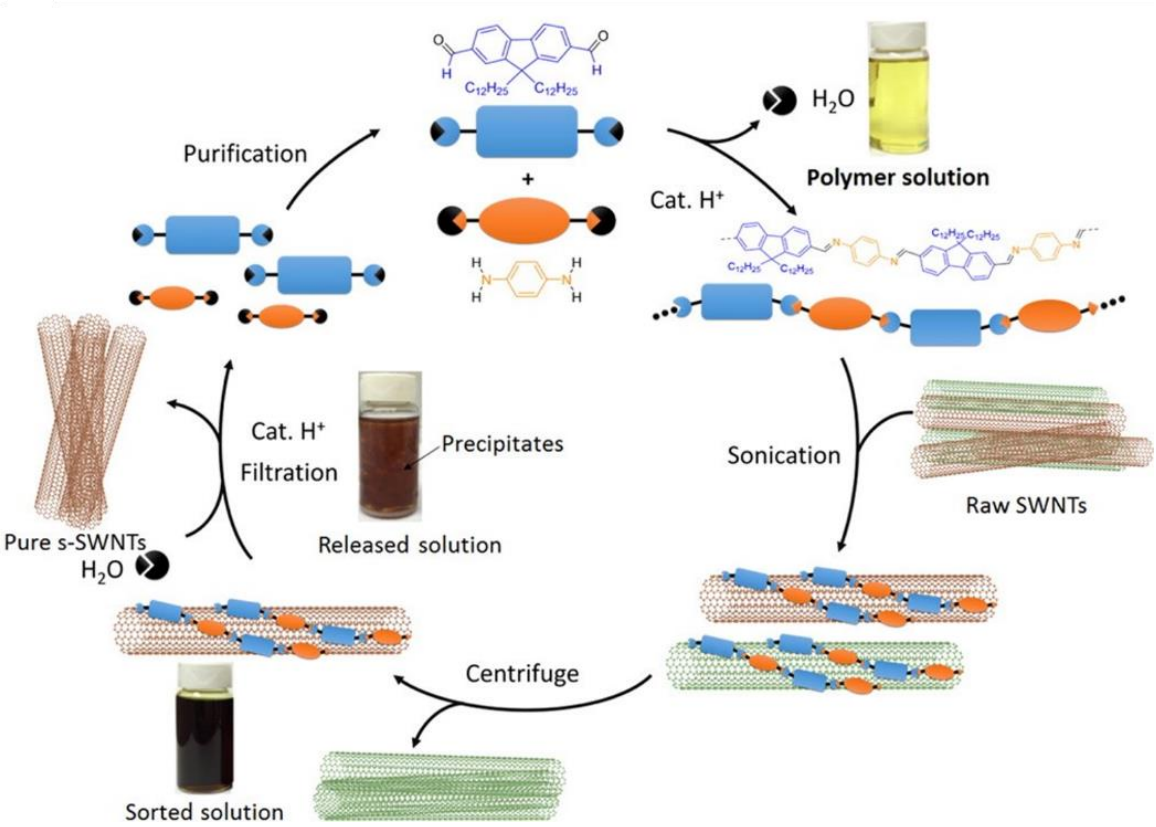

Figure 1.38. Separation circle proposed by Bao *et al*. for sorting s-SWCNTs with a removable imine-based copolymer.[71]

Conjugated polyimines, or polyazomethins (PAMs) are polymers with imine bonds (C=N) in the backbone structure, which can be easily protonated by acid and thus triggered. Barner-Kowollik *et al*. first applied fluorene-based polyimines for the dispersion of s-SWCNTs.[145] Later, Loi and co-workers reported the ability of polyimines with thienylene subunits to extract s-SWCNTs with high yield.[146] However, the removal of such imine-based polymers have not been

discussed by either of them. In 2016, Bao and co-workers presented a fluorene-based polyimine for dispersion of large diameter s-SWCNTs and took advantage of the imine bonds for the total removal and the recyclability of the polymer (Figure 1.38).[71] In their work, the copolymer was synthesize by polycondensation of 9,9-didodecyl-9*H*-fluorene-2,7-dicarbaldehyde with *p*-phenylenediamine. The obtained copolymer was used to selective disperse large diameter s-SWCNTs with the yield up to 23.7% and the purity of the sorted s-SWCNTs up to 99.7%. Upon exposure to catalytic amount of acid, the polymer degraded into monomers within several minutes. The quantitative removal of the polymers on the nanotubes was confirmed by absorption spectroscopy and X-ray photoelectron spectroscopy (XPS). The similar work was also reported by Gopalan *et al*.[147] They synthesized PFO-N-Bpy via a catalyst-free aza-*Wittig* reaction. Compare to the commercially available PFO-Bpy, this copolymer has a similar performance for s-SWCNTs sorting and the advantage of its degradability. After sorting the nanotubes with PFO-N-Bpy, they managed to align the wrapped s-SWCNTs into a monolayer array, which was then treated with a catalytic amount of trifluoroacetic acid (TFA) in toluene, rinsed and annealed. Scanning electron microscopy (SEM) image of the aligned arrays after this process indicates the total removal of the polymers, as shown in Figure 1.39.

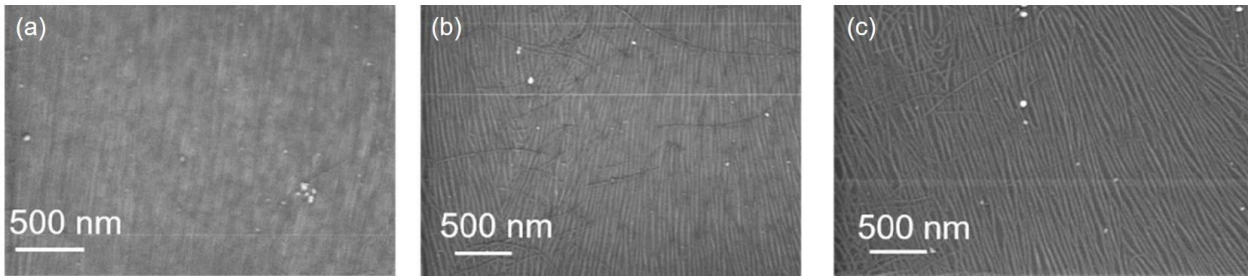

Figure 1.39. SEM images of aligned arrays before and after removal of the polymers: (a) as deposited; (b) TFA rinsed; (c) TFA rinsed and annealed.[147]

1.8.5.4 Postulated mechanisms for s-SWCNTs sorting by conjugated polymers

The sorting of SWCNTs with conjugated polymers have been developed over a decade but the mechanism behind this process has not yet been comprehensively understood. In general, the sorting process includes: 1) mixing and sonication of the polymer and as-produced SWCNTs mixture in the solvent; 2) centrifugation for the sedimentation of the aggregates and m-SWCNTs; 3) collection of the supernatants for characterization or further purification process.[9]

The sonication step is essential to improve interaction of polymer chains with an individual nanotube in the solvent, since it causes debundling of the SWCNTs. It is commonly believed that during the sonication, backbones of the conjugated polymers are wrapping along the nanotube sidewalls via non-covalent π-π interaction, while the side chains are solubilizing the individual nanotubes in organic solvents.[129,148,128] The hypothesized helical wrapping of polymer chain on a single nanotube was observed and demonstrated with high-resolution transmission electron microscopy (HRTEM) by Therien and co-worked, as shown in Figure 1.40.[149] The parameters that can affect the selectivity and sorting yield of s-SWCNTs during sonication have been summarized and discussed by Bao *et al.* and Adronov *et al*., including solvent (medium), polymer structure and molecular weight, polymer/SWCNT ratio, sonication time and temperature.[90,150]

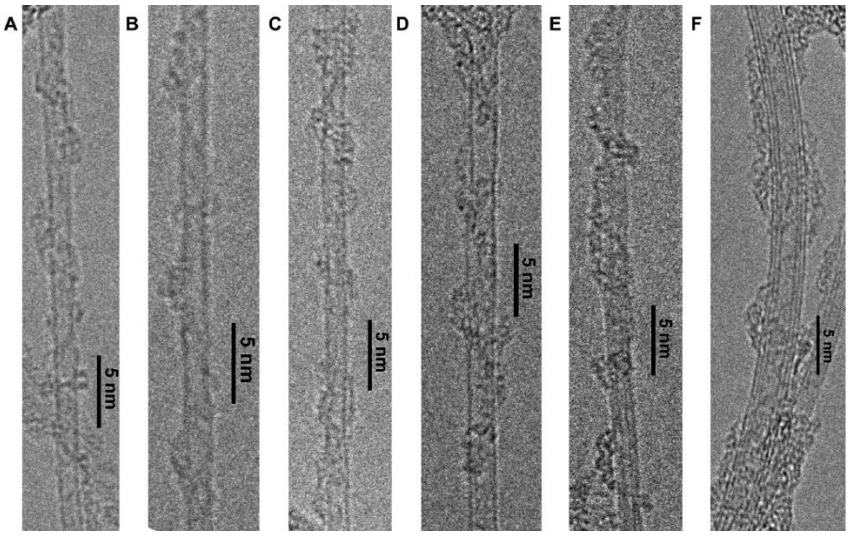

Figure 1.40. TEM images of left-handed helical structures observed from PLV SWCNTs wrapped by ionic arylene-ethynylene polymers bearing (*S*)-1,1´-binaphth-2-ol components.[149]

In the centrifugation step, well wrapped s-SWCNTs remain in the supernatant whereas the m-SWCNTs and the aggregates precipitate. This different behavior of s- and m-SWCNTs during the centrifugation could be explained by a polarizability-based mechanism.[151] Grossman *et al*. investigated the interface between poly-3-hexylthiophene (P3HT) and s-/m-SWCNTs by DFT calculations. The calculations revealed that the m-SWCNTs interact electrostatically more strongly with P3HT than s-SWCNTs due to a significant amount of charge transfer between polymer and nanotube, as demonstrated in Figure 1.41. This theoretical result is consistent with the intrinsic high polarizability of m-SWCNTs. Hence, the more polar m-SWCNT/polymer complexes

aggregate into bundles in non-polar solvents and precipitate during centrifugation, while the less polar s-SWCNT/polymer complexes remain individual in the supernatant.

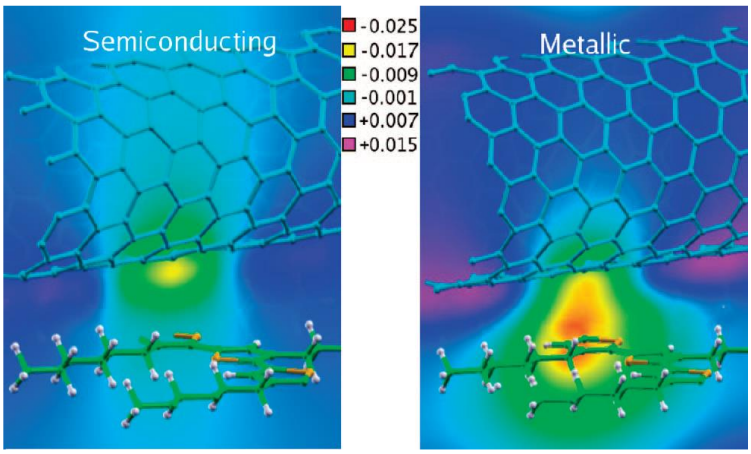

Figure 1.41. Induced electrostatic potential by the interface formation between P3HT and s-/m-SWCNT.[151]

As for single-chirality sorting, Nakashima and co-workers tried to explain the high selectivity of PFO-BPy for (6,5) SWCNT using the molecular-mechanics simulation, but the calculated binding energy difference between (6,5)/PFO-BPy and other SWCNT/PFO-BPy complexes was rather low for a clear discrimination.[133]

1.8.6 Handedness separation of SWCNT

The recent summit of SWCNTs sorting is the handedness separation, since each chiral (n,m) species consists of left-handed and right-handed enantiomers. To achieve the handedness separation, the special dispersants and methods are required. In this chapter, methods for enantiomeric separation of SWCNTs will be discussed.

1.8.6.1 Small molecule wrapping

Pioneering work for handedness separation of SWCNTs was accomplished by Komatsu *et al.* in 2007.[125] They designed and synthesized chiral nano-tweezers comprising *meta*-phenylene-bridged zinc(II) diporphyrins with *R*- or *S*-configuration for the separation of left- (*M*-) and right- (*P*-) handed enantiomers of SWCNTs from raw CoMoCAT materials (Figure 1.42). For the very first time, they recorded CD spectra of the optically enriched SWCNTs.

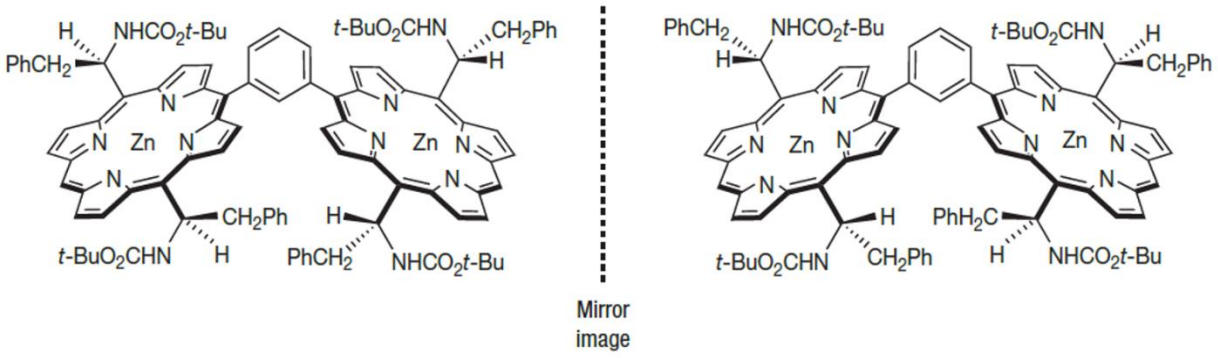

Figure 1.42. Mirror image of chiral nano-tweezers comprising *meta*-phenylene-bridged zinc(II) diporphyrins with *R*- or *S*-configuration.[125]

Later, Komatsu and co-workers made modifications to the chiral diporphyrins by changing the bridging unit. 2,6-Pyridylene-bridged diporphyrins showed the more stable complex formation with SWCNTs than the previous *meta*-phenylene-bridged ones, which leads to an improved optical enrichment ability. Molecular modeling calculations supported the handedness discrimination between *M*- and *P*-(6,5) nanotubes by 2,6-pyridylene-bridged diporphyrins, but the relative affinity difference was only 0.22 kcal/mol.[152] 3,6-Carbazolylene-bridged diporphyrins optically enriched (7,5) SWCNTs and allowed the observation of opposite CD signs from type 2 (7,5) tubes in comparison with type 1 (6,5) tubes.[153] By introducing phenanthrene between the two porphyrins, (6,5) SWCNTs were optically enriched with an enantiomeric excess of 67%.[50]

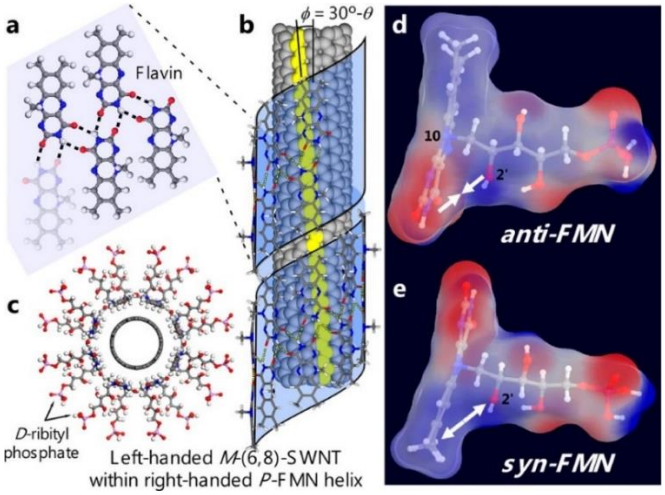

Figure 1.43. (a) FMN molecules stabilized by H-bonds; (b) helical wrapping of FMN molecules around a left-handed SWCNT; (c) chiral $_{D}$-ribityl phosphate chains on the sidewall of the nanotube with right-handed helix; (d, e) induced *anti*- and *syn*-conformation of FMN ring.[154]

Besides the diporphyrins, flavin mononucleotide (FMN) has been reported to enrich left-handed SWCNTs owing to the induced right-handed helix of its chiral $_D$-ribityl phosphate chain.[154] The enantioselectivity originates from the sp^3 nitrogen atom anchoring the sugar moiety to the flavin ring, which produces *syn*-and *anti*-conformation of FMN (Figure 1.43). Inspired by this work, Kataura and co-workers developed the methodology to determine the enantiomeric purity (EP) of any (6,5) enantiomeric mixtures.[155] The evaluation is based on the handedness-dependent interactions of (6,5) and (11,-5) enantiomers with the FMN molecules, which causes the different transition energies in optical absorption, PL and CD spectra, hence enable the estimation of the concentration of each enantiomer, namely, the EP. The experimental CD_{norm} value was confirmed to have a linear relationship with the EP, as shown in Figure 1.44. Therefore, the enantiopurity of a (6,5) SWCNT sample can be calculated by the equation EP (*M*)-(6,5) (%) = 50 + αCD_{norm} and EP (*P*)-(6,5) (%) = 50 - αCD_{norm}, where CD_{norm} is the CD value of the E_{22} transition peak of (6,5) SWCNT after normalization[50] and α is a linear scaling factor which is set as 0.421±0.030 $mdeg^{-1}$.[155]

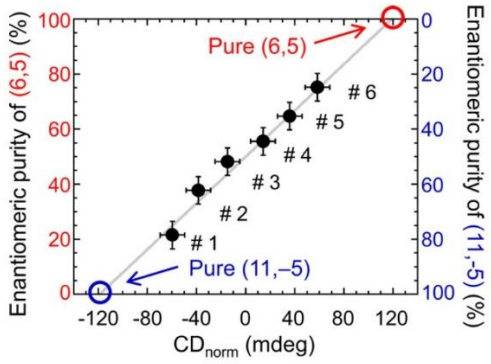

Figure 1.44. Plot of the enantiomeric purities as a function of the experimental CD_{norm} values of the six samples. The enantiomeric purities were estimated by fitting the E_{11} optical absorption peak. The grey line is the fitted linear relation.[155]

1.8.6.2 Density gradient ultracentrifugation (DGU)

Enantiomer separation of SWCNT using DGU was first reported by Hersam *et al*. in 2009.[156] In this approach, the chiral surfactant sodium cholate (SC) was utilized to discriminate SWCNTs according to their handedness, inducing a slight difference in the buoyant densities of SC-

encapsulated left- and right-handed SWCNTs. The handedness separation was then achieved via a single centrifugation step with a linear density gradient.

Later in 2010, Weisman and co-workers improved the performance of DGU for the separation left- and right-handed SWCNTs by the combination of co-surfactants and tailored nonlinear density gradients.[108] They successfully isolated both enantiomers of seven SWCNT species from polydispersed HiPco samples. Figure 1.45 shows the *in-situ* absorption spectra of the isolated (6,5) enantiomers. The two enantiomers have a ~ 4 nm shift in the absorption spectra due to the non-equivalent surfactant coating, which is the key to the enantiomeric separation in DGU. Owing to the high purity of the (6,5) enantiomers, their enantiomeric excess (*ee*) was considered to be 100% at that time and the CD_{norm} value of 36 mdeg was then commonly used as a standard value for quick evaluation of any optically active SWCNT samples by CD spectroscopy.

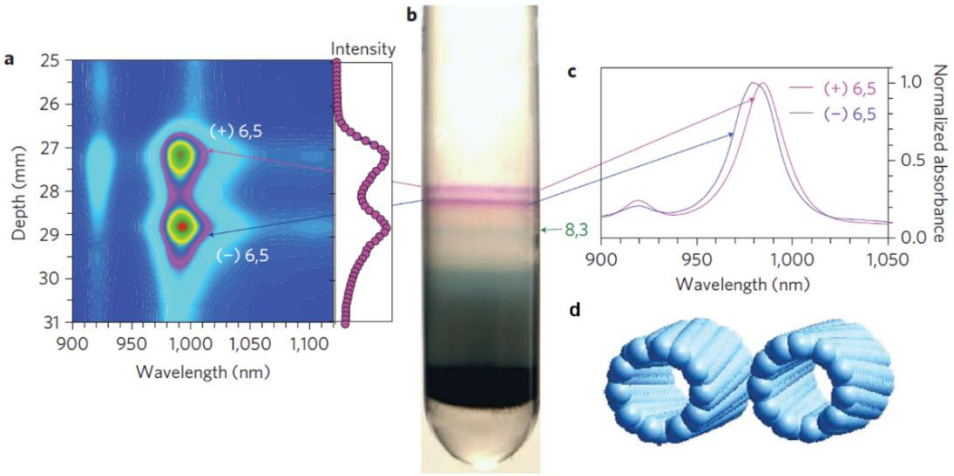

Figure 1.45. (a) Vertical fluorescence spectral map of separated (6,5) enantiomer bands (excited at 783 nm); (b) image of the centrifuge tube with separated (6,5) enantiomer bands; (c) in-situ absorption spectra of the two bands; (d) model structures of (6,5) enantiomers. Here, (6,5) enantiomers with positive and negative CD signals at E_{22} transition are labeled with (+) and (-), respectively. [108]

1.8.6.3 Gel column chromatography

Similar to the chirality sorting, the handedness sorting of SWCNTs by gel column chromatography relies on the selective interaction of surfactant dispersed SWCNT enantiomers with allyl dextran-based gel bearing the chiral moieties.

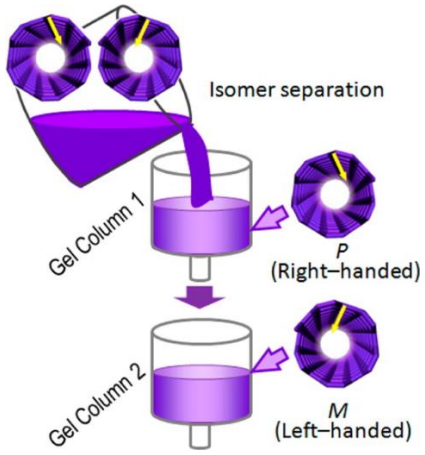

Figure 1.46. Illustration of a multi-column system for simultaneous chirality and handedness separation of SWCNTs.[157]

In 2014, Kataura *et al*. reported the separation of optical isomers of nine (n,m) species from as-produced HiPco nanotubes.[157] The SDS-dispersed SWCNTs were introduced to a multi-column system for stepwise elution and the procedure was repeated multiple times in order to achieve the simultaneous separation of chirality and handedness (Figure 1.46). Theoretical calculation revealed that the adsorption energy of allyl dextran towards *P*-(6,5) SWCNT is 0.519 kcal/mol higher than that of *M*-(6,5) SWCNT, which enable the separation of both enantiomers on such gel column.

By using a pre-separated metallic SWCNT mixture as the starting material, Kataura and co-workers further extended the application of this method to separate enantiomers of m-SWCNTs and obtained highly enriched (10,4) SWCNT enantiomers.[158] Later on, they combined the gel column method with stepwise elution to separate twelve different single-chirality enantiomers, as presented in Figure 1.47.[49] The high enantiopurity of the isolated enantiomers allowed them to analyze excitonic band structure of SWCNT from the obtained CD spectra (Figure 1.47c).

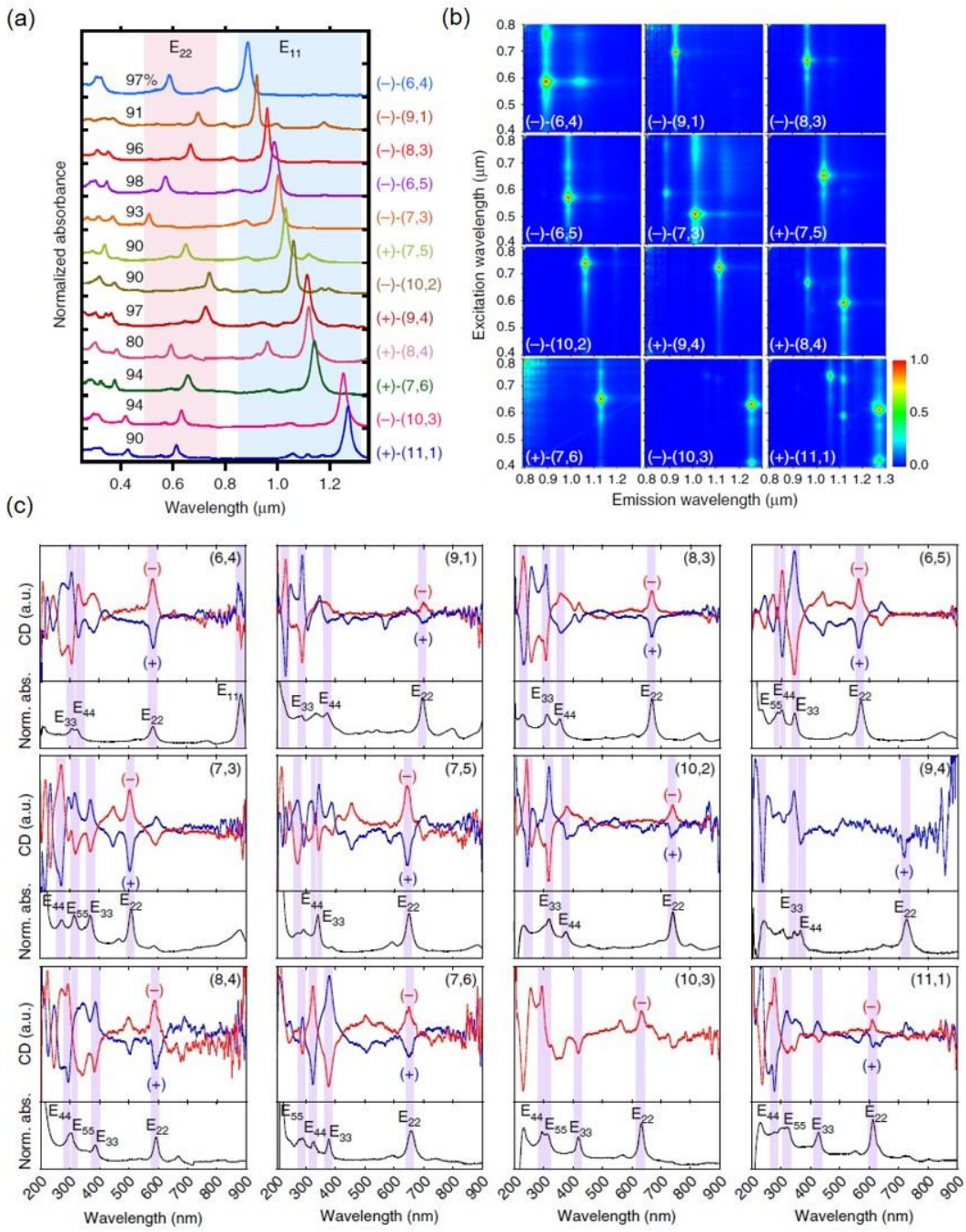

Figure 1.47. (a) Absorption spectra and (b) PLE maps and (c) CD spectra of twelve isolated SWCNT enantiomers.[49]

1.8.6.4 DNA assisted aqueous two-phase extraction (ATPE)

The handedness sorting of SWCNTs via DNA assisted ATPE is highly sequence-dependent. DNA strands selectively wrap around SWCNT by π-π stacking of the DNA bases with the hydrophobic nanotube sidewall, forming DNA-SWCNT hybrids with different hydration energies, allowing the discrimination according to the chirality and handedness in the aqueous two-phase system. In 2006, Brus *et al*. first showed that a racemic mixture of SWCNTs can exhibit CD signals when wrapped with DNA.[159] However, after removal of the DNA and redispersion in a non-chiral surfactant, the CD signals disappeared. They attributed this phenomenon to the induced circular dichroism resulting from the differences in DNA-SWCNT transition moment coupling of the two enantiomers.

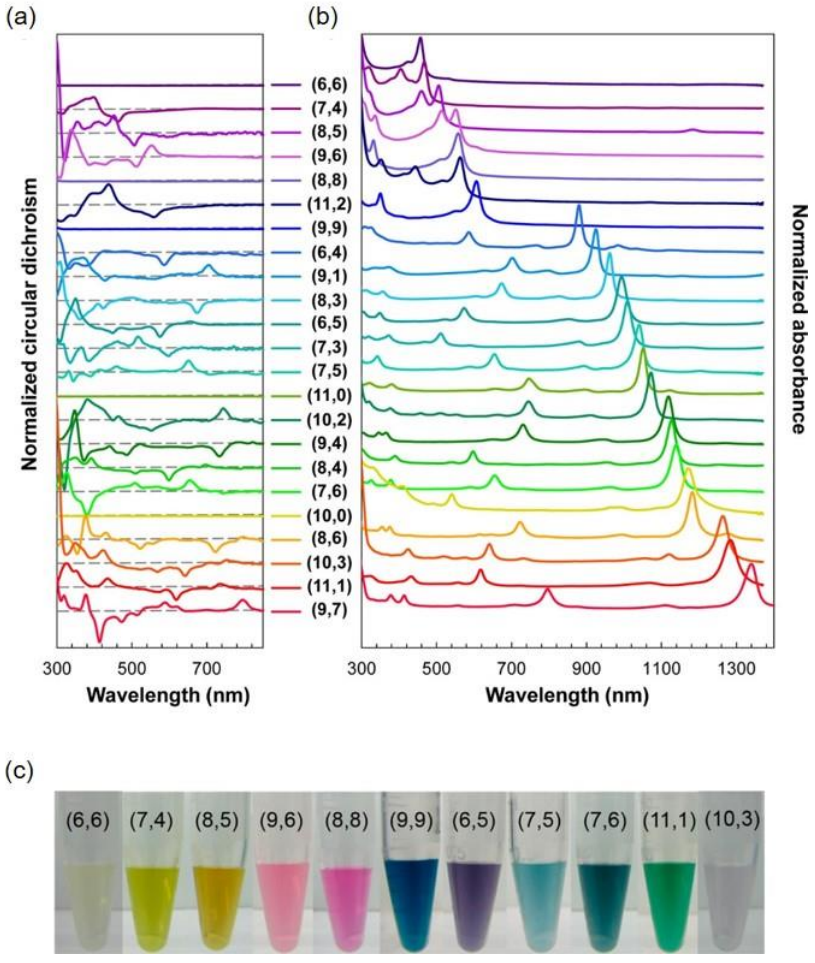

Figure 1.48. (a) CD spectra of isolated SWCNT enantiomers by DNA assisted ATPE (normalized at E_{22} peak position); (b) absorption spectra of isolated SWCNT enantiomers (normalized at E_{11} peak position); (c) Photos of several isolated SWCNT enantiomers.[160]

Recently in 2016, Zheng and co-workers screened over 300 short single-stranded DNA sequences and reported the successful isolation of more than 20 single-chirality enantiomeric SWCNTs (Figure 1.48).[160] Replacement of wrapped DNA with different non-chiral surfactants confirmed that the CD signals were intrinsic to the isolated enantiomers. Detailed study on (6,5) nanotubes suggested that the DNA sequence adopts two different folding patterns on the left-handed and right-handed enantiomers, causing the different dielectric environment and chemical reactivity of the complexes. A hydration-energy-driven mechanism was proposed by them to explain the enantiomeric discrimination of DNA-SWCNT hybrids in ATP system.

1.8.6.5 Conjugated polymers

Conjugated polymers have been extensively studied and applied for the sorting of SWCNTs according to the electronic type or chirality owing to their tunable structure and strong π-π interaction with nanotube sidewalls. Hence, separation of left- and right-handed SWCNT enantiomers via conjugated polymers has also been investigated by introducing chiral recognition moiety into the polymer backbone.

In 2012, Nakashima *et al*. designed and synthesized a series of fluorene-based copolymers for one-pot separation of s-SWCNT enantiomers.[161] PFO was chosen as one monomeric unit due to its well-known ability of exclusively extract s-SWCNTs with the narrow chirality distribution. To realize the enantioselectivity of the polymer, they introduced as the second repeating unit a chiral binaphthol moiety, (*R*)- or (*S*)-2,2´-dimethoxy-1,1´-binaphthyl-6,6´-diyl (RBN or SBN), as shown in Figure 1.49a. The copolymerization was carried out via Yamamoto coupling reaction of the both monomers and lead to different composition ratios of monomeric units. The resulting ratios of the PFO and RBN (SBN) monomers were determined quantitatively by ^{1}H NMR spectroscopy. The obtained chiral polymers selectively enriched semiconducting (6,5) and (7,5) SWCNTs owing to the PFO moiety in the backbone structure. The CD spectra confirmed the enrichment of nanotube enantiomers, however the CD signals are rather noisy, not fully symmetric and thus hard to interpret (Figure 1.49b). The missing E_{33} and E_{44} transition peaks in the CD spectra are probably overlapped with the signals of the wrapped conjugated polymers. Figure 1.49c shows the effect of the composition ratio of RBN and SBN in $(PFO)_x(RBN)_y$ and $(PFO)_x(SBN)_y$ on the CD intensity of (6,5) SWCNT at E_{22} transition. For both chiral copolymers, highest CD intensities were

achieved with y ratio around 33%. Upon increasing the ratio of the chiral moiety RBN and SBN over 40%, the preference of the polymers for left- or right-handed SWCNTs reversed, as shown in Figure 1.49c. This phenomenon was supported by molecular mechanics simulations calculating the bind energies between (6,5) SWCNT enantiomers and chiral copolymers with different y ratios. The obtained binding energy differences were in the range of 8-16 kcal/mol and much higher than the reported difference of 0.22 kcal/mol for diporphyrins, suggesting a higher enantioselectivity of such conjugated polymers.

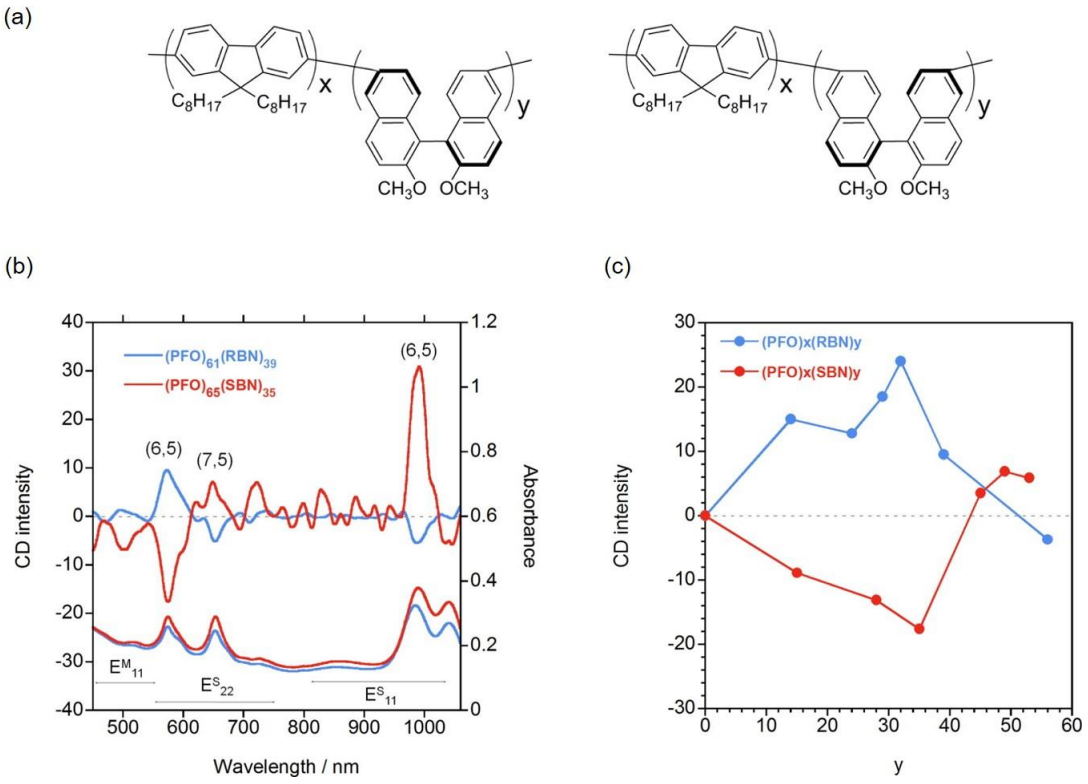

Figure 1.49. (a) Chemical structure of $(PFO)_x(RBN)_y$ (left) and $(PFO)_x(SBN)_y$ (right); (b) absorption and CD spectra of SWCNTs extracted by $(PFO)_{61}(RBN)_{39}$ and $(PFO)_{65}(RBN)_{35}$; (c) CD intensities of (6,5) E_{22} transition at 574 nm of all extracted SWCNT samples as a function of RBN or SBN ratio in $(PFO)_x(RBN)_y$ or $(PFO)_x(SBN)_y$.[161]

2 Motivation

The unique properties of s-SWCNTs and their potential for future applications have been comprehensively introduced. To obtain highly pure s-SWCNTs, post-processing purification of as-produced SWCNTs has advantages of large-scale production, high purity, and easy processability in solution. Among those solution-based purification methods, polymer sorting is one of the most promising approaches, however with the drawback of a residual polymer content in purified SWCNTs. In order to meet the demand for pure polymer-free s-SWNTs, desired polymers should fulfill three criteria: a) high selectivity towards s-SWNTs; b) high yield; c) easy and quantitative release upon polymer triggering. The first two criteria can be achieved by introducing carbazole subunits into the backbone of polyfluorene since polycarbazoles are capable of dispersing s-SWNTs with chiral indices (n-m) ≥ 2 in a high yield, while polyfluorenes enrich SWCNTs mostly near-armchair species with (n-m) ≤ 2.

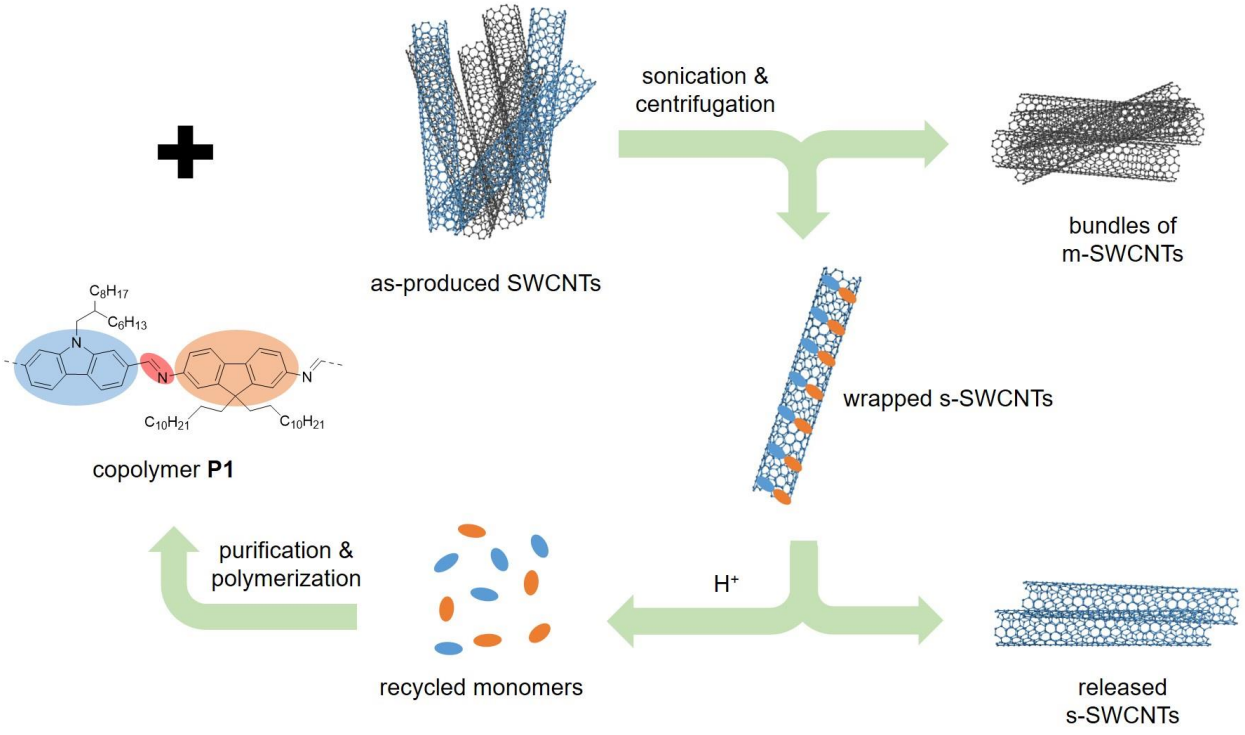

Figure 2.1. Designed copolymer for highly selective dispersion of s-SWCNTs and its subsequent release from the pre-sorted s-SWCNTs via an acid treatment.

Thus, copolymers with both fluorene- and carbazole-moieties are believed to harvest s-SWNTs with a wide range of chiral angles and high yield. Furthermore, by incorporating imine bonds into the polymer backbone structure as bridging bonds to interlink the monomeric units, the last criteria can be fulfilled. However, such acid cleavable imine-based fluorene-carbazole copolymer has not yet been reported. Here in this thesis, an acid cleavable fluorene-carbazole copolymer will be presented for highly selective dispersion of s-SWCNTs (Figure 2.1). Subsequent release of the s-SWCNTs from the polymers upon acid triggering provides naked nanotubes for further applications and studies, such as chirality enrichment or handedness sorting with another polymer.

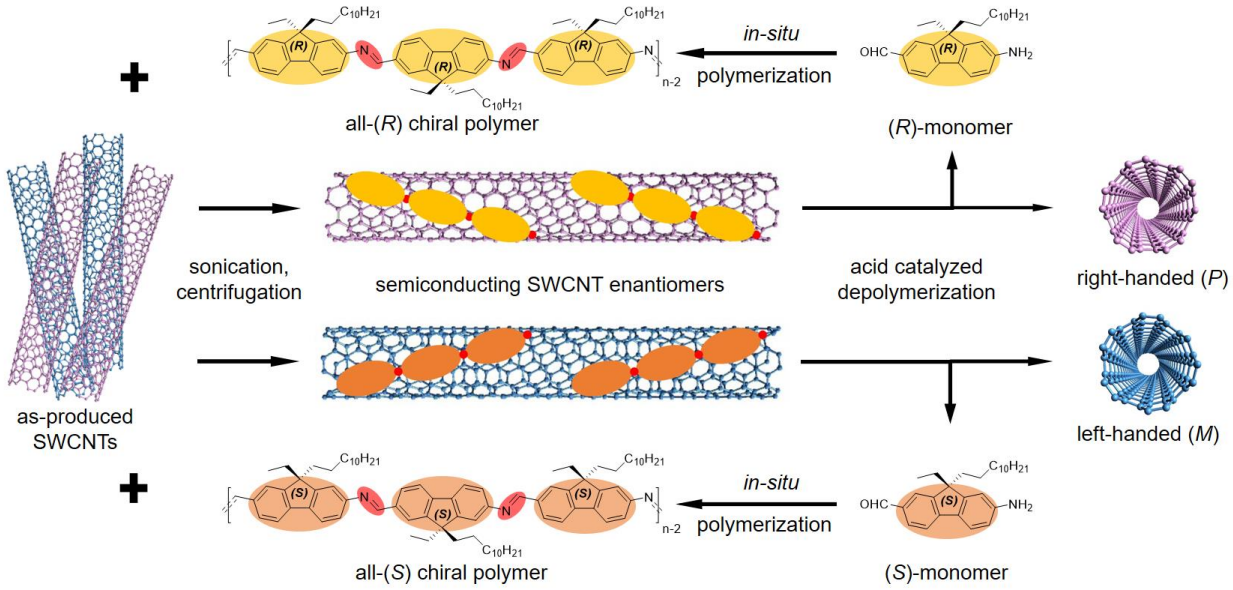

Figure 2.2. Designed all-(*R*) and all-(*S*) acid cleavable chiral homopolymers for enantiomeric separation of s-SWCNTs.

The pre-sorted and released s-SWCNTs contain left- and right-handed enantiomers of each (n,m) chirality. Due to the equimolar amount of the both enantiomers, the s-SWCNT ensemble is optically inactive (racemate). Recently, fluorene-based copolymers which have chiral binaphthols in the backbone (Figure 1.49) have been reported for the SWCNTs separation according to their handedness.[161] However, the enantioselectivity of such chiral copolymers has not been as good as the other methods (DGU, gel chromatography, ATPE, and etc.). Possible explanation of such chiral recognition weakness can be: a) a random composition ratio of chiral binaphthol and fluorene building blocks within the polymeric structure; b) low molecular weight of the polymer;

c) reduced interaction between polymer chain and SWCNT sidewall due to the twisted geometry of sterically hindered binaphthol subunits to form the tight geometry of the chiral polymer along the carbon nanotubes and thus increase the difference between the two handedness-wrapping scenarios. Taking all those drawbacks into consideration, we aimed to design and synthesize one pair of imine-based acid cleavable homo-polyfluorenes for enantiomeric separation of s-SWCNTs (Figure 2.2). To achieve this, we first synthesized enantiomeric monomers with absolute configuration (*R*) or (*S*) by introducing two different alkyl chains to the sp^3 carbon in the position 9 of the fluorene ring and additional functionalities in the position 2 (amine) and 7 (aldehyde) of the fluorene scaffold for the regioselective polymerization. Owing to the strict head-to-tail connection of the monomers during the polycondensation, the obtained chiral polymers maintain all-(*R*) or all-(*S*) configuration, as shown in Figure 2.2. The fluorene backbone ensures the selectivity of the chiral polymers towards s-SWCNTs and the chiral center (*R* or *S*) in each repeating unit spontaneously brings the ability for handedness sorting of nanotubes, as well as the unique molecular design of the chiral polymer maximize the π-π interactions between chiral polymers and SWCNT enantiomers for the selective chiral extraction. The simplicity of the monomer structure offers the polymer a defined structure and high molecular weight under easy polycondensation. Moreover, the chiral polymers can be readily removed from the nanotubes upon acid triggering due to the imine bonds in the polymer structure. This approach enables high selective isolation of polymer-free s-SWCNT enantiomers for their further applications in CNT-devices owing to their optical activity and high sensitivity to chiral molecules.

3 Results and discussion

3.1 Acid cleavable fluorene-carbazole copolymer for highly selective dispersion of s-SWCNTs

This chapter is focused on the synthesis and performance of the designed fluorene-carbazole copolymer for selective dispersion of s-SWCNTs. The fluorene- and carbazole-based monomers were both synthesized in two steps and then polymerized under a condensation reaction. Degradation of the polymer under acidic condition was studied by absorption spectroscopy. For sorting of nanotubes, HiPco and PLV SWCNTs were used as a raw material. The obtained nanotube solutions after sorting and purification process contain nicely dispersed s-SWCNTs with high purity, which were characterized by spectroscopic methods to evaluate the quality and to identify their (n,m) indices. Upon triggering with an acid, the s-SWCNTs were released from the polymer. The quantitative removal of the polymer from SWCNTs was confirmed by XPS. Rewrapping of the released nanotubes was performed with the copolymer **P1** (Scheme 3.2) and with the standard PFO.

3.1.1 Preliminary work

Fluorene-and carbazole-based polymers have been synthesized and studied comprehensively for the sorting of SWCNTs. However, imine-based fluorene-carbazole copolymers have not yet been reported. Under this circumstance, imine-based fluorene-carbazole copolymer **P2** was synthesized for the preliminary study along with other imine-based copolymers **P3**, **P4**, and **P5** for a comparison (Figure 3.1). The synthesis of the copolymers was done by Dr. Michal Valášek and the sorting from raw HiPco SWCNTs was performed by Dr. Frank Hennrich and Regina Fischer.

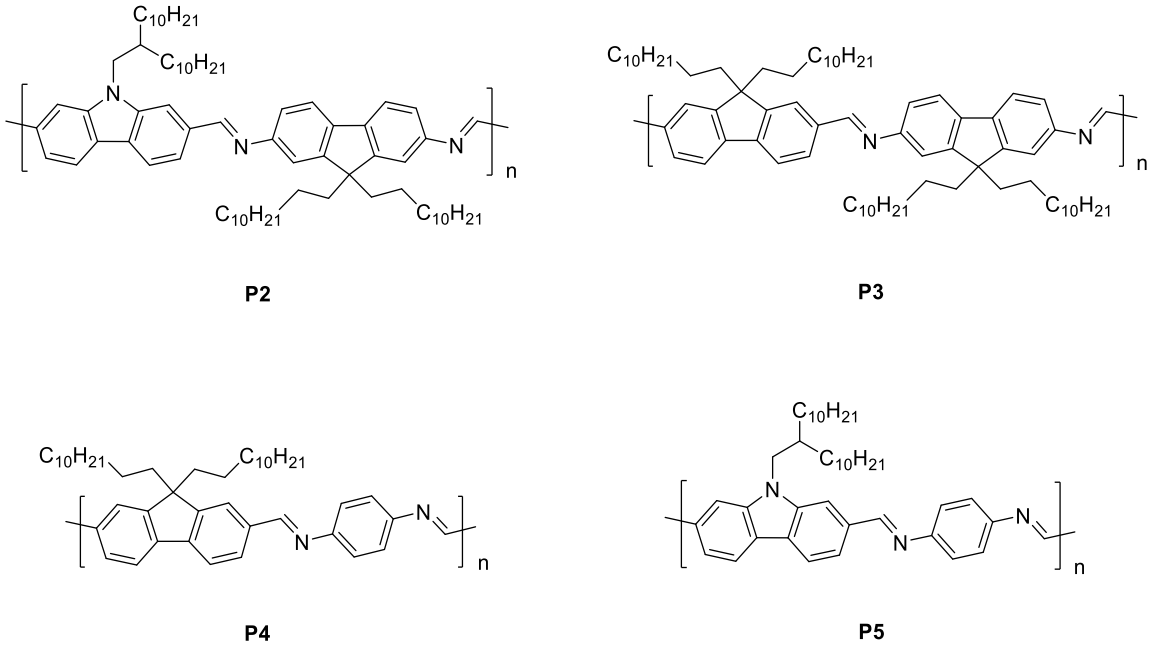

Figure 3.1. Structures of imine-based copolymers **P2**, **P3**, **P4**, and **P5**.

Copolymers **P2**, **P3**, and **P4** are well soluble in toluene and were tested with raw HiPco SWCNTs, whereas **P5** is surprisingly insoluble in almost all organic solvents and therefore has not been tested. The **P2**, **P3**, and **P4** sorted HiPco SWCNTs were characterized with absorption and PLE spectroscopy and the results are shown in Figure 3.2. Copolymers **P3** and **P4** show high selectivity towards certain (n,m) species owing to the fluorene units in the polymer structure, while copolymer **P2** is not as selective with respect to carbon nanotube chiralities (Figure 3.2b vs Figure 3.2c,d). However, **P3** and **P4** extract nanotubes with much less yield when compared to **P2**, as seen in the absorption spectra (Figure 3.2a). Copolymer **P2** extracts over 20 nanotube species with a wide range of diameter, which is comparable to the performance of surfactants. Moreover, no obvious signs of m-SWCNTs were found in the absorption region between ~ 500-600 nm from the **P2** sorted sample, indicating a high selectivity towards s-SWCNTs. This preliminary work proves that the imine-based copolymer **P2**, comprising fluorene and carbazole subunits in the structure, can not only extract SWCNTs with high yield in terms of nanotube species, but also show high selectivity towards s-SWCNTs. In the following work, commercially available 2-hexyldecyl bromide was used for the alkylation of carbazole unit instead of 2-decyldodecylbromide, which requires four synthetic steps.

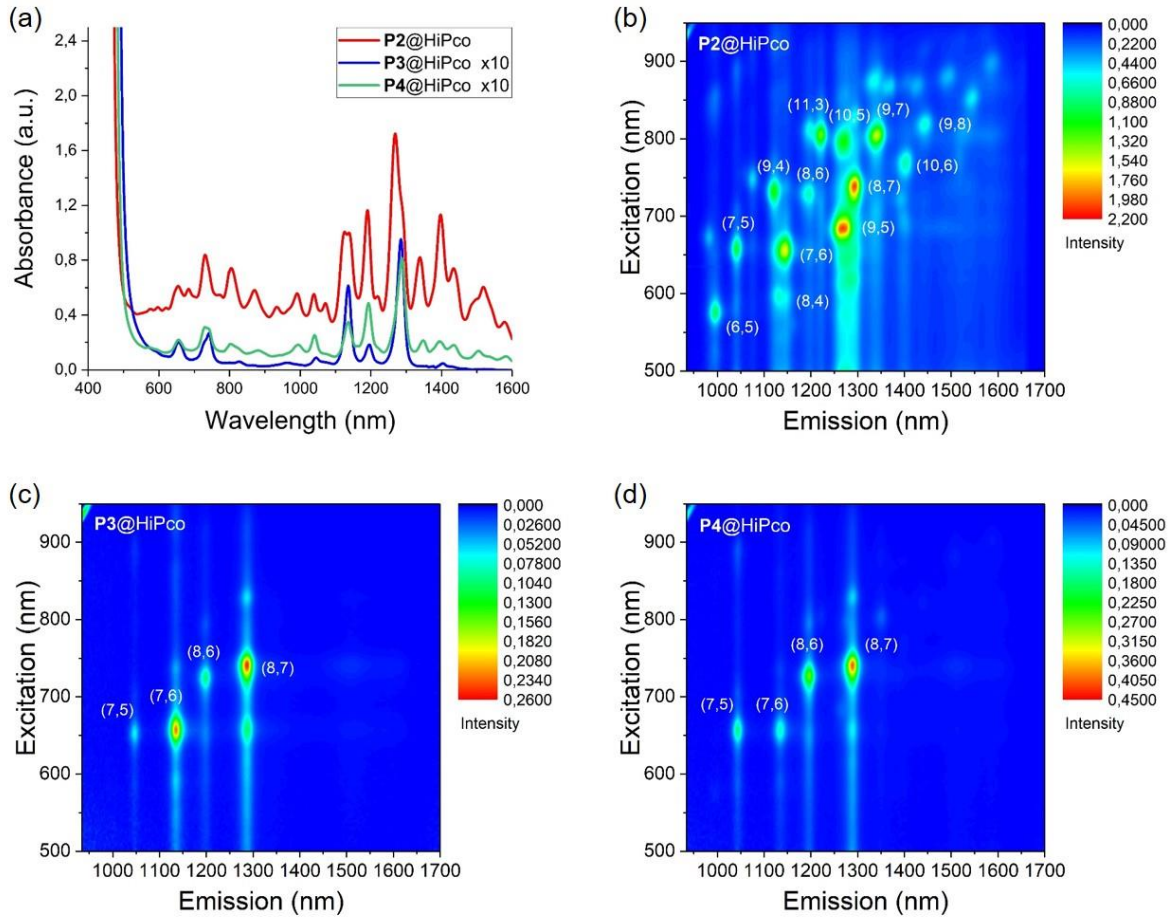

Figure 3.2. (a) Absorption spectra of copolymer **P2**, **P3**, and **P4** sorted HiPco SWCNTs. All samples were measured in toluene at room temperature. (b,c,d) PLE maps of copolymer **P2**, **P3**, and **P4** sorted HiPco SWCNTs. All samples were measured in toluene at 14 °C.

3.1.2 Synthesis and characterization of the monomers

Fluorene-based polyimines can be synthesized either by aza-*Wittig* condensation of bifunctional aldehydes and azides,[145,147] or by polycondensation of bifunctional aldehydes and amines.[71] The aza-*Wittig* condensation reaction requires a phosphine derivative as the dehydrating agent, which forms corresponding phosphine oxide as byproduct. Moreover, the fluorene-based polyimines which were synthesized by this approach are with low molecular weight ($M_n \leq 15$ kDa), as reported by Barner-Kowollik *et al*.[145] and Gopalan *et al*.[147] In this work, the latter approach was chosen to achieve higher molecular weight. Aldehyde groups and amino groups were introduced to the carbazole backbone and fluorene backbone, respectively. These functional groups for imine bond formation are in the 2- and 7-positions to ensure the favorable conformation of the polymer chain for the efficient wrapping process, whereas the 3,6-connectivity of the monomers yields polymers with unfavorable conformations and causes the precipitating of the nanotube suspensions within minutes.[136]

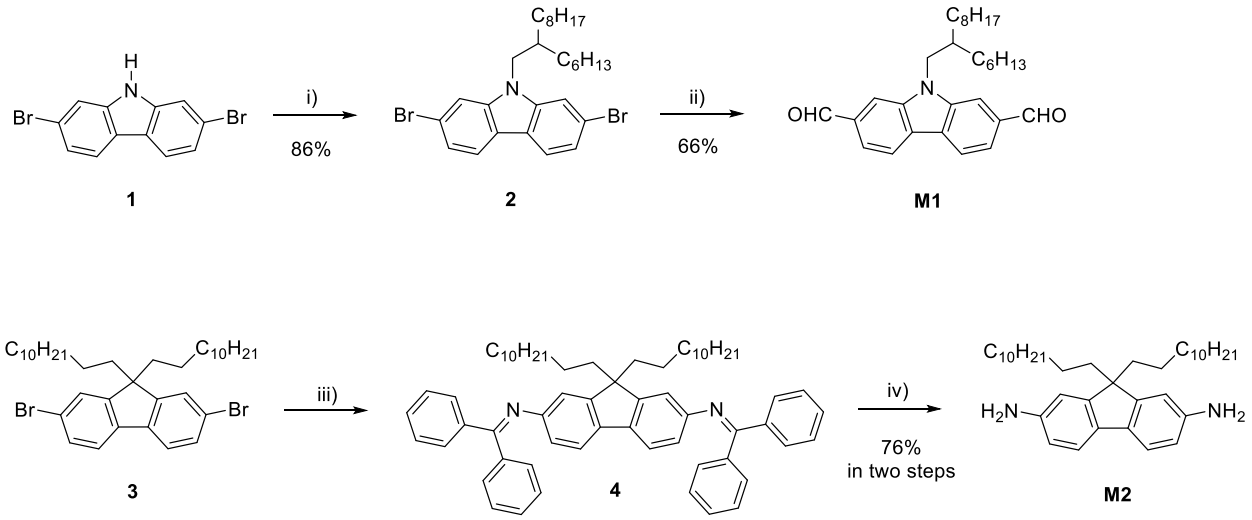

Scheme 3.1. Synthetic strategy towards the monomers **M1** and **M2**. Reagents and conditions: i) sodium hydride, 2-hexyldecylbromide, DMF, RT; ii) a) *n*-BuLi, THF, -78 °C, b) DMF; iii) benzophenone imine, Pd_2dba_3, *rac*-BINAP, KO^{t}Bu, toluene, 100 °C; iv) HCl (aq., 10%), THF, RT.

The carbazole- and fluorene-based bifunctional monomers **M1** and **M2** were both synthesized in two steps as outlined in Scheme 3.1. The monomer **M1** was prepared from the commercially available 2,7-dibromocarbazole **1**. Deprotonation of **1** was carried out with sodium hydride (60% w/w in mineral oil) in DMF following a literature procedure,[136] and the completion of this reaction was indicated by the disappearance of the hydrogen gas evolution in the solution. Subsequent

alkylation with branched 2-hexyldecylbromide provided 2,7-dibromo-*N*-(2-hexyl)decylcarbazole **2** as a colorless oil with a yield of 86%. Due to the presence of long alkyl chains, the solubility of obtained compound **2** in organic solvents increased which allowed its purification with column chromatography in hexane. Lithiation of aryl halide **2** with *n*-BuLi at -78 °C followed by formylation with DMF afforded the desired 2,7-diformyl-*N*-(2-hexyl)decylcarbazole **M1** as a yellow solid in 66% yield.[162] In this step, the progress of the lithiation and the subsequent formylation was observed by GC/MS. The ^{1}H NMR spectrum of **M1** confirms its structure and the purity, as shown in Figure 3.3. All peaks in the aromatic region are assigned to the corresponding protons of carbazole ring. The aldehyde groups of **M1** give a characteristic singlet at 10.19 ppm while the methylene protons adjacent to the nitrogen atom contribute a doublet at 4.30 ppm.

Synthesis of monomer **M2** was performed according to the reported procedure.[163] It started with the palladium catalyzed Buchwald-Hartwig amination of 2,7-dibromo-9,9-didodecyl-9*H*-fluorene **3** with benzophenone imine, which serves as a convenient ammonia equivalent.[164] The reaction was carried out in toluene at 100 °C with Pd_2dba_3 as Pd(0) source in the presence of potassium *tert*-butoxide as base and *rac*-BINAP as bidentate phosphine ligand. After completion of the reaction which was observed by thin-layer chromatography (TLC), the crude product containing desired *N*,*N*-bis(diphenylmethylene)-9,9-didodecyl-9*H*-fluorene-2,7-diamine **4** was collected as a yellow-brownish oil. Further purification of the crude product by column chromatography was not carried out due to the close R_f value of **4** and benzophenone imine which was used with an excess amount. Hydrolysis of the mixture containing **4** was performed in THF with the addition of aqueous HCl (10%) and monitored by TLC. The target monomer 9,9-didodecyl-9*H*-fluorene-2,7-diamine **M2** was isolated by column chromatography (deactivated with 5% of NEt_3) as a red-brownish wax with a yield of 76% in two steps. The amino groups on **M2** give a characteristic broad peak at 3.65 ppm in ^{1}H NMR spectrum which is pH sensitive, as shown in Figure 3.3.

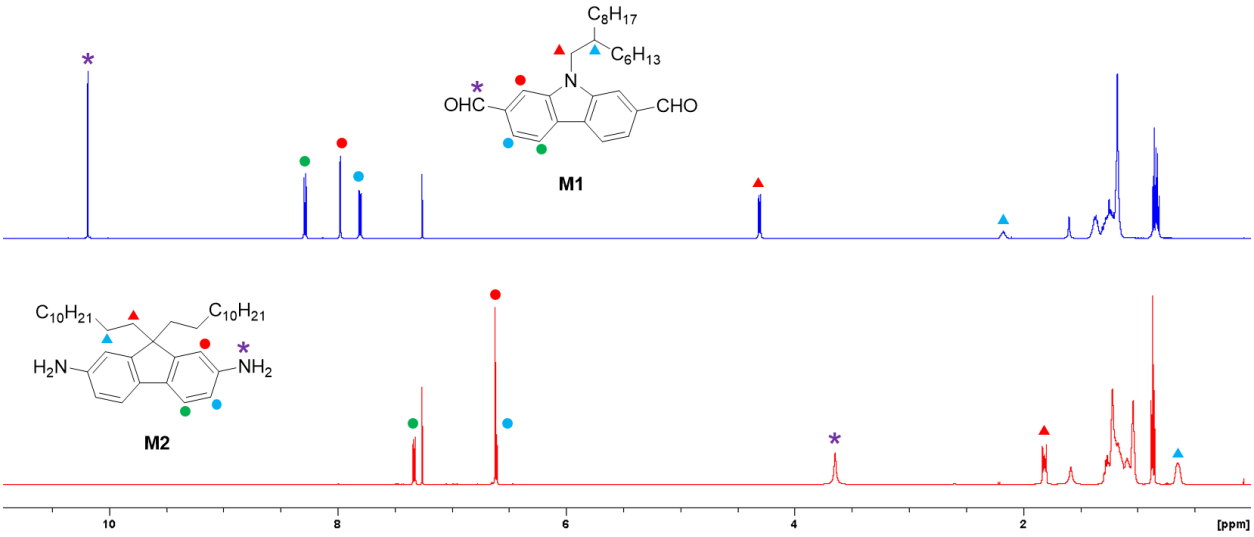

Figure 3.3. ^{1}H NMR spectra (500 MHz) of monomers **M1** and **M2**. Both samples were measured in $CDCl_3$ at room temperature.

3.1.3 Synthesis and characterization of the copolymer

In general, an imine (*Schiff* base) can be formed between an aldehyde (or ketone) and a primary amine under acid catalysis, as shown in Figure 3.4.

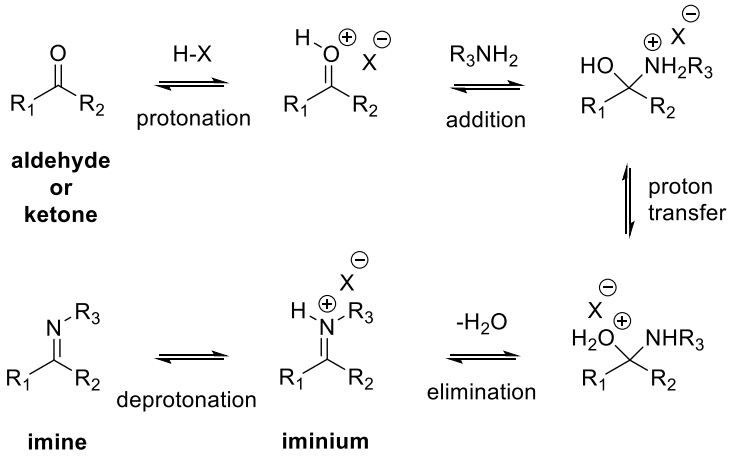

Figure 3.4. Mechanism of imine (*Schiff* base) formation.

In the first step, the acid protonates the carbonyl group and makes it more electrophilic. The amino group of the primary amine thus attacks the carbonyl group as a nucleophile, forming a

carbinolamine which undergoes proton transfer and subsequent elimination, leading to an iminium. Deprotonation of the iminium gives desired imine (*Schiff* base) with a C=N bond.[165]

Here, polyimine {(9,9-di-*n*-dodecylfluorene-2,7-diamine)-*alt*-[*N*-(2-hexyl)decylcarbzole-2,7-dialdehyde]} **P1** was synthesized by polycondensation of monomers **M1** and **M2** in toluene at 110 °C in the presence of *p*-toluenesulfonic acid (PTSA) as a catalyst and LiCl as a drying agent (Scheme 3.2).

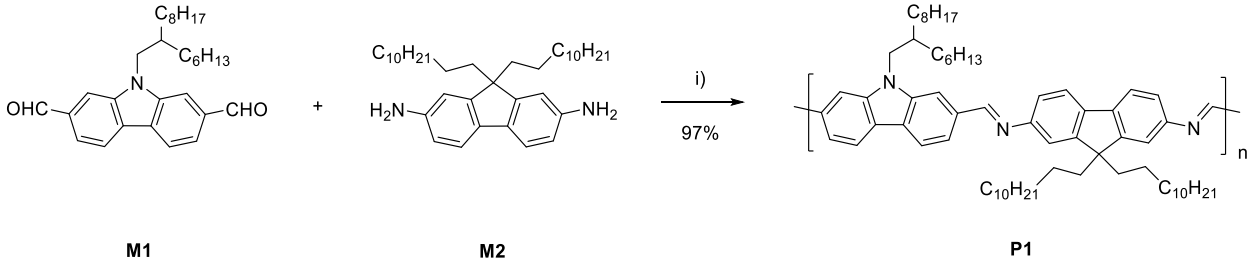

Scheme 3.2. Synthetic strategy towards copolymer **P1**: i) *p*-TsOH, LiCl, toluene, 110 °C.

An equimolar ratio of **M1** and **M2** was kept exactly 1:1 to achieve quantitative yield and moreover, no extra end-capping reagents have been used. The amount of PTSA as catalyst is an important factor. On one hand, PTSA accelerates this acid-catalyzed polyimine condensation between both monomers by increasing the electrophilicity of the aldehyde groups of **M1**. On the other hand, an excess of PTSA can also protonate the obtained imine bonds and thus suppressing the degree of polymerization especially in the presence of trace amount of water. Thus in this work, different amount of PTSA was tested for the polymerization of **P1**, from 5 mol% as reported by Bao *et al.*[71] to less than 1 mol%. The obtained results showed that for the polycondensation between **M1** and **M2**, a few crystals of PTSA (less than 1 mol%) provide **P1** with a high molecular weight. Besides the catalyst, the employment of LiCl is also essential. Excess amount of LiCl serves as a drying agent and ensures the removal of the generated water, hence promoting the polymerization. Lithium chloride is as well a weak Lewis acid and thus slightly promote this polycondensation. After completion of the polymerization, the reaction mixture was poured into methanol to precipitate the polymer, which was then washed and sonicated with water and acetone to remove short oligomers and an excess of LiCl.

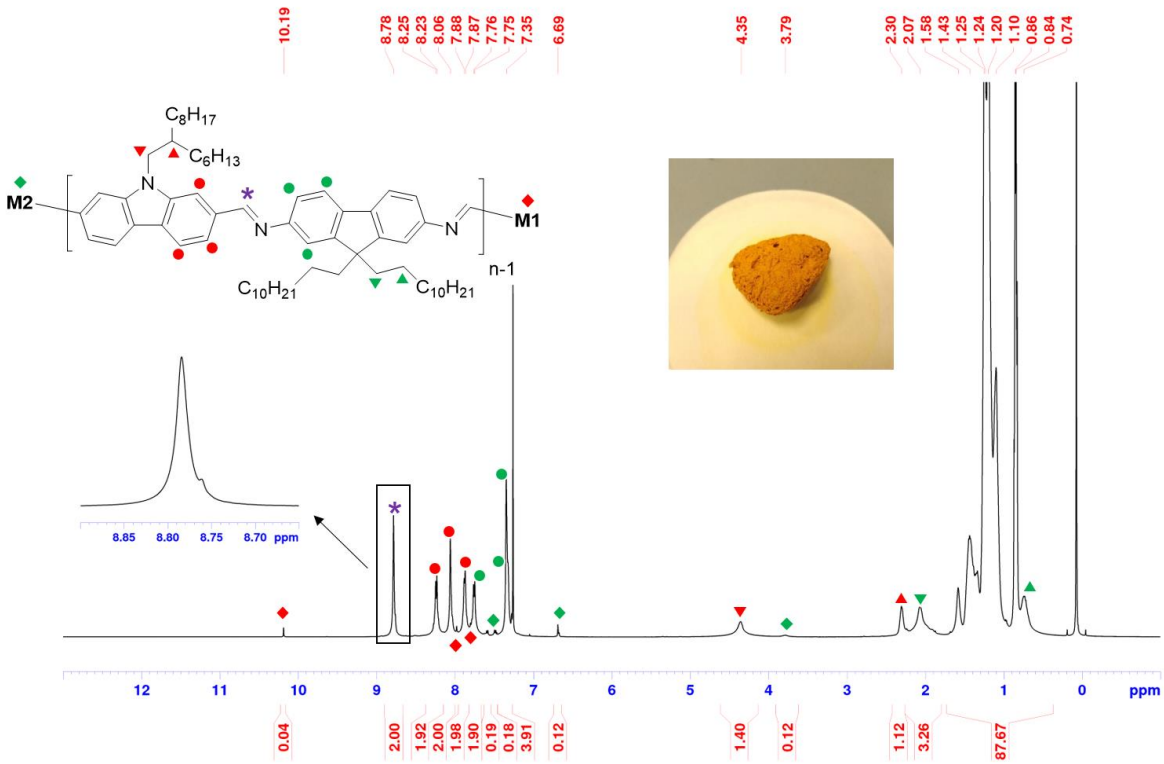

Figure 3.5. ^{1}H NMR spectrum (500 MHz) of copolymer **P1**. The protons from **M1** moiety are labeled with different shapes in red and the protons from **M2** moiety are labeled in green. The sample was measured in $CDCl_3$ at room temperature.

The obtained copolymer **P1** was first characterized by ^{1}H NMR in $CDCl_3$ at room temperature and the spectrum is shown in Figure 3.5. Owing to the good solubility of **P1** in organic solvents, the main peaks in the aromatic region are well separated from each other and can be easily assigned to the corresponding aromatic protons from the monomeric **M1** and **M2** moieties with the help of 2D NMR spectra. The doublets at 8.24 ppm and 7.88 ppm along with the singlet at 8.06 ppm can be assigned to the aromatic protons of carbazole ring, while the doublet at 7.76 ppm and the overlapped peak at 7.35 ppm can be assigned to aromatic protons of fluorene ring. Each repeating unit of **P1** contains two imine bonds, which contribute a peak at 8.78 ppm. The small shoulder of this peak indicates the existence of *syn*- and *anti*-configurations in the polymer backbone, with one of them much favored. Interestingly, the proton signals from the chain-termini **M1** and **M2** are also observed. The weak singlet at 10.19 ppm can be assigned to the terminal aldehyde group from the chain-termini **M1** while the very weak broad peak at 3.79 ppm can be assigned to the terminal

amino group from the chain-termini **M2**. Besides the aromatic protons, the aliphatic protons adjacent to the aromatic rings also give distinguishable peaks, as identified in Figure 3.5.

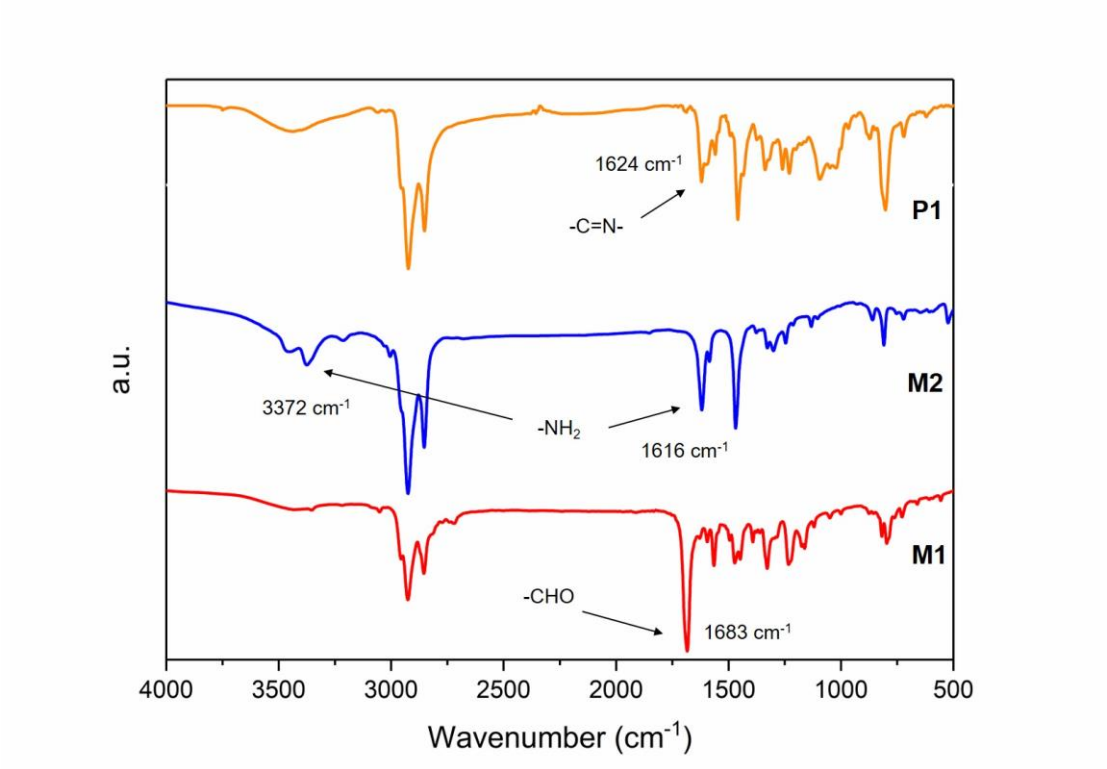

Figure 3.6. FTIR spectra of monomer **M1**, **M2**, and polymer **P1**. All samples were measured in KBr pellet at room temperature.

Polymer **P1** was further characterized by FTIR spectroscopy in KBr pellet and the spectrum is plotted in Figure 3.6 along with the spectra from monomer **M1** and **M2**. The strong vibrations at ca. 2920 cm^{-1} and 2850 cm^{-1} are attributed to the C-H stretching vibrations of alkyl chains. Monomer **M2** has a characteristic peak at 3372 cm^{-1} and 1616 cm^{-1} of the amino group while **M1** has a characteristic peak at 1683 cm^{-1} of the aldehyde group. All these vibrations disappeared or decreased significantly in FTIR spectrum of **P1**, indicating the formation of imine bonds which can be further confirmed by the presence of characteristic stretching C=N vibration at 1624 cm^{-1}.

GPC measurement revealed that the copolymer **P1** has a number-average molecular weight (M_n) of 43 kDa and a weight-average molecular weight (M_w) of 91 kDa, which are much higher than the polyimines reported by Gopalan *et al.*[147] and Bao *et al.*[71] Purification of **P1** was carried out with Soxhlet extraction to remove the oligomers and low molecular weight fractions. Hot acetone extracted mostly the oligomers containing up to five repeating units, while hot hexane

washed away the polymer chains with molecular weight lower than 10 kDa. In order to study the relationship between the molecular weight and the sorting performance of the polymer, **P1** was further purified by size-exclusion gel chromatography to obtain fractions with a similar molecular weight. For this purpose, two types of gel were used which are the Toyopearl® HW-75 and the Bio-Beads™ S-X1. Both gels are not designed for the use in organic solvents, so the gels were washed with methanol and THF to get rid of the water then swelled in THF over night before loading in the column. Despite of the attempts with different elution rate and polymer amount, the purification according the molecular weight with size-exclusion chromatography was not successful. Both gels can exclude the first or the last fraction with highest or lowest molecular weight, but not the fractions with a similar molecular weight.

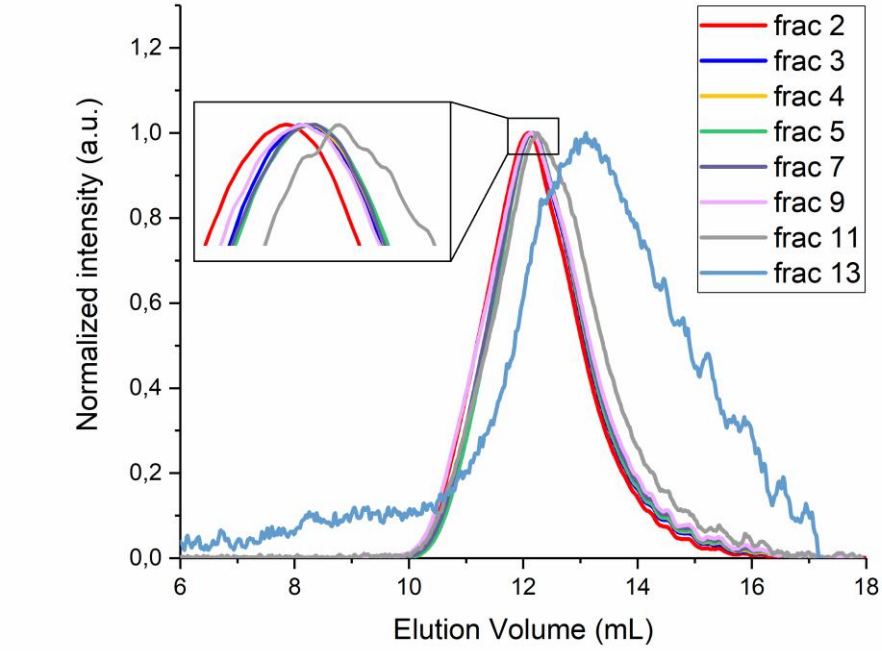

Figure 3.7. GPC results of the fractions obtained after size-exclusion chromatography of **P1** with Bio-Beads™ S-X1 gel. All samples were measured in THF at room temperature. Polystyrene was used as a calibration standard.

Figure 3.7 shows the GPC results of the fractions obtained after size-exclusion chromatography of **P1** with Bio-Beads™ S-X1 gel in THF. The fraction 13 which contains polymer with the lowest peak molecular weight of M_p = 32.4 kDa was well separated from the main fractions. However, in the main fractions as shown in an expanded view, fraction 2

(M_p = 96.7 kDa) and 11 (M_p = 81.7 kDa) were just slightly separated from the fractions 3-9 which all have the similar peak molecular weight between 90-93 kDa. Toyopearl® HW-75 gel can isolate the fractions containing polymer with the highest and lowest molecular weight, but the main fractions were not separated accordingly. For the further separation, a suitable size-exclusion gel for the purification of conjugated polymer in organic solvents is required.

Polymer **P1** is designed for the sorting and the subsequent release of SWCNTs. Hence, the efficient degradation of **P1** upon acid treatment is of great importance in this work. In order to study the efficient triggering of imine bond, several conditions in toluene with different concentrations of the polymer and trifluoroacetic acid (TFA) were tested. TFA has been chosen as a strong organic acid which is highly volatile and thus can be easily and quantitatively removed after polymer hydrolysis. In general, a catalytic amount of TFA and a few drops of water are required for successful depolymerization of **P1** into monomers. Since this reaction is basically acid hydrolysis, the presence of a little amount of water is crucial, otherwise the degradation process takes much longer and might be incomplete. Sonication and heating accelerate this process and is found to be quite essential for an efficient triggering of more concentrated polymer samples.

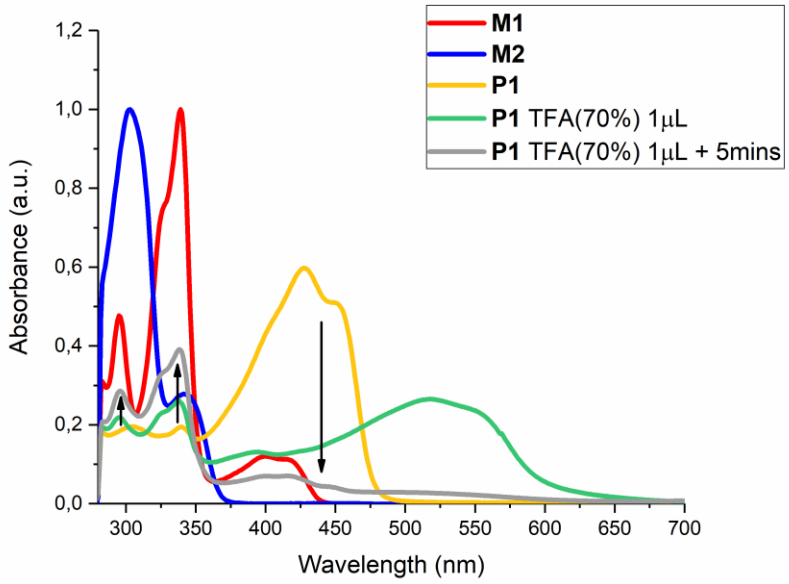

Figure 3.8. Absorption spectra of polymer **P1** before and after the addition of TFA (70%). For a comparison, the absorption spectra of monomers **M1** and **M2** are also plotted with normalized intensities. All samples were measured in toluene at room temperature.

To directly observe the degradation process with UV-Vis-NIR spectroscopy, a polymer solution with concentration in the range of 10^{-5} M was loaded in a quartz cuvette (1 mL). After the addition of 1 µL TFA (70%, aq. solution), the color of the solution turned immediately from yellow to red and the main absorption peak of **P1** at 428 nm is red-shifted to 518 nm due to the protonation of the imine bonds, as shown in Figure 3.8. After five minutes, the degradation was already completed which can be indicated by the disappearance of the polymer peak around 400 nm and the appearance of the both monomer peaks around 300 nm and 330 nm. ^{1}H NMR spectra after acid treatment confirmed the total cleavage of the imine bonds and the partial recovery of **M1**, however the signals of **M2** were not clearly identified possibly due to the protonation of amino groups or instability of such monomer.

Additionally, polyimine **P1** is stable under ambient conditions with a decomposition temperature around 450 °C as confirmed by TGA analysis (Figure 3.9). The residue after decomposition (< 20%) could be from the solid LiCl which was not totally washed out from the polymer in the purification step. Moreover, in the absence of acid, no degradation of **P1** was observed in toluene at 100 °C.

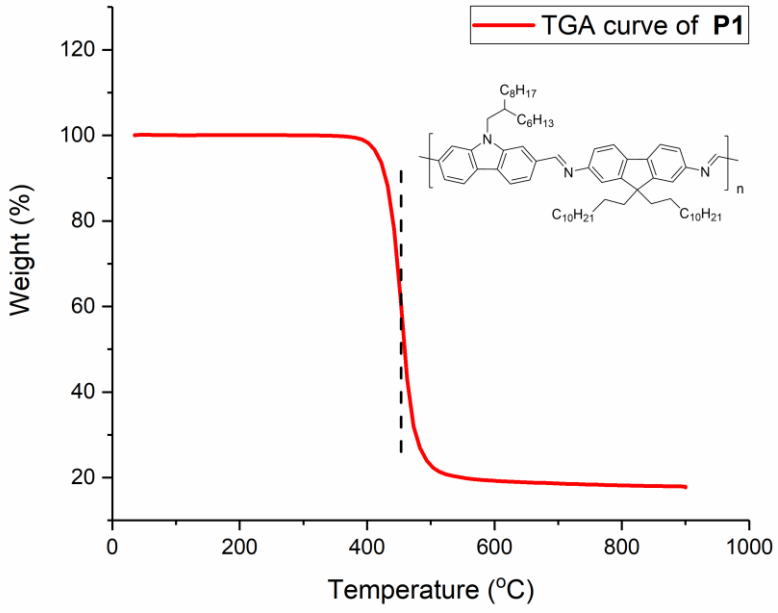

Figure 3.9. TGA curve of polymer **P1**.

3.1.4 Characterization of sorted/wrapped HiPco SWCNTs

Commercially available as-produced HiPco SWCNTs were first high-shear mixed with polymer **P1** in toluene and then sonicated in a water-circulation bath. After sonication, the suspension was centrifuged and the supernatant was filtered off. Further purification was performed by size-exclusion chromatography (SEC) with Toyopearl® HW-75 resin to remove solid impurities and an excess of polymer. Typical method and detailed procedure of this sorting process is described in experimental part.

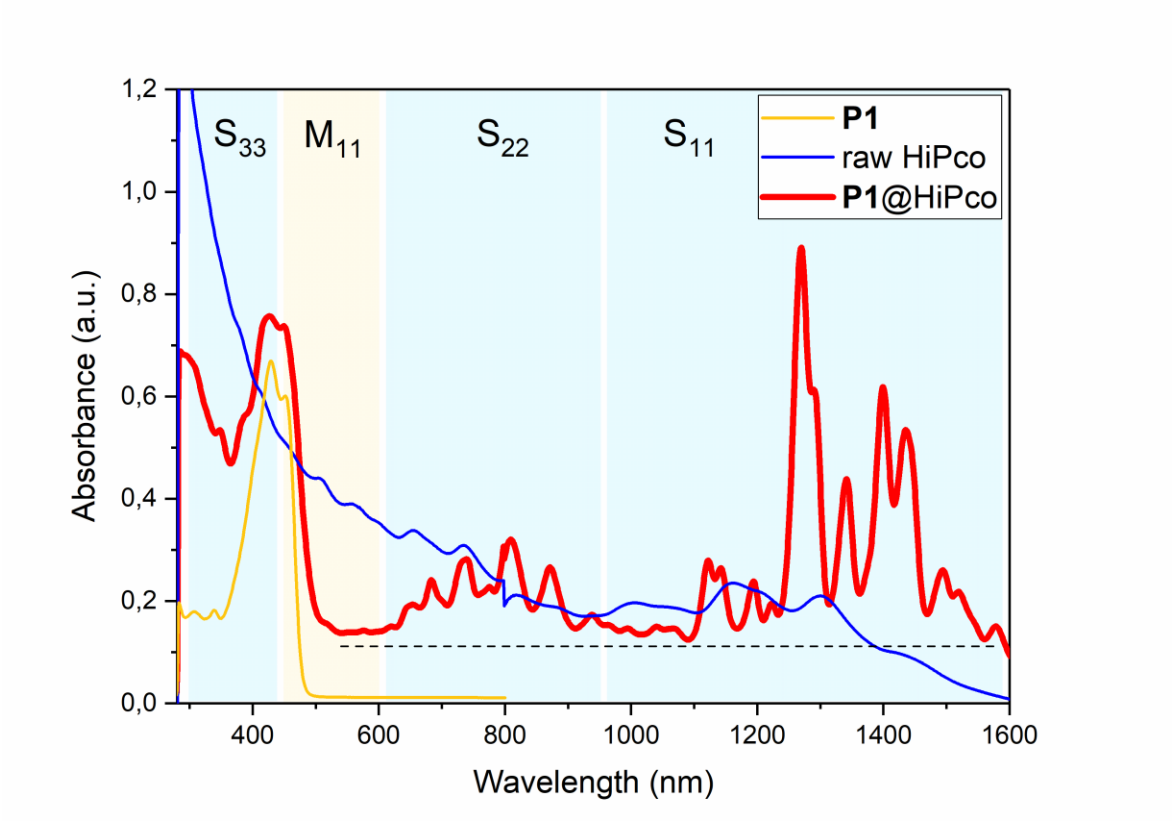

Figure 3.10. Absorption spectra of polymer **P1**, raw HiPco SWCNTs, and **P1** sorted HiPco SWCNTs. All samples were measured in toluene at room temperature.

The sorted HiPco SWCNTs were first characterized with absorption spectroscopy, as shown in Figure 3.10. For HiPco SWCNTs, the absorption regions around 950-1600 nm, 600-950 nm, and 300-450 nm can be assigned to S_{11}, S_{22}, and S_{33}, namely the E_{11}, E_{22}, and E_{33} interband transitions of semiconducting SWCNTs, respectively. The absorption region of metallic SWCNTs is typically around 450-600 nm and is denoted as M_{11}.

In comparison to the raw material, the absorption spectrum of **P1** sorted HiPco SWCNTs clearly shows distinguishable S_{11}, S_{22} region, and a polymer region which partially overlaps with M_{11} and S_{33} region. Despite of the non-zero value of the baseline which is quite common for carbon nanotubes, the S_{11} and S_{22} regions of the sorted sample share one flat baseline owing to the post-sorting purification with SEC, as depicted with a dashed line. The absorption peaks in S_{11} region are well separated, which means the sorted SWCNTs within the sample are well individualized and dispersed. The main peaks at around 1270-1438 nm are attributed to (9,5), (10,5), (8,7), (9,7), (10,6) and (9,8) SWCNTs with an average diameter of 1.0 nm.[131] Minor species such as (7,6) and (11,7) SWCNTs at 1120 and 1520 nm extend an average diameter of the obtained sample between 0.90-1.25 nm, corresponding to the diameter range of raw HiPco tubes. This means that the selectivity of polymer **P1** for SWCNTs is diameter-independent. In S_{22} region, much less peaks are observed due to the overlap of second transition peaks from the nanotubes. For instance, the S_{22} peak at around 810 nm can be assigned to (10,5), (9,7) and (9,8) SWCNTs.[27]

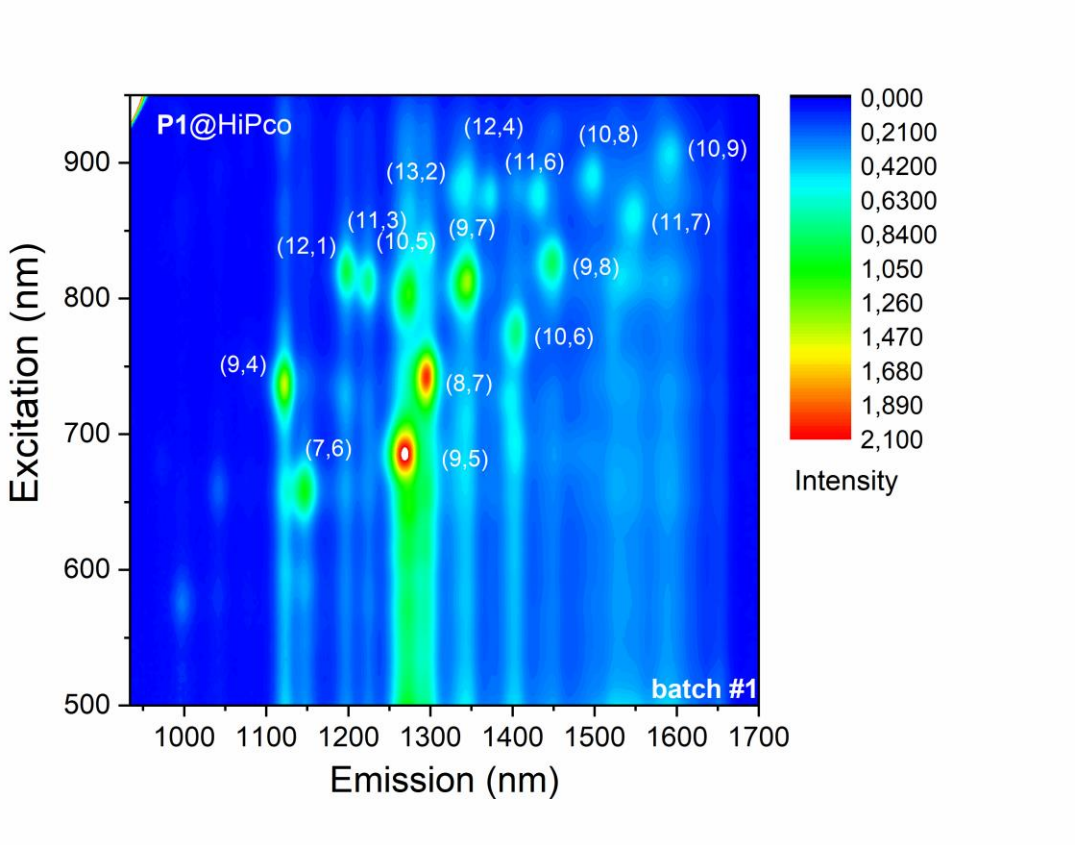

Figure 3.11. PLE map of polymer **P1** sorted HiPco SWCNTs. The sample was measured in toluene at 14 °C.

In order to identify all the SWCNT species in this sample, PLE mapping was performed and the results are shown in Figure 3.11. The assignment of the spots in this spectrum to the corresponding chiral indices of carbon nanotubes was achieved by correlation of the excitation and emission wavelengths with the reference data.[27,29] This map is in good agreement with the absorption spectrum, showing that (9,5) and (8,7) SWCNTs are the most abundant nanotube species in this sample. Besides that, more nanotube species with low intensities are identified in PLE map which gives a total number of (n,m) indices up to 16. Comparing with the performance of the reported fluorene- and carbazole-based homopolymers,[135,136]copolymer **P1** has an enhanced ability to disperse SWCNTs with both $(n\text{-}m) \leq 2$ and $(n\text{-}m) \geq 2$. The harvest of near-armchair species (7,6), (8,7), (9,7), (9,8), (10,8) and (10,9) is owing to the fluorene moiety of **P1**, while the carbazole moiety is responsible for the extraction of nanotubes with smaller chiral angles ($\theta \approx 20°$) such as (9,4), (9,5), (10,5), (10,6), (11,6) and (11,7) SWCNTs. Moreover, the PLE map reveals that **P1** has also extracted SWCNT species (11,3) and (12,4) with $\theta \approx 10°$, and even near-zigzag nanotubes (12,1) and (13,2). Hence, the selectivity of **P1** towards s-SWCNTs can be concluded as chiral angle-independent which covers the range from near-armchair to near-zigzag. The relative intensities of each extracted SWCNT species are summarized in Table 3.1.

Table 3.1. Relative intensities of the extracted SWCNT species from the PLE map in Figure 3.11.

Assignment	Relative Intensity	Assignment	Relative Intensity
(7,6)	6.67%	(10,6)	5.09%
(9,4)	9.19%	(9,8)	5.45%
(9,5)	13.79%	(13,2)	3.57%
(8,7)	12.76%	(12,4)	3.20%
(12,1)	5.93%	(11,6)	3.56%
(11,3)	4.86%	(10,8)	3.41%
(10,5)	7.21%	(11,7)	3.53%
(9,7)	8.69%	(10,9)	3.09%

While the S_{11} and S_{22} transition regions give information about the extracted s-SWCNTs, the presence of m-SWCNTs can be observed in the M_{11} transition region of the absorption spectrum. As shown in Figure 3.10, the M_{11} region between 500-600 nm is quite flat, indicating the absence

of metallic tubes. However, the M_{11} region is partially overlapped with the absorption band of **P1** so that the estimation of s-SWCNTs purity by calculating the absorption ratio between M_{11} and S_{22} is not possible.[166] For the purpose of evaluating the quality of the **P1** wrapped SWCNTs and to prove the removal of metallic species in the sample, Raman spectra were recorded. For G/D mode, 785 nm was chosen as excitation wavelength in order to excite more semiconducting species and to evaluate the **P1**@SWCNT complexes.

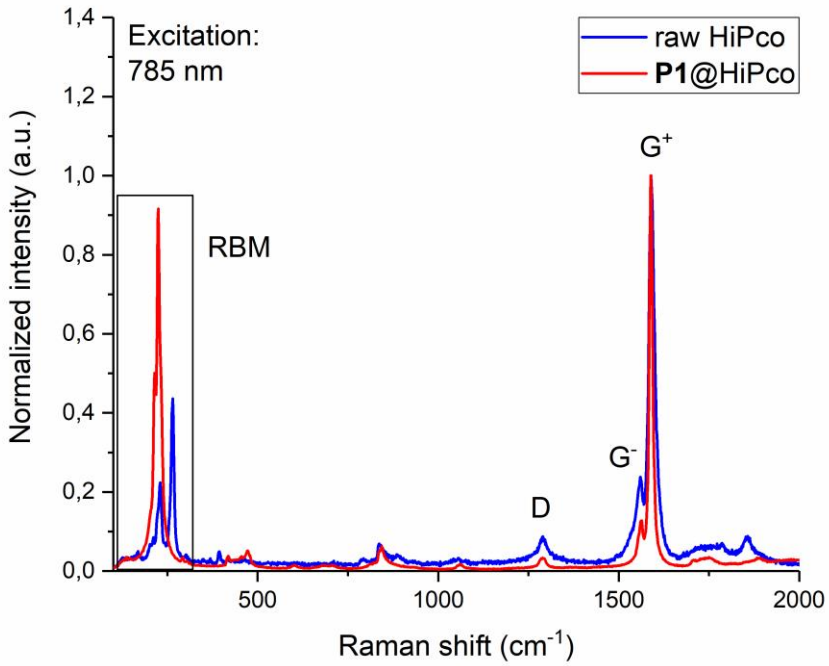

Figure 3.12. Raman spectra of raw and **P1** sorted HiPco SWCNTs excited at 785 nm. Both spectra were normalized at 1590 cm^{-1}.

As shown in Figure 3.12, the Raman spectrum of the complexes exhibits characteristic G and D bands at 1590 and 1290 cm^{-1}, respectively. The G^+ and G^- denote the split components of G band, which are resulted from the vibrations of carbon atoms along the nanotube axis and circumference. The decreased G^- band at 1560 cm^{-1} indicates a strong interaction between polymer **P1** and the circumference of the nanotubes.[167] The weak D band confirms that the non-covalent interaction keeps the intrinsic structure and electronic properties of the SWCNTs.

In the RBM region of the Raman spectrum, the existence of m-SWCNTs within a nanotube sample can be observed. Figure 3.13 shows the RBM regions from the Raman spectra of raw and

P1 sorted HiPco SWCNTs. The excitation wavelength was set as 633 nm so that both s-SWCNTs and m-SWCNTs can be excited. With the help of the experimental Kataura plot reported by Thomsen *et al.*, the region between ca. 180-230 cm^{-1} can be assigned to metallic nanotubes as highlighted in grey. And the semiconducting nanotubes give rise to the peaks at 230-300 cm^{-1}. For the raw HiPco tubes, the broad peak at 192 cm^{-1} in the metallic region can be assigned to (9,9) SWCNT while the sharp peak at 215 cm^{-1} can be assigned to (12,3) SWCNT.[168] In the sorted **P1**@HiPco sample, the metallic peaks are clearly missing. Hence, an efficient removal of m-SWCNTs by sorting with polymer **P1** is evidenced.

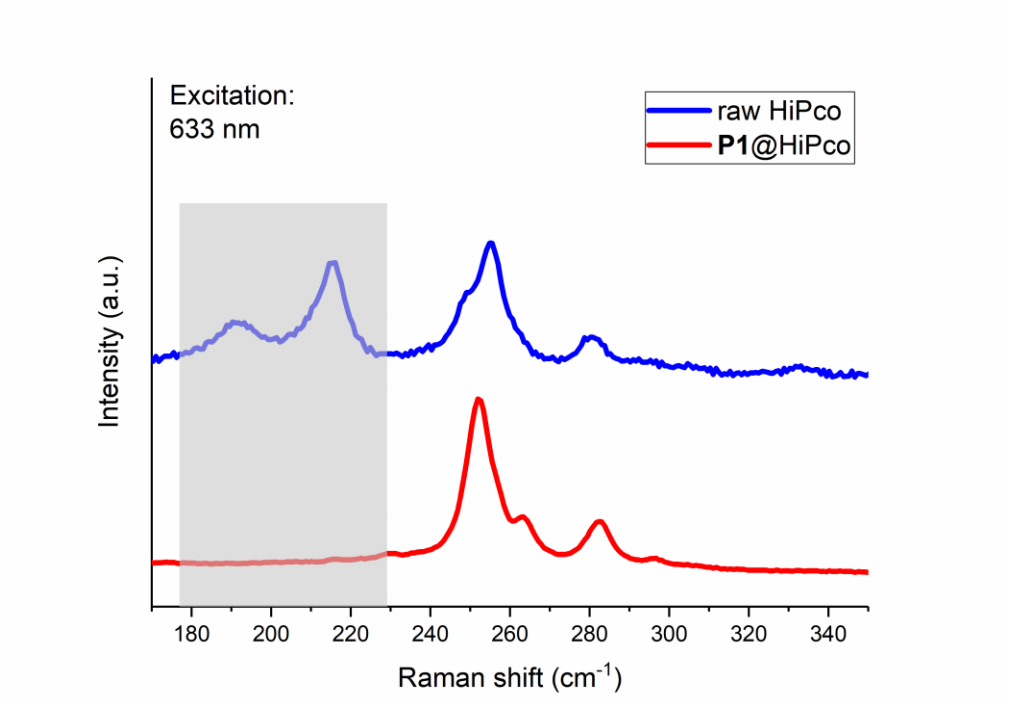

Figure 3.13. Raman spectra (RBM regions) of raw and **P1** sorted HiPco SWCNTs excited at 633 nm. Metallic region is highlighted in grey. Both spectra were normalized and vertically shift for comparison.

The absorption band of the wrapping polymer **P1** on dispersed SWCNTs is located between 366-500 nm and is consistent with the neat polymer. The relative intensity of the polymer absorption peak at 428 nm is higher than the transition peak of SWCNTs at 1270 nm when there is an excess amount of polymer **P1** in the sample (Figure 3.10). After removal of the polymer excess by size-exclusion chromatography (SEC), the intensity of the polymer peak decreases and then remains as seen in Figure 3.10, which means this peak can be attributed only to the remaining

polymers on the tubes. This feature can be considered as a tool to identify the polymer excess in the sample.

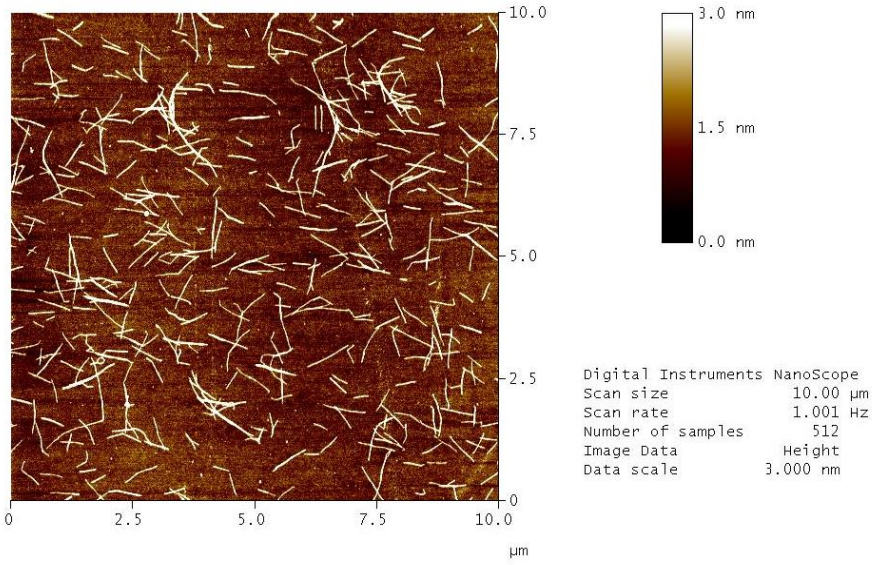

Figure 3.14. AFM image of **P1** sorted HiPco SWCNTs recorded on a silicon wafer with tapping mode in air.

After the removal of excess polymer, the wrapped nanotubes can be visualized by performing the atomic force microscopy (AFM) as presented in Figure 3.14. This image reveals that the obtained sample contains a high concentration of SWCNTs which are well individualized. The entanglement of several tubes is more likely due to the overlapping of individual nanotubes rather than their bundling or aggregation. Statistical calculation and Gaussian distribution fitting give this sample an average length of 500 nm.

In general, the whole sorting process for the enrichment of s-SWCNTs from raw HiPco material with polymer **P1** is fully reproducible and scalable. The obtained s-SWCNTs dispersions in toluene are stable and can be stored at ambient conditions for a month (Figure 3.15a). All batches of enriched s-SWCNT samples from repeated sorting process have similar diameter distribution and chiral angles with difference only in the concentration of several CNT species. In Figure 3.15, PLE maps of the sorted s-SWCNT from three different batches are shown for a comparison. In all batches, (8,7) and (9,5) SWCNTs remain the most abundant species. More of (6,5) and (7,5) SWCNTs were extracted in batch #2 than in other batches, while (9,4) and (7,6) SWCNTs are found more abundant in other two batches #3 and #4, which is most probably due to

the different molecular weights of the polymers among those three batches (M_n of 40 kDa, 30 kDa, and 29 kDa for the polymer used in batch #2, #3, and #4, respectively).

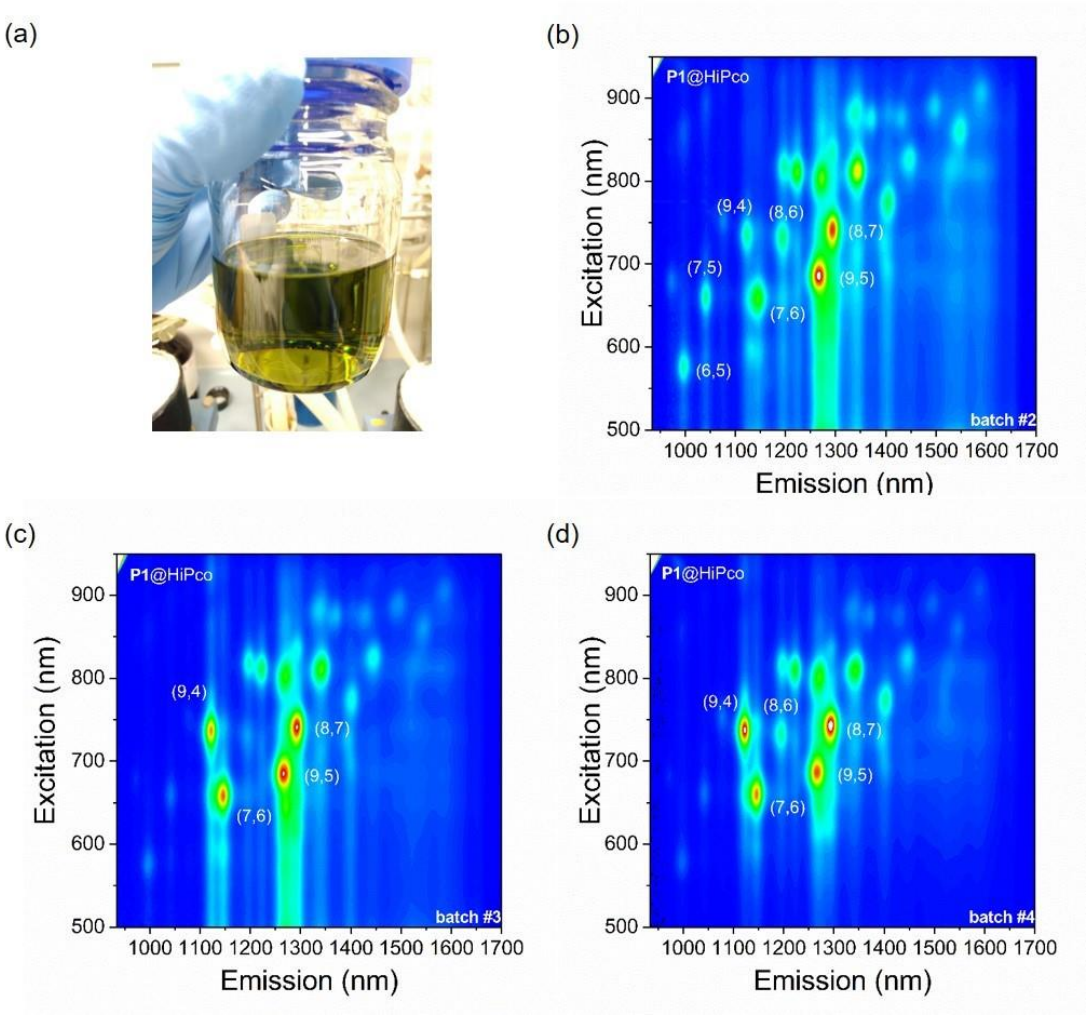

Figure 3.15. (a) Photograph of **P1** wrapped s-SWCNTs stored in a glass bottle, three weeks after sorting and purification process; (b) PLE map of sorted sample from batch #2; (c) PLE map of sorted sample from batch #3; (d) PLE map of sorted sample from batch #4. All samples were measured in toluene at 14 °C.

3.1.5 Characterization of triggered/released HiPco SWCNTs

The imine bonds in the polymer structure enable the easy and efficient removal of **P1** from the sorted and wrapped SWCNTs upon triggering under mild acidic condition. A general procedure for the removal of wrapped polymer is based on the addition of a small amount of trifluoroacetic acid (1% v/v of 90% TFA) and sonication for several minutes. Subsequent dilution with acetone leads to the precipitation of naked tubes, which can be washed on a PTFE membrane filter (0.20 μm) and dried in air/vacuum. The obtained naked SWCNTs can be re-dispersed in toluene to CNT aggregate for their further characterization.

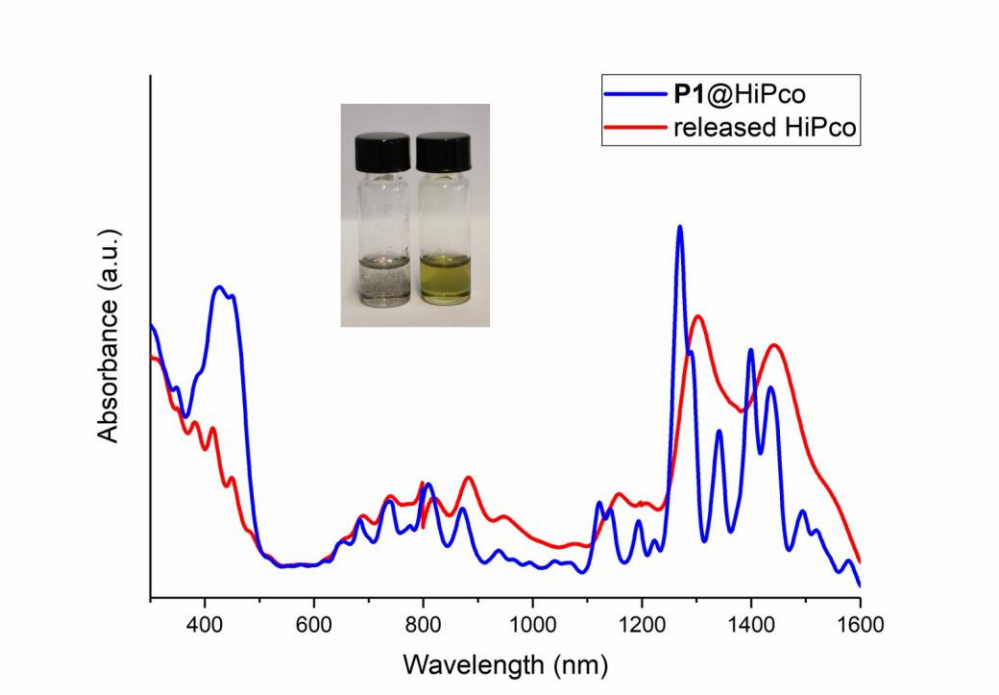

Figure 3.16. Absorption spectra of polymer **P1** sorted HiPco SWCNTs and the released nanotubes after triggering, washing, and re-dispersing in toluene. All samples were measured in toluene at room temperature. Photographs of wrapped (right) and released nanotubes (left) in toluene are also shown here.

As seen from the photograph in Figure 3.16, the polymer wrapped HiPco sample (right vial) has a yellowish-green color and is well dispersed. After the triggering, washing, and re-dispersing, the released nanotubes form aggregates and have a typical black color (left vial). Characterization of the released HiPco sample was carried out with absorption spectroscopy quickly after 10 minutes of sonication and the obtained spectrum is shown in Figure 3.16 together with the absorption spectrum of polymer wrapped sample as a reference. The absorption band of polymer

P1 at 366-500 nm is clearly missing in the released sample after triggering, showing only the S_{33} transition bands of the nanotubes. The characteristic S_{33} peaks of HiPco SWCNTs are at around 382, 416, and 450 nm. In the S_{11} and S_{22} region, the absorption peaks of naked tubes are quite broad and red-shifted due to the aggregation of the naked tubes during the measurement.

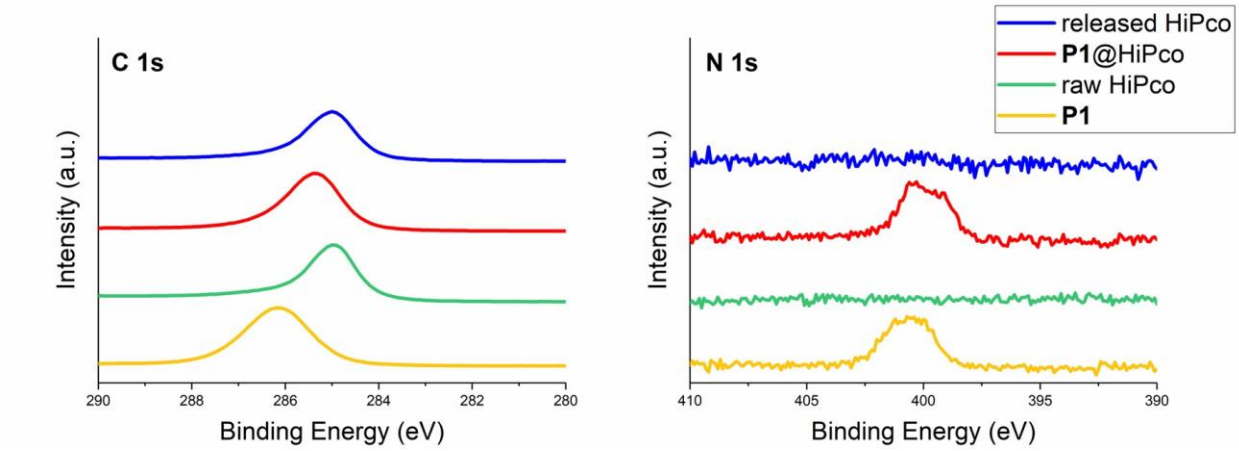

Figure 3.17. XPS C 1s (left) and N 1s (right) spectra of the released, wrapped, and raw HiPco SWCNTs as well of the neat polymer **P1**.

Nevertheless, the evaluation of the naked tubes by absorption spectroscopy is only qualitative. Owing to the nitrogen atoms in the polymer backbone of **P1**, the removal of the polymer from sorted SWCNTs after acid treatment can be therefore quantitatively inspected by performing X-ray photoelectron spectroscopy (XPS) measurements.

Figure 3.17 presents the XPS results for the released, wrapped, and raw HiPco SWCNTs as well the neat polymer **P1** for a comparison. In the N 1s spectrum of **P1** wrapped HiPco SWCNTs, the nitrogen peak has a small shift of 0.68 eV in comparison to the neat polymer, which indicates a weak interaction between the polymer chain and the nanotube sidewall. After polymer triggering, the N 1s peak totally disappeared in the released nanotube sample, hence proving the quantitative removal of the nitrogen-containing polymer **P1** from the sorted SWCNTs. In the C 1s spectra, the released and raw HiPco SWCNTs have almost the same peak position, indicating the existing of only graphitic sp^2-carbons in both samples. To note, the C 1s peak of the polymer@SWCNT complex is slightly shifted and is located between the peaks of the released SWCNTs and the neat polymer, which can be explained by the co-existence of graphitic sp^2-, aromatic sp^2-, and aliphatic sp^3-carbons in this sample.

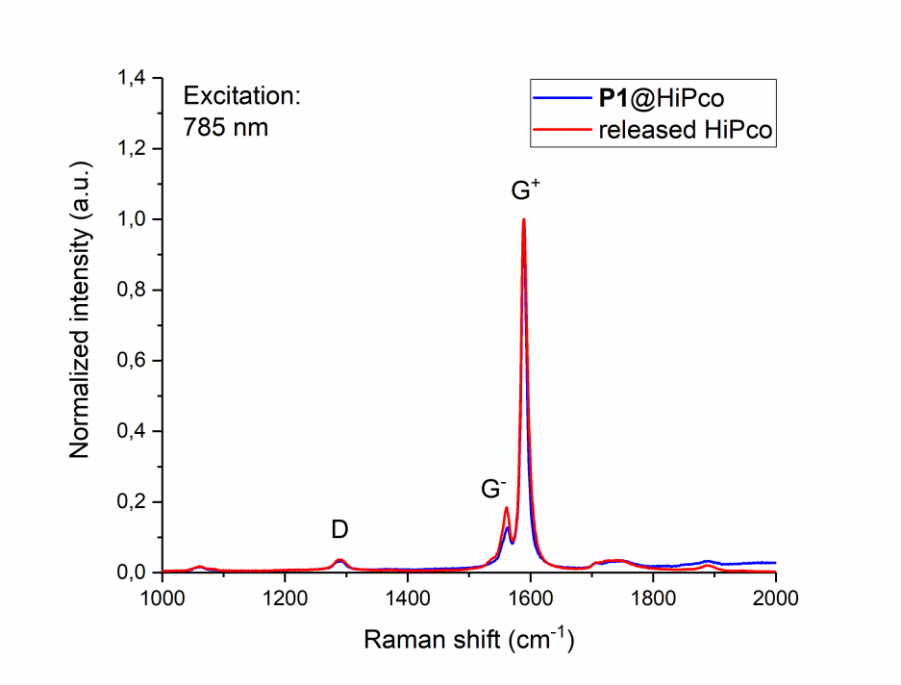

Figure 3.18. Raman spectra of **P1** sorted and released HiPco SWCNTs excited at 785 nm. Both spectra were normalized at 1590 cm^{-1}.

Raman spectrum shows no difference in G/D mode between wrapped and released nanotubes, proving that no structural defect was introduced to the nanotube sidewall by the treatment with TFA (Figure 3.18). PLE mapping was performed for the released sample, however no interpretable map was obtained due to the aggregation of the nanotubes. The released s-SWCNTs can be stored as a thin film (Figure 3.19) after the collection from the membrane filter, which can be used for re-dispersing with another polymer or other measurements.

Figure 3.19. Photograph of a thin film of released s-SWCNTs.

3.1.6 Characterization of rewrapped HiPco SWCNTs

Copolymer **P1** has the ability to sort and extract s-SWCNTs from raw HiPco tubes with a wide range of chiral angles and diameters, hence high yield in terms of nanotube species. After the removal of the polymer, the pre-sorted and naked semiconducting nanotubes can be further processed with various surfactants or dispersants for different purposes, such as chirality enrichment or handedness separation. For this purpose, the released nanotubes were again rewrapped with **P1** to show that the polymer triggering and processing is not affecting their ability to be again quantitatively rewrapped. Later on, the standard PFO polymer was used to selectively enrich nanotube species with $(n\text{-}m) \leq 2$ from the released sample. The process of rewrapping involves only the sonication and centrifugation. Detailed rewrapping procedure is described in the experimental part.

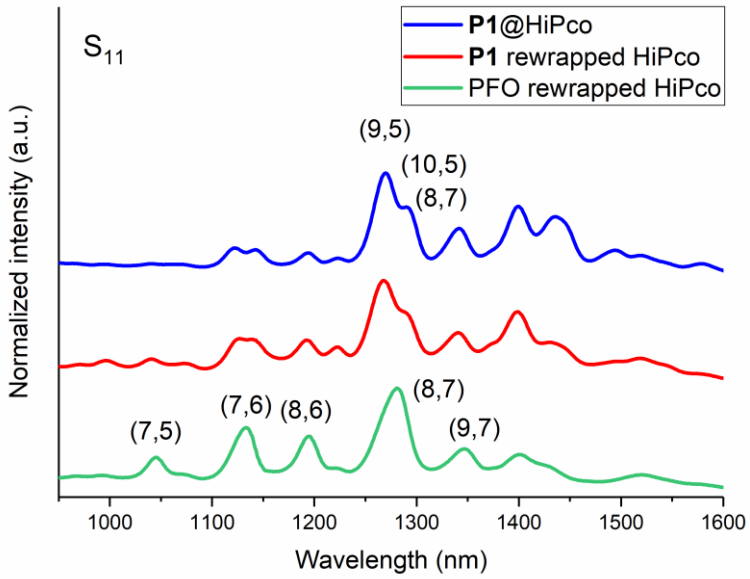

Figure 3.20. Absorption spectra (S_{11} transition region) of polymer **P1** freshly sorted HiPco SWCNTs, and polymer **P1** and PFO rewrapped released HiPco SWCNTs. All samples were measured in toluene at room temperature.

Both rewrapped samples were first characterized by absorption spectroscopy, as shown in Figure 3.20. For a better comparison of the dispersed nanotube species in both samples, only S_{11} transition region is presented here. As can be seen from the spectra, both polymers successfully re-disperse the released nanotubes which can be proved by the sharp and separated absorption

peaks as well the flat baseline. The polymer **P1** rewrapped sample has quite similar pattern in the S_{11} region as the freshly wrapped sample. (9,5), (10,5) and (8,7) SWCNTs are still the most favored nanotube species by **P1** and contribute to the main peak at 1268 nm. This result confirms that the released SWCNTs can be further functionalized by conjugated polymer and the process of "wrapping-release-rewrapping" is reproducible. As can be seen for the PFO rewrapped sample, the absorption spectrum looks cleaner which indicates a higher selectivity of PFO polymer towards the specific nanotube chirality than **P1** polymer, such as (7,6), (8,6), and (8,7) SWCNTs. PLE mapping of both samples were performed to identify all the nanotube species and the results are presented in Figure 3.21. Both samples show individual spots with high resolution, which indicates that the nanotubes are well dispersed in both samples with no aggregates or bundles. For the **P1** rewrapped sample, the assigned (n,m) chiralities are consistent with the freshly sorted **P1**@HiPco sample (Figure 3.15b, batch #2). Only the minor species such as (12,4), (11,6), (10,8) and (10,9) are missing in this map. For PFO rewrapped sample, all observed nanotubes are near-armchair, showing the expected selectivity of PFO towards nanotubes with (n-m) ≤ 2.[169,135] Hence, by rewrapping with PFO, the possibility of released and pre-sorted SWCNTs for further chirality enrichment has been proved.

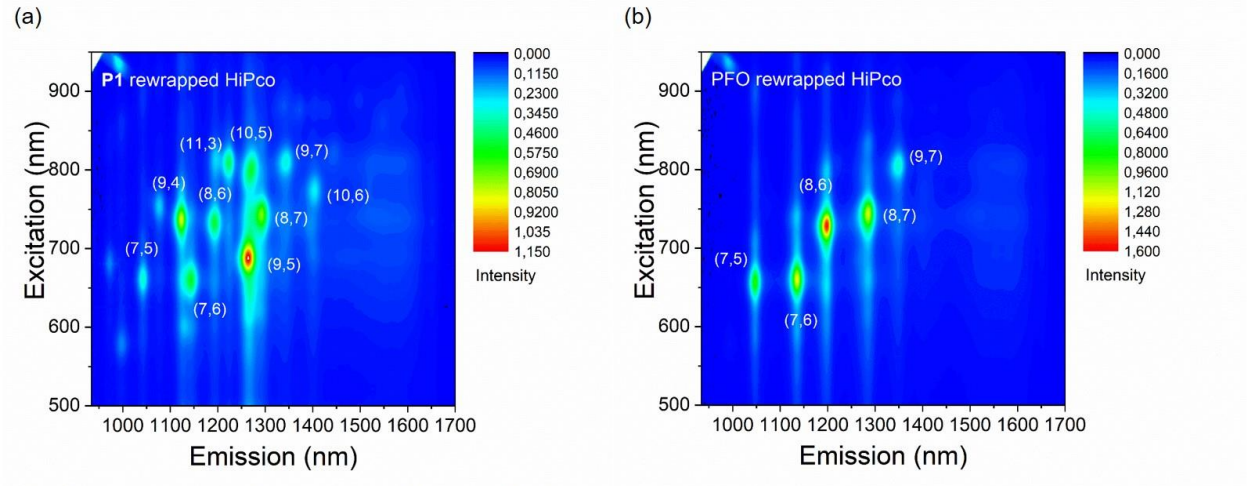

Figure 3.21. PLE maps of polymer **P1** (a) and PFO (b) rewrapped HiPco SWCNTs. The released nanotubes were taken from batch #2. All samples were measured in toluene at 14 °C.

3.1.7 Characterization of sorted PLV SWCNTs

Large-diameter SWCNTs are of great advantage for building electronic devices owing to their smaller Schottky barrier and higher current density.[71] To test the ability of polymer **P1** for sorting of SWCNTs with large diameters, commercially available PLV SWCNTs (*d*=1.2-1.5 nm) were used as a raw material and sorted according to the same procedure as previously for HiPco SWCNTs. The sorted PLV SWCNTs were first characterized by absorption spectroscopy and the obtained results are shown in Figure 3.22(a).

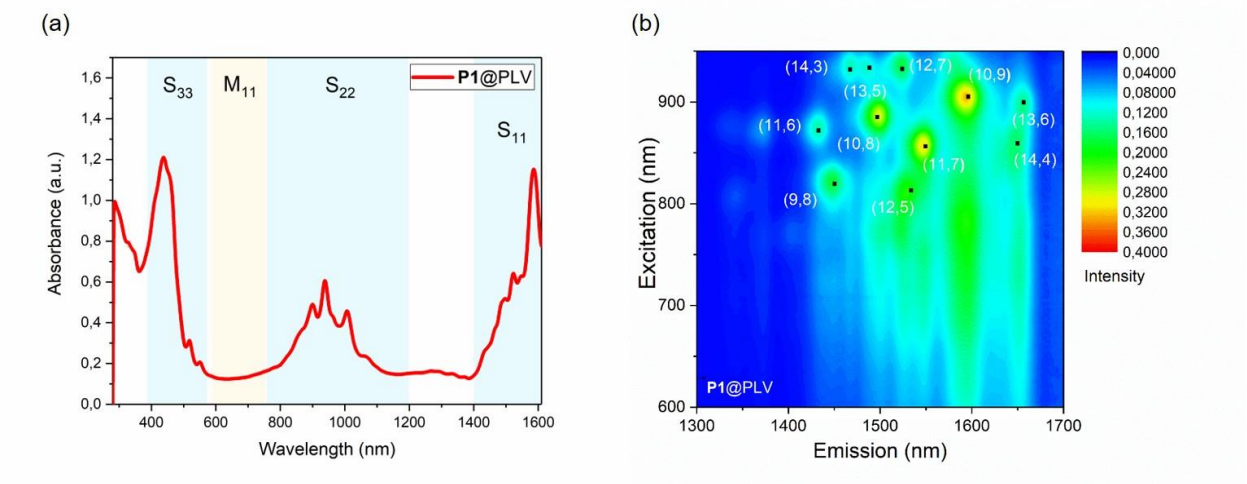

Figure 3.22. (a) Absorption spectra of polymer **P1** sorted PLV SWCNTs. The sample was measured in toluene at room temperature; (b) PLE map of polymer **P1** sorted PLV SWCNTs. The sample was measured in toluene at 14 °C.

The spectrum has a quite flat baseline and the feature fits with the reported absorption spectra of a large-diameter SWCNTs, such as plasma torch SWCNTs (0.9-1.5 nm)[71,170] and arc discharge SWCNTs (1.3-1.7 nm).[147] The absorption bands can be categorized into semiconducting S_{11} region (1400-1900 nm), S_{22} region (750-1200 nm), S_{33} region (400-580 nm), and metallic M_{11} (580-750 nm) region.[71,170] The S_{11} region is only partially shown here because of the strong interference with the first overtone region of C-H bond of toluene in near-IR region above 1650 nm. The sharp peak at 1586 nm can be assigned to the (10,9) SWCNT with a diameter of 1.3 nm. In the S_{22} region, three main peaks at 900 nm, 938 nm, and 1007 nm are contributed by multiple species with quite similar diameters. The absorption band of polymer **P1** covers the S_{33} region of PLV SWCNTs and the position of the peak is consistent with the neat **P1**. Almost no detectable peaks can be observed in the M_{11} region at 580-750 nm, indicating the absence of metallic species

in this sorted nanotube sample. The s-SWCNT purity of this sample can be estimated based on the absorption peak ratio ϕ in the E_{22} transition region between 1190-625 nm which is defined by Malenfant *et al.*,[166] where they claimed a s-SWCNT purity of 99% with a ϕ value of 0.406. In this work, the sorted PLV SWCNTs has a ϕ value of 0.467, indicating a s-SWCNT purity over 99%.

Further characterization of the sample was carried out by PLE spectroscopy and the spectrum is shown in Figure 3.22(b). In comparison with the sorted HiPco SWCNTs (Figure 3.11), the sorted PLV SWCNTs have generally lower PL intensities, which is caused not only by the difference in concentration but also by the fact that the PL quantum yield generally decreases with increasing SWCNT diameter.[171] Eleven nanotube species are identified from the map and are labelled with corresponding chiral indices.[172] Among these, near-armchair (10,9) SWCNT has the highest intensity with S_{11} at 1593 nm and S_{22} at 904 nm, which is consistent with the absorption spectrum. Other near-armchair nanotube species such as (9,8) and (10,8) are also observed with well resolved spots. (14,3), (13,5), and (12,7) SWCNTs have almost the same excitation wavelength at 933 nm and contribute to the highest absorption peak at 938 nm in Figure 3.22(a). The existence of nanotubes with both $(n-m) \leq 2$ and $(n-m) \geq 2$ indicates that the selectivity of **P1** towards semiconducting species in PLV sample is also chiral angle independent, same as for the HiPco samples.

The sorted and raw PLV SWCNTs were characterized by Raman spectroscopy with excitation wavelength of 785 nm. The spectra are shown in Figure 3.23 with G/D mode as well RBM region. The sorted PLV SWCNTs has a high G/D ratio, showing the good quality of the tubes. The G^- peak of raw PLV tubes shows a slightly broader shoulder at 1545 nm, which fits the feature of BWF line shape of metallic tubes. However, it is not observed in the sorted sample. RBM region confirms the complete absence of metallic tubes, showing no detectable signals at 135-190 cm^{-1} as highlighted in the spectra. This result is consistent with the absorption spectrum (Figure 3.22a).

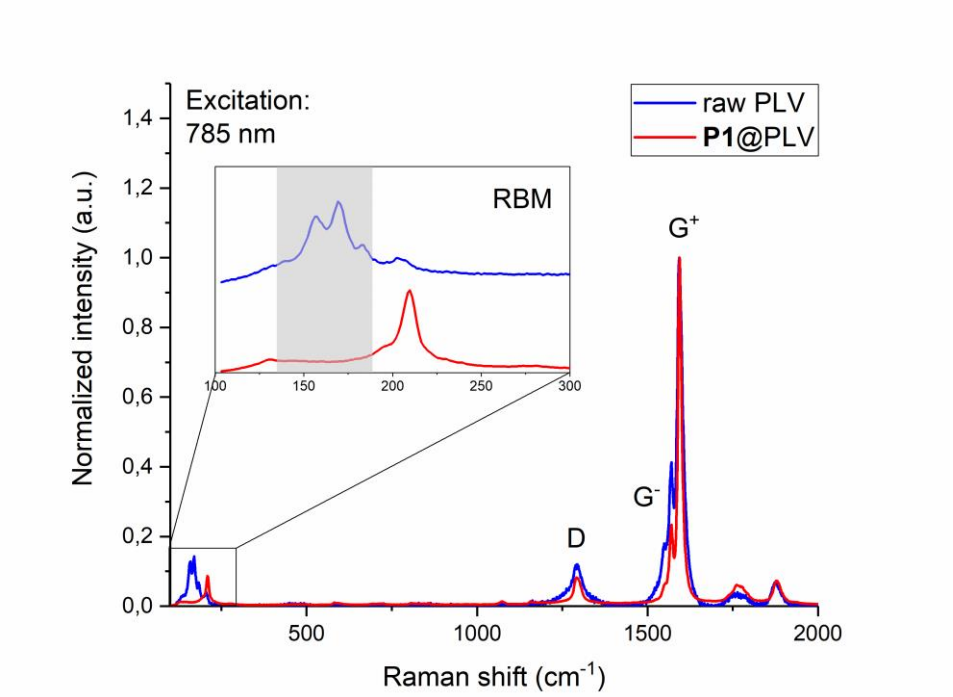

Figure 3.23. Raman spectra and RBM regions of raw and **P1** sorted PLV SWCNTs excited at 785 nm. The metallic region is highlighted in grey. Both full spectra were normalized at 1595 cm^{-1}.

The sorted PLV SWCNTs are stable in toluene under ambient conditions and can be used directly as nanotubes ink for the deposition on surfaces or for device printing, such as thin-film transistors.[71,166]

3.1.8 Characterization of released and rewrapped PLV SWCNTs

The sorted and wrapped PLV SWCNTs has a yellowish brown color and can be readily triggered by the addition of a catalytic amount of acid (1% v/v of 90% TFA). The released nanotubes were re-dispersed in toluene and characterized as aggregates.

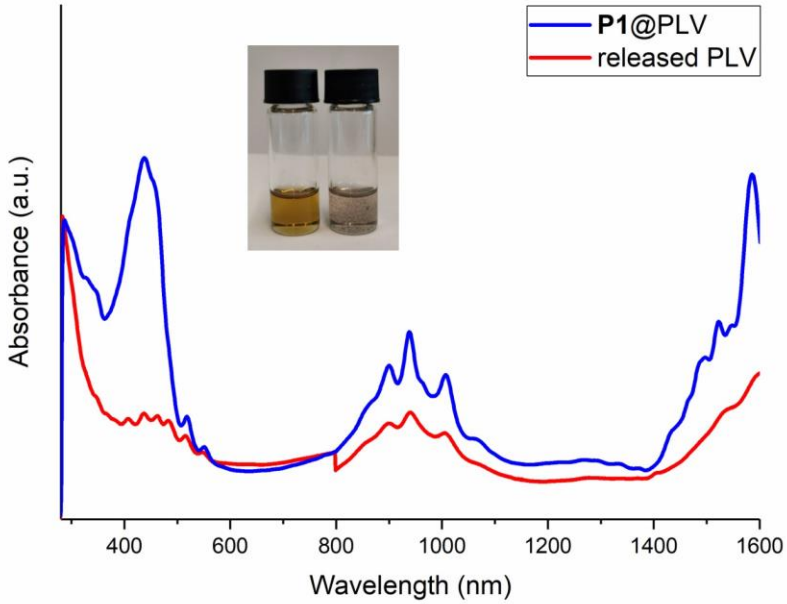

Figure 3.24. Absorption spectra of polymer **P1** sorted PLV SWCNTs and the released nanotubes after triggering, washing, and re-dispersing in toluene. The spectra were normalized and shifted horizontally for a better comparison. All samples were measured in toluene at room temperature. Photographs of wrapped (left) and released nanotubes (right) in toluene are also shown.

Figure 3.24 shows the absorption spectra of polymer **P1** sorted and released PLV SWCNTs in toluene. The absorption peaks from the released sample are much broader in S_{11} and S_{22} regions due to the aggregation of the nanotubes during the measurement. After the cleavage and removal of the polymer, the S_{33} region is not overlapped with the polymer absorption and a few absorption peaks are observed with a good resolution. The released PLV SWCNTs were rewrapped with the polymer **P1** and the commercially available PFO following the same procedure as for rewrapping of HiPco SWCNTs. Absorption spectra of both samples were similar in the S_{22} region and no obvious absence of specific nanotube species was observed, as shown in Figure 3.25.

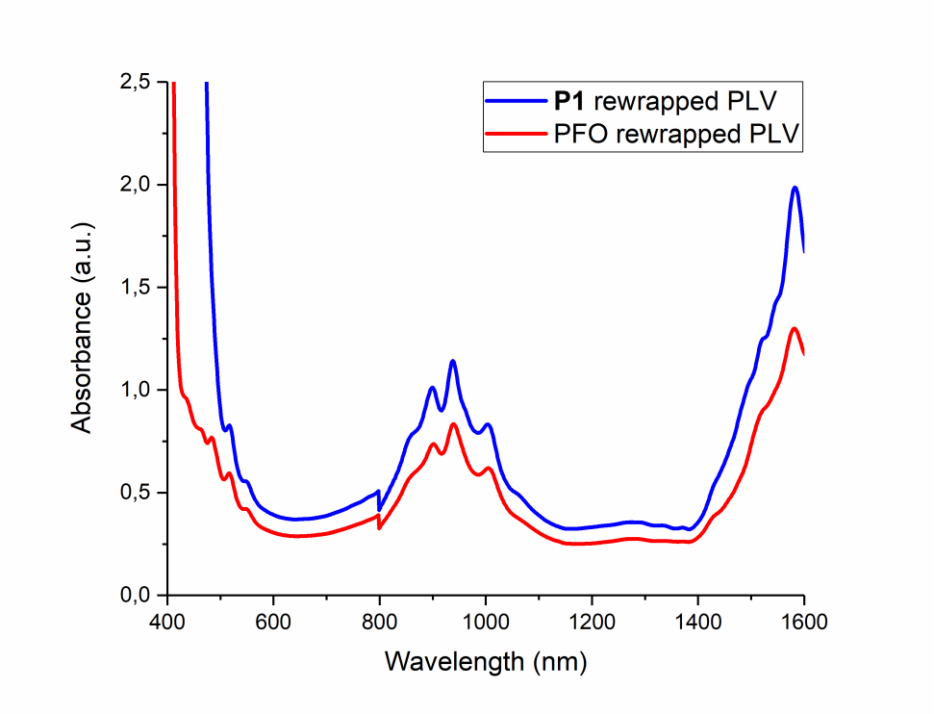

Figure 3.25. Absorption spectra of polymer **P1** and PFO rewrapped PLV SWCNTs. All samples were measured in toluene at room temperature.

Both samples were further characterized by PLE spectroscopy and the spectra are shown in Figure 3.26. In the **P1** rewrapped sample, (11,7), (10,9), (9,8), (10,8), and (12,7) SWCNTs are found as main species, which is consistent with the freshly sorted sample (Figure 3.22). In the PFO rewrapped sample, near-armchair nanotube species (8,6), (8,7), (9,7), (9,8), (10,8) and (10,9) SWCNTs are observed owing to the selectivity of PFO for nanotubes with (n-m) $\leq$ 2, which is in agreement with the published results.[36] However, only (10,9) SWCNT appears as most abundant nanotube species, while the other near-armchair species are with a very low intensity.

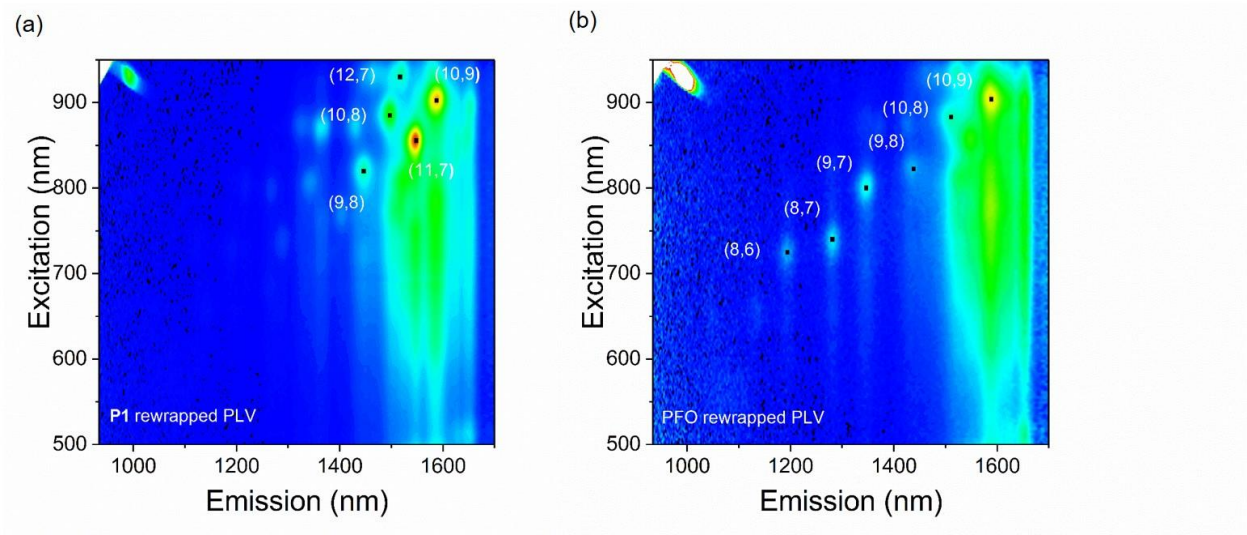

Figure 3.26. PLE maps of polymer **P1** (a) and PFO (b) rewrapped PLV SWCNTs. All samples were measured in toluene at 14 °C.

3.1.9 Conclusions of electronic type sorting

In conclusion, a novel imine-based degradable fluorene-carbazole copolymer **P1** was designed and synthesized for the sorting and selective dispersion of s-SWCNTs from as-produced raw materials. The combination of carbazole and fluorene for the construction of desired copolymer was chosen based on our preliminary work and results. The introduction of imine bonds as monomer interlink in the polymer backbone ensures the readily cleavage of the polymer upon acid treatment. Copolymer **P1** was synthesized by polycondensation and the procedure is highly reproducible and scalable up to 2 g. Characterization of **P1** was performed by NMR, Raman spectroscopies, TGA, and GPC, confirming the alternating backbone structure and the high molecular weight of obtained polymer. Degradation of **P1** upon triggering with TFA was studied by absorption spectroscopy, showing the cleavable feature of imine-based polymer. The sorting of s-SWCNTs from a raw HiPco and PLV materials with an acid cleavable copolymer **P1** and the subsequent purification process provided nicely dispersed nanotube samples. Characterization of sorted tubes was performed by various techniques, such as absorption, PLE, and Raman spectroscopy. The results showed that copolymer **P1** can selectively disperse s-SWCNTs from both HiPco and PLV raw materials with a high purity and high yield in terms of nanotube species. In the sorted samples, the original diversity of semiconducting species is preserved. In both cases,

the wrapping polymer can be easily removed from the nanotube sidewall by the addition of a catalytic amount of acid (1% v/v of 90% TFA). Moreover, the released nanotubes can be quantitatively rewrapped with both the **P1** polymer and the standard PFO polymer, exhibiting the further chirality sorting which is fully depend on the polymer used for such rewrapping process. This result shows the potential application of polymer **P1** pre-sorted and released s-SWCNTs for the further functionalization or chirality enrichment with various molecules.

3.2 Acid cleavable chiral polyfluorenes for enantiomeric separation of s-SWCNTs

This chapter is focused on the synthesis and performance of cleavable chiral homo-polyfluorenes for enantiomeric separation of s-SWCNTs. The racemic monomer was synthesized in five steps and the two enantiomers of the monomer were separated by chiral flash chromatography. Determination of the absolute configuration of the enantiomeric monomers was realized by the Mosher's derivatization method with the help of NOESY 2D NMR analysis. Both optically pure monomers were then polymerized to the corresponding chiral polymers and characterized by various spectroscopic methods. The performance of the chiral polymers was first tested with pre-sorted and chirality enriched SWCNT samples, and the general procedure for handedness sorting of SWCNTs was established. Further progress was achieved for the one-pot enantiomeric separation of s-SWCNTs from as-produced CoMoCAT SWCNTs. The obtained enantiomerically separated SWCNTs were characterized by CD spectroscopy and their enantiomeric excess was calculated. Triggering of the chiral polymer was achieved by acid treatment and the rewrapping of the released enantiomerically pure nanotubes was performed with an achiral polymer to confirm the origin of the CD signal from the CNT enantiomers. Molecular mechanics simulations were performed to understand the origin of the enantioselectivity of the chiral polymers towards SWCNT enantiomers.

3.2.1 Design of the chiral polymers

Conjugated chiral copolymers have been synthesized and used for handedness recognition of s-SWCNTs by Nakashima et al.[161] In their copolymers, as described in the Introduction (Figure 1.49), fluorene units extract s-SWCNT while chiral binaphthol units discriminate the handedness of the extracted tubes. However, due to the random composition ratio of both building units in the polymeric structure, the obtained copolymers show different handedness recognition ability. To solve this random selectivity, one might consider to synthesize the alternating copolymer which has 1:1 composition ratio of the fluorene unit and chiral binaphthol unit. However, the maximum ratio of the chiral unit will be limited to 50 mol% in the copolymer structure. Taking all those into consideration, we aim to introduce chiral center to each fluorene-

based monomer instead of adding extra chiral comonomer such as chiral binaphthol derivative, thus maximizing the ratio of chiral unit and simultaneously utilizing the ability of polyfluorene for extracting s-SWCNTs. Moreover, same as for the copolymer **P1**, the desired chiral polyfluorenes should be interlinked by imine bond, hence acid cleavable. To achieve those requirements, homo-polyfluorenes with repeating unit bearing two different substituents at C-9 position and two different functional groups on the aromatic ring for the formation of imine bonds during the polycondensation are desired, as shown in Figure 3.27(a).

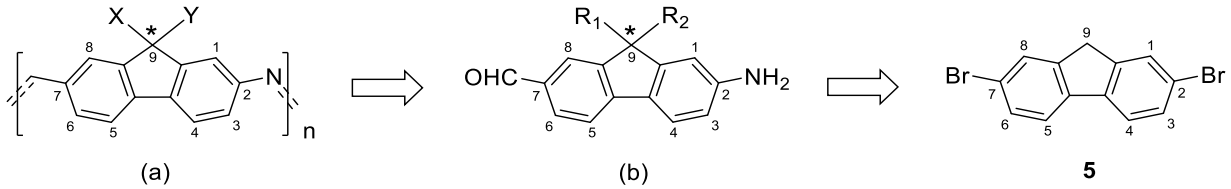

Figure 3.27. Retrosynthetic strategy of designed chiral polyfluorenes.

As substituents at C-9 position, alkyl chains with different length can be introduced for increasing the solubility of the polymer in organic solvents and form the stereocenter in the position 9. The amino group and aldehyde group for imine bond formation are designed to be at C-2 and C-7 position to ensure the favorable conformation of the polymer chain for the efficient wrapping process, as explained for the copolymer **P1**. Hence, as shown in Figure 3.27(b), the ideal racemic monomer has a chiral center at C-9 position, which can be separated into (*R*) and (*S*) enantiomeric monomer. By strict head-to-tail polycondensation feature, the absolute configuration of the monomer can be preserved and the obtained chiral homopolymers can have all-(*R*) or all-(*S*) configuration on the polymer chains. For the synthesis, commercially available 2,7-dibromofluorene **5** was used as starting compound.

3.2.2 Synthesis and characterization of the racemic monomer

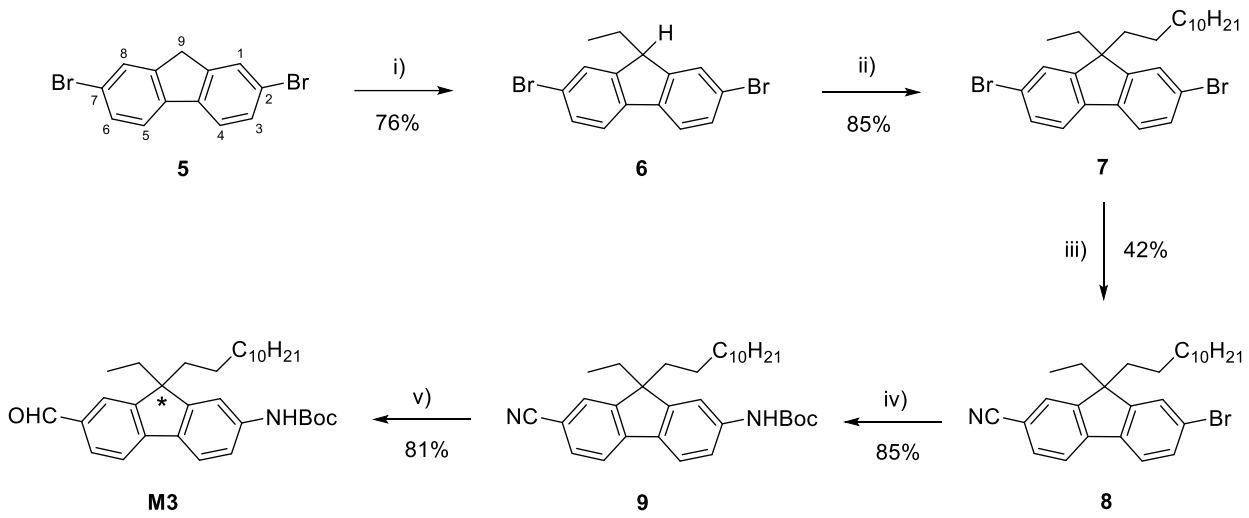

Scheme 3.3. Synthetic strategy towards the racemic monomer **M3**. Reagents and conditions: i) *n*-BuLi, iodoethane, THF, -78 °C; ii) KO^{t}Bu, 1-iodododecane, THF, 0 °C; iii) CuCN, NMP, 210 °C; iv) Boc-NH_2, $Pd_2dba_3 \cdot CHCl_3$, ^{t}BuXPhos, NaO^{t}Bu, toluene, RT; v) DIBAL, toluene, -5 °C.

The synthetic strategy used for the preparation of monomer **M3** is outlined in Scheme 3.3. The required monomer **M3** as a racemic mixture was prepared in five reaction steps starting from the commercially available 2,7-dibromofluorene **5**. Deprotonation of **5** with 1.05 eq. of *n*-BuLi and subsequent alkylation with iodoethane allowed the introduction of one ethyl group to the position 9 of fluorene unit and thus provided 2,7-dibromo-9-ethyl-9*H*-fluorene **6** with a yield of 76%.[173] Diethyl derivative of **6** was found as a side product and brought difficulty to the purification because of the similar polarity as **6**. Alternative approach was tried with LDA as a base, however with much lower isolated yield of **6**. Further deprotonation of **6** was performed with a weaker base potassium *tert*-butoxide owing to the increased acidity of the proton in the position 9, which provided 2,7-dibromo-9-dodecyl-9-ethyl-9*H*-fluorene **7** with a yield of 85% after the alkylation with 1-iodododecane. The progress of alkylation was observed with TLC and the crude product was purified by column chromatography in hexane. The subsequent mono cyanation of aryl halide **7** via the Rosenmund-von Braun protocol using copper(I) cyanide in NMP at high temperature afforded the desired 2-bromo-9-dodecyl-9-ethyl-9*H*-fluorene-2-carbonitril **8** in 42% yield.[174] After completion of the reaction, the solvent NMP was hydrolyzed by the addition of NaOH solution and the remaining copper salts were coordinated by $EDTA^-Na^+$ solution (10%). Alternatively the cyanation reaction was also tried with zinc(II) cyanide in DMF at 145 °C with

$Pd(PPh_3)_4$ as catalyst. Despite the addition of only 0.5 eq. of zinc(II) cyanide, double cyanation was favored under these conditions. Therefore Rosenmund-von Braun protocol was used for the preparation of **8**. The subsequent palladium-catalyzed Buchwald-Hartwig amination of **8** with *tert*-butyl carbamate provided *tert*-butyl *N*-(7-cyano-9-dodecyl-9-ethyl-9*H*-fluoren-2-yl)carbamate **9** in 85% yield, where the terminal amine is protected with the Boc group (*tert*-butyloxycarbonyl). Further reduction of nitrile **9** with a mild reducing agent DIBAL gave the target compound *tert*-butyl *N*-(9-dodecyl-9-ethyl-7-formyl-9*H*-fluoren-2-yl)carbamate **M3** with a yield of 81%.[174] The obtained racemic monomer **M3** was characterized by ^{1}H NMR spectroscopy in $CDCl_3$ at room temperature and the spectrum is shown in Figure 3.28. The characteristic protons from the aldehyde group and the secondary amine are found at 10.03 ppm and 6.68 ppm, respectively. All six protons on the aromatic ring of **M3** are located at 7.85-7.30 ppm and are assigned to the corresponding peaks in the spectrum.

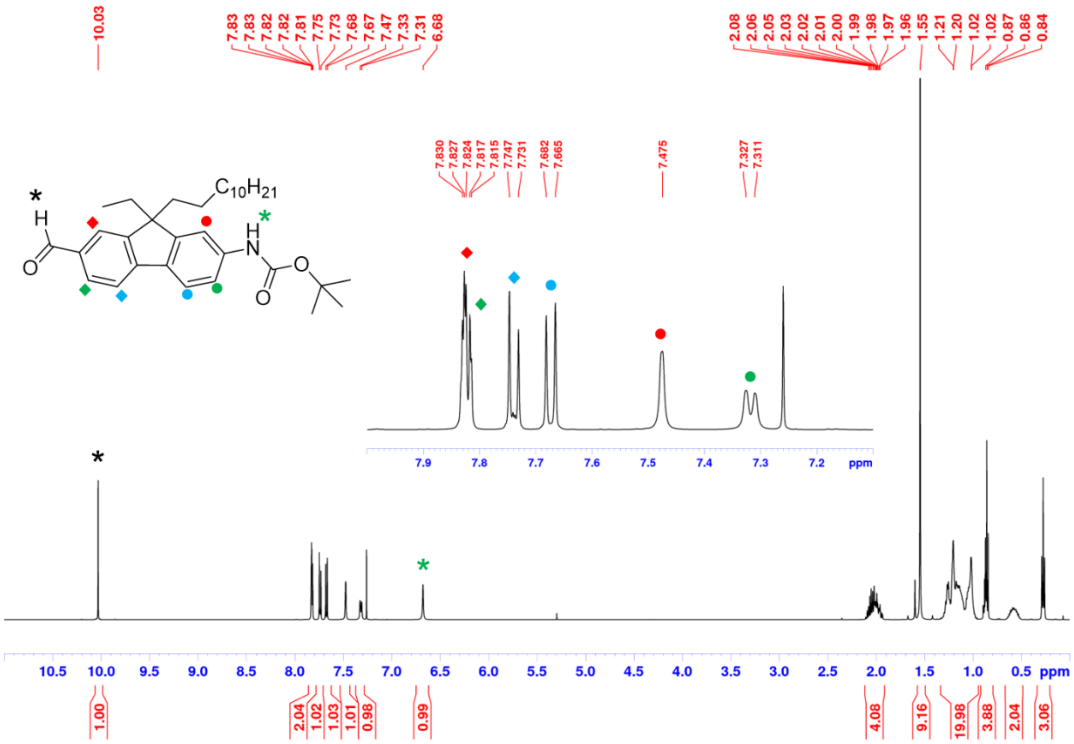

Figure 3.28. ^{1}H NMR spectrum (500 MHz) of the racemic monomer **M3**. The peaks in the aromatic region are assigned to the corresponding protons on the monomer. The sample was measured in $CDCl_3$ at room temperature.

3.2.3 Enantiomeric separation and characterization of monomers

The two enantiomers of **M3** were separated by chiral flash chromatography from SHIMADZU LC-20AT HPLC, which was equipped with CHIRALPAK® IB N-5 HPLC column (250×30 mm, *n*-heptane:isopropanol = 96:4), with a flowrate of 45 mL/min and UV detection at 254 nm. For each run, 100 mg of the racemic mixture was loaded. The enantiomers were labelled as **M3-1** and **M3-2** with the retention time of 9.66 min and 13.95 min respectively, as shown in Figure 3.29(a).

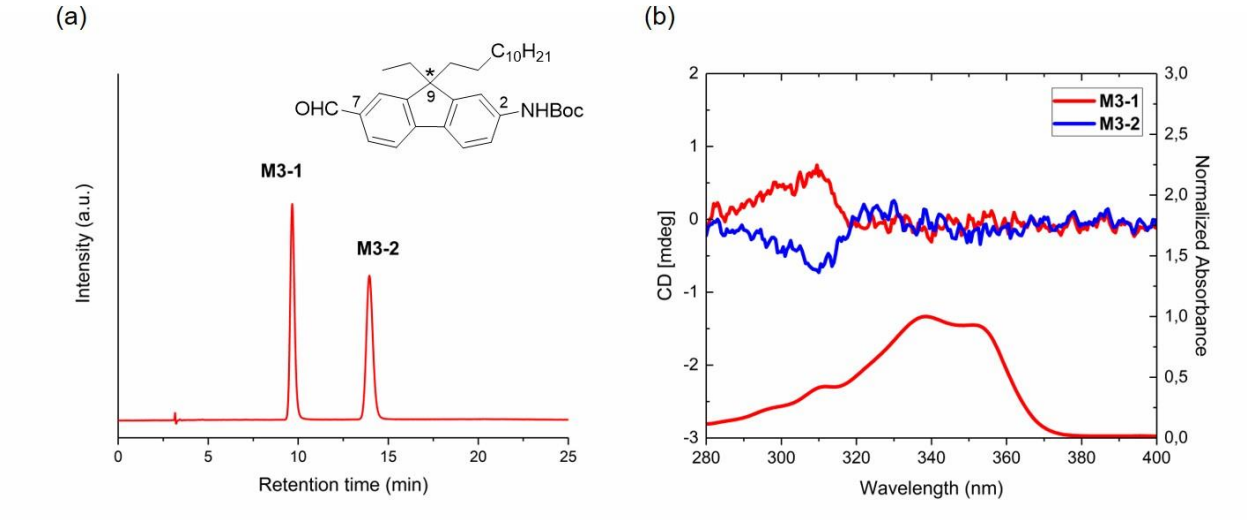

Figure 3.29. a) Chiral HPLC chromatogram of racemic monomer **M3** (*n*-heptane:IPA = 96:4); b) CD (top) and absorption (bottom) spectra of separated enantiomeric monomers **M3-1** and **M3-2**. The samples were measured with a concentration of ~ 4×10^{-4} M in toluene at room temperature.

In order to prove that both separated compounds are chiral, **M3-1** and **M3-2** were characterized with CD spectroscopy. In Figure 3.29(b), both monomers show identical absorption spectrum due to the randomly polarized light in absorption spectroscopy. In the CD spectra, both **M3-1** and **M3-2** exhibit quite weak and noisy signals. However, symmetric peaks with opposite signs are observed at around 310 nm. This mirror image in the CD spectra confirms that both compounds are chiral enantiomers of racemic monomer **M3**. Interestingly, the symmetric peaks in the CD spectra only correspond to a minor peak in the absorption spectra while the main absorption peak at around 340 nm shows no obvious CD signal even with a high concentration up to 10^{-4} M. This phenomenon can be explained by the unique molecular structure of the enantiomeric monomers. Chirality of the monomers originates from the presence of asymmetric sp^3 carbon at the 9 position of fluorene chromophore bearing two non-polar alkyl chains which differs only in the chain length

(ethyl *vs* dodecyl). As well, the other two substituents which are in positions 2 and 7 of the fluorene ring are far away from the chiral sp^3 carbon in the position 9 and thus contribute very little to the overall chirality of such enantiomeric monomer **M3**. Therefore, this minor substitution effect together with the rigidity of the fluorene structure and the steric hindrance of the chiral C9 center, lead to the low response of the chiral monomers to circularly polarized light. Further characterization of the enantiomers **M3-1** and **M3-2** was performed with NMR spectroscopy, which obviously gives identical shifts in both ^{1}H and ^{13}C NMR spectra of the both enantiomers.

3.2.4 Determination of the absolute configuration of the enantiomeric monomers

To determine the absolute configurations (AC) of the optically active **M3-1** and **M3-2**, X-ray diffractometric analysis can be employed. However, this approach requires single-crystals which is not feasible for such oily compounds with long alkyl chains. Alternatively, chiral derivatizing agents are commonly used to determine the AC of chiral compounds by NMR spectroscopy.[175,176] Among the agents and techniques used, Mosher's ester method is one of the most reliable methods for the AC assignment of optically active amines and alcohols.[177–179] Hence in this work, Mosher's method was employed for the AC assignment of both enantiomers **M3-1** and **M3-2**. It starts with the derivatization of both enantiomers with chiral auxiliary (*S*)-(+)-α-methoxy-α-(trifluoromethyl)phenylacetyl chloride ((*S*)-(+)-MTPA-Cl) to the corresponding diastereomeric amides, which can be distinguished by ^{1}H, ^{19}F, and 2D NMR spectroscopy.[180]

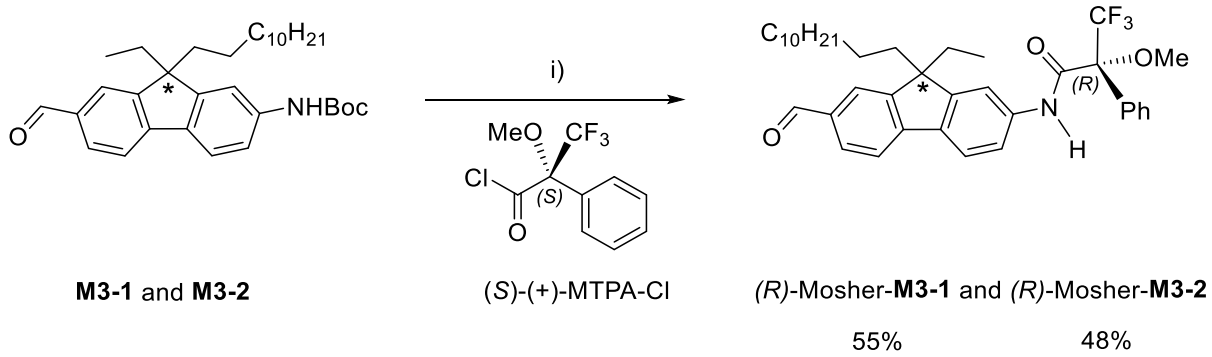

Scheme 3.4. Synthetic strategy towards the (*R*)-Mosher-amide diastereomers. Reagents and conditions: i) (a) TFA, thioanisole, DCM, RT; (b) NEt_3, (*S*)-(+)-MTPA-Cl, DCM, RT.

The synthetic strategy used for the preparation of corresponding Mosher-amides is outlined in Scheme 3.4. The cleavage of the Boc protecting group from the monomers was carried out by the treatment with an excess amount of TFA and 1.0 eq. of thioanisole in anhydrous DCM.[174] The deprotonation progress was monitored by TLC. After the reaction completion, the excess of TFA was purged out from the resulting red-orange solution with argon, and the obtained solution was neutralized with NaOH solution (10% aq.), extracted with DCM, and dried over $MgSO_4$. Several attempts have been made to isolate the unprotected monomers from the crude product, however without success. The free amino and aldehyde groups form immediately imine bonds and lead to the polymerization of the monomers right after the removal of the solvent. Due to this feature, the organic phase was only concentrated after the work up and directly transferred to the reaction vial under argon atmosphere. After purging with argon, an excess amount of NEt_3 was added to the solution to release the free amine from the TFA salt obtained after Boc deprotection. Subsequent acetylation of the free amine with (*S*)-(+)-MTPA-Cl enantiomer provided the desired Mosher-amides (*R*)-Mosher-**M3-1** and (*R*)-Mosher-**M3-2** with a yield of 55% and 48%, respectively. After the formation of amides, the configuration of the chiral Mosher auxiliary was converted from (*S*) to (*R*) and the resulting diastereomeric adducts have differences in the resonances and chemical shifts.

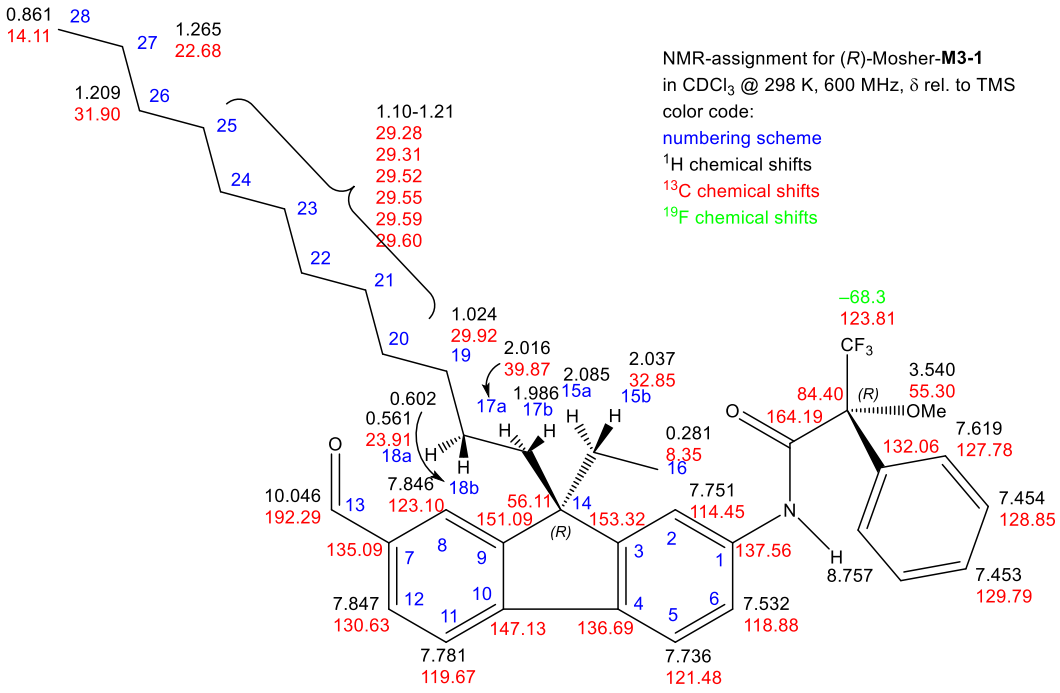

Figure 3.30. NMR assignment (600 MHz, $CDCl_3$) of (*R*)-Mosher-**M3-1**.

For the Mosher analysis the resonances of the (*R*)-Mosher amides of **M3-1** and **M3-2** were determined using routine 2D-NMR spectra, including COSY, NOESY, HSQC, and HMBC (see Figure 8.1-Figure 8.6 in Appendix). The assignment was according to the atom numbering as shown in Figure 3.30. In a second step the ^{1}H chemical shifts of both amides were compared and $\Delta\delta^{S-R}$ (defined as: $\Delta\delta^{S-R}$ = (δ ((*S*)-Mosher-**M3-2** amide) – δ ((*R*)-Mosher-**M3-1** amide)) were determined, which are shown in Table 3.2 by graphically determining pairwise the offset between the individual peaks which is more precise than simply subtracting the chemical shift values. The analysis of these shifts reveals, that the aliphatic protons 15a, 15b and 16 show all negative $\Delta\delta^{S-R}$, whereas the protons 17a, 17b and 18b display positive $\Delta\delta^{S-R}$, while proton 18a that shows a weak negative shift, points towards the ethyl group (see Figure 8.7 in Appendix). It is important to note that the orientation of the amide group relative to the aromatic protons 2 and 6 has unambiguously been determined by NOE in both compounds (Figure 3.31).

Table 3.2. ^{1}H chemical shifts of (*R*)-Mosher-**M3-1** and (*R*)-Mosher-**M3-2**. $\Delta\delta^{S-R}$ is defined as the result of δ (**M3-2** amide) – δ (**M3-1** amide). The measurements were performed in $CDCl_3$ at 298 K (600 MHz).

Atom number	δ[(*R*)-Mosher-**M3-1**] in ppm	δ[(*R*)-Mosher-**M3-2**] in ppm	$\Delta\delta^{S-R}$ in ppb
NH	8.750	8.757	-6.5
2	7.760	7.751	+8.4
5	7.735	7.736	-1.1
6	7.519	7.532	-13.3
8	7.846	7.846	–0.6
11	7.780	7.781	–0.4
12	7.847	7.847	0.0
13	10.046	10.046	0.0
15a	2.081	2.085	–4.6
15b	2.030	2.037	–6.6
16	0.276	0.281	–5.6
17a	2.019	2.016	+3.0
17b	1.993	1.986	+6.8
18a	0.560	0.561	–1.0

18b	0.611	0.602	+8.1
28	0.860	0.861	–0.7

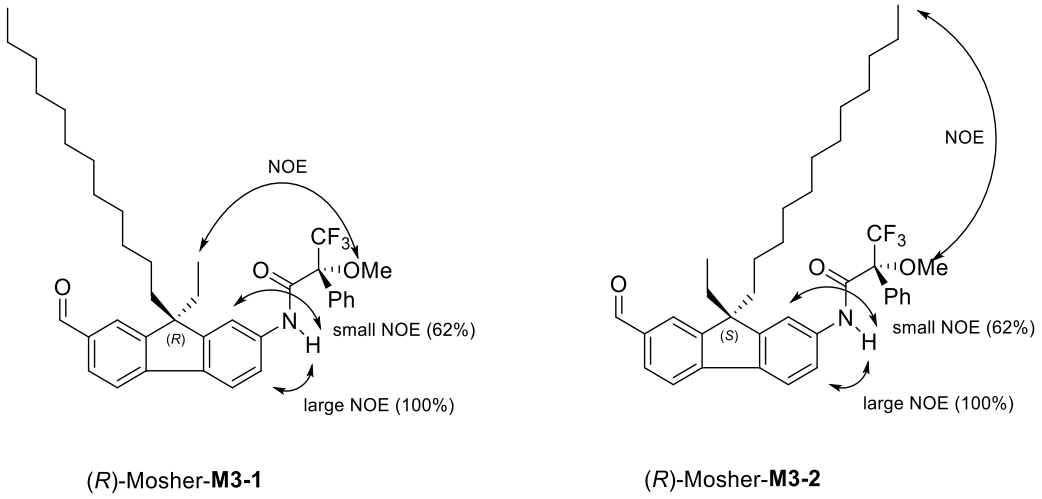

Figure 3.31. Key NOE correlations for (*R*)-Mosher-**M3-1** and (*R*)-Mosher-**M3-2** amides.

Therefore, all necessary conditions for the assignment of the absolute configuration by the Mosher technique are fulfilled and **M3-1** can be assigned the (*R*)-configuration at the stereogenic sp^3 carbon while **M3-2** can be assigned the (*S*)-configuration, as shown in Figure 3.32. This finding is corroborated by the observation of NOEs between the protons of the OMe-group and methyl group 16 in **M3-1**, whereas in **M3-2** the OMe-group displays an NOE to methyl protons 28 (see Figure 8.8 and Figure 8.9 in Appendix).

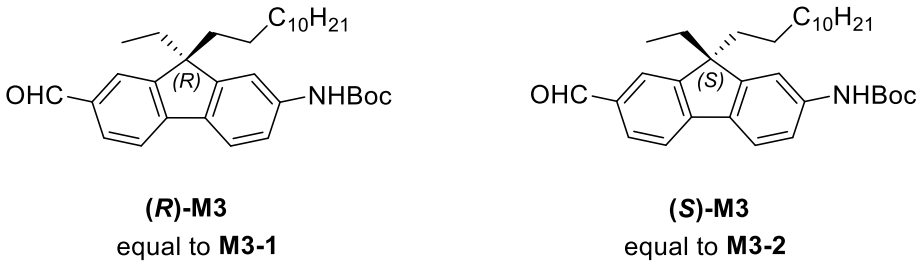

Figure 3.32. AC assignment of enantiomeric monomer **M3-1** and **M3-2** to (*R*) and (*S*) configuration at the stereogenic center.

3.2.5 Theoretical calculation of CD spectra of (*R*)-M3 and (*S*)-M3

To better interpret the observed CD spectra of the monomers, TD-DFT calculations were used to simulate the UV and CD spectra and to determine the electronic transitions. These calculations were performed in toluene with PCM solvation model.[181] The geometry optimization of **(*R*)-M3** and **(*S*)-M3** have been performed using B3LYP functional and TZVP basis set. For each optimized structure, a frequency analysis at the same level of theory was used to verify that it corresponds to a minimum in the potential energy surface. For all the minima, the number of imaginary frequencies was zero. Excited states were computed using TD-DFT/B3LYP/TVZP.[182] The applied functions have been previously shown to produce reasonable results in calculation of the electronic CD spectra of different molecules while it has been shown that the choice of basis set does not have a pronounced effect on the calculated CD spectra.[183–185] All calculations were performed with Gaussian09[186] and analysis of excited states was carried out with GaussSum.[187]

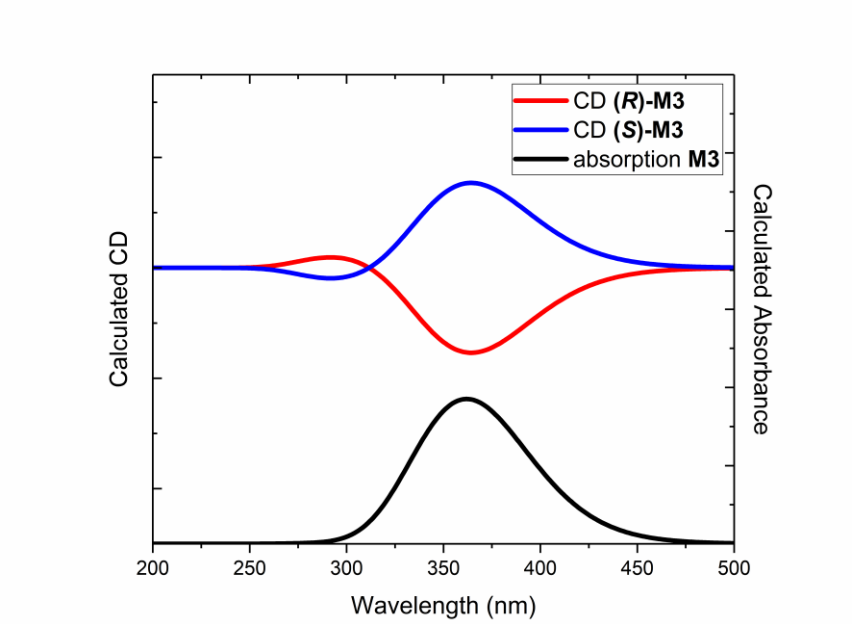

Figure 3.33. Theoretically calculated CD and absorption spectra of **(*R*)-M3** and **(*S*)-M3**.

The calculated absorption spectrum of monomer **M3** has a strong peak at 362 nm with the excitation energy of 3.42 eV (Figure 3.33). This corresponds to the HOMO-->LUMO transition with the oscillator strength of 0.91. Furthermore, two excited states with small oscillator strengths (0.0001 and 0.0049) were calculated at 336 and 293 nm with excitation energies of 3.68 eV and 4.22 eV which correspond to HOMO-2-->LUMO and HOMO-->LUMO+1 transition, respectively.

In the calculated CD spectra of **(*R*)-M3** and **(*S*)-M3** as shown in Figure 3.33, the main peak at 365 nm corresponds to the HOMO-->LUMO transition which is missing in the experimental CD spectra (Figure 3.29b). However, the minor peak in the calculated CD spectra at 292 nm correlates with the CD peak observed in the experimental spectra at 310 nm, and can be attributed to the HOMO-->LUMO+1 transition.

3.2.6 Synthesis and characterization of the chiral polymers

As aforementioned, the unprotected monomers easily polymerized to the corresponding polyimines even during the work up while removing volatiles. Hence in this work, homopolymerization of **(*R*)-M3**, **(*S*)-M3** enantiomers, and racemic **M3** monomers was proceeded directly after the Boc group deprotection and work up without any solvent or catalysts. The synthetic strategy used for the preparation of corresponding chiral polymers (CP) is outline in Scheme 3.5.

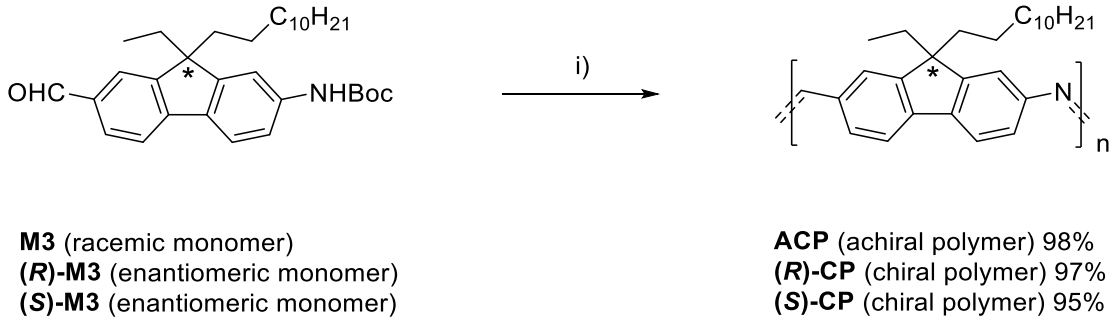

Scheme 3.5. Synthetic strategy towards achiral polymer **ACP**, and chiral polymers **(*R*)-CP** and **(*S*)-CP**. Reagents and conditions: i) (a) TFA, thioanisole, DCM, RT; (b) *in-situ* neat polymerization, 100 °C.

The deprotection of the monomers was carried out with TFA and thioanisole in DCM at room temperature. The work up process included the neutralization with sat. $NaHCO_3$ solution, extraction with DCM, washing with brine, and drying with $MgSO_4$. After removal of the solvent, the monomers were *in-situ* neat polymerized at 100 °C under reduced pressure. The corresponding achiral polymer **ACP**, and chiral polymers **(*R*)-CP**, **(*S*)-CP** were obtained as yellow thin films with a yield of 98%, 97%, and 95%, respectively. Due to the quick polymerization under mild conditions and the unique rigid molecular structure of monomers for head-to-tail polymerization with a stable quaternary stereocenter at the 9 position of the fluorene unit, the obtained **(*R*)-CP**

and **(*S*)-CP** are thus maintaining all-(*R*) and all-(*S*) configuration from the corresponding monomers, respectively.

Characterization of the obtained polymers was first performed with GPC. The GPC results presented in Figure 3.34(a) show that all three polymers have a broad distribution of molecular weight over 118 kDa (n > 300), referred to the polystyrene molecular-weight standards. The comparable molecular weights of both chiral polymers benefit the evaluation and comparison of their enantiomeric recognition ability. This synthetic procedure to chiral polymers is scalable up to 100 mg and fully reproducible. Further characterization of both chiral polymers was carried out with absorption and CD spectroscopy. The CD spectra in Figure 3.34(b) exhibit symmetric peaks with the opposite signs from **(*R*)-CP** and **(*S*)-CP**, confirming their enantiopurity. However, the CD signals are weak and noisy even with concentration up to 10^{-4} M, similar as for the chiral monomers. Three peaks are observed in the CD spectra, which are located at around 305 nm, 415 nm, and 460 nm. The CD peaks at 415 nm and 460 nm are consistent with the main peak in the absorption spectra, which can be assigned to the π-π* transition of the polymers. And the CD peak at 305 nm correlates to a minor absorption peak.

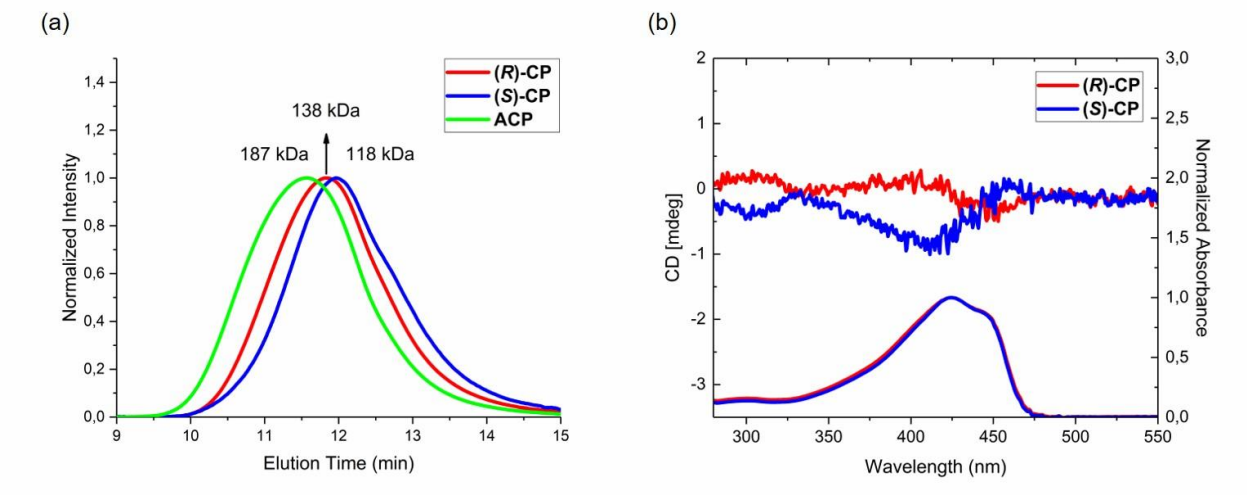

Figure 3.34. (a) GPC results of **(*R*)-CP**, **(*S*)-CP**, and **ACP** with peak molecular weight of 138 kDa (n ~ 356), 118 kDa (n ~ 304), and 187 kDa (n ~ 482), respectively. All samples were measured with a concentration of 1 mg/mL in THF at room temperature. (b) CD (top) and absorption (bottom) spectra of chiral polymer **(*R*)-CP** and **(*S*)-CP**. The samples were measured with a concentration of ~ 4 × 10^{-4} M in toluene at room temperature.

As already explained for the enantiomeric monomers, the intrinsic chirality of the monomer is quite low due to the location of the chiral center in the sterically hindered position 9 of the

chromophore and a very little substituent difference. This could be one of the reasons for the weak CD response of the chiral polymers. Moreover, the chiroptical properties of chiral polymers can be induced by specific helical conformations. In this case, when **(*R*)-CP** and **(*S*)-CP** are dissolved and measured at 25 °C in toluene, which is a good solvent, the polymeric chains are flexible and adopt random coil-like rather than ordered helical conformation. Fujiki *et al*. comprehensively discussed the effects of chiral side chains of polyfluorene derivatives toward CD signs and magnitudes in solution, aggregates, and films.[188] Inspired by that, several co-solvents (DCM/MeOH, DCM/Hexane, toluene/MeOH, toluene/Hexane) were tested to induce the helical conformation in a bad solvent system via aggregation, but no enhancement of CD intensity was observed.

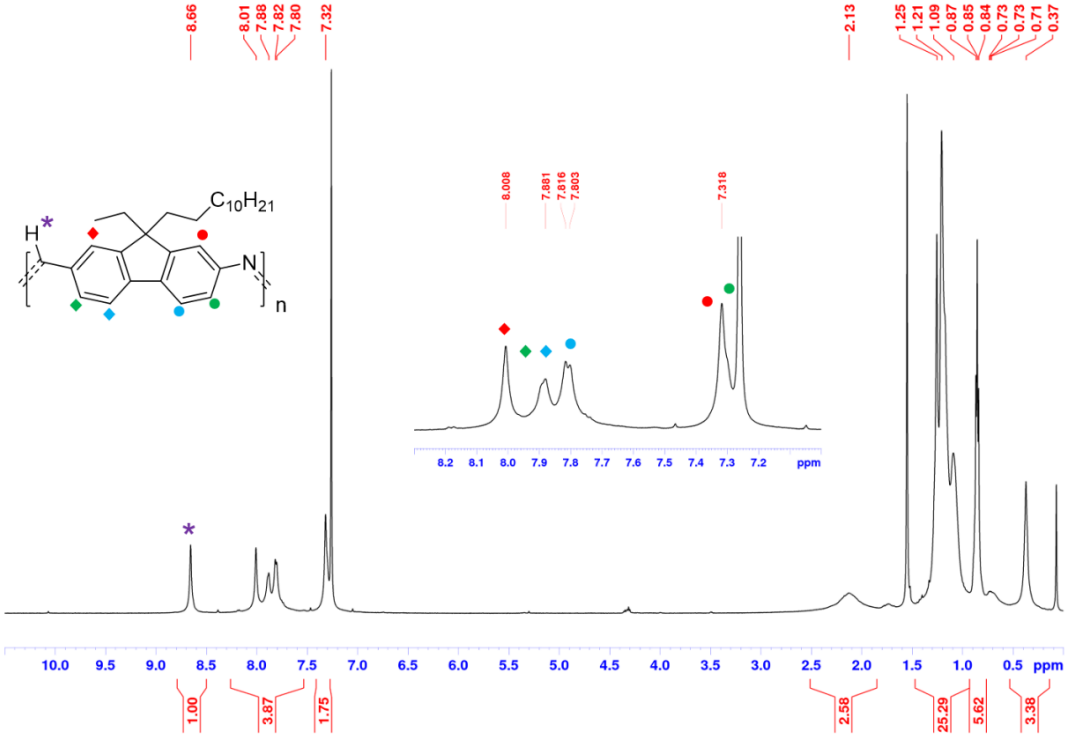

Figure 3.35. ^{1}H NMR spectrum (500 MHz) of the achiral polymer **ACP**. The peaks in the aromatic region are assigned to the corresponding protons of the repeating unit. The sample was measured in $CDCl_3$ at room temperature.

^{1}H NMR measurements were performed for **(*R*)-CP**, **(*S*)-CP**, and **ACP** to investigate the head-to-tail imine bond linked polymeric structure. All three polymers show the same proton NMR

spectra and as an example the NMR spectrum of achiral **ACP** polymer is shown in Figure 3.35. The sharp singlet at 8.66 ppm can be assigned to the proton on the imine bond in each repeating unit. The aromatic protons which are located near to the chiral center of the fluorene backbone contribute to the singlet at 8.01 ppm and 7.32 ppm. The rest of the aromatic protons are also assigned but not well resolved due to the peak overlap. The terminal aldehyde and amino groups are observed at 10.07 ppm and 4.32 ppm as very weak peaks, and their integration should be consistent with the high molecular weight of **ACP**. In Figure 3.35, the terminal aldehyde group has an integration of 0.007 while the imine bond has an integration of 1. Hence, the average number of repeating units can be calculated as 143, corresponding to an average molecular weight of 55 kDa. However, due to the high polydispersity index (PDI) of **ACP** (3.14) and the low accuracy of the NMR integration, the estimated molecular weight by NMR differs from the real molecular weight obtained from GPC measurement.

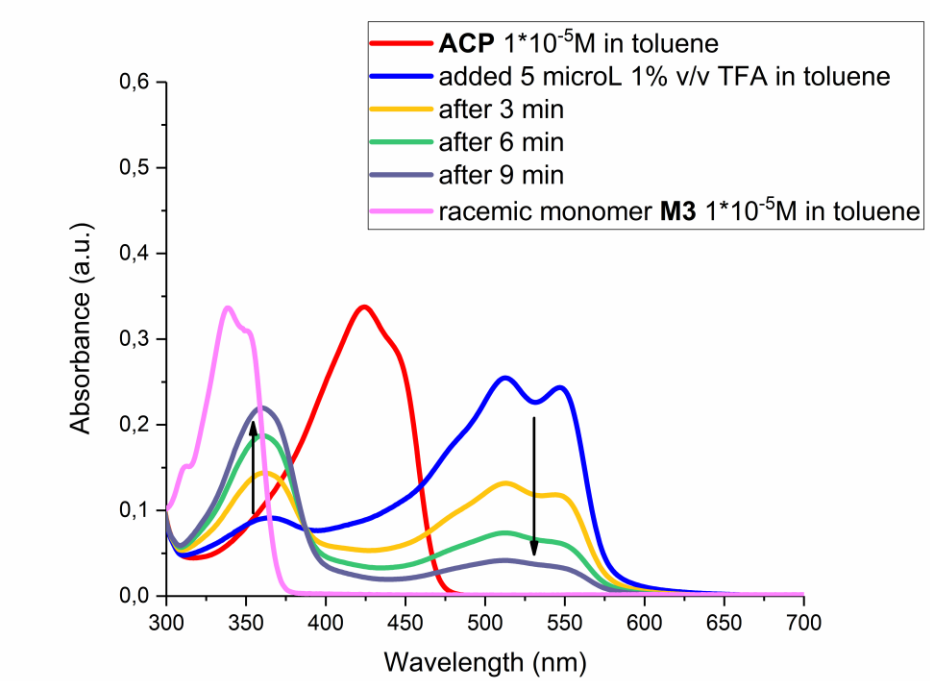

Figure 3.36. Degradation of achiral polymer **ACP** by acid treatment recorded by absorption spectroscopy. All samples were measured in toluene at room temperature.

The degradation of the polymer was comprehensively studied after the addition of a small amount of TFA to a solution of achiral polymer **ACP** in toluene and followed by absorption spectroscopy (Figure 3.36). After addition of TFA, **ACP** was first protonated and an obvious red-

shift of the main absorption peak occurred (blue plot). After a few minutes of shaking degradation of the polymer was observed. The arrows indicate the vanishing polymer absorption peak and the appearance of the corresponding monomer peak (as ammonium salt). Based on these observations, a diluted acid (90% TFA) was used for the hydrolysis of the polymer wrapped along the carbon nanotubes to force the cleavage of the imine bond and release of the polymer.

3.2.7 Enantiomeric separation of pre-sorted HiPco and PLV SWCNTs

The performance of the designed chiral polymer **(*R*)-CP** and **(*S*)-CP** for enantiomeric separation of SWCNTs was tested with pre-sorted HiPco and PLV SWCNTs, which were first sorted with the previously used **P1** copolymer, then released and washed. This procedure includes just sonication, centrifugation and washing, all details are described in the experimental part.

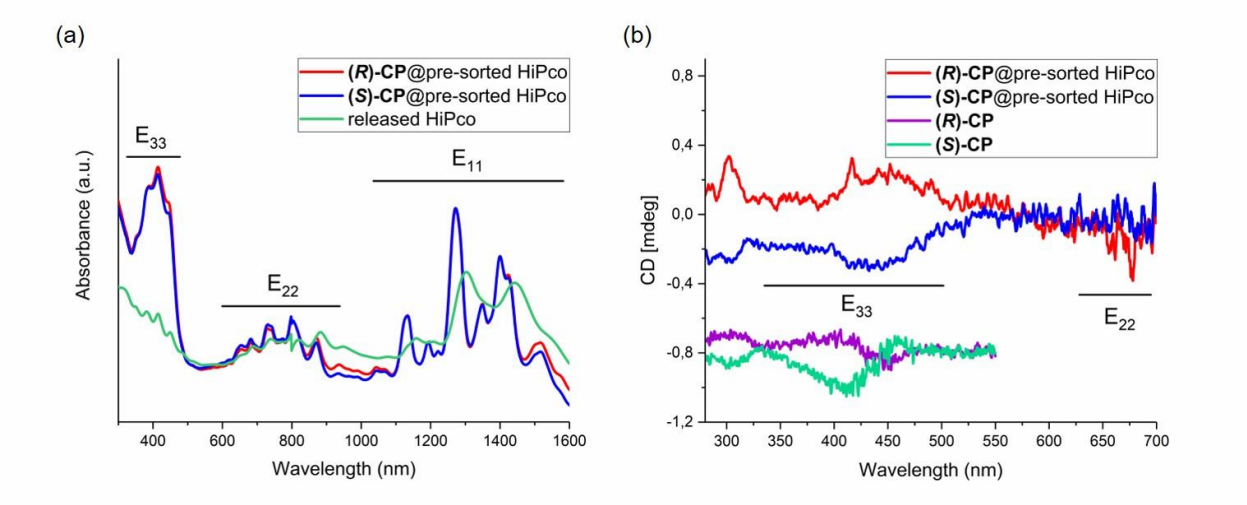

Figure 3.37. (a) Absorption spectra of **(*R*)-CP** and **(*S*)-CP** wrapped pre-sorted HiPco SWCNTs. Both spectra are normalized at 1272 nm. For a comparison, the spectrum of released HiPco SWCNTs used for this rewrapping is also plotted; (b) CD spectra of **(*R*)-CP** and **(*S*)-CP** wrapped pre-sorted HiPco SWCNTs. CD spectra of neat chiral polymers are also shown here but shifted vertically for a better comparison. All samples were measured in toluene at room temperature.

Figure 3.37 shows the absorption and CD spectra of **(*R*)-CP** and **(*S*)-CP** wrapped pre-sorted HiPco SWCNTs. The absorption spectra reveal that both chiral polymers nicely wrap the pre-sorted nanotubes, similarly to the acid cleavable copolymer **P1**. After normalization at 1272 nm, both spectra have almost the same shape and features, indicating that **(*R*)-CP** and **(*S*)-CP** have the same ability for wrapping the nanotubes and same selectivity towards nanotube species. Moreover,

the diversity of (n,m) chirality is well preserved after wrapping with chiral polymers in comparison with the freshly sorted samples by copolymer **P1** (Figure 3.10), which shows similar E_{11} region like in Figure 3.37(a).

Further characterization of the wrapped samples was performed with CD spectroscopy, which can directly prove whether the chiral polymers have the ability to distinguish left- and right-handed HiPco nanotubes. As can be seen in Figure 3.37(b), **(*R*)-CP** and **(*S*)-CP** wrapped pre-sorted HiPco samples give a quite noisy but symmetric CD spectra, indicating the existence of optically active species. In comparison with the neat polymers, the CD spectra of wrapped tubes show the different features. For instance, in the CD spectra of wrapped samples a peak maximum is observed around 440 nm. However, in the CD spectra of neat polymers, a crossing point with CD value of zero is located around 440 nm. Hence, the CD signals from the polymer wrapped samples are more likely from the nanotubes instead of the chiral polymers. Due to the wide diversity of nanotube species in pre-sorted HiPco, the evaluation of the CD spectra is quite difficult. If **(*R*)-CP** and **(*S*)-CP** indeed preferentially extracted nanotubes with one of the specific handedness (left or right), then all the species within one sample should have enantiomeric excess of one handedness over another, resulting in differential absorption of left- and right-handed circular polarized light, which leads to observable CD signals. Hence, the CD spectra of such ensemble samples are contributed by all the nanotubes species inside. According to the E_{11} region in the absorption spectra in Figure 3.37(a), the main species in both samples are (9,4), (7,6), (9,5), (8,7), (10,5), (9,7), (10,6), (9,8). (12,1), (11,3). Those nanotubes can be categorized into type 1 or type 2 depending on mod(n-m,3) equals 1 or 2,[48,49] thus giving exact five type 1 and five type 2 main species in both samples. As aforementioned, type 1 and type 2 nanotubes show opposite signs of E_{ii} transition peak when they have same handedness. Hence, the CD signals from all those ten main nanotube species might cancel each other, resulting in weak overall signals in the E_{33} region as labelled in Figure 3.37(b). Therefore, the observed positive and negative broad peak feature in the E_{33} region is due to the concentration difference between type 1 and type 2 nanotubes in obtained solution. In the E_{22} region in Figure 3.37(b), the assignment of the signals is not convincing due to the noisy background signal near 700 nm. The CD peaks around 300 nm look similar to the CD peaks from neat polymer, but it can be also contributed by the E_{33} transition of the nanotubes.

For the pre-sorted PLV SWCNTs, **(*R*)-CP** and **(*S*)-CP** exhibit also the similar wrapping performance and selectivity, as shown in the absorption spectra in Figure 3.38(a). The diversity of (n,m) chiralities is as well preserved after the wrapping with chiral polymers, in comparison with the freshly sorted samples by copolymer **P1** (Figure 3.22a). In the CD spectra of **(*R*)-CP** and **(*S*)-CP** wrapped pre-sorted PLV samples, broad and weak signals are also observed, as shown in Figure 3.38(b). Both samples seem to have a quite different enantiomeric excess, resulting large difference in the intensity of the peaks. The **(*S*)-CP** wrapped PLV sample shows alternating behavior, which is not observed for the previous HiPco sample. The broad CD peak at 336 nm might be attributed to the E_{44} transitions of the PLV nanotubes, while the broad peaks between 375 nm and 570 nm can be assigned as the E_{33} transitions of the PLV nanotubes. Similarly to the HiPco samples, the CD spectra of the PLV samples are contributed by various nanotubes, which makes their interpretation difficult.

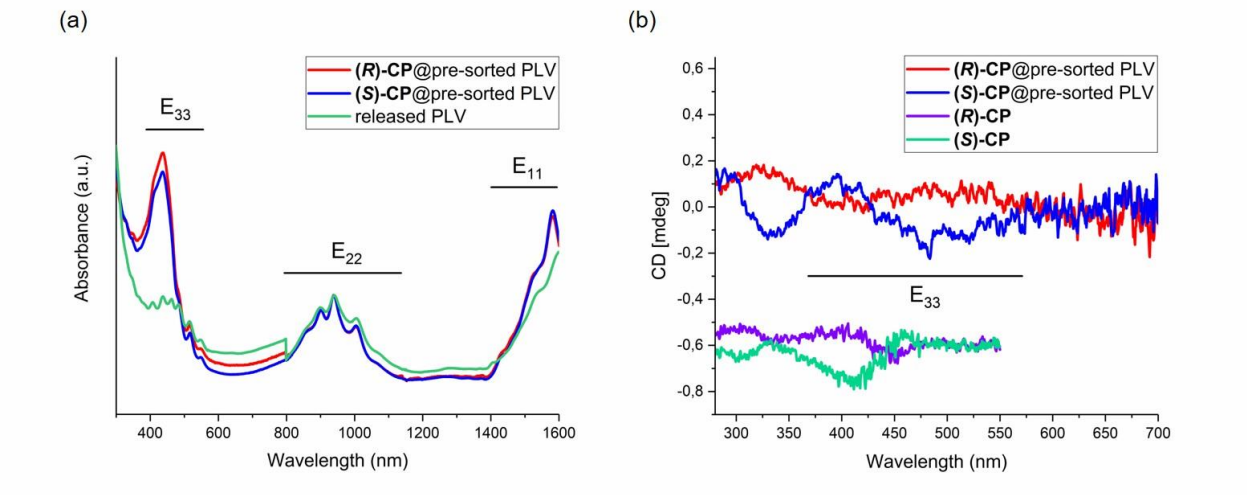

Figure 3.38. (a) Absorption spectra of **(*R*)-CP** and **(*S*)-CP** wrapped pre-sorted PLV SWCNTs. Both spectra are normalized at 939 nm. For a comparison, the spectrum of released PLV SWCNTs is also plotted; (b) CD spectra of **(*R*)-CP** and **(*S*)-CP** wrapped pre-sorted PLV SWCNTs. CD spectra of neat chiral polymers are also shown here but shifted vertically for a better comparison. All samples were measured in toluene at room temperature.

In general, by wrapping with chiral polymers both pre-sorted HiPco and PLV SWCNTs show CD signals with roughly a symmetric pattern, proving the recognition ability of the chiral polymers towards left- and right-handed SWCNTs. However, the obtained CD spectra are not good enough for the peak assignment and the evaluation of the enantiopurity due to the large number of different nanotube species present in the samples.

3.2.8 Enantiomeric separation of enriched (6,5) SWCNTs

To further investigate the recognition ability of chiral polymer **(*R*)-CP** and **(*S*)-CP** towards SWCNT enantiomers, highly enriched (6,5) SWCNTs (up to 80-90% of (6,5) purity) were used as starting material. The enrichment of (6,5) SWCNTs was achieved by the extraction of as-produced CoMoCAT SWCNTs with cleavable copolymer **P1**. The procedure was developed and performed by Dr. Frank Hennrich and Regina Fischer. Detailed procedure is described in experimental part.

The chirality enriched sample contains mainly (6,5) SWCNTs as one can see in the absorption spectrum and PLE map in Figure 3.39. The strong absorption peak at 995 nm can be assigned to the E_{11} transition of (6,5) SWCNT and the peak at 576 nm can be assigned to the E_{22} transition. The absorption region of copolymer **P1** is between 380-500 nm as highlighted in grey in Figure 3.39(a). In the absence of excess polymer, the E_{33} and E_{44} transition peaks can be found at 348 nm and 305 nm, respectively. PLE map in Figure 3.39(b) confirms the enrichment of (6,5) SWCNTs in the sample. Minor species (8,3) and (7,5) SWCNTs are also found in the map.

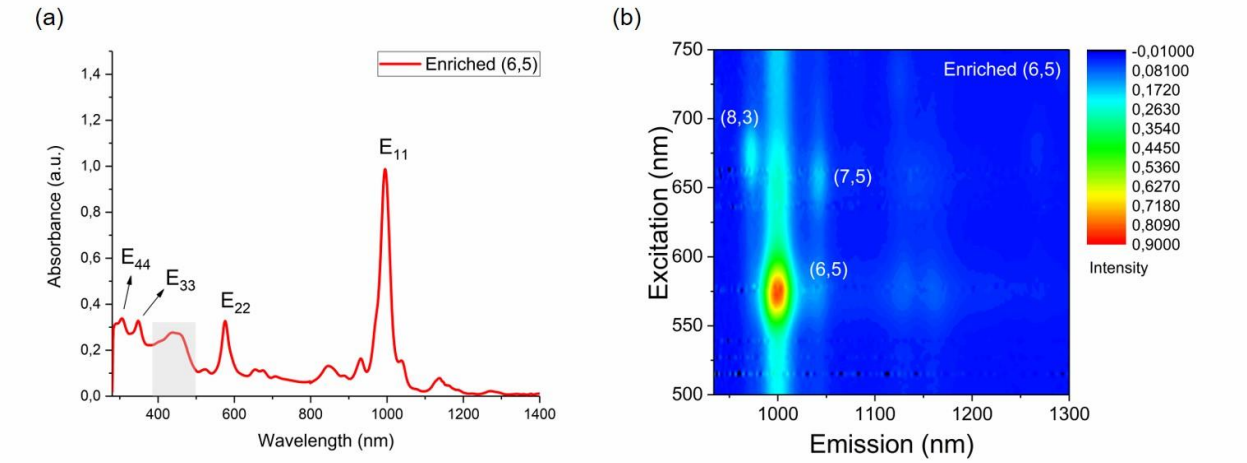

Figure 3.39. (a) Absorption spectrum of polymer **P1** enriched (6,5) SWCNTs. E_{ii} transition peaks of (6,5) nanotube are assigned and labelled. The absorption region of **P1** is highlighted in grey. The sample was measured in toluene at room temperature. (b) PLE map of enriched (6,5) SWCNTs. The sample was measured in toluene at 14 °C.

The enriched sample was triggered and purified with the same procedure as for the HiPco and PLV tubes described before, and was subsequently rewrapped with chiral polymers **(*R*)-CP** and **(*S*)-CP** for the further handedness separation. The resulted samples were characterized with absorption and CD spectroscopy and the corresponding spectra are given in Figure 3.40.

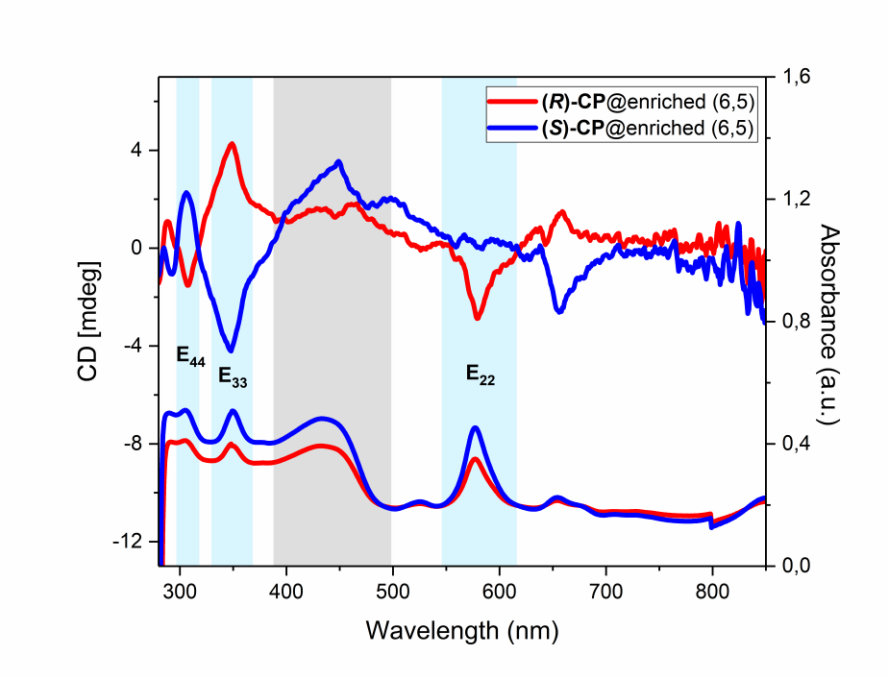

Figure 3.40. Absorption (bottom) and CD spectra (top) of chiral polymer **(*R*)-CP** and **(*S*)-CP** dispersed enriched (6,5) SWCNTs. The E_{ii} transition peaks in both spectra are highlighted and labelled. All samples were measured in toluene at room temperature.

In the absorption spectra, both samples show clear E_{22}, E_{33}, and E_{44} transition peaks (cyan color) and polymer peaks (grey color). However, both samples have different concentrations which can be resulted by the loss of nanotubes while processing and transferring the samples between vials, centrifuge tubes, and cuvettes. The CD spectra show much improved and distinguishable peaks in comparison to the HiPco and PLV samples. The alternating signs of E_{33} and E_{44} CD peaks from both samples and the mirror image between 300-390 nm strongly indicate the successful separation of (6,5) SWCNT enantiomers. In E_{44} and E_{33} regions, the CD peaks are in a good correlation with the absorption peaks in regarding to the position and intensity. As reported by Kataura *et al.*,[49,155] the E_{33} peak of (6,5) SWCNT is higher than the E_{44} peak in CD spectrum. The same feature is also observed here, which further proves that those peaks originate from the (6,5) enantiomers. In the region between 390-500 nm where **(*R*)-CP** and **(*S*)-CP** polymers absorb, different features are observed for both samples. The **(*S*)-CP** dispersed sample have a positive peak at around 450 nm which can be presumably assigned to the cross-polarized E_{31} transition of (6,5) SWCNT.[49] However, the **(*R*)-CP** dispersed sample has a much higher baseline in this region and shows no obvious peak. Also, the polymers seem to have no contributions to the observed CD

peaks in this region. A negative E_{22} CD peak is observed at 580 nm for **(*R*)-CP** dispersed sample, corresponding to the positive E_{33} at 350 nm and the negative E_{44} at 306 nm. For **(*S*)-CP** dispersed sample, the E_{22} peak is missing in the CD spectrum. At 656 nm, **(*R*)-CP** and **(*S*)-CP** dispersed samples give a positive and a negative CD peak respectively, which can be assigned to the cross-polarized E_{12} transition.[155]

The normalized CD value (CD_{norm}) of **(*R*)-CP** dispersed (6,5) sample was calculated as -8.2 mdeg according to Komatsu *et al*.[50] Despite several attempts and modifications in the procedure, no improvement was achieved to obtain perfect CD spectra with all E_{22}, E_{33}, and E_{44} transition peaks from both **(*R*)-CP** and **(*S*)-CP** dispersed (6,5) SWCNTs. One of the possible reasons is the existence of an unknown polymer impurity in the enriched (6,5) SWCNT sample, which was possibly introduced to the sample during the size-exclusion gel column purification process. This unknown polymer was later identified as PFO according to the absorption, emission and ^{1}H-NMR spectra. The PFO polymer was believed to interact with the naked tubes after the triggering of copolymer **P1** and remained on the sidewall of the triggered tubes, which then interfere with the subsequent rewrapping of the chiral polymers.

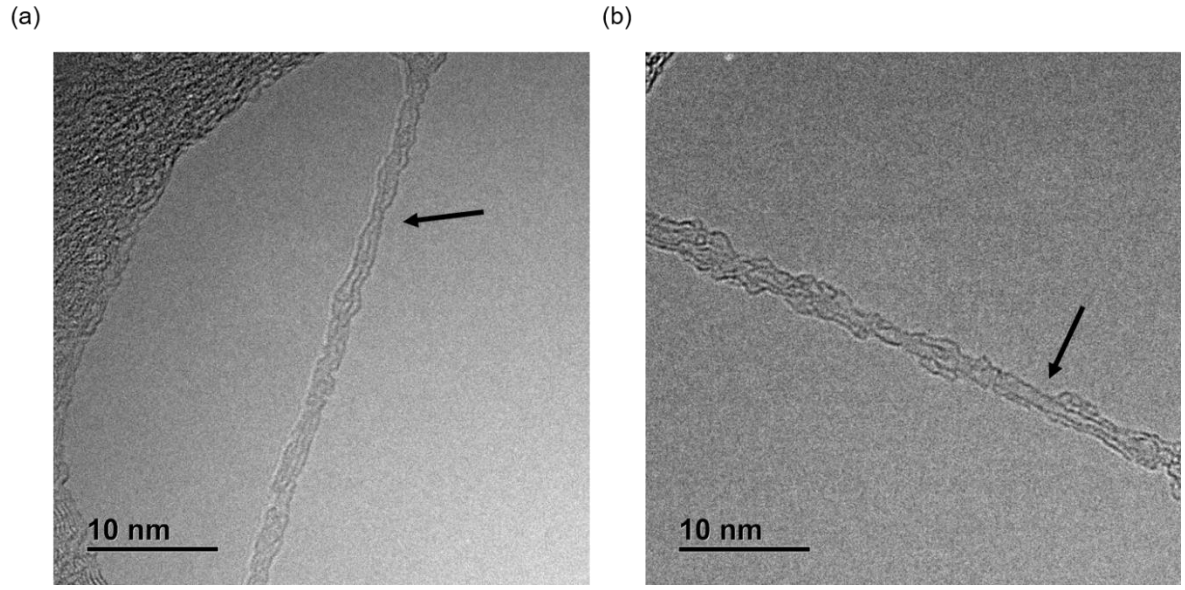

Figure 3.41. TEM images of **(*R*)-CP** or **(*S*)-CP** wrapped (6,5) SWCNT.

Structural characterization of the polymer/SWCNT complex was performed with transmission electron microscopy (TEM). A racemic nanotube sample was prepared by dispersing of (6,5) SWCNTs with **(*R*)-CP** and **(*S*)-CP** polymers and further purified by washing with toluene, DCM,

and acetone. The purified sample was then drop casted on a holey carbon supported copper grid and dried. During the TEM measurement, the contamination from the sample was found as a major problem. Shortly after exposure to the electron beam, contaminations started to stack around the focused area and hindered the measurement. Another problem was the aggregation of the nanotubes in acetone, which happened possibly even during the evaporation of acetone on the grid. Despite of that, a single strain of individual SWCNTs were still found. In Figure 3.41(a), the nanotube is totally wrapped with the chiral polymers and the tube sidewall is hidden. This is actually expected and can be explained by the strong interaction between the polymer and the nanotube sidewall. The helical wrapping pattern of the polymer around the nanotube is not clearly observed due to the flatness of the polymer chain and a low resolution of such sample. However, a twisted structure is seen in Figure 3.41(a) as pointed by the arrow, which can be assigned as the polymer chain wrapping along a tube. In Figure 3.41(b), the nanotube sidewall is partially visible as indicated by the arrow. According to the scale bar, the diameter of the nanotube is around 0.80 nm, which is consistent with the expected diameter of such (6,5) SWCNTs (0.76 nm).

3.2.9 Enantiomeric separation of as-produced CoMoCAT SWCNTs

The handedness recognition ability of chiral polymer **(*R*)-CP** and **(*S*)-CP** was further investigated with as-produced CoMoCAT SWCNTs (SG65i, CHASM Advanced Materials, Canton, MA, U.S.A.) with 95% purity of s-SWCNTs and above 40% (6,5) SWCNTs content as starting material instead of the pre-sorted SWCNTs. This handedness sorting process involves only sonication, centrifugation, and washing. Detailed procedure is given in the experimental part.

3.2.9.1 Characterization of handedness sorted CoMoCAT SWCNTs

After the wrapping process and removal of excess polymer, the sorted samples were first characterized with absorption spectroscopy and the recorded spectra are given in Figure 3.42. Each pair of enantiomeric samples and spectra discussed below are from one parallel trial. The absorption spectra of polymer-wrapped SWCNTs exhibit sharp electronic absorption peaks and flat baselines when compared to pristine tubes (see Figure 8.10 in Appendix), which are associated with well-dispersed samples of individually suspended carbon nanotubes.

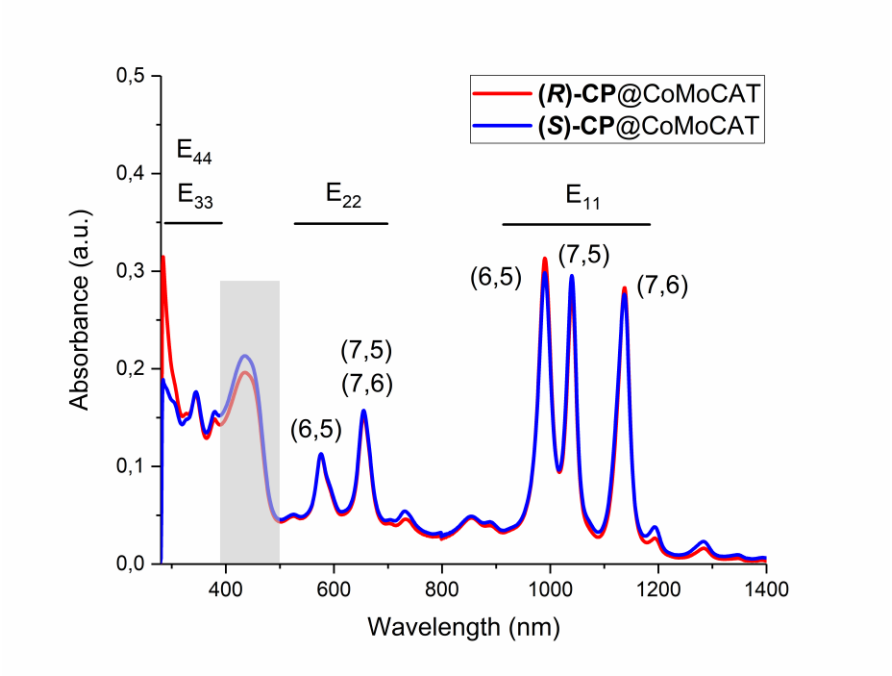

Figure 3.42. Absorption spectra of chiral polymer **(*R*)-CP** and **(*S*)-CP** dispersed CoMoCAT SWCNTs. The highlighted grey area corresponds to the absorption of wrapping polymer. All samples were measured in toluene at room temperature.

The absorption peaks in semiconducting E_{11} and E_{22} regions in Figure 3.42 are labelled with chiral indices (n,m), indicating that both **(*R*)-CP** and **(*S*)-CP** disperse mainly (6,5), (7,5), and (7,6) s-SWCNTs with comparable intensity. The E_{11} peaks of (6,5) and (7,5) locate separated at 990 nm and 1040 nm, while the E_{22} peaks are overlapped at 654 nm. (6,5) nanotubes have E_{11} peak at 990 nm and an individual E_{22} peak at 577 nm. The polymer region between 400 nm and 500 nm might partially overlap with the E_{33} of (7,5) and (7,6) tubes but not with the E_{33} transition of (6,5) tubes, which is assigned the sharp peak at 345 nm. For better interpretation of the overlapped area, the absorption spectrum of polymer wrapped tubes is plotted together with the neat polymer, as shown in Figure 8.11 in Appendix.

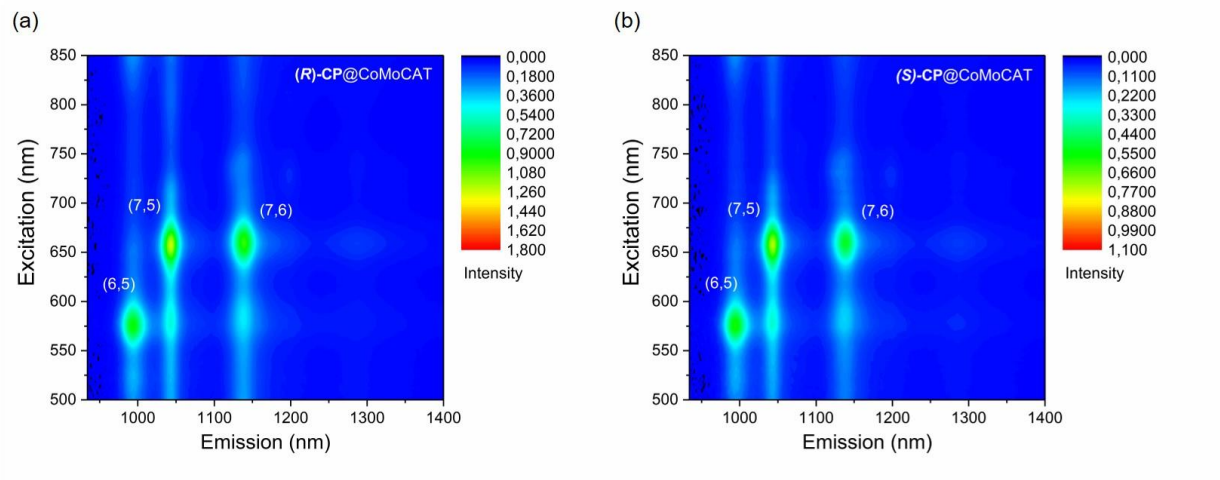

Figure 3.43. PLE maps of chiral polymer (a) **(*R*)-CP** and (b) **(*S*)-CP** dispersed CoMoCAT SWCNTs. All samples were measured in toluene at 14 °C.

The PLE maps in Figure 3.43 confirm the similar performance of both chiral polymers to wrap mainly the three chiral tubes. The content of these (6,5), (7,5), and (7,6) SWCNTs is calculated according to the relative intensity of those three chiral indices in the PLE maps. For both samples, the relative content of (6,5), (7,5), and (7,6) SWCNTs is approximately 30%, 40%, and 30%, respectively. AFM images in Figure 3.44(a,b) prove that the SWCNTs in both samples are individualized. The white spots in the images are most likely from the residue of metal catalysts and amorphous carbon particles. Unlike the copolymer **P1** sorted HiPco and PLV samples, the chiral polymer sorted CoMoCAT samples were not purified by SEC after the wrapping process due to the low yield of presorting process and to avoid the loss of tubes which could be stacked on the SEC gel column. Therefore, all carbon and catalyst-based impurities in the samples cannot be

efficiently removed. The length distribution of the nanotubes within the samples was statistically calculated by extracting length data from multiple AFM images and fitted with Gauss function as shown in Figure 3.44(c,d). An average length of about 300 nm was found for both samples.

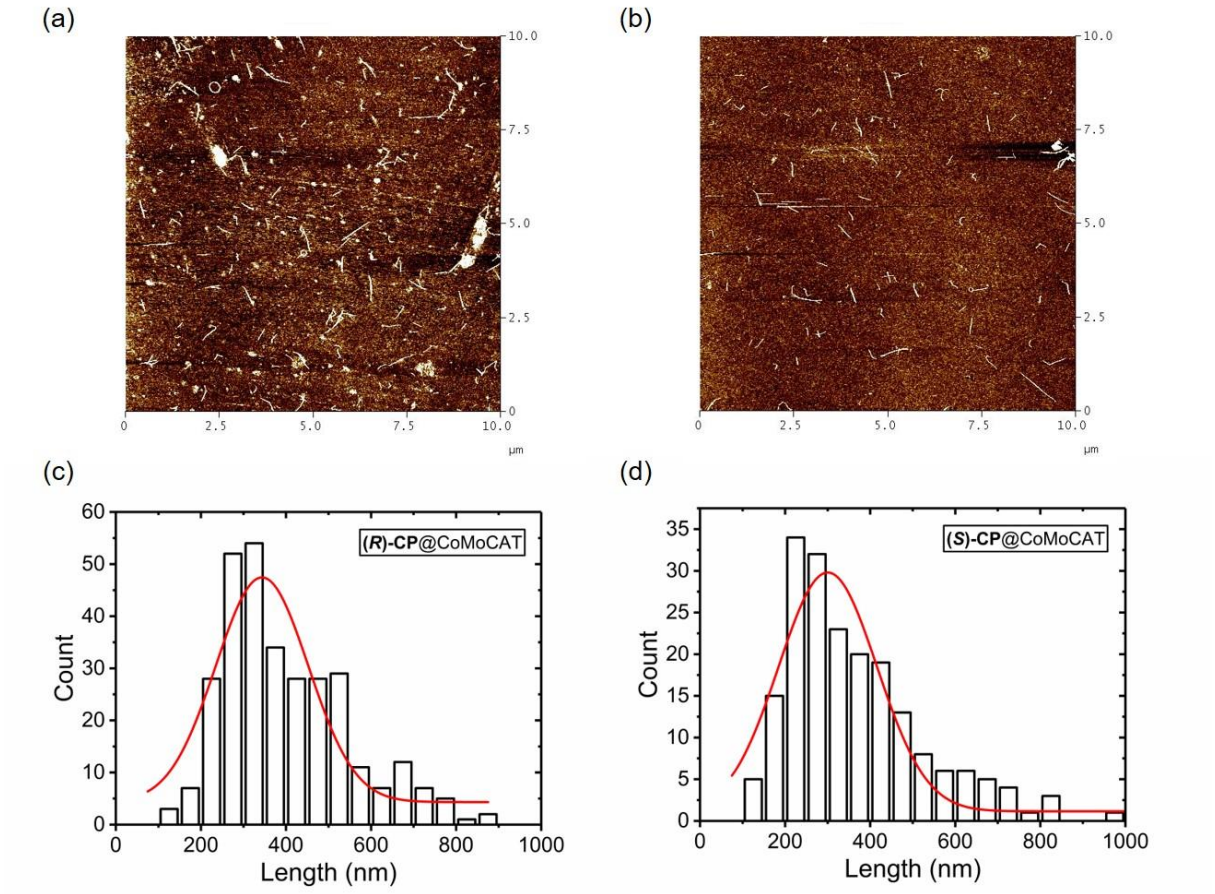

Figure 3.44. (a,b) AFM images of **(*R*)-CP** (left) and **(*S*)-CP** (right) dispersed CoMoCAT SWCNTs; (c,d): length statistics extracted from AFM images of **(*R*)-CP** and **(*S*)-CP** dispersed CoMoCAT SWCNTs. The red curves are the Gauss function fitted length distributions.

Raman measurements were performed for the **(*R*)-CP** and **(*S*)-CP** dispersed CoMoCAT samples and the spectra are shown in Figure 3.45. The G^+ bands of CoMoCAT samples locate at around 1588 cm^{-1} and the D bands are at around 1310 cm^{-1}. The D bands of the chiral polymer-wrapped SWCNTs decrease dramatically in comparison to the raw material, indicating the sorted nanotubes are less defected and the chiral polymer wrapping is of non-covalent nature. Interesting features are observed in the region of the G^- bands. For HiPco and PLV SWCNTs, the G^- band locates at 1560 cm^{-1} and 1570 cm^{-1}, respectively. However, for the CoMoCAT SWCNTs the G^- bands are found split into two subbands at 1527 cm^{-1} and 1544 cm^{-1}, which are red shifted. This

relationship between the nanotube diameter and the position of the G^- band was investigated by Doorn *et al.*[189] They revealed that the G^- band position red shifts strongly with a decreasing nanotube diameter, which makes the G^- band position an alternative way for the chirality assignment. According to these results, the G^- subband in the expanded view (inset) at 1527 cm^{-1} can be assigned to (6,5) SWCNT while the subbands at 1544 cm^{-1} correspond to (7,5) and (7,6) SWCNT, which is consistent with the previous absorption and PLE results (Figure 3.42 and Figure 3.43).

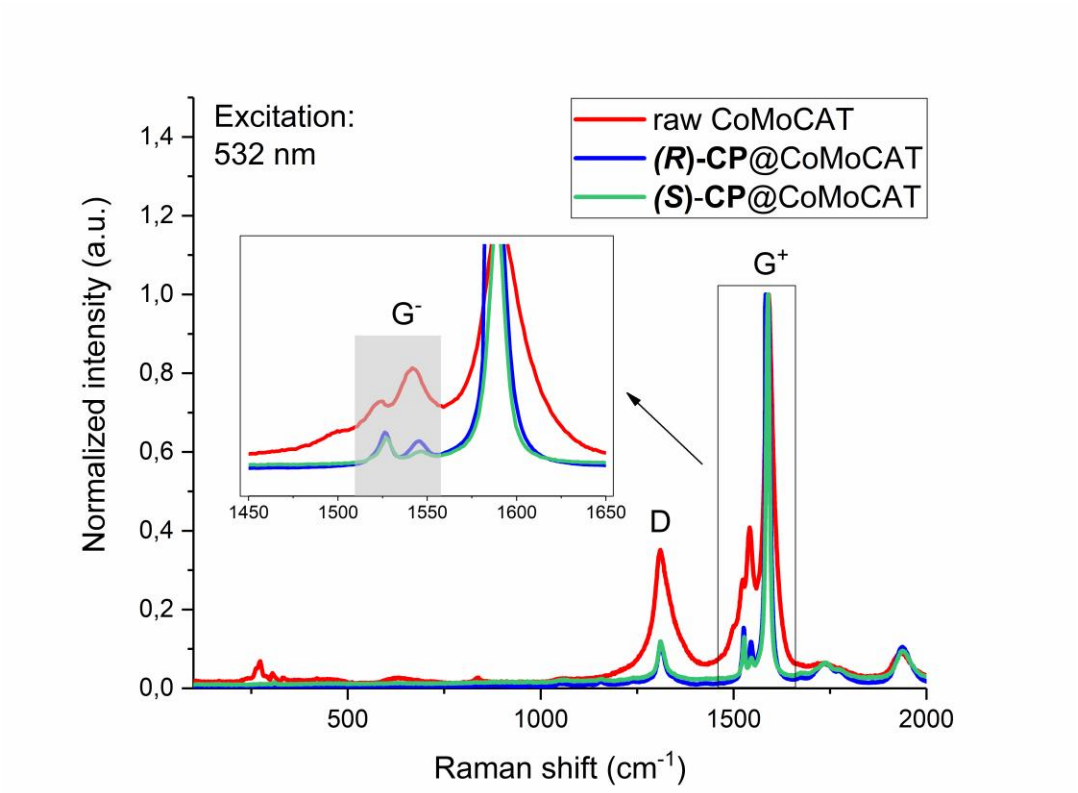

Figure 3.45. Raman spectra of raw CoMoCAT and chiral polymer-wrapped CoMoCAT samples. All samples were excited at 532 nm.

In the radial breathing mode (RBM) region, as shown in Figure 3.46, the absence of the metallic tubes in both wrapped samples is evidenced by a flat curve in the grey region in contrast to the raw material. The peaks at 309 cm^{-1} in both samples correspond to (6,5) SWCNT.

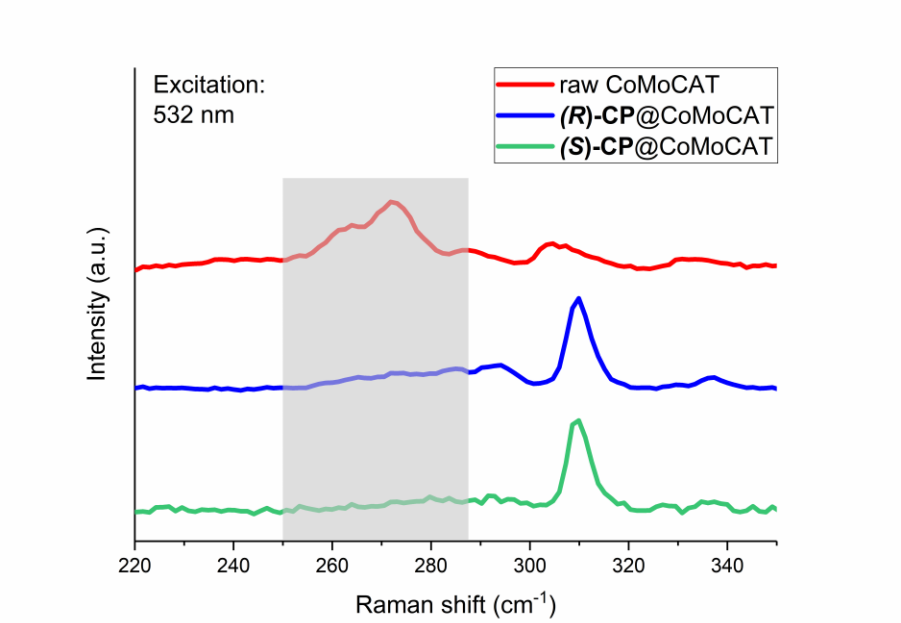

Figure 3.46. Radial breathing mode (RBM) regions of the Raman spectra of raw CoMoCAT and chiral polymer-wrapped CoMoCAT samples. Metallic region is highlighted in grey. All samples were excited at 532 nm and the spectra were normalized and shifted vertically for clarity.

Based on the previous results, it is not necessary to remove the chiral polymers wrapped around the tubes and redisperse the sample with achiral polymer **ACP** before performing the CD and absorption experiments in order to obtain all four E_{ii} peaks of SWCNTs interband transitions. Because the absorption peak of the polymer itself (highlighted in grey in Figure 3.42) is outside the characteristic E_{ii} tube transitions and the CD spectrum of the neat polymer is very weak (Figure 3.34b) to affect the obtained results of handedness sorted nanotubes. Therefore, the optical activity of the **(*R*)-CP** and **(*S*)-CP** dispersed CoMoCAT samples was measured by CD spectroscopy before removing the chiral polymers.

With the help of an additional light source (halogen lamp) and the second InGaAs detector, the CD measurements were extended to the NIR region. The obtained CD spectra from both samples are plotted in Figure 3.47 together with the UV-Vis-NIR spectra. The alternating positive and negative signs, as well the mirror symmetry of the CD spectra indicate that we obtained two enantiomerically enriched samples. In comparison to the CD spectra of chiral polymer dispersed enriched (6,5) SWCNTs, the sorted raw SG65i CoMoCAT samples show all the E_{ii} transition peaks with symmetric patterns which can be better compared and analyzed with the reported results.

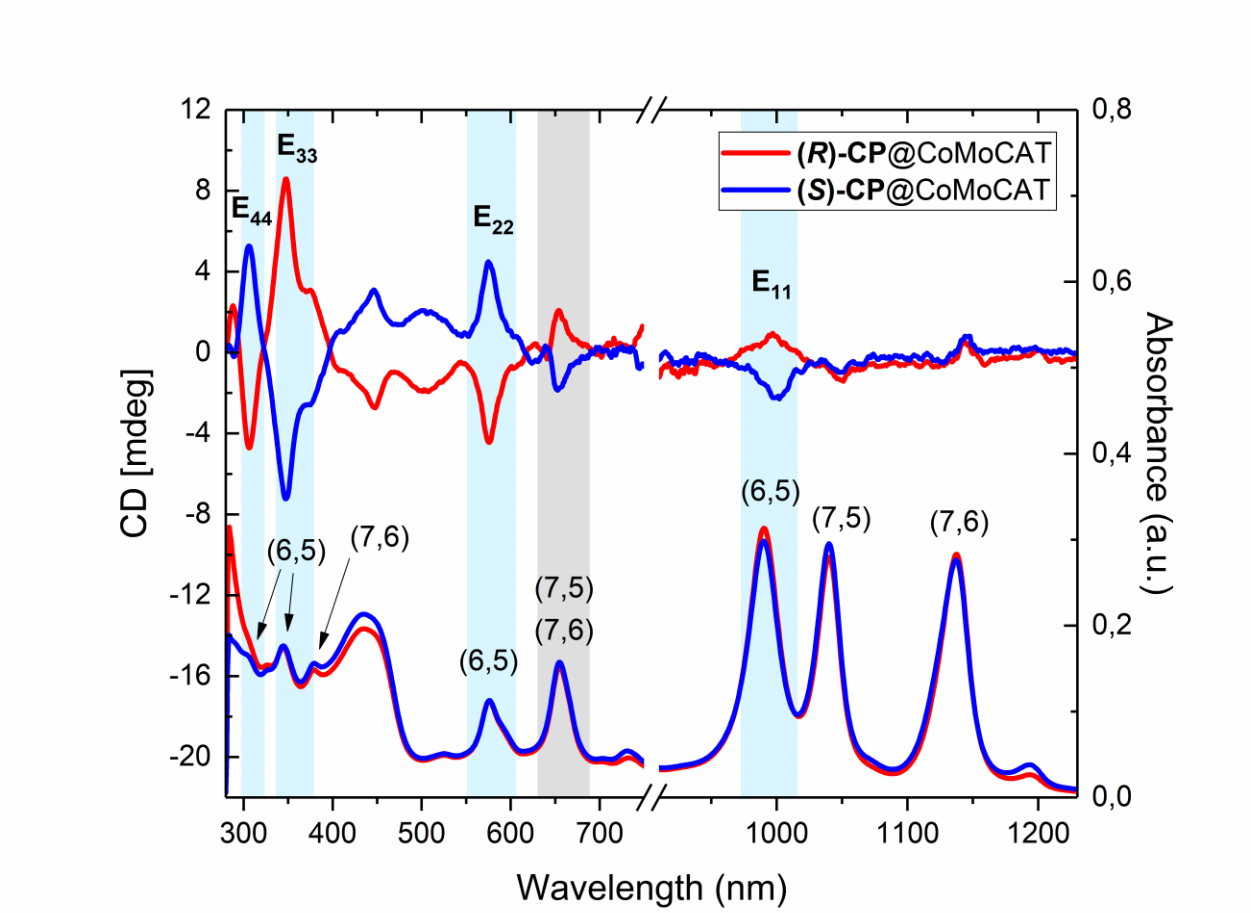

Figure 3.47. UV-Vis-NIR absorption and CD spectra of chiral polymer **(*R*)-CP** and **(*S*)-CP** dispersed CoMoCAT SWCNTs. All samples were measured in toluene at room temperature.

In the UV-Vis region, the highlighted (blue) semiconducting transition bands E_{22}, E_{33} and E_{44} fit well with the published results of (6,5) SWCNT enantiomers.[155] To assign the CD spectra to the corresponding nanotube enantiomers, different nomenclatures have been applied. Weisman *et al.* and Zheng *et al.* assigned positive and negative E_{22} peak to (+)- and (-)-enantiomer respectively,[108,160] whereas Kataura *et al.* denote positive and negative E_{22} peak to (-)- and (+)-enantiomer, respectively.[49] In some cases, (n,m) and (n+m,-m) are also used to assign the spectra of the both enantiomers.[48,155] In this work, the (6,5) enantiomers which give a positive or negative E_{22} CD peak at 576 nm are assigned as left-handed (*M*) (blue plot) or right-handed (*P*) (red plot) enantiomer, respectively, based on the IUPAC terminology[13] and the reported data from Komatsu *et al.*,[152] where they first related the CD spectra to the corresponding (6,5) enantiomers with a specific handedness according to the molecular modeling calculation.

The small shoulders at 376 nm in the CD spectra belong to the E_{33} transition of (7,6) SWCNT, and the broad peaks between 395 nm and 540 nm correspond to the cross-polarized E_{ij} transition of (6,5) SWCNT.[49] (7,5) and (7,6) SWCNTs have E_{22} transition energies of 1.90 eV and 1.89 eV respectively,[190] so that they share the peak at 654 nm in the absorption spectra, as highlighted in grey. However, the intensity of the E_{22} transition peak of (7,5) and (7,6) tubes in the corresponding CD region (grey) is significantly lower than expected also compared to the E_{22} peak intensity of (6,5) SWCNTs at 576 nm. In addition, the CD peaks in this grey area are more likely attributed to the E_{21} transition of (6,5) SWCNTs.[155] To explain this phenomenon, all three tube species need to be first categorized into Type-1 or Type-2 SWCNTs. According to Kataura *et al.*, [49] (6,5) and (7,6) are Type-1 SWCNTs whereas (7,5) is a Type-2 SWCNT. More importantly, Type-1 and Type-2 SWCNTs with a specific handedness have opposite signs of the CD signals and this statement is supported by theoretical calculations of CD spectra.[48] In this case, the hypothesis is that each chiral polymer extracts all three nanotube species with similar handedness preferentially, so that the E_{22} CD signals of (7,5) and (7,6) SWCNTs might cancel each other, in particular because both samples with the same handedness are present in similar concentrations. Therefore, in the grey area one can probably only observe the E_{21} transition of (6,5) SWCNT. Moreover, the presence of the E_{33} peak from (7,6) enantiomers at 376 nm in the CD spectra proves that the handedness recognition of the chiral polymers is not limited to (6,5) SWCNT only. Based on the CD results in the UV-Vis region and theoretical calculations (Chapter 3.2.9.4), it is clear that **(*R*)-CP** polymer selectively extracts (*P*)-(6,5), (*P*)-(7,6), and (*P*)-(7,5) SWCNTs, whereas **(*S*)-CP** polymer selectively extracts (*M*)-(6,5), (*M*)-(7,6), and (*M*)-(7,5) SWCNTs. In the NIR region, the highlighted CD peaks belong to the E_{11} transition of (6,5) enantiomers and the signs are consistent with the alternating behavior of E_{ii} CD signals of both (6,5) enantiomers. However, no symmetric signals were obtained from (7,5) and (7,6) enantiomers in the E_{11} transition region. A possible explanation for this phenomenon may be the low sensitivity of the detector and the high noise level of the CD spectra in the NIR region.

In order to determine the optical purity of the enantiomerically separated samples in terms of the (6,5) SWCNT enantiomers, the equation $CD_{norm} = (CD_{raw}/L_{CD})/(A_{E22}/L_{abs})$ is applied, where CD_{norm} and CD_{raw} are the CD values of the E_{22} transition peaks of (6,5) SWCNT after and before normalization, A_{E22} is the absorbance at E_{22} transition of (6,5) SWCNT, L_{CD} and L_{abs} are the optical path lengths (cm) of the cell used for the CD and absorption analysis.[50] The calculated

CD_{norm} in this work is -39 mdeg for (*P*)-(6,5) SWCNT in **(*R*)-CP**@CoMoCAT sample and +40 mdeg for (*M*)-(6,5) SWCNT in **(*S*)-CP**@CoMoCAT sample, indicating that the chiral polymers have the same handedness recognition ability owing to their all-(*R*) and all-(*S*) configuration. The obtained CD_{norm} values are higher than those reported by Weisman *et al.*[108] using the DGU method (±36 mdeg) and Nakashima *et al.*[161] using chiral copolymer wrapping (+24 mdeg), however, lower than those reported by Kataura *et al.*[49] using gel column chromatography (+93, -85 mdeg) and Zheng *et al.*[191] using DNA differentiation (±84 mdeg). To further estimate the enantiomeric purity (EP) of the samples with calculated CD_{norm} values, the following equations EP (*M*)-(6,5) (%) = 50 + αCD_{norm} and EP (*P*)-(6,5) (%) = 50 - αCD_{norm} were applied as reported by Kataura *et al.* using gel column chromatography for handedness sorting of CNTs and the subsequent redispersion of nanotube enantiomers in a Flavin mononucleotide aqueous solution.[155] Here, α is a linear scaling factor which is set as 0.421±0.030 $mdeg^{-1}$. Thus, the EP values of **(*R*)-CP**@CoMoCAT and **(*S*)-CP**@CoMoCAT sample are (66.4±1.2)% and (66.8±1.2)%, respectively.

To note, the CD_{norm} values were calculated without the baseline correction of the CD and absorption spectra, which might have a strong influence on the final values. In some cases, the baseline can be higher or lower than the zero-value line in the CD spectra as shown in Figure 3.48, which brings difficulty to the quantitative evaluation of such results. The CD spectra in Figure 3.48 were obtained from the samples which were processed with the similar procedure as for the previous **(*R*)-CP**@CoMoCAT and **(*S*)-CP**@CoMoCAT sample. The reasons for such difference in the CD spectra and CD_{norm} value could be resulted by the little different treatment of samples in the process, such as sonication time, centrifugation time and the impurities which remain during the removal of excess polymer.

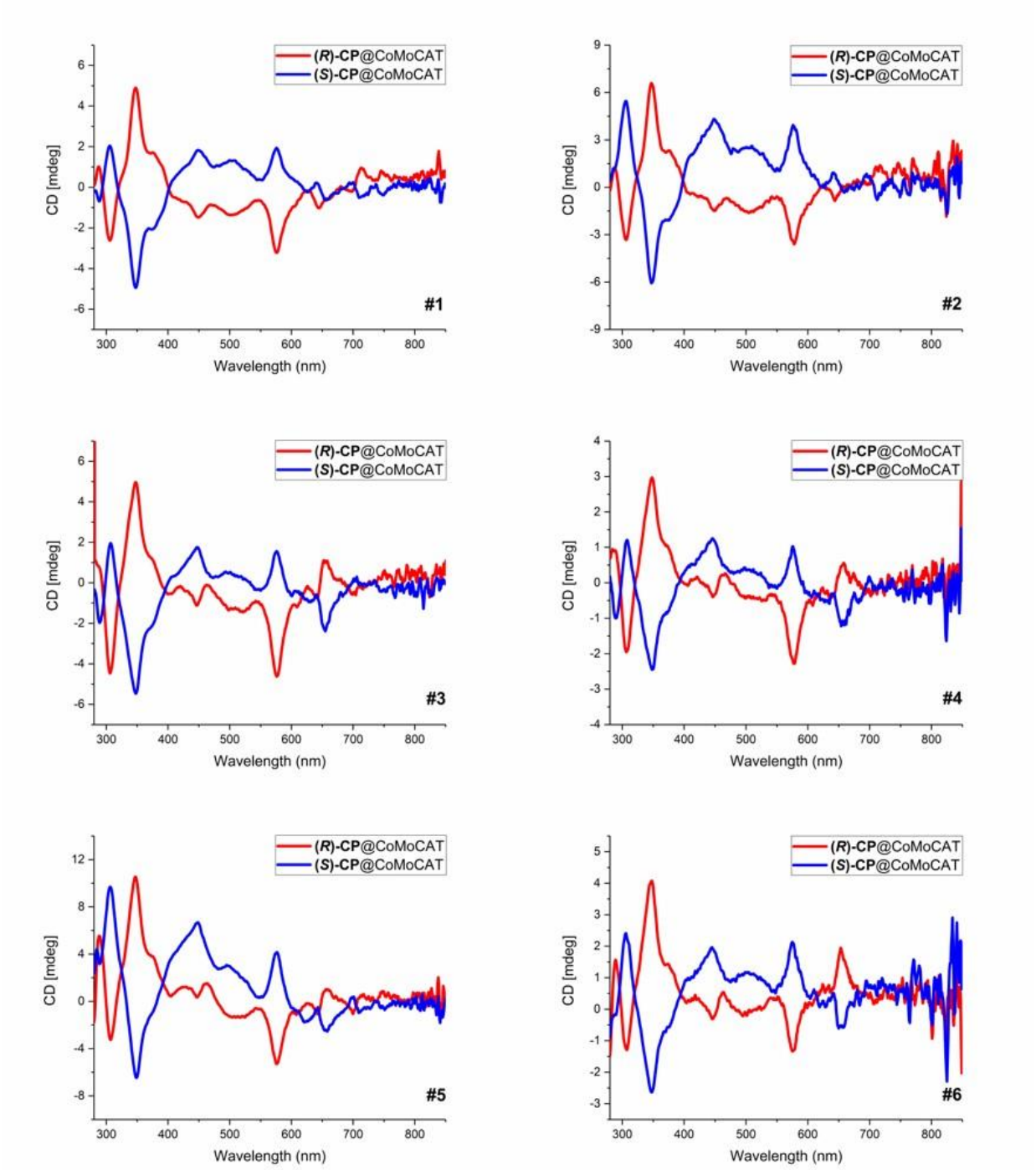

Figure 3.48. CD spectra of chiral polymer dispersed CoMoCAT SWCNTs from different trials. All samples were measured in toluene at room temperature.

3.2.9.2 Cleavage of the polymer

After the separation process, the wrapping polymers can be quantitatively removed by cleaving the imine bonds (C=N) in the polymer backbone with a catalytic amount of acid, yielding dispersant-free single-handed s-SWCNTs. Upon an addition of a catalytic amount of acid, the polymer quickly degrades into oligomers and monomers, thus detaches from the nanotubes and causes the quantitative precipitation of naked SWCNTs. The advantage of this dynamic imine bond cleavage approach is that the monomers can be recovered almost quantitatively and be reused in the synthesis of the chiral polymers.[192]

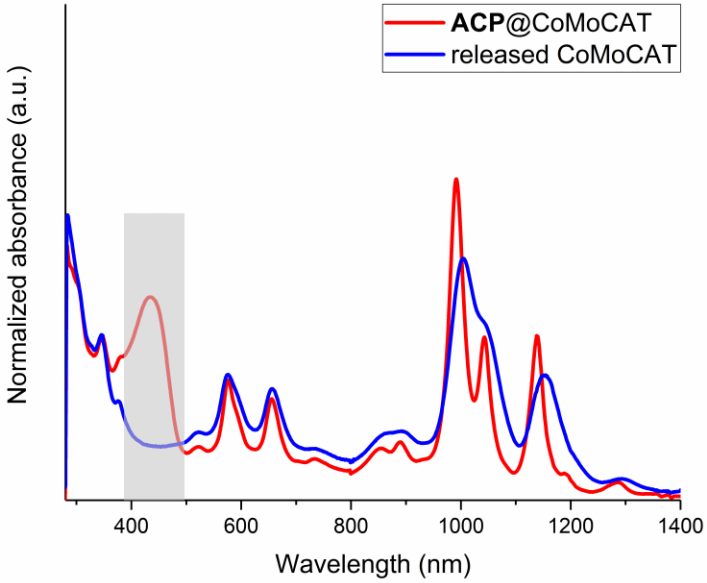

Figure 3.49. Absorption spectra of **ACP** polyimine dispersed CoMoCAT SWCNTs before and after acid treatment and subsequent washing of monomers with acetone and toluene. All samples were measured in toluene at room temperature.

Acid degradation of the polyimine polymer was tested on the achiral polymer (**ACP**) wrapped SWCNTs. For this a small amount of trifluoroacetic acid (1% v/v of 90% TFA) was added to a polymer wrapped sample in toluene. The mixture was sonicated for 10 min and subsequently diluted with acetone to yield the precipitate of the naked nanotubes. The sample was filtrated and copiously washed on a PTFE membrane filter (0.20 μm) with acetone and toluene. The released nanotubes were dried in air and then re-dispersed in toluene as aggregates. The absorption spectra

of **ACP** polyimine dispersed CoMoCAT SWCNTs before and after acid treatment and subsequent washing are shown in Figure 3.49.

In the absorption spectra, as shown in Figure 3.49, the polymer peak disappears after acid treatment and washing of monomers with toluene. The absence of absorption band in the released SWCNT sample between 400-500 nm also indicates the absence of metallic SWCNTs. The quantitative cleavage of the polymer was further corroborated by X-ray photoelectron spectroscopy (XPS) measurement, where the N 1s peak attributed to the N atoms in the polyimine disappeared in the released SWNT sample, as shown in Figure 3.50(b). In the C 1s spectrum in Figure 3.50(a), the released and wrapped nanotubes have almost the same peak position while the raw material has an obvious shift to the low energy region, indicating the existence of carbon impurities such as amorphous carbon.

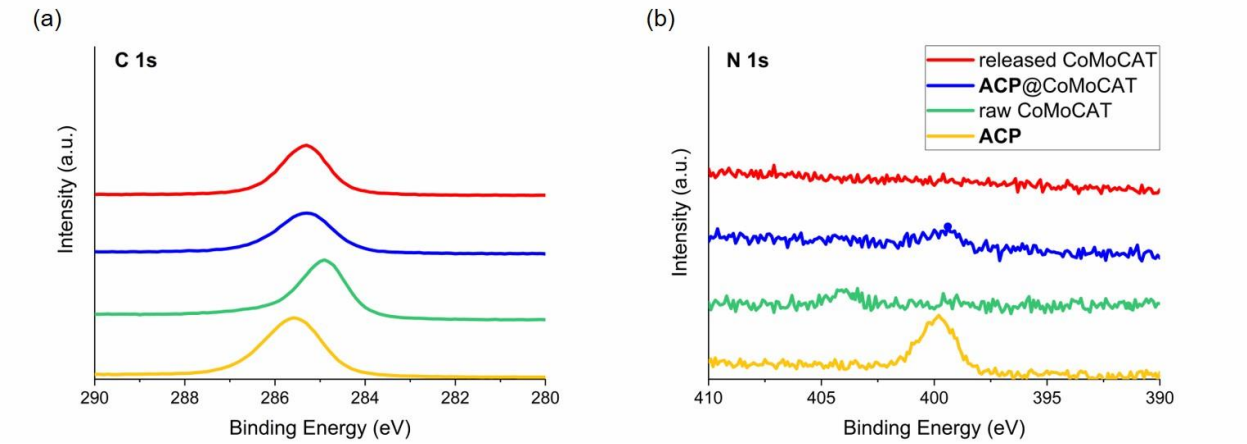

Figure 3.50. C 1s (a) and N 1s (b) XPS spectra of achiral polymer **ACP**, raw CoMoCAT, **ACP** wrapped and triggered CoMoCAT samples.

3.2.9.3 Rewrapping of naked and handedness sorted SWCNTs with non-chiral Polymer

In order to confirm that the chiral polymers **(*R*)-CP** and **(*S*)-CP** have only minor effects on the CD spectra and the obtained CD signal is intrinsic to the SWCNT enantiomers, the chiral polymers were degraded and the enantiomerically pure SWCNTs were subsequently rewrapped with the commercially available achiral PFO-Bpy polymer, which has been reported to have a specific selectivity for the (6,5) nanotubes.[133] In the absorption spectrum of PFO-Bpy polymer rewrapped sample, as shown in Figure 3.51, the rewrapping efficiency with PFO-Bpy polymer is proven by the absence of the typical **(*S*)-CP** absorption peak at around 400-500 nm and the appearance of the PFO-Bpy absorption peak at around 320-400 nm. In the CD spectra as shown in Figure 3.51, negligible changes in CD intensities of E_{22}, E_{33}, and E_{44} transitions are observed, confirming that the CD signal is intrinsic to the nanotube sample and not induced by the chiral polymers helically wrapped around a SWCNT.

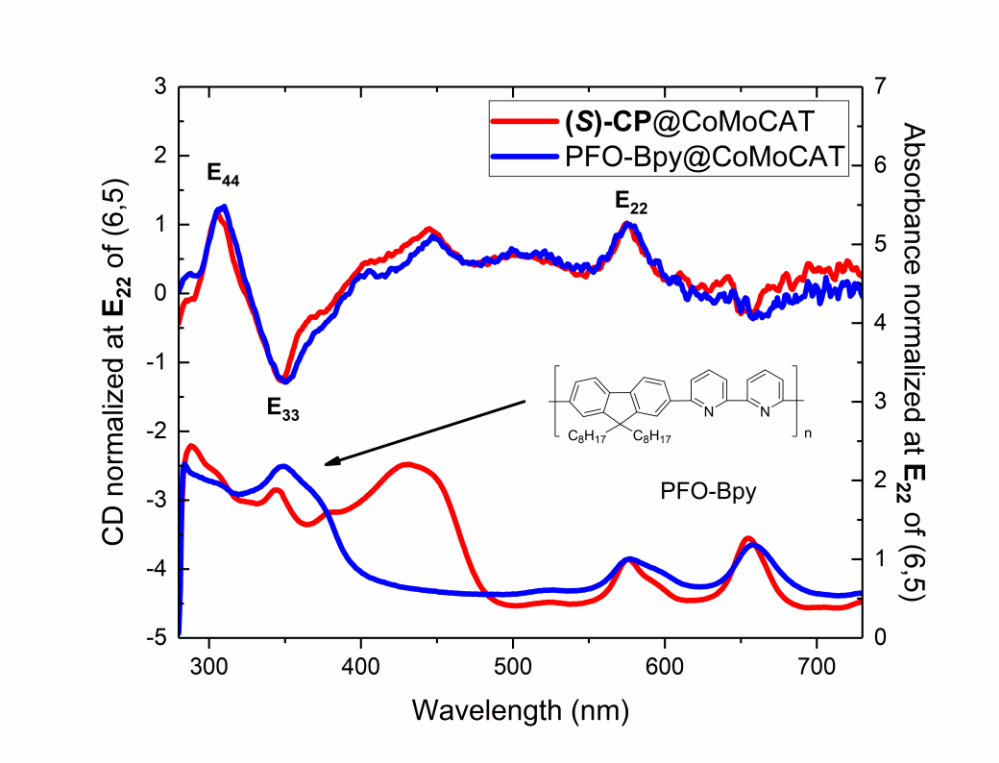

Figure 3.51. Absorption (bottom) and CD spectra (top) of chiral polymer **(*S*)-CP** dispersed and PFO-Bpy redispersed CoMoCAT SWCNTs after triggering. All the spectra were normalized at E_{22} peak of (6,5)

SWCNT. The structure of PFO-Bpy polymer is shown. All samples were measured in toluene at room temperature.

3.2.9.4 Molecular dynamics simulation

In order to understand the origin of the wrapping selectivity towards handedness sorting of SWCNTs observed in the experiments, molecular mechanics simulations were performed. Because the full conformational relaxation of the polymer around the SWCNT is a very slow process, low-energy conformations of the twisted polymer using Monte Carlo (MC) simulations were first computed. Statistical fluctuations in the MC simulations automatically generate conformations with two wrapping directions, i.e. clockwise (+) and anticlockwise (-). For each polymer-CNT complex, two wrapping directions have been considered as the initial conformations for MD simulation. These conformations were then relaxed in molecular dynamic (MD) simulations modelling **(*R*)-CP**-*M*-(6,5) and **(*S*)-CP**-*M*-(6,5) complexes. Structures extracted from the last 1 ns of MD simulations for four different systems are shown in Figure 3.52.

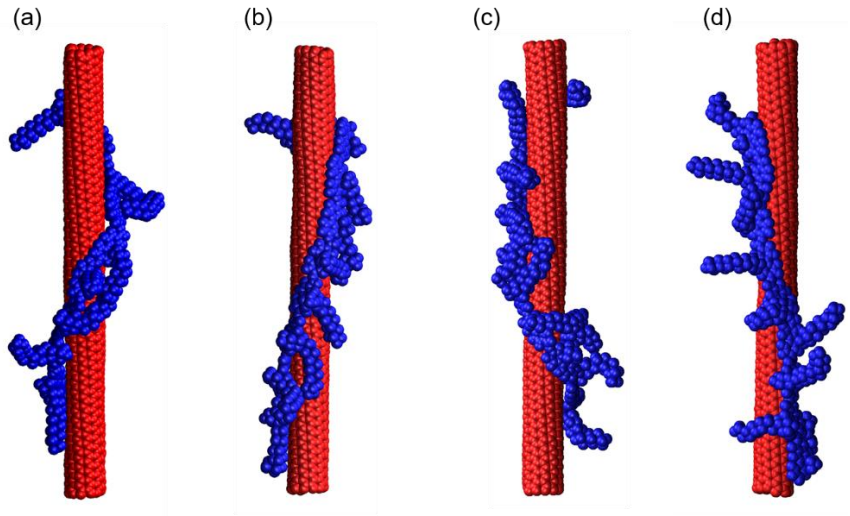

Figure 3.52. Structures extracted from MD simulation (solvent molecules are hidden) for (a) **(*R*)-CP**-*M*-(6,5) clockwise wrapped, (b) **(*S*)-CP**-*M*-(6,5) clockwise wrapped, (c) **(*R*)-CP**-*M*-(6,5) anticlockwise wrapped, (d) **(*S*)-CP**-*M*-(6,5) anticlockwise wrapped.

The binding energy (E_{bind}) of the wrapped SWCNT was calculated by the equation: $E_{bind} = E_{poly-CNT-sol} - E_{poly-sol} - E_{CNT-sol} - E_{poly} - E_{CNT} - E_{sol}$, where $E_{poly\text{-}CNT\text{-}sol}$ is the total energy, $E_{poly\text{-}sol}$ is the interaction energy between polymer and solvent, $E_{CNT\text{-}sol}$ is the interaction

energy between SWCNT and solvent. E_{poly}, E_{CNT}, and E_{sol} are the energies of free polymer, SWCNT, and solvent, respectively. The calculated potential energies are summarized in Table 3.3.

Table 3.3. Binding energies (E_{bind}) and contributions of π-π stacking interactions ($E_{\pi-\pi}$) for each enantiomeric complex with polymer wrapping direction clockwise (+) or anticlockwise (-). All energies are averaged from the last 2 ns of MD simulations and are reported in kcal/mol.

Complex	$E_{bind\ (+)}$	$E_{\pi-\pi\ (+)}$	$E_{bind\ (-)}$	$E_{\pi-\pi\ (-)}$
(*R*)-CP-*M*-(6,5)	51	-125	105	-68
(*R*)-CP-*P*-(6,5)	-386	-494	-165	-311
(*S*)-CP-*M*-(6,5)	-165	-311	-386	-494
(*S*)-CP-*P*-(6,5)	105	-68	51	-125

More favorable binding energies were found for the **(*R*)-CP**-*P*-(6,5) and **(*S*)-CP**-*M*-(6,5) complexes compared to the **(*S*)-CP**-*P*-(6,5) and **(*R*)-CP**-*M*-(6,5) complexes in both cases where the polymer wraps SWCNT in the clockwise (+) or anticlockwise (-) directions. These results are in full agreement with the previous experimental CD results, where **(*R*)-CP** polymer preferentially extracts right-handed (*P*)-SWCNTs and **(*S*)-CP** polymer preferentially extracts left-handed (*M*)-SWCNTs.

Since it is expected that the binding energy for such systems is influenced by specific non-covalent interaction of the polymer and SWCNT,[132] the contributions of the π-π stacking interaction to the binding energies are also reported for each complex in Table 3.3. The calculated $E_{\pi-\pi}$ indicates that the increased tendency for **(*R*)-CP** (or **(*S*)-CP**) to wrap around *P*-(6,5) (or *M*-(6,5)) SWCNT originates from an increased π-π interaction between polymer and SWCNT, which is made possible by the favorable geometry of the polymer aromatic rings to interact with the SWCNT surface. Furthermore, free energy calculations show that **(*S*)-CP** interacts more favorably with *M*-(6,5) SWCNT in the anticlockwise direction (-) than in the clockwise (+) direction (Table 3.3 & Figure 3.52d). In this case, the backbone of **(*S*)-CP** lies along the vector line of *M*-(6,5) SWCNT, thus maximizing the contacts as well as the π-π interactions between the polymer and SWCNT aromatic rings, while the long side chains stretch into the solvent thus reducing the steric effects, as shown in Figure 3.52(d). Hence, it can be concluded that maximizing the π-π stacking non-bonded interactions along with minimizing the steric effects of the long side chains

are the driving force for the selective interaction between chiral polymers and SWCNT enantiomers.

Owing to the all-(*R*) or all-(*S*) configuration of the chiral polymers, the obtained binding energy difference between **(*R*)-CP**-*P*-(6,5) and **(*R*)-CP**-*M*-(6,5) complexes in the clockwise direction or between **(*S*)-CP**-*M*-(6,5) and **(*S*)-CP**-*P*-(6,5) complexes in the anticlockwise direction is 437 kcal/mol. This value is significantly higher than the one calculated previously for binaphthol-fluorene based chiral copolymers supporting the tight geometry of the chiral polymer along the carbon nanotubes and thus increasing the difference between these two wrapping scenarios.[161] The assignment of positive and negative E_{22} CD peaks of (6,5) SWCNTs to the left-handed (*M*) and right-handed (*P*) enantiomers is therefore also strongly supported by these calculations.

3.2.10 Conclusions of handedness sorting

In conclusion, one pair of novel acid cleavable chiral homo-polyfluorenes were designed and synthesized for handedness sorting of semiconducting SWCNTs. Chiral center on the monomeric fluorene backbone was created by introducing two different alkyl chains to the sp^3 carbon in the position 9 and two interlinkable groups to the 2- and 7-positions, namely aldehyde and Boc-protected amino group. The racemic monomers were separated by chiral flash chromatography and their absolute configurations were identified by 2D-NMR experiments, giving enantiomerically pure **(*R*)-M3** and **(*S*)-M3** monomers. The optical activity of the enantiomeric monomers was confirmed by CD spectroscopy and the obtained spectra were supported by theoretically calculated CD spectra. *In situ* polymerization of the monomers after removal of the Boc-protecting group afforded the corresponding imine based chiral polymers **(*R*)-CP** and **(*S*)-CP** with high molecular weights. CD measurements confirmed the optical activity of the polymers and their depolymerization was studied by absorption spectroscopy to prove that the chiral polymers can be readily cleaved upon acid triggering and find the best cleavage conditions. The recognition ability of the chiral polymer **(*R*)-CP** and **(*S*)-CP** towards SWCNT enantiomers was firstly investigated with pre-sorted HiPco and PLV SWCNTs, as well with pre-sorted enriched (6,5) SWCNTs. Our results showed that the designed chiral polymers can successfully disperse nanotube enantiomers as giving the symmetric peaks and opposite signs in CD spectra. However, the obtained CD spectra were not complete and the optical purities of such nanotube enantiomers were low. Further studies were carried out with the raw CoMoCAT SWCNTs (SG65i) with which fabulous results were achieved. Each chiral polymer selectively extracts either left-handed or right-handed (6,5), (7,5), and (7,6) s-SWCNTs in one-pot from commercially available CoMoCAT SWCNTs with high enantiomeric excess according to its respective preference. In the experimental CD spectra, all four typical E_{11}, E_{22}, E_{33}, and E_{44} transitions of polymer wrapped optically enriched (6,5) SWCNT enantiomers are clearly observed, while the E_{22} CD signals of (7,5) and (7,6) SWCNTs have opposite signs and cancel each other due to the different type of SWCNT index. Quantitative removal of the chiral polymer was achieved by an acid treatment and the released nanotubes can be easily rewrapped with a non-chiral polymer. Results obtained from all-atom MD simulations are in good qualitative agreement with the experimental observations, indicating that **(*R*)-CP** polymer tends to wrap around the right-handed (*P*)-(6,5) SWCNT in the clockwise direction while **(*S*)-CP** polymer tends to wrap around the left-handed (*M*)-(6,5) SWCNT in the

anticlockwise direction. This approach to sort enantiomerically pure polymer-free s-SWCNTs is beneficial in terms of low cost, high selectivity and high purity of sorted nanotubes. Consequently, it provides for easier access to handedness-selected SWCNTs with better electronic properties for future electronic applications.

4 General conclusions and outlooks

This thesis has been focused on the design, synthesis, and performance of the fluorene-based polymers for SWCNTs sorting according to their electronic type and handedness. In Chapter 1, the unique electronic structure and interesting optical properties of SWCNTs were first described and followed by the production methods of SWCNTs and their applications to build electronic devices. For sorting of as-produced SWCNTs according to their electronic type, chiral index, and handedness, various approaches have been developed over the last two decades, as described in Chapter 1.8. Among those, polymer wrapping has been proved to be one of the most promising method due to their high selectivity, tunable structure and simple processability. In particular, fluorene-based polymers have been intensively studied and used for SWCNT sorting. By altering the backbone structure, fluorene-based polymers have achieved the enrichment of s-SWCNTs with high purity, the single-chirality enrichment, and even the handedness separation of SWCNTs. Recently, imine-based polymers which can be easily removed after the sorting process have been reported and provide a promising approach for isolation of dispersant-free s-SWCNTs. Under this background, we designed and synthesized an acid cleavable fluorene-carbazole copolymer for highly selective dispersion of s-SWCNT with a wide range of chiral index. Furthermore, to reach the summit of SWCNT sorting, we designed and synthesized one pair of cleavable chiral polyfluorenes for enantiomeric separation of s-SWCNTs.

In Chapter 3.1, the synthesis and performance of the fluorene-carbazole copolymer **P1** was discussed. The combination of carbazole and fluorene units for the construction of desired copolymer was chosen based on our preliminary work. The monomer **M1** and **M2** (Figure 4.1) were both synthesized in two steps and polymerized *via* an acid catalyzed polycondensation reaction which is highly reproducible and scalable up to 2 g. Characterization of the obtained copolymer **P1** confirmed the alternating backbone structure and its high molecular weight. The cleavable feature of this imine-based copolymer was investigated by absorption spectroscopy upon the addition of TFA. The performance of the copolymer **P1** was first tested with as-produced HiPco SWCNTs, showing that **P1** can selectively disperse s-SWCNT with high purity and more importantly with a wide range of chiral indices. Similar results were obtained with the raw PLV SWCNTs, showing that the sorting ability of copolymer **P1** can be extended to large diameter nanotubes. In both cases, the wrapping polymer can be easily removed from the nanotube sidewall

by the addition of catalytic amount of acid (1% v/v of 90% TFA). The released dispersant-free s-SWCNTs can be further quantitatively rewrapped with **P1** and standard PFO polymer, showing their potential application as starting material for various purposes, such as chirality enrichment.

For future work, field-effect transistor (FET) devices and thin-film transistors (TFT) could be build based on the copolymer **P1** sorted s-SWCNT to quantitatively determine the purity in terms of electronic type, as well to characterize the performance of the nanotubes before and after the removal of the polymer by electrical measurements.

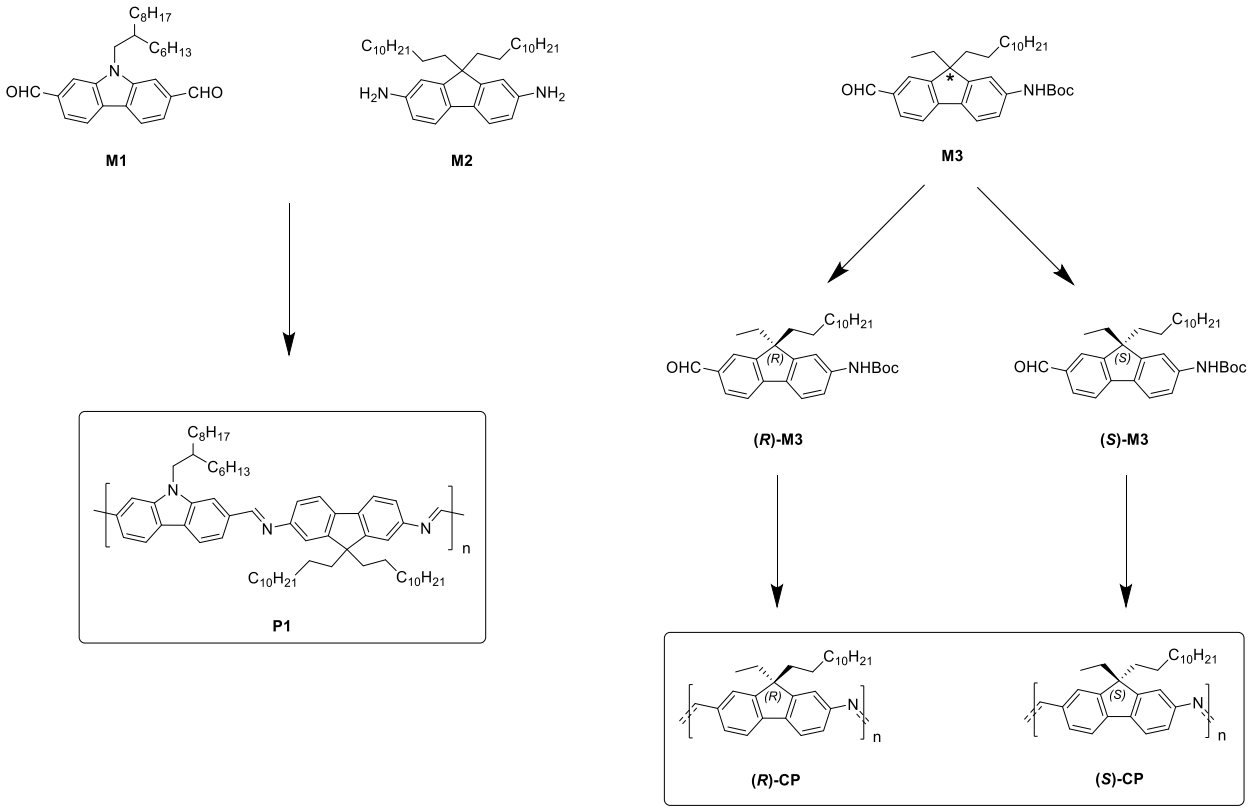

Figure 4.1. Structures of the synthesized monomers and polymers in this work.

In Chapter 3.2, the design and synthesis of the acid cleavable chiral polyfluorenes were presented, followed by the study of their performance for handedness sorting of SWCNTs. By introducing two different alkyl chains to the sp^3 carbon in the position 9 and two interlinkable functional groups to the 2- and 7-position, a chiral center was created on the monomeric fluorene backbone (Figure 4.1). Chiral flash chromatography of the racemic monomer **M3** provides enantiomerically pure monomers with unknown absolute configuration, which were later identified by Mosher's ester method with the help of 2D-NMR experiments. The separated

enantiomeric monomers **(*R*)-M3** and **(*S*)-M3** were polymerized *in situ* directly after the removal of the Boc protecting group to afford one pair of chiral polyfluorenes with all-(*R*) and all-(*S*) configuration, respectively. Both chiral monomers and polymers were characterized by CD spectroscopy, confirming their optical activity. The cleavable feature of the chiral polyfluorenes were observed by absorption spectroscopy upon acid triggering. The obtained chiral polymer **(*R*)-CP** and **(*S*)-CP** were firstly investigated with pre-sorted HiPco and PLV SWCNTs for their handedness recognition ability, showing the CD spectra with broad peaks and opposite signs. However, due to the diversity of the chiral index within the samples, the spectra are difficult to interpret. Further investigation was carried out with pre-sorted enriched (6,5) SWCNTs, which showed symmetric and alternating E_{44} and E_{33} transition peaks but not E_{22} transition peak. The reason for this abnormality in the CD spectrum is still under investigation. Excellent results were obtained from the raw CoMoCAT (SG65i) SWCNTs. Each chiral polymer selectively extracts either left-handed or right-handed (6,5), (7,5), and (7,6) SWCNTs in one-pot according to its preference. In the CD spectra, all four typical E_{11}, E_{22}, E_{33}, and E_{44} transitions of (6,5) SWCNT were observed from the polymer wrapped sample, while the E_{22} CD signal of type 2 (7,5) SWCNT and type 1 (7,6) SWCNT cancel each other due to opposite signs. Based on the signals from the (6,5) SWCNTs in the samples, the enantiomeric purity was estimated to be 66% for both samples. Exchange of the wrapping polymer from chiral polyfluorene to a non-chiral polymer was achieved by acid triggering and subsequent rewrapping process, showing that the CD signals are intrinsic to the nanotube enantiomers. The observed experimental results were fully supported by the MD simulations, indicating that **(*R*)-CP** polymer prefers to wrap around the right-handed (*P*)-(6,5) SWCNT in the clockwise direction while **(*S*)-CP** polymer prefers to wrap around the left-handed (*M*)-(6,5) SWCNT in the anticlockwise direction. The handedness separated s-SWCNTs are expected to have wide applications for future electronic devices.

For future work, the chiral polymers need to be synthesized in a larger scale so that the handedness sorting procedure can be further modified and the enantiomeric purity could be improved. Moreover, the handedness sorted samples should be purified by SEC in order to remove all carbon and catalyst impurities. Further characterization of the handedness separated nanotubes can be carried out with HRTEM, which might provide direct evidence and imaging of the handedness sorted SWCNTs.

5 Experimental part

5.1 General remarks

5.1.1 Reagents and solvents

All starting materials and reagents were purchased from commercial suppliers (*Alfa Aesar* (Karlsruhe, Germany), *Sigma-Aldrich* (Schnelldorf, Germany), *TCI Chemicals* Europe (Zwijndrecht, Belgium), *Merck* (Darmstadt, Germany) and used without further purification. Solvents utilized for crystallization, chromatography and extraction were used in technical grade. Anhydrous tetrahydrofuran, toluene and dichloromethane were taken from MBraun Solvent Purification System equipped with drying columns. HPLC grade toluene (99.7% min.) was purchased from *Alfa Aesar*. Trimethylamine was dried and distilled from CaH_2 under argon atmosphere. TLC was performed on silica gel 60 F_{254} plates, spots were detected by fluorescence quenching under UV light at 254 nm and 366 nm. Column chromatography was performed on silica gel 60 (particle size 0.040-0.063 mm). Size exclusion chromatography of the copolymer was performed on glass column or pipette with Bio-Beads™ S-X1 (styrene divinylbenzene beads, 400-14000 MW range, BIO RAD) and Toyopearl® HW-75 (hydroxylated methacrylic polymer, 100-10000 kDa MW range, TOSOH).

5.1.2 SWCNTs and standard polymers

HiPco® SWCNTs were purchased from NanoIntegris. The raw material was used directly without purification or modification.

PLV SWCNTs were prepared by pulsed laser vaporization of carbon targets doped with 1 atom % Ni and Co catalyst in 0.5 bar argon atmosphere flowing at ~ 80 sccm through an oven operated at 1050 °C.[193]

CoMoCAT® SWCNTs were purchased from CHASM Advanced Materials (LOT# SG65i-L64). The raw material was used directly without purification or modification.

PFO polymer was purchased from Sigma Aldrich (Lot# MKBP2103V).

PFO-Bpy polymer was purchased from American Dye Source, Inc. (ADS153UV, Lot# 15L007A1).

5.1.3 Instrumentation

^{1}H-Nuclear Magnetic Resonance (^{1}H NMR)

^{1}H NMR spectra were recorded on a Bruker Avance 500 spectrometer at room temperature in $CDCl_3$. ^{1}H NMR (500 MHz) spectra were referred to the solvent residual proton signal ($CDCl_3$, δ_H = 7.26 ppm). The coupling constants (^{n}J) are cited in Hertz (Hz) with superscript n indicating the bond distance. The spin multiplicities are specified as: s = singlet, d = doublet, t = triplet, q = quartet, ds = doublet of singlet, dd = doublet of doublet, m = multiplet.

The NMR experiments for Mosher analysis were performed on a Bruker Avance III NMR spectrometer operating at 600.13 MHz proton frequency. The instrument was equipped with an indirect 5-mm BBFO probe with self-shielded z-gradient. The experiments were performed at 298 K and the temperature was calibrated using a methanol standard showing accuracy within +/- 0.2 K. For the COSY spectra, 2k data points were acquired in the direct and 512 increments with 4 scans in the indirect dimension, resulting in acquisition times of 155 ms and 39 ms respectively and total experiment times were 45 min. NOESY experiments were performed with 2k/1k data points in F2/F1 using 24 scans and acquisition times of 155 ms and 78 ms, resulting in total experiment times of 18.5 hours. The sensitivity enhanced HSQC as well as the HMBC experiment were recorded with 2k/1k data points and 155 /17 ms acquisition times in F2/F1 using 2 scans for the HSQC and 16 for the HMBC. Total experiment times were 41 min and 168 min respectively. All spectra were processed with shifted square sine apodization and zero-filling by a factor of 2 using the topspin 3.5 software package (Bruker, Fällanden 2017).

^{13}C-Nuclear Magnetic Resonance (^{13}C NMR)

^{13}C NMR spectra were recorded on a Bruker Avance 500 spectrometer at room temperature in $CDCl_3$. ^{13}C NMR (125 MHz) with total decoupling of protons were referred to the solvent

($CDCl_3$, δ_C = 77.16 ppm). For correct assignment of both ^1H and ^{13}C NMR spectra, ^1H-^1H COSY, ^{13}C DEPT-135, HSQC, HMBC experiments were performed.

Mass Spectroscopy (MS)

EI MS spectra were recorded with a Thermo Trace 1300-ISQ GC/MS instrument (samples were dissolved in dichloromethane or introduced directly using direct injection probes DIP, DEP) and *m/z* values are given along with their relative intensities (%) at an ionizing voltage of 70 eV. Matrix-assisted Laser Desorption Ionization Time of Flight (MALDI-TOF) mass spectra were recorded with a MALDI-TOF Synapt G2–S High Definition mass spectrometer.

Fourier Transfer Infrared Spectrometry (FT-IR)

IR spectra were either measured with a Perkin Elmer GX spectrometer in KBr pellets or with a Nicolet iS50FT-IR spectrometer under ATP mode. Analytical samples were dried at 40-100 °C under reduced pressure (10^{-2} mbar). The bands intensity is indicated as w = weak, m = medium, s = strong or br = broad.

Elemental Analysis (EA)

Elemental analyses were obtained with a *Vario MicroCube CHNS* analyzer and measured by Mrs. Milena Staub. The values are expressed in mass percentage.

Melting Point

Melting points were measured with a Büchi Melting point M-560 apparatus and are uncorrected.

Ultraviolet-Visible-Near Infrared Spectroscopy (UV-Vis-NIR)

UV-Vis-NIR absorption spectra were recorded with a Varian Cary 500 Scan spectrophotometer in a 1 cm quartz cell at ambient temperature (excitation coefficient ε is given in units of L mol^{-1} cm^{-1}).

Chiral Flash Chromatography

Chiral separation was performed with a chiral flash chromatography from SHIMADZU LC-20AT HPLC, which was equipped with CHIRALPAK® IB N-5 HPLC column (*n*-heptane:IPA = 96:4) and a UV-Vis detector. The flow rate was set as 45 mL/min.

Gel-Permeations Chromatography (GPC)

GPC results were obtained with Agilent HPLC system equipped with two PLgel GPC/SEC columns (5 μm, 300 × 7.5 mm) and polystyrene as standard. All samples were measured with a concentration ~ 1 mg/mL in THF at room temperature.

Circular Dichroism Chromatography (CD)

The CD spectra were recorded on a JASCO J-1500 CD spectrometer with a PMT detector and a Xe lamp as light source for UV-Vis region. For NIR region, an InGaAs detector and a halogen lamp as light source were used. All the CD spectra were acquired with 2s digital integration time and 4 nm bandwidth at room temperature. Quartz cuvettes with path length of 1 mm were used for the monomers and polymers, while the nanotube containing samples were measured with quartz cuvettes with path length of 1 cm.

Photoluminescence Emission Spectroscopy (PLE)

The PLE maps were measured in the emission range of 934-1700 nm and excitation range of 500-950 nm (scanned in 3 nm steps) using a modified FTIR spectrometer (Bruker IFS66) equipped with a liquid-nitrogen-cooled Ge photodiode and a monochromatized excitation light source.[35]

Raman Spectroscopy

Raman spectra were obtained with Renishaw inVia Raman microscopes (532 nm, 785 nm) and Witec CRM200 (633 nm) from SWCNTs samples in toluene which were dropped on a glass wafer (2 × 2 cm) and dried with a nitrogen flow.

Atomic Force Microscopy (AFM)

AFM measurements were performed in air with a multimode head and Nanoscope III controller (Digital Instruments), operating in tapping mode. Commercially available silicon cantilevers with fundamental frequency of 320 kHz were used. 10 × 10 μm or 5 × 5 μm topographic (height) and amplitude images were collected simultaneously at a scan rate of 1 Hz with the parameters set point, amplitude, and feedback control optimized for each sample. AFM samples were prepared by dropping 0.5 μL of polymer wrapped SWCNT solution onto a ~ 1 cm^2 silicon wafer and spin coating at 4000 rpm for 1 min.

X-ray Photoelectron Spectroscopy (XPS)

X-ray photoelectron spectra (XPS) were measured with a custom-built spectrometer with a base pressure of 1.9×10^{-9} mbar.[194] X-rays are generated by using SPECS, XR50 X-ray source equipped with a Al and Mg Anode, providing non-monochromatized radiation. The generated photoelectrons are energy analyzed by a SPECS Phoibos Hemispherical Energy Analyzer 150. Toluene solutions of the nanotube samples were drop casted onto gold-coated Si (100) wafers (typically 10×10 mm) with 5 nm Ti and 200 nm Au (Georg-Albert-PVD, Germany) and all volatiles were evaporated in vacuum prior to XPS analysis.

Transmission Electron Microscopy (TEM)

The TEM specimens were examined with two transmission electron microscopes. One is a FEI Titan 80-300 electron microscope equipped with CEOS image spherical aberration corrector, operating at 300 kV accelerating voltage. The electron micrographs were acquire by Gatan Ultrascan 1000 CCD camera. The other is a Philips Tecnai F20 ST microscope, operating at 200 kV accelerating voltage. The electron micrographs were acquired by Gatan Orius SC600 CCD camera. The solvent (toluene) of the nanotube samples was removed by filtration on a PTFE membrane filter (0.20 μm) and the nanotubes were washed with HPLC grade acetone. After redispersion in acetone and sonication, the nanotube samples were prepared by drop casting on copper TEM grids with holey carbon and followed by drying under vacuum.

5.2 Methods

General procedure for wrapping as-produced HiPco and PLV SWCNTs

100 mg of raw SWCNTs and 100 mg of copolymer were high-shear mixed in 100 mL of toluene for 1.5 h and subsequently sonicated using a titanium sonotrode (Bandelin, ~20% power) for 4 h. During sonication, the suspension was placed in a water-circulation bath for continuous cooling. After sonication, the suspension was then centrifuged for 1.5 h at 20000g and the supernatant was filtered and collected. The same procedure was repeated several times with the same filter cake and all the supernatants were combined. To generate the starting dispersion for purification by SEC the supernatants were concentrated by evaporating 80% of toluene. The SEC purification was performed in a glass column (40 mm ×200 mm) filled with Toyopearl HW-75F resin. After applying 5 mL of SWCNT starting dispersion to the column, the sample passed through the gel by gravitational force with a flow rate of ~ 4 mL/min with toluene as eluent. Raman spectra at 785 nm excitation were obtained directly at the outlet of the glass column with a Kaiser Optical Holospec spectrograph which comprises a fiber optic probe head incorporating both excitation laser aperture and collection optics. Sample fractions were collected in ~ 5 mL portions. The early fractions were without excess polymer and were used for the characterization.

General procedure for wrapping as-produced CoMoCAT SWCNTs

0.5 mg of CoMoCAT SWCNTs and 1.5 mg of chiral polymer were dispersed in 5 mL of toluene under bath sonication for 6 h. The temperature during the sonication was kept around 15 °C. The suspension was then centrifuged at 17920 RCF for 1 h and the upper solution was collected and further centrifuged at 112000 RCF for 3 h. The precipitate was redispersed, sonicated, and centrifuged again to remove excess polymer in toluene. The resulted sample was dispersed in 1 mL of toluene for the characterization.

General procedure for triggering of the polymer wrapped SWCNTs

To a polymer wrapped sample in toluene, a small amount of trifluoroacetic acid (1% v/v of 90% TFA) was added. The mixture was sonicated for 10 min and subsequently diluted with acetone to yield the precipitate of naked nanotubes. The sample was filtrated and copiously washed on a PTFE membrane filter (0.20 μm) with acetone and toluene. The released nanotubes were dried in air and then re-dispersed in toluene to form aggregates.

General procedure for rewrapping the released SWCNTs

0.1 mg of released SWCNTs and 1 mg of polymer were dispersed in 5 mL of toluene under bath sonication for 8 h. The temperature during the sonication was kept around 15 °C. The suspension was then centrifuged at 17920 RCF for 1 h and the upper solution was collected and further centrifuged at 112000 RCF for 3 h. The precipitate was redispersed, sonicated, and centrifuged again to remove excess polymer in toluene. The resulted sample was dispersed in 1 mL of toluene for the characterization.

Computational method

A fully atomistic molecular model was utilized in the simulations, which treats all atoms and solvent explicitly. (6,5) SWCNTs of 11 nm length were generated as model SWCNTs using VMD[195] and the unsaturated boundary effect was avoided by adding hydrogen atoms at the ends of the tubes. A trimer structure of the polymer optimized using the B3-LYP exchange correlation functional and the def2-SV(P) basis set using Turbomole,[196] were used to generate a polymer of 10 repeating units using ambertools.[197] Monte Carlo sampling was performed to obtain the lowest energy configuration of the polymer using SIMONA,[198] where the torsions of the molecule were sampled via the backbone dihedral angles to create a helical conformation that fits around the SWCNT. To create (*R*) and (*S*) polymers, the backbone configuration from Monte Carlo calculations was kept completely the same but the side chains were substituted with different chirality.

The solvent molecules (toluene) were added to the box of size 5×5×15 nm (~29000 atoms) modeled with the experimental density 0.87 g/mL using packmol.[199] MD simulations were carried out with LAMMPS using the COMPASS force field.[200–202] After minimizing and eliminating any voids in the system, a 1 ns NPT simulation was carried out to equilibrate the system at 1 atmosphere and 300 K. These equilibration steps were followed by a 4 ns production run to collect statistical data. In the production run, the time step was 1.0 fs, structures were saved every 0.2 ps, and cubic periodic boundary conditions (PBC) were applied in all directions. Electrostatic interactions were calculated using the particle-particle particle-mesh method (pppm) with a real space cut-off of 12 Å.[203]

5.3 Synthetic procedures

2,7-Dibromo-*N*-(2-hexyl)decylcarbazole (2)

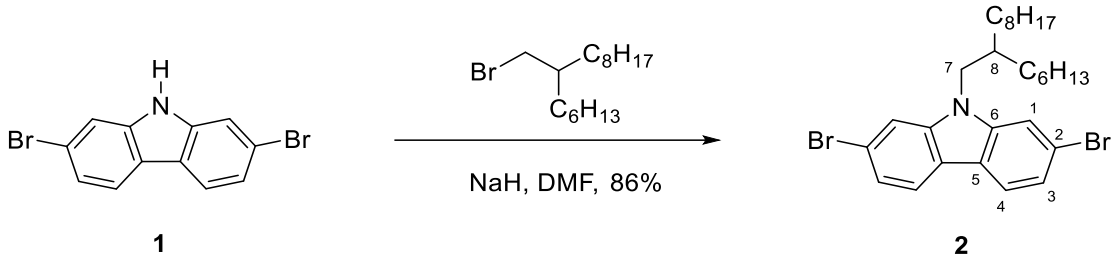

A 100 mL Schlenk-flask was charged with 2,7-dibromocarbazole **1** (1.90 g, 5.85 mmol) and anhydrous DMF (40 mL) under argon atmosphere. The solution was cooled to 0 °C in an ice-bath and NaH (340 mg, 8.50 mmol, 1.4 eq., 60% w/w in mineral oil) was added in one portion. The reaction mixture was stirred at 0 °C for 30 min with a flow of argon and another 1 h at room temperature. 2-Hexyldecylbromide (2.26 g, 7.40 mmol, 1.3 eq) was added and the reaction mixture was stirred at room temperature overnight. The reaction mixture was cooled to 0 °C and quenched with water. After extraction with DCM (3 × 80 mL) the combined organic phase was washed with NH_4Cl solution (10%, 100 mL), brine (100 mL), dried over $MgSO_4$ and passed through a silica plug. All solvents were removed under reduced pressure and the residue was purified by column chromatography (hexane). 2.75 g (86%) of a colorless sticky oil was obtained as the desired compound **2** (R_f = 0.31, hexane). ^{1}H NMR ($CDCl_3$, 500 MHz): δ ppm = 7.88 (d, $^3J_{H\text{-}H}$ = 8.2 Hz, 2H, H-4), 7.50 (ds, $^4J_{H\text{-}H}$ = 1.5 Hz, 2H, H-1), 7.33 (dd, $^3J_{H\text{-}H}$ = 8.2 Hz, $^4J_{H\text{-}H}$ = 1.5 Hz, 2H, H-3), 4.04 (d, $^3J_{H\text{-}H}$ = 7.5 Hz, 2H, H-7), 2.07 (m, 1H, H-8), 1.41-1.14 (m, 24H, CH_2), 0.87 (m, 6H, CH_3); ^{13}C NMR ($CDCl_3$, 125 MHz): δ ppm = 142.0 (C-6), 122.6 (C-3), 121.5 (C-4), 121.4 (C-5), 119.8 (C-2), 112.4 (C-1), 48.0 (C-7), 37.7 (C-8), 32.0 (CH_2), 31.9 (CH_2), 31.8 (2CH_2), 30.0 (CH_2), 29.7 (CH_2), 29.6 (CH_2), 29.4 (CH_2), 26.52 (CH_2), 26.50 (CH_2), 22.80 (CH_2), 22.77 (CH_2), 14.26 (CH_3), 14.23 (CH_3); IR (υ/cm^{-1}, KBr): 3060 (vw, υ(=CH)), 2933 (vs, υ_{as}(CH_2, CH_3)), 2854 (vs, υ_s(CH_2, CH_3)), 1585 (m, υ(C=C)), 1450 (m, υ(C=C)), 1425 (m), 1326 (w), 1055 (w), 835 (w), 790 (m, υ(=CH)); UV-Vis (λ_{max}[nm], ε, toluene) 308 (25288); MALDI-TOF MS (+) calcd. for $C_{28}H_{39}Br_2N$ (M^+, 549.14); Found: 549.10; Elemental Analysis Calcd. (%) for $C_{28}H_{39}Br_2N$ (549.44): C 61.21, H 7.15, N 2.55; Found: C 61.65, H 7.07, N 2.53.

2,7-Diformyl-*N*-(2-hexyl)decylcarbazole (M1)

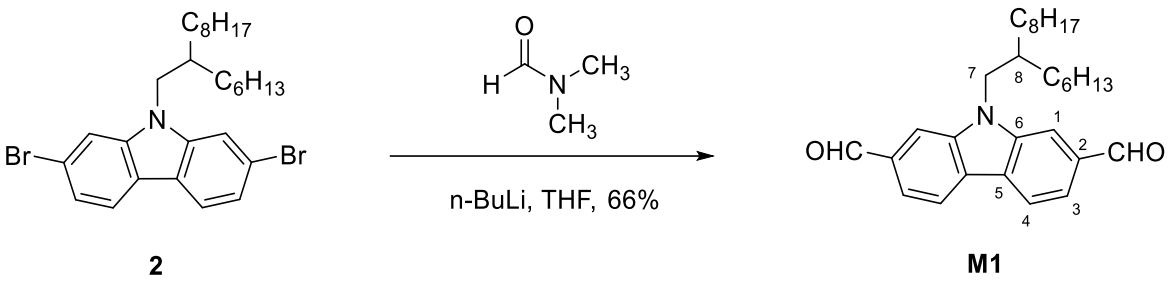

2 **M1**

A 100 mL Schlenk-flask was charged with 2,7-dibromo-*N*-(2-hexyl)decylcarbazole **2** (2.36 g, 4.30 mmol) and anhydrous THF (40 mL) under an argon atmosphere. The solution was cooled to -78 °C and *n*BuLi (1.6 M in hexane, 5.90 mL, 9.45 mmol, 2.2 eq.) was added dropwise over 20 min. The reaction mixture was stirred at -78 °C for 1 h and a solution of anhydrous DMF (2.0 mL, 26.00 mmol, 6.0 eq.) in THF (3 mL) was added dropwise. The light yellow suspension was stirred at -78 °C for 1 h and slowly brought to room temperature overnight. The reaction mixture was quenched with aqueous HCl (1M, 40 mL) and extracted with Et_2O (3 × 50 mL). The combined organic phase was washed with water (2 × 50 mL) and brine (100 mL), dried over $MgSO_4$ and passed through a silica plug. The solvent was removed under reduced pressure and the residue was purified by column chromatography (hexane/EtOAc, 10/1). 1.27 g (66%) of a yellow solid was obtained as the title compound **M1** (R_f = 0.28, hexane/EtOAc, 10/1) ^{1}H NMR ($CDCl_3$, 500 MHz): δ ppm = 10.19 (s, 2H, CHO), 8.28 (d, $^3J_{H\text{-}H}$ = 8.1 Hz, 2H, H-4), 7.98 (s, 2H, H-1), 7.80 (dd, $^3J_{H\text{-}H}$ = 8.1 Hz, $^4J_{H\text{-}H}$ = 1.1 Hz, 2H, H-3), 4.30 (d, $^3J_{H\text{-}H}$ = 7.7 Hz, 2H, H-7), 2.18 (m, 1H, H-8), 1.41-1.18 (m, 24H, CH_2), 0.84 (m, 6H, CH_3); ^{13}C NMR ($CDCl_3$, 125 MHz): δ ppm = 192.5 (CHO), 142.3 (C-6), 135.3 (C-2), 127.0 (C-5), 121.9 (C-4), 121.4 (C-3), 110.9 (C-1), 48.4 (C-7), 38.1 (C-8), 31.95 (CH_2), 31.93 ($2CH_2$), 31.84 (CH_2), 30.0 (CH_2), 29.7 (CH_2), 29.6 (CH_2), 29.3 (CH_2), 26.6 (CH_2), 26.5 (CH_2), 22.76 (CH_2), 22.71 (CH_2), 14.23 (CH_3), 14.18 (CH_3); IR (υ/cm^{-1}, KBr): 3052 (vw, υ(=CH)), 2925 (vs, υ_{as}(CH_2, CH_3)), 2855 (vs, υ_s(CH_2, CH_3)), 2715 (vw, CHO), 1683 (vs, υ(C=O)), 1563 (m, υ(C=C)), 1470 (m, υ(C=C)), 1329 (m), 1232 (m), 1150 (m) 800 (m, υ(=CH)); M.p.: 73.4 °C; UV-Vis (λ_{max}[nm], ε, toluene) 339 (36751); MALDI-TOF MS (+) calcd. for $C_{30}H_{41}NO_2$ (M^+, 447.31); Found: 447.29; Elemental Analysis Calcd. (%) for $C_{30}H_{41}NO_2$ (447.66): C 80.49, H 9.23, N 3.13; Found: C 80.61, H 8.93, N 3.11.

***N*,*N*-Bis(diphenylmethylene)-9,9-didodectyl-9*H*-fluorene-2,7-diamine (4)**

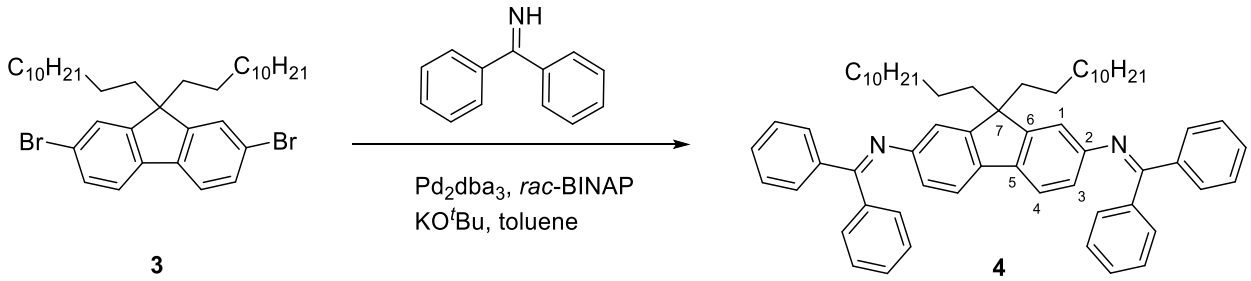

3 **4**

A 250 mL Schlenk-flask was charged with 2,7-dibromo-9,9-didodecylfluorene **3** (6.00 g, 9.08 mmol), benzophenone imine (3.7 mL, 22.05 mmol, 2.4 eq.), KO^{t}Bu (3.06 g, 27.25 mmol, 3.0 eq.) and anhydrous toluene (120 mL) under an argon atmosphere. Pd_2dba_3 (207.1mg, 0.23 mmol, 2.5 mol%) and (±)-BINAP (284.7 mg, 0.46 mmol, 5.0 mol%) were added subsequently and the suspension was stirred at 100 °C overnight. The reaction mixture was diluted with DCM (250 mL) and passed through a silica plug. The solvent was removed under reduced pressure and the residue was purified by column chromatography (hexane/EtOAc, 15/1). 7.10 g of a yellow-brownish sticky oil was obtained as a mixtureof **4** and benzophenone imine and was used directly for the next step. Little amount of the mixture was further purified for the characterization of compound **4** (R_f = 0.33, hexane/EtOAc, 10/1). ^{1}H NMR ($CDCl_3$, 500 MHz): δ ppm = 7.77 (d, $^3J_{H\text{-}H}$ = 7.0 Hz, 4H), 7.48 (t, $^3J_{H\text{-}H}$ = 7.4 Hz, 2H), 7.41 (t, $^3J_{H\text{-}H}$ = 7.4 Hz, 4H), 7.38 (d, $^3J_{H\text{-}H}$ = 8.0 Hz, 2H, H-4), 7.24-7.20 (m, 6H), 7.17-7.12 (m, 4H), 6.75 (dd, $^3J_{H\text{-}H}$ = 7.9 Hz, $^4J_{H\text{-}H}$ = 1.9 Hz, 2H, H-3), 6.53 (d, $^4J_{H\text{-}H}$ = 1.9 Hz, 2H, H-1), 1.63-1.55 (m, 4H, CH_2), 1.35-0.96 (m, 36H, CH_2), 0.95-0.82 (m, 6H, CH_3), 0.34-0.23 (m, 4H, CH_2); ^{13}C NMR ($CDCl_3$, 125 MHz): δ ppm = 168.2, 151.1, 150.2, 139.9, 136.7, 136.6, 130.8, 129.7, 129.4, 128.6, 128.3, 127.9, 120.3, 119.3, 115.4, 54.9 (C-7), 41.0 (CH_2), 32.0 (CH_2), 30.4 (CH_2), 30.0 (CH_2), 29.83 (CH_2), 29.79 (CH_2), 29.7 (CH_2), 29.5 (CH_2), 23.6 (CH_2), 22.8 (CH_2), 14.3 (CH_3); IR (υ/cm^{-1}, KBr): 3057 (vw, υ(=CH)), 2923 (vs, υ_{as}(CH_2, CH_3)), 2849 (vs, υ_s(CH_2, CH_3)), 1612 (m, C=N), 1597 (m, υ(C=C)), 1572 (m, υ(C=C)), 1460 (m), 1320 (m), 1288 (m), 1251 (m), 826 (w, υ(=CH)), 696 (m, υ(=CH)); MALDI-TOF MS (+) calcd. for $C_{63}H_{76}N_2$ (M^+, 860.60); Found: 861.61.

9,9-Didodectyl-9*H*-fluorene-2,7-diamine (M2)

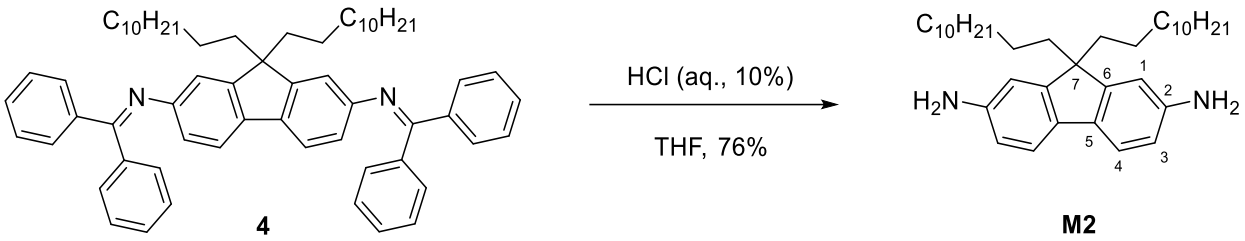

A 250 mL Schlenk-flask was charged with *N*,*N*-bis(diphenylmethylene)-9,9-didodectyl-9*H*-fluorene-2,7-diamine **4** (crude mixture, not further purified, 7.00 g) and THF (120 mL). After addition of aqueous HCl (10%, 15 mL) the solution was stirred at room temperature overnight. The reaction mixture was neutralized with NaOH solution (2M) until pH = 8 and subsequently extracted with EtOAc (2 × 150 mL). The organic phase was washed with water (2 × 150 mL) and brine (150 mL), dried over $MgSO_4$ and passed through a silica plug. The solvent was removed under reduced pressure and the residue was purified by column chromatography (hexane/EtOAc, 20/1 & 5/1, deactivated with 5% of NEt_3). 3.67 g (76% yieldin two steps) of a red-brownish sticky oil was obtained as the desired compound **M2** (R_f = 0.13, hexane/EtOAc, 20/1). ^{1}H NMR ($CDCl_3$, 500 MHz): δ ppm = 7.33 (dd, $^3J_{H\text{-}H}$ = 7.3 Hz, $^4J_{H\text{-}H}$ = 1.1 Hz, 2H, H-4), 6.62-6.60 (m, 4H, H-1, H-3), 3.65 (s, 4H, NH_2), 1.83-1.80 (m, 4H, CH_2), 1.30-0.99 (m, 36H, CH_2), 0.87 (t, $^3J_{H\text{-}H}$ = 6.9 Hz, 6H, CH_3), 0.70-0.60 (m, 4H, CH_2); ^{13}C NMR ($CDCl_3$, 125 MHz): δ ppm = 151.7 (C-6), 144.6 (C-2), 133.2 (C-5), 119.1 (C-4), 113.9 (C-3), 110.2 (C-1), 54.7 (C-7), 46.3 (CH_2), 41.0 (CH_2), 32.0 (CH_2), 30.4 (CH_2), 29.84 (CH_2), 29.75 (CH_2), 29.74 (CH_2), 29.52 (CH_2), 29.47 (CH_2), 23.9 (CH_2), 22.8 (CH_2), 14.3 (CH_3); IR (υ/cm^{-1}, KBr): 3372 (w, υ(N-H)), 3215 (w, υ(N-H)), 2922 (vs, υ_{as}(CH_2, CH_3)), 2848 (vs, υ_s(CH_2, CH_3)), 1616 (m, υ(N-H)), 1580 (w, υ(C=C)), 1472 (m, υ(C=C)), 1332 (w), 1302 (w), 1237 (w), 806 (w, υ(=CH)). UV-Vis (λ_{max}[nm], ε, toluene) 303 (27275); MALDI-TOF MS (+) calcd. for $C_{37}H_{60}N_2$ (M^+, 532.48); Found: 532.45; Elemental Analysis Calcd. (%) for $C_{37}H_{60}N_2$ (532.90): C 83.39, H 11.35, N 5.26; Found: C 83.56, H 11.07, N 5.23.

Poly(9,9-Di-*n*-dodecylfluorene-2,7-diamine)-*alt*-[*N*-(2-hexyl)decylcarbzole-2,7-dialdehyde] (P1)

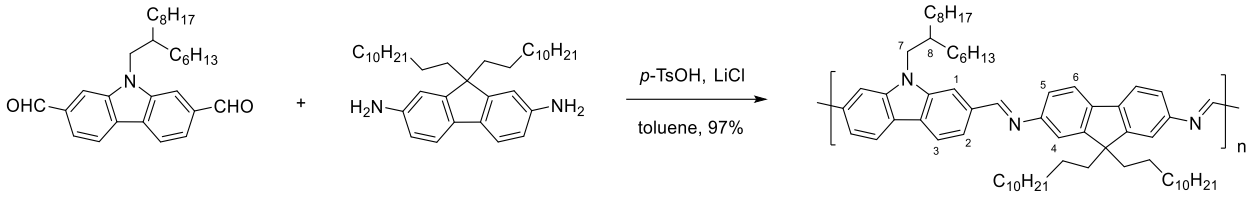

A 100 mL Schlenk-flask was charged with 2,7-diformyl-*N*-(2-hexyl)decylcarbazole **M1** (298.7 mg, 0.67 mmol), 9,9-didodectyl-9*H*-fluorene-2,7-diamine **M2** (357.3 mg, 0.67 mmol), anhydrous THF (9 mL) and toluene (27 mL) under argon atmosphere. LiCl (0.91 g, 21.47 mmol) and p-TsOH (a few crystalls) were added to the solution subsequently. The reaction mixture was stirred at 110 °C for 48 h. The resulting viscous mixture was cooled down to room temperature and precipitated in methanol. The obtained polymer was collected by filtration and washed with water, methanol and acetone. 613 mg (97%) of an orange solid was obtained as the title compound **P1**. ^{1}H NMR ($CDCl_3$, 500 MHz): δ ppm = 8.78 (s, 2H, N=CH), 8.24 (d, *J*= 8.3 Hz, 2H, H-3), 8.06 (s, 2H, H-1), 7.88 (d, *J*= 7.3 Hz, 2H, H-2), 7.76 (d, *J*= 8.3 Hz, 2H, H-6), 7.41-7.28 (m, 4H, H-4, H-5), 4.53-4.17 (m, 2H, H-7), 2.40-2.28 (m, H-8), 2.24-2.18 (m, 4H, CH_2), 1.52-0.93 (m, 60H, CH_2), 0.91-0.50 (m, CH_2, CH_3); GPC: M_n= 43 kDa, M_w= 91 kDa, Đ = 2.1. IR (υ/cm^{-1}, KBr): 3060 (vw, υ(=CH)), 2921 (vs, υ_{as}(CH_2, CH_3)), 2850 (vs, υ_s(CH_2, CH_3)), 1624 (m, υ(C=N)), 1563 (w, υ(C=C)), 1462 (w, υ(C=C)), 1338 (m), 1260 (m), 1090 (m), 804 (s, υ(=CH)). UV-Vis (λ_{max}[nm], ε, toluene) 429 (65874).

2,7-Dibromo-9-ethyl-9*H*-fluorene (6)

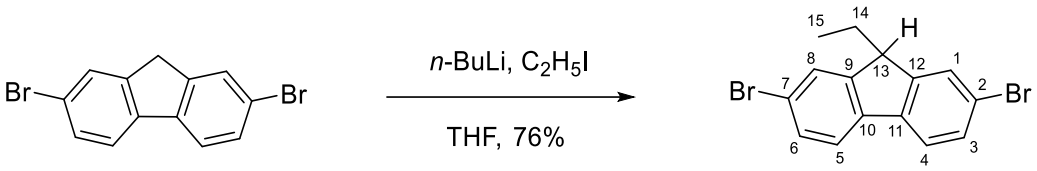

5 **6**

A 250 mL Schlenk-flask was charged with 2,7-dibromofluorene **5** (5.00 g, 15.43 mmol) and anhydrous THF (75 mL) under an argon atmosphere. The solution was cooled to -78 °C and *n*-BuLi (1.6 M in hexane, 10.1 mL, 16.20 mmol, 1.05 eq.) was added dropwise. The reaction mixture was stirred for 1 h subsequently a solution of iodoethane (2.5 mL, 30.86 mmol, 2.0 eq.) in THF (3 mL) was added. The resulting mixture was stirred at -78 °C for 1 h then warmed up to room temperature and kept stirring overnight. The dark purple solution was quenched with ice, treated with NH_4Cl solution (10%) and extracted with Et_2O. The combined organic phase was washed with brine, dried over $MgSO_4$ and passed through a silica plug. All volatiles were removed under reduced pressure and the residue was purified by column chromatography (hexane/DCM, 20/1) to yield 4.15 g (76%) of the title compound **6** as a yellowish white solid (R_f = 0.48, hexane/DCM, 10/1). ^{1}H NMR (500 MHz, $CDCl_3$): δ ppm = 7.62 (s, 2H, H-1, H-8), 7.57 (d, $^3J_{H\text{-}H}$ = 7.9 Hz, 2H, H-4, H-5), 7.49 (dd, $^3J_{H\text{-}H}$ = 7.9 Hz, $^4J_{H\text{-}H}$ = 1.5 Hz, 2H, H-3, H-6), 3.95 (t, $^3J_{H\text{-}H}$ = 5.5 Hz, 1H, H-13), 2.10-2.04 (m, 2H, H-14), 0.68 (t, $^3J_{H\text{-}H}$ = 7.4 Hz, 3H, H-15); ^{13}C NMR (125 MHz, $CDCl_3$): δ ppm = 149.0 (C-9, C-12), 139.5 (C-10, C-11), 130.4 (C-3, C-6), 127.8 (C-1, C-8), 121.3 (C-2, C-4, C-5, C-7), 48.5 (C-13), 25.5 (C-14), 9.6 (C-15); IR (ATP) ν cm^{-1}: 3058 (vw, υ(=CH)), 2958 (s, $\upsilon_{as}(CH_3)$), 2930 (s, $\upsilon_{as}(CH_2)$), 2871 (s, $\upsilon_s(CH_2, CH_3)$), 1603 (w, υ(C=C)), 1566 (w, υ(C=C)), 1451 (s), 1418 (m), 1399 (m), 1377 (m), 1163 (m), 1062 (s), 886 (m), 801 (vs, υ(=CH)), 782 (m), 770 (m); Mp = 81 °C; UV-Vis (λ_{max}[nm], ε, CH_2Cl_2) 314 (15020); EI MS m/z (%) 351.96 (5, M^+), 322.93 (4), 271.04 (3), 244.00 (3), 192.13 (56), 163.07 (20), 81.54 (9), 71.12 (5), 49.00 (7), 44.01 (100); Elemental Analysis Calcd. (%) for $C_{15}H_{12}Br_2$ (352.07): C 51.17, H 3.44; Found: C 51.35, H 3.37.

2,7-Dibromo-9-dodecyl-9-ethyl-9*H*-fluorene (7)

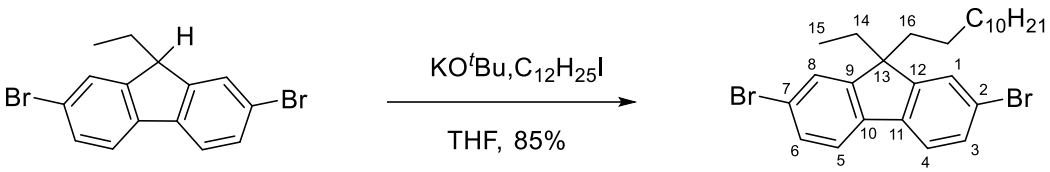

6 **7**

A 250 mL Schlenk-flask was charged with **6** (3.73 g, 10.59 mmol) and anhydrous THF (75 mL) under an argon atmosphere. The solution was cooled to 0 °C and potassium 2-methylpropan-2-olate (1.43 g, 12.71 mmol, 1.20 eq.) was added in 3 portions. The resulting red solution was kept stirring at 0 °C for 0.5 h and subsequently at room temperature for 1 h. After cooling down to 0 °C, 1-iodododecane (3.14 mL, 12.71 mmol, 1.20 eq.) was added dropwise. The dark greenish mixture was kept stirring at 0 °C for 1 h and finally at room temperature overnight. The resulting greenish-white mixture was quenched with water (75 mL) and extracted with Et_2O. The combined organic phase was washed with brine, dried over $MgSO_4$ and passed through a silica plug. The solvents were removed under reduced pressure and the residue was purified by column chromatography (hexane). After drying, 4.67 g (85%) of a colorless oil was obtained as the target compound **7** (R_f = 0.50, hexane). ^{1}H NMR (500 MHz, $CDCl_3$): δ ppm = 7.52 (d, $^3J_{H\text{-}H}$ = 8.0 Hz, 2H, H-4, H-5), 7.45 (dd, $^3J_{H\text{-}H}$ = 8.0 Hz, $^4J_{H\text{-}H}$ = 1.6 Hz, 2H, H-3, H-6), 7.44 (s, 2H, H-1, H-8), 1.98 (q, $^3J_{H\text{-}H}$ = 7.3 Hz, 2H, H-14), 1.94-1.91 (m, 2H, H-16), 1.29-1.05 (m, 18H, CH_2), 0.87 (t, $^3J_{H\text{-}H}$ = 7.3 Hz, 3H, CH_3), 0.61-0.57 (m, 2H, CH_2), 0.30 (t, $^3J_{H\text{-}H}$ = 7.3 Hz, 3H, H-15). ^{13}C NMR (125 MHz, $CDCl_3$): δ ppm = 152.3 (C-9, C-12), 139.4 (C-10, C-11), 130.3 (C-3, C-6), 126.4 (C-1, C-8), 121.6 (C-2, C-7), 121.2 (C-4, C-5), 56.3 (C-13), 40.0 (C-16), 33.1 (C-14), 32.0 (CH_2), 30.0 (CH_2), 29.7 (2CH_2), 29.7 (CH_2), 29.6 (CH_2), 29.5 (CH_2), 29.3 (CH_2), 23.9 (CH_2), 22.8 (CH_2), 14.3 (CH_3), 8.4 (C-15); IR (ATP) ν cm^{-1}: 3054 (vw, υ(=CH)), 2917 (vs, υ_{as}(CH_2, CH_3)), 2850 (vs, υ_s(CH_2, CH_3)), 1597 (w, υ(C=C)), 1570 (w, υ(C=C)), 1468 (m), 1452 (m), 1444 (m), 1416 (m), 1397 (m), 1063 (m), 1004 (m), 871 (m), 808 (s, υ(=CH)). UV-Vis (λ_{max}[nm], ε, CH_2Cl_2) 315 (20050); EI MS m/z (%) 520.13 (50, M^+), 491.09 (2), 441.22 (3), 410.19 (6), 352.94 (10), 322.91 (46), 285.06 (8), 272.03 (85), 191.11 (86), 189.09 (46), 85.12 (40), 71.10 (59), 57.08 (100). Elemental Analysis Calcd. (%) for $C_{27}H_{36}Br_2$ (520.39): C 62.32, H 6.97; Found: C 62.11, H 6.79.

2-Bromo-9-dodecyl-9-ethyl-9*H*-fluorene-2-carbonitrile (8)

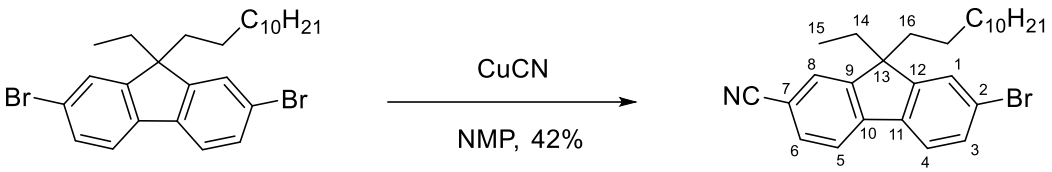

7 **8**

A 250 mL Schlenk tube was charged with **7** (6.50 g, 12.49 mmol) and NMP (60 mL) under an argon atmosphere followed by addition of CuCN (1.12 g, 12.49 mmol, 1.0 eq.) in one portion. The resulting mixture was heated up to 210 °C and kept stirring overnight. After cooling down to room temperature, NaOH solution (2M) was added to the dark brown mixture and stirred for 1 h. The brown mixture was extracted with Et_2O, washed with $EDTA^-Na^+$ solution (10%), water and brine. The organic layer was dried over $MgSO_4$ and passed through a silica plug. The solvents were removed under reduced pressure and the residue was purified by column chromatography (hexane/EtOAc, 15/1) to obtain 2.43 g (42%) of the desired compound **8** as a colorless oil (R_f = 0.28, hexane/EtOAc, 15/1). ^{1}H NMR (500 MHz, $CDCl_3$): δ ppm = 7.74 (d, $^3J_{H\text{-}H}$ = 7.9 Hz, 1H, H-5), 7.64 (dd, $^3J_{H\text{-}H}$ = 7.9 Hz, $^4J_{H\text{-}H}$ = 1.4 Hz, 1H, H-6), 7.61 (d, $^3J_{H\text{-}H}$ = 7.9 Hz, 1H, H-4), 7.59 (s, 1H, H-8), 7.51 (dd, $^3J_{H\text{-}H}$ = 7.9 Hz, $^4J_{H\text{-}H}$ = 1.7 Hz, 1H, H-3), 7.50 (s, 1H, H-1), 2.06-1.99 (m, 2H, H-14), 1.98-1.93 (m, 2H, H-16), 1.29-1.04 (m, 18H, CH_2), 0.86 (t, $^3J_{H\text{-}H}$ = 7.0 Hz, 3H, CH_3), 0.61-0.50 (m, 2H, CH_2), 0.29 (t, $^3J_{H\text{-}H}$ = 7.4 Hz, 3H, H-15); ^{13}C NMR (125 MHz, $CDCl_3$): δ ppm = 153.3 (C-12), 150.8 (C-9), 144.9 (C-10), 138.5 (C-11), 131.6 (C-6), 130.8 (C-3), 126.7 (C-8), 126.6 (C-1), 123.4 (C-2), 122.3 (C-4), 120.5 (C-5), 119.7 (CN), 110.6 (C-7), 56.5 (C-13), 39.8 (C-16), 32.9 (C-14), 32.0 (CH_2), 30.0 (CH_2), 29.7 ($2CH_2$), 29.7 (CH_2), 29.6 (CH_2), 29.5 (CH_2), 29.3 (CH_2), 23.9 (CH_2), 22.8 (CH_2), 14.3 (CH_3), 8.4 (C-15); IR (ATP) ν cm^{-1}: 3077 (vw, υ(=CH)), 2916 (vs, υ_{as}(CH_2, CH_3)), 2849 (vs, υ_{as}(CH_2, CH_3)), 2225 (s, -CN), 1610 (m, υ(C=C)), 1466 (m), 1453 (m), 1405 (m), 815 (s, υ(=CH)); UV-Vis (λ_{max}[nm], ε, CH_2Cl_2) 318 (36170); EI MS m/z (%) 467.22 (15, M^+), 438.18 (3), 386.29 (2), 310.04 (2), 297.03 (19), 268.00 (25), 232.13 (15), 217.11 (100), 203.08 (16), 190.10 (16), 151.07 (2), 99.12 (4), 85.12 (15), 71.10 (24), 57.08 (40), 44.01 (56). Elemental Analysis Calcd. (%) for $C_{28}H_{36}BrN$ (466.51): C 72.09, H 7.78, N 3.00; Found: C 72.21, H 7.60, N 2.96.

***tert*-Butyl *N*-(7-cyano-9-dodecyl-9-ethyl-9*H*-fluorene-2-yl)carbamate (9)**

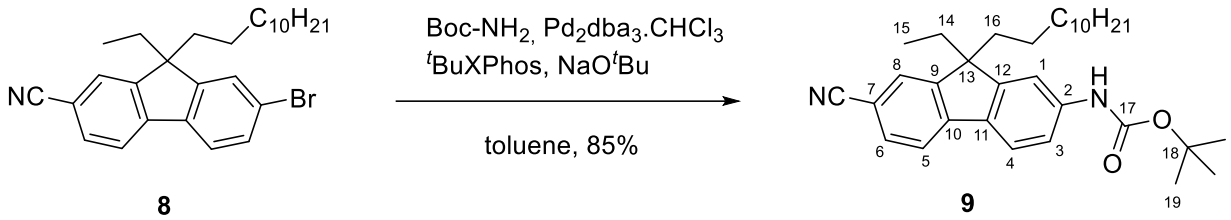

8 **9**

A 250 mL Schlenk-flask was charged with **8** (2.25 g, 4.83 mmol), *tert*-butyl carbamate (851 mg, 7.25 mmol, 1.50 eq.), sodium 2-methylpropan-2-olate (698 mg, 7.26 mmol, 1.50 eq.) and anhydrous toluene (60 mL) under an argon atmosphere. $Pd_2dba_3 \cdot CHCl_3$ (176 mg, 0.17 mmol, 3.5 mol%) and ^{t}BuXPhos (207 mg, 0.49 mmol, 10.0 mol%) were added subsequently and the suspension was stirred at room temperature overnight. The reaction mixture was diluted with Et_2O and passed through a silica plug. All volatiles were removed under reduced pressure and the residue was purified by column chromatography (hexane/EtOAc, 5/1). After drying in vacuo, 1.56 g (64%) of a yellowish oil was obtained as the titled compound **9** (R_f = 0.40, hexane/DCM, 1/2). ^{1}H NMR (500 MHz, $CDCl_3$): δ ppm = 7.66 (d, $^3J_{H\text{-}H}$ = 8.0 Hz, 1H, H-5), 7.63 (d, $^3J_{H\text{-}H}$ = 8.1 Hz, 1H, H-4), 7.60 (dd, $^3J_{H\text{-}H}$ = 7.9 Hz, $^4J_{H\text{-}H}$ = 1.5 Hz, 1H, H-6), 7.55 (s, 1H, H-8), 7.48 (s, 1H, H-1), 7.30 (dd, $^3J_{H\text{-}H}$ = 8.2 Hz, $^4J_{H\text{-}H}$ = 1.2 Hz, 1H, H-4), 6.65 (s, NH), 2.01 (q, $^3J_{H\text{-}H}$ = 7.4 Hz, 2H, H-14), 1.95 (t, $^3J_{H\text{-}H}$ = 8.2 Hz, 2H, H-16), 1.54 (s, 9H, H-19), 1.29-1.03 (m, 18H, CH_2), 0.86 (t, $^3J_{H\text{-}H}$ = 7.1 Hz, 3H, CH_3), 0.63-0.50 (m, 2H, CH_2), 0.27 (t, $^3J_{H\text{-}H}$ = 7.4 Hz, 3H, CH_3); ^{13}C NMR (125 MHz, $CDCl_3$): δ ppm = 152.64 (C-17), 152.60 (C-12), 150.9 (C-9), 145.9 (C-10), 139.6 (C-2), 134.5 (C-11), 131.5 (C-6), 126.4 (C-8), 121.5 (C-4), 120.1 (CN), 119.7 (C-5), 117.6 (C-3), 112.9 (C-1), 109.1 (C-7), 80.9 (C-18), 56.3 (C-13), 40.0 (C-16), 33.0 (C-14), 32.0 (CH_2), 30.1 (CH_2), 29.74 (2CH_2), 29.68 (2CH_2), 29.5 (CH_2), 29.4 (CH_2), 28.5 (3CH_3), 24.0 (CH_2), 22.8 (CH_2), 14.3 (CH_3), 8.4 (C-15); IR (ATP) ν cm^{-1}: 3330 (s, N-H), 3072 (vw, υ(=CH)), 2965 (m, υ_{as}(CH_3)), 2926 (vs, υ_{as}(CH_2)), 2853 (s, υ_s(CH_2, CH_3)), 2223 (s, -CN), 1695 (s, C=O), 1592 (s, υ(C=C)), 1537 (s, N-H), 1493 (m), 1465 (m), 1430 (m), 1368 (m), 1288 (m), 1240 (s), 1155 (s), 1142 (s), 1056 (s, C-O), 823 (s, υ(=CH)); UV-Vis (λ_{max}[nm], ε, CH_2Cl_2) 335 (36740); EI MS m/z (%) 502.38 (1, M^+), 446.33 (11), 402.33 (29), 373.27 (1), 278.13 (2), 247.15 (4), 233.13 (25), 218.10 (26), 205.09 (21), 190.07 (7), 151.09 (2), 97.10 (5), 83.99 (10), 56.09 (54), 44.01 (100). Elemental Analysis Calcd. (%) for $C_{33}H_{46}N_2O_2$ (502.74): C 78.84, H 9.22, N 5.57; Found: C 79.10, H 9.13, N 5.51.

***tert*-Butyl *N*-(9-dodecyl-9-ethyl-7-formyl-9*H*-fluoren-2-yl)carbamate (M3)**

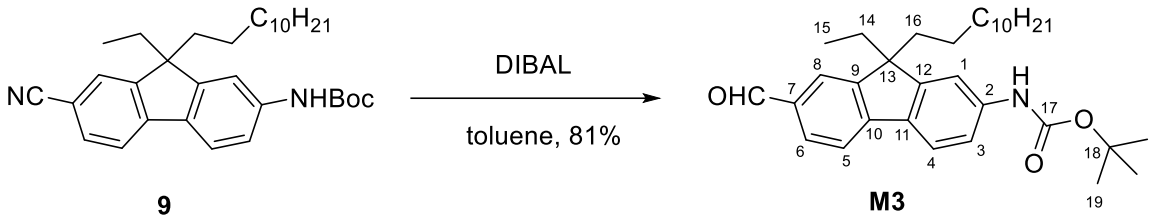

A 100 mL Schlenk-flask was charged with **9** (1.40 g, 2.78 mmol) and anhydrous toluene (35 mL) under an argon atmosphere. The solution was cooled to ca. -10 °C and DIBAL (1.0 M in hexane, 7 mL, 7.00 mmol, 2.52 eq.) was added dropwise. The reaction mixture was kept stirring at room temperature overnight. The resulting yellow solution was quenched with sat. $NaHCO_3$ solution and extracted with EtOAc. The combined organic phase was washed with brine, dried over $MgSO_4$ and passed through a silica plug. All solvents were removed under reduced pressure and the residue was purified by column chromatography (hexane/DCM, 1/2) to yield 1.15 g (82%) of the target compound **M3** as a light yellow oil (R_f = 0.16, hexane/DCM, 1/2). ^{1}H NMR (500 MHz, $CDCl_3$): δ ppm = 10.03 (s, 1H, CHO), 7.83-7.81 (m, 2H, H-6, H-8), 7.74 (d, $^3J_{H\text{-}H}$ = 8.1 Hz, 1H, H-5), 7.67 (d, $^3J_{H\text{-}H}$ = 8.2 Hz, 1H, H-4), 7.47 (s, 1H, H-1), 7.32 (d, $^3J_{H\text{-}H}$ = 8.2 Hz, 1H, H-3), 6.68 (s, 1H, NH), 2.11-1.93 (m, 4H, H-14, H-16), 1.55 (s, 9H, H-19), 1.28-1.02 (m, 18H, CH_2), 0.86 (t, $^3J_{H\text{-}H}$ = 7.0 Hz, 3H, CH_3), 0.64-0.52 (m, 2H, CH_2), 0.28 (t, $^3J_{H\text{-}H}$ = 7.2 Hz, 3H, H-15); ^{13}C NMR (125 MHz, $CDCl_3$): δ ppm = 192.5 (CHO), 153.4 (C-12), 152.6 (C-17), 150.9 (C-9), 147.8 (C-10), 139.5 (C-2), 134.9 (C-7), 134.8 (C-11), 130.9 (C-6), 123.1 (C-8), 121.6 (C-4), 119.4 (C-5), 117.5 (C-3), 113.0 (C-1), 80.9 (C-18), 56.0 (C-13), 40.1 (C-16), 33.1 (C-14), 32.0 (CH_2), 30.1 (CH_2), 29.7 ($2CH_2$), 29.69 (CH_2), 29.67 (CH_2), 29.45 (CH_2), 29.43 (CH_2), 28.5 (C-19), 24.0 (CH_2), 22.8 (CH_2), 14.3 (CH_3), 8.5 (C-15); IR (ATP) ν cm^{-1}: 3327 (s, N-H), 3073 (vw, υ(=CH)), 2961 (m, υ_{as}(CH_3)), 2925 (s, υ_{as}(CH_2)), 2853 (s, υ_s(CH_2, CH_3)), 1693 (s, C=O), 1590 (s, υ(C=C)), 1535 (s, N-H), 1495 (m), 1419 (m), 1367 (m), 1291 (m), 1239 (s), 1155 (s), 1141 (s), 1055 (s, C-O), 817 (s, υ(=CH)); UV-Vis (λ_{max}[nm], ε, CH_2Cl_2) 338 (33730); EI MS m/z (%) 505.39 (1, M^+), 449.31 (10), 405.34 (2), 280.13 (3), 252.11 (2), 208.13 (5), 193.11 (5), 83.98 (6), 56.09 (61), 44.00 (100). Elemental Analysis Calcd. (%) for $C_{33}H_{47}NO_3$ (505.74): C 78.37, H 9.37, N 2.77; Found: C 78.63, H 9.24, N 2.71.

Enantiomeric separation of M3

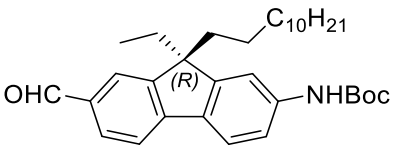

(*R*)-M3

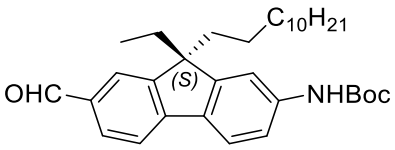

(*S*)-M3

The enantiomers **(*R*)-M3** and **(*S*)-M3** were separated by chiral flash chromatography from SHIMADZU LC-20AT HPLC, which was equipped with CHIRALPAK® IB N-5 HPLC column (250×30 mm, *n*-heptane:isopropanol = 96:4), with a flowrate of 45 mL/min and UV detection at 254 nm. Retention times: 9.66 min for **(*R*)-M3** and 13.95 min for **(*S*)-M3**.

Chiral polyimines (*R*)-CP and (*S*)-CP

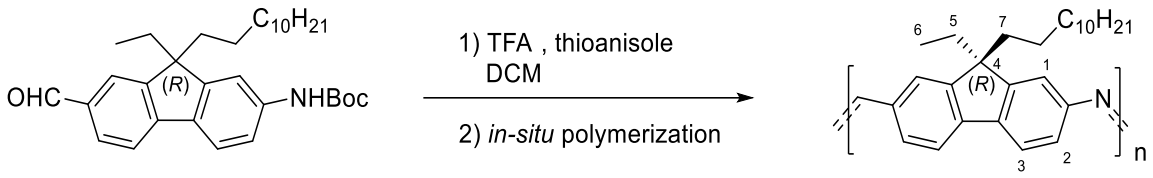

(*R*)-M3 (*R*)-CP

A 25 mL Schlenk-flask was charged with a pure enantiomer **(*R*)-M3** (100 mg, 0.20 mmol) and anhydrous DCM (8 mL) under an argon atmosphere. TFA (1.6 mL, 99%) and thioanisole (48 µL, 0.40 mmol, 2.0 eq.) were added subsequently and the mixture was stirred at room temperature overnight. The resulting red mixture was quenched with sat. $NaHCO_3$ solution and extracted with DCM. The combined organic phase was washed with brine, dried over $MgSO_4$ and filtrated. All solvents were removed under reduced pressure and the residue was polymerized directly in the flask at 100 °C under vacuum (ca. 10^{-2} mbar) for 48h. The chiral polymer **(*R*)-CP** was obtained (75 mg, 97%) as a yellow polymeric film. ^{1}H NMR (500 MHz, $CDCl_3$): δ ppm = 8.66 (s, 1H, N=CH), 8.01-7.80 (m, 4H), 7.32 (m, 2H), 2.13 (m, 4H, H-5, H-7), 1.27-1.10 (m, 18H), 0.85 (t, $^3J_{H-H}$ = 7.0 Hz, 3H), 0.70 (m, 2H), 0.37 (m, 3H, H-6); ^{13}C NMR (125 MHz, $CDCl_3$): δ ppm = 56.2 (C-4), 40.1 (CH_2), 32.1 (CH_2), 29.80 (CH_2), 29.76 (CH_2), 29.74 (CH_2), 29.6 (CH_2), 29.5 (CH_2), 22.8 (CH_2), 14.3 (CH_3), 8.6 (C-6); GPC: M_n= 60 kDa, M_w= 188 kDa, Đ = 3.13; IR (ATP) ν cm^{-1}: 3316 (vw, υ(=CH)), 2958 (m, $\upsilon_{as}(CH_3)$), 2922 (s, $\upsilon_{as}(CH_2)$), 2852 (s, $\upsilon_s(CH_2, CH_3)$), 1625 (w, C=N), 1588 (m, υ(C=C)), 1465 (m), 1153 (w, υ(C=C)), 818 (m, υ(=CH)); UV-Vis (λ_{max}[nm], ε, CH_2Cl_2) 424 (33290).

Chiral polymer **(*S*)-CP** and achiral polymer **ACP** were synthesized under the same procedure. For **(*S*)-CP**: Yield: 95%; GPC: M_n= 48 kDa, M_w= 153 kDa, Đ = 3.19; For **ACP**: Yield: 98%; GPC: M_n= 90 kDa, M_w= 287 kDa, Đ = 3.14.

(2*R*,9*R*)-*N*-(9-dodecyl-9-ethyl-7-formyl-9*H*-fluoren-2-yl)-3,3,3-trifluoro-2-methoxy-2-phenylpropanamide ((*R*)-Mosher-(*R*)-M3) & (2*R*,9*S*)-*N*-(9-dodecyl-9-ethyl-7-formyl-9*H*-fluoren-2-yl)-3,3,3-trifluoro-2-methoxy-2-phenylpropanamide ((*R*)-Mosher-(*S*)-M3)

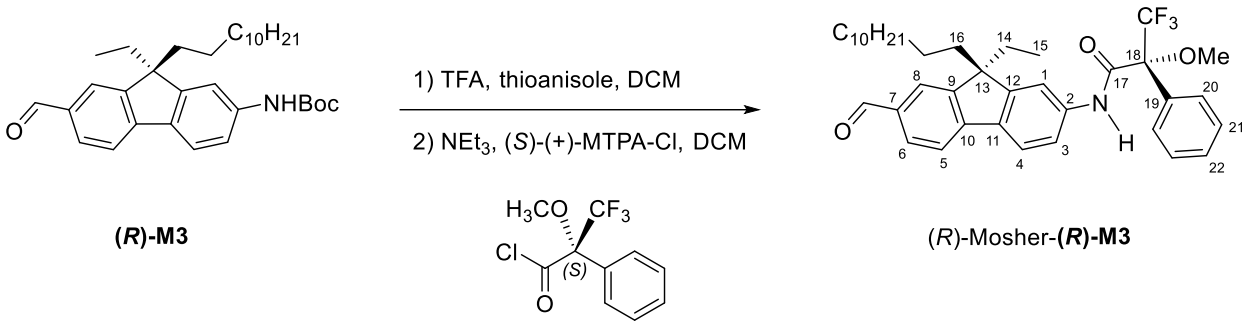

(***R*)-M3**

(*R*)-Mosher-(***R*)-M3**

A 10 mL screw vial was charged with **(*R*)-M3** (31.3 mg, 0.062 mmol) and anhydrous DCM (4 mL) under an argon atmosphere. The solution was cooled down to 0 °C, TFA (99%, 140 µL, 30.0 eq.) and thioanisole (7 µL, 1.0 eq.) were added subsequently. The mixture was stirred at 0 °C for 2 h and then at room temperature overnight. The resulting red mixture was quenched with a diluted aqueous NaOH solution (10%) and extracted with DCM. The combined organic phase was washed with brine, dried over $MgSO_4$ and filtrated. The obtained solution was concentrated under reduced pressure till approx. 3 mL. The remaining solution was transferred into a 10 mL screw vial and purged with argon. The solution was cooled to 0 °C before NEt_3 (43 µL, 0.31 mmol, 5.0 eq.) and (*S*)-(+)-MTPA-Cl (58 µL, 0.31 mmol, 5.0 eq.) were added. The mixture was stirred at 0 °C for 2 h and at room temperature overnight. The resulting yellow solution was quenched with sat. Na_2CO_3 solution and extracted with DCM. The combined organic phase was washed with brine, dried over $MgSO_4$ and passed through a silica plug. All volatiles were removed under reduced pressure and the residue was purified by column chromatography (hexane/DCM, 1/2) to afford 21.3 mg (55%) of the titled compound (*R*)-Mosher-**(*R*)-M3** as a greyish-brown oil (R_f = 0.44, hexane/EtOAc, 1/1). ^{1}H NMR (500 MHz, $CDCl_3$): δ ppm = 10.05 (s, 1H, CHO), 8.76 (s, 1H, NH), 7.85-7.84 (m, 2H, H-6, H-8), 7.78 (d, $^3J_{H\text{-}H}$ = 8.1 Hz, 1H, H-5), 7.75 (ds, $^4J_{H\text{-}H}$ = 1.8 Hz, 1H, H-1), 7.74 (d, $^3J_{H\text{-}H}$ = 8.2 Hz, 1H, H-4), 7.63-7.61 (m, 2H, H-20), 7.53 (dd, $^3J_{H\text{-}H}$ = 8.2 Hz, $^4J_{H\text{-}H}$ = 1.9 Hz, 1H, H-3), 7.49-7.44 (m, 3H, H-21, H-22), 3.55 (s, 3H, OCH_3), 2.12-1.94 (m, 4H, H-14, H-16), 1.25-1.02 (m, 18H, CH_2), 0.86 (t, $^3J_{H\text{-}H}$ = 7.1 Hz, 3H, CH_3), 0.62-0.53 (m, 2H, CH_2), 0.28 (t, $^3J_{H\text{-}H}$ = 7.3 Hz, 3H, H-15); ^{13}C NMR (125 MHz, $CDCl_3$): δ ppm = 192.4 (CHO), 164.3 (C-17), 153.4 (C-12), 151.2 (C-9), 147.3 (C-10), 137.7 (C-2), 136.8 (C-11), 135.2 (C-7), 132.2 (C-19), 130.8 (C-

6), 129.9 (C-22), 129.0 (C-23), 127.9 (C-20), 123.9 (q, CF_3), 123.2 (C-8), 121.6 (C-4), 119.8 (C-5), 119.0 (C-3), 114.6 (C-1), 84.5 (q, C-18), 56.2 (C-13), 55.4 (OCH_3), 40.0 (C-16), 33.0 (C-14), 32.0 (CH_2), 30.0 (CH_2), 29.8 (CH_2), 29.72 (CH_2), 29.68 (CH_2), 29.65 (CH_2), 29.44 (CH_2), 29.41 (CH_2), 24.0 (CH_2), 22.8 (CH_2), 14.2 (CH_3), 8.5 (C-15). ^{19}F NMR (470 MHz, $CDCl_3$): δ ppm = -68.28.

(*R*)-Mosher-**(*S*)-M3** was synthesized with the same procedure and isolated in a yield of 48% (R_f = 0.44, hexane/EtOAc, 1/1). ^{1}H NMR (500 MHz, $CDCl_3$): δ ppm = 10.05 (s, 1H, CHO), 8.76 (s, 1H, NH), 7.85-7.84 (m, 2H, H-6, H-8), 7.78 (d, $^3J_{H\text{-}H}$ = 8.1 Hz, 1H, H-5), 7.76 (ds, $^4J_{H\text{-}H}$ = 1.7 Hz, 1H, H-1), 7.73 (d, $^3J_{H\text{-}H}$ = 8.1 Hz, 1H, H-4), 7.63-7.61 (m, 2H, H-20), 7.52 (dd, $^3J_{H\text{-}H}$ = 8.2 Hz, $^4J_{H\text{-}H}$ = 1.8 Hz, 1H, H-3), 7.48-7.44 (m, 3H, H-21, H-22), 3.54 (s, 3H, OCH_3), 2.09-1.98 (m, 4H, H-14, H-16), 1.25-1.02 (m, 18H, CH_2), 0.86 (t, $^3J_{H\text{-}H}$ = 7.1 Hz, 3H, CH_3), 0.62-0.53 (m, 2H, CH_2), 0.27 (t, $^3J_{H\text{-}H}$ = 7.3 Hz, 3H, H-15); ^{13}C NMR (125 MHz, $CDCl_3$): δ ppm = 192.4 (CHO), 164.3 (C-17), 153.5 (C-12), 151.2 (C-9), 147.3 (C-10), 137.7 (C-2), 136.8 (C-11), 135.2 (C-7), 132.2 (C-19), 130.8 (C-6), 129.9 (C-22), 129.0 (C-23), 127.9 (C-20), 123.9 (q, CF_3), 123.2 (C-8), 121.6 (C-4), 119.8 (C-5), 119.0 (C-3), 114.6 (C-1), 84.5 (q, C-18), 56.2 (C-13), 55.4 (OCH_3), 40.0 (C-16), 33.0 (C-14), 32.0 (CH_2), 30.1 (CH_2), 29.8 (CH_2), 29.73 (CH_2), 29.70 (CH_2), 29.66 (CH_2), 29.44 ($2CH_2$), 24.0 (CH_2), 22.8 (CH_2), 14.3 (CH_3), 8.5 (C-15); ^{19}F NMR (470 MHz, $CDCl_3$): δ ppm = -68.26.

6 List of abbreviations

0D	Zero-dimensional
1D	One-dimensional
2D	Two-dimensional
3D	Three-dimensional
Å	Angstrom
µg	Microgram
µL	Microliter
µm	Micrometer
°C	Grad Celsius
AC	Absolute configuration
ACP	Achiral polymer
AD	Arc discharge
AFM	Atomic force microscopy
ATP	Aqueous two-phase
ATPE	Aqueous two-phase extraction
aq.	Aqueous
BINAP	2,2-Bis(diphenylphosphino)-1,1-binaphthyl
Boc	*tert*-Butyloxycarbonyl
br	Broad
BWF	Breit-Wigner-Fano line shape
BZ	Brillouin zone
calcd.	Calculated
CD	Circular dichroism
CDH	Cyclodehydrogenation
cm^{-1}	Wavenumber
CNT	Carbon nanotube
CNTFET	Carbon nanotube field effect transistor
COSY	Correlation spectroscopy
CP	Chiral polymer

CPP	Cycloparaphenylene
CVD	Chemical vapor deposition
d	Doublet
Đ	Polydispersity
DCM	Dichloromethane
dd	Doublet of doublet
DFT	Density functional theory
DIBAL	Diisobutylaluminium hydride
DMF	*N*,*N*-Dimethylformamide
DNA	Deoxyribonucleic acid
DGU	Density gradient ultracentrifugation
DOC	Sodium deoxycholate
DOS	Density of electronic states
DPV	Differential pulse voltammogram
ds	Doublet of singlet
EA	Elemental analysis
ee	Enantiomer excess
EE	Epitaxial elongation
EP	Enantiomeric purity
eq.	Equivalent
Et_2O	Diethyl ether
EtOAc	Ethyl acetate
eV	Electron volt
FET	Field-effect transistor
FMN	Flavin mononucleotide
frac	Fraction
FT-IR	Fourier-transform infrared spectroscopy
g	Gram
GCE	Glass carbon electrode
GC/MS	Gas chromatography–mass spectrometry
GPC	Gel permeation chromatography

h	Hour
HCl	Hydrochloride acid
HiPco	High pressure CO disproportionation
HMBC	Heteronuclear multiple-bond correlation spectroscopy
HOMO	Highest occupied molecular orbital
HPLC	High performance liquid chromatography
HRTEM	High-resolution transmission electron microscopy
HSQC	Heteronuclear single-quantum correlation spectroscopy
Hz	Hertz
IR	Infrared
IUPAC	International Union of Pure and Applied Chemistry
K	Kalvin
kcal	Kilocalories
kDa	Kilodalton
LC	Liquid chromatography
LCP	Left-handed circularly polarized light
LUMO	Lowest occupied molecular orbital
m	Multiplet
m	Medium
M	Molar
(*M*)	Left-handed
MALDI-TOF	Matrix-assisted laser desorption ionization-time of flight
mbar	Millibar
MC	Monte Carlo
MD	Molecular dynamic
mdeg	Millidegree
MeOH	Methanol
mg	Milligram
MHz	Megahertz
min	Minute
mL	Milliliter

mm	Millimeter
mmol	Millimol
M_n	Number-average molecular weight
m.p.	Melting point
M_p	Peak molecular weight
ms	Millisecond
MS	Mass spectroscopy
m-SWCNT	Metallic single-walled carbon nanotubes
M_w	Weight-average molecular weight
(*M*)	Left-handed
MW	Molecular weight
m/z	Mass per charge
NEt_3	Triethylamine
NIR	Near-infrared
(n,m)	Chiral index
nm	Nanometer
NMP	*N*-Methyl-2-pyrrolidone
NMR	Nuclear magnetic resonance
NOE	Nuclear overhauser effect
NOESY	Nuclear overhauser effect spectroscopy
norm	Normalized
ns	Nanosecond
(*P*)	Right-handed
P3HT	Poly-3-hexylthiophene
PAM	Polyazomethine
PBC	Periodic boundary condition
PCM	Polarizable continuum model
PDI	Polydispersity index
PEG	Polyethylene glycol
PFO	Poly(9,9-dioctylfluorenyl-2,7-diyl)
PFO-Bpy	Poly[(9,9-dioctylfluorenyl-2,7-diyl)-*alt*-*co*-(6,6´-{2,2´-bipyridine})]

PL	Photoluminescence
PLE	Photoluminescence excitation
PLV	Pulsed laser vaporization
PODOF	Poly(9,9-di-*n*-dodecylfluorenyl-2,7-diyl)
PPh_3	Triphenylphosphine
ppm	Parts per million
pppm	Particle-particle particle-mesh
PTFE	Polytetrafluoroethylene
PTSA	*p*-Toluenesulfonic acid
q	Quartet
rac	Racemate
RBM	Radial breathing mode
RCF	Relative centrifugal force
RCP	Right-handed circularly polarized light
RT	Room temperature
s	Singlet
s	Strong
SC	Sodium cholate
SDBS	Sodium dodecylbenzene sulfonate
SDS	Sodium dodecyl sulfate
SEC	Size-exclusion chromatography
SEM	Scanning electron microscopy
s-SWCNT	Semiconducting single-walled carbon nanotubes
SWCNT	Single-walled carbon nanotube
t	Triplet
T	Temperature
TB	Tight bonding
TD-DFT	Time-dependent density functional theory
TEM	Transmission electron microscopy
TFA	Trifluoroacetic acid
TFT	Thin-film transistor

TGA	Thermogravimetric analysis
THF	Tetrahydrofuran
TLC	Thin-layer chromatography
UV	Ultraviolet
UV-Vis	Ultraviolet-visible
UV-Vis-NIR	Ultraviolet-visible-near infrared
VHS	Van Hove singularity
w	Weak
wt%	Weight percentage
XPhos	2-Dicyclohexylphosphino-2´, 4´, 6´-triisopropylbiphenyl
XPS	X-ray photoelectron spectroscopy

7 References

[1] H. W. Kroto, J. R. Heath, S. C. O'Brien, R. F. Curl, R. E. Smalley, *Nature* **1985**, *318*, 162–163.

[2] S. Iijima, *Nature* **1991**, *354*, 56–58.

[3] K. S. Novoselov, A. K. Geim, S. V. Morozov, D. Jiang, Y. Zhang, S. V. Dubonos, I. V. Grigorieva, A. A. Firsov, *Science* **2004**, *306*, 666–669.

[4] A. K. Geim, K. S. Novoselov, *Nat. Mater.* **2007**, *6*, 183–191.

[5] Y. Cao, V. Fatemi, S. Fang, K. Watanabe, T. Taniguchi, E. Kaxiras, P. Jarillo-Herrero, *Nature* **2018**, *556*, 43–50.

[6] Y. Cao, S. Cong, X. Cao, F. Wu, Q. Liu, Moh. R. Amer, C. Zhou, in *Single-Walled Carbon Nanotubes: Preparation, Properties and Applications* (Eds.: Y. Li, S. Maruyama), Springer International Publishing, Cham, **2019**, pp. 189–224.

[7] X. Liang, J. Xia, G. Dong, B. Tian, L. Peng, in *Single-Walled Carbon Nanotubes: Preparation, Properties and Applications* (Eds.: Y. Li, S. Maruyama), Springer International Publishing, Cham, **2019**, pp. 225–256.

[8] I. Jeon, Y. Matsuo, S. Maruyama, in *Single-Walled Carbon Nanotubes: Preparation, Properties and Applications* (Eds.: Y. Li, S. Maruyama), Springer International Publishing, Cham, **2019**, pp. 271–298.

[9] F. Yang, M. Wang, D. Zhang, J. Yang, M. Zheng, Y. Li, *Chem. Rev.* **2020**, *120*, 2693-2758.

[10] J. W. G. Wilder, L. C. Venema, A. G. Rinzler, R. E. Smalley, C. Dekker, *Nature* **1998**, *391*, 59–62.

[11] R. Saito, M. Fujita, G. Dresselhaus, M. S. Dresselhaus, *Appl. Phys. Lett.* **1992**, *60*, 2204–2206.

[12] M. S. Strano, *Nat. Nanotechnol.* **2007**, *2*, 340–341.

[13] G. P. Moss, *Pure Appl. Chem.* **1996**, *68*, 2193–2222.

[14] X. Peng, F. Wang, A. K. Bauri, A. F. M. M. Rahman, N. Komatsu, *Chem. Lett.* **2010**, *39*, 1022–1027.

[15] S. Friedrichs, J. Sloan, M. L. H. Green, J. L. Hutchison, R. R. Meyer, A. I. Kirkland, *Phys. Rev. B* **2001**, *64*, 045406.

[16] Ge. G. Samsonidze, A. Grüneis, R. Saito, A. Jorio, A. G. Souza Filho, G. Dresselhaus, M. S. Dresselhaus, *Phys. Rev. B* **2004**, *69*, 205402.

[17] P. R. Wallace, *Phys. Rev.* **1947**, *71*, 622–634.

[18] R. Saito, G. Dresselhaus, M. S. Dresselhaus, *Physical Properties of Carbon Nanotubes*, Imperial College Press, **1998**.

[19] Ge. G. Samsonidze (**2007**), *Photophysics of Carbon Nanotubes*, Doctoral Dissertation, Massachusetts Institute of Technology, Cambridge, USA.

[20] Ge. G. Samsonidze, A. R. Saito, D. A. Jorio, E. M. A. Pimenta, E. A. G. Souza Filho, F. A. Grüneis, D. G. Dresselhaus, M. S. Dresselhausa, *J. Nanosci. Nanotechnol.* **2003**, *3*, 431–458.

[21] W. Gao, J. Kono, *R. Soc. Open Sci.* **2019**, *6*, 181605.

[22] R. Saito, G. Dresselhaus, M. S. Dresselhaus, *Phys. Rev. B* **2000**, *61*, 2981–2990.

[23] A. Jorio, R. Saito, T. Hertel, R. B. Weisman, G. Dresselhaus, M. S. Dresselhaus, *MRS Bull.* **2004**, *29*, 276–280.

[24] G. R. Ahmed Jamal, S. M. Mominuzzaman, *J. Nanosci. Nanoengin.* **2015**, *1*, 11.

[25] H. Ajiki, T. Ando, *Physica B Condens. Matter* **1994**, *201*, 349–352.

[26] H. Kataura, Y. Kumazawa, Y. Maniwa, I. Umezu, S. Suzuki, Y. Ohtsuka, Y. Achiba, *Synth. Met.* **1999**, *103*, 2555–2558.

[27] R. B. Weisman, S. M. Bachilo, *Nano Lett.* **2003**, *3*, 1235–1238.

[28] M. S. Arnold, A. A. Green, J. F. Hulvat, S. I. Stupp, M. C. Hersam, *Nat. Nanotechnol.* **2006**, *1*, 60–65.

[29] S. M. Bachilo, M. S. Strano, C. Kittrell, R. H. Hauge, R. E. Smalley, R. B. Weisman, *Science* **2002**, *298*, 2361–2366.

[30] T. Koyama, K. Asaka, N. Hikosaka, H. Kishida, Y. Saito, A. Nakamura, *J. Phys. Chem. Lett.* **2011**, *2*, 127–132.

[31] H. Qian, C. Georgi, N. Anderson, A. A. Green, M. C. Hersam, L. Novotny, A. Hartschuh, *Nano Lett.* **2008**, *8*, 1363–1367.

[32] J. E. Riggs, Z. Guo, D. L. Carroll, Y.-P. Sun, *J. Am. Chem. Soc.* **2000**, *122*, 5879–5880.

[33] H. N. Pedrosa (**2006**), *The Optical Properties of Single-walled Carbon Nanotubes*, Doctoral Dissertation, University of Rochester, Rochester, USA.

[34] Y. Piao, B. Meany, L. R. Powell, N. Valley, H. Kwon, G. C. Schatz, Y. Wang, *Nat. Chem.* **2013**, *5*, 840–845.

[35] S. Lebedkin, F. Hennrich, O. Kiowski, M. M. Kappes, *Phys. Rev. B* **2008**, *77*, 165429.

[36] F. Hennrich, W. Li, R. Fischer, S. Lebedkin, R. Krupke, M. M. Kappes, *ACS Nano* **2016**, *10*, 1888–1895.

[37] M. S. Dresselhaus, G. Dresselhaus, R. Saito, A. Jorio, *Phys. Rep.* **2005**, *409*, 47–99.

[38] H. Kawamoto, T. Uchida, K. Kojima, M. Tachibana, *J. Appl. Phys.* **2006**, *99*, 094309.

[39] L. R. Powell, Y. Piao, Y. Wang, *J. Phys. Chem. Lett.* **2016**, *7*, 3690–3694.

[40] M. S. Dresselhaus, G. Dresselhaus, A. Jorio, A. G. Souza Filho, M. A. Pimenta, R. Saito, *Acc. Chem. Res.* **2002**, *35*, 1070–1078.

[41] J. Maultzsch, H. Telg, S. Reich, C. Thomsen, *Phys. Rev. B* **2005**, *72*, 205438.

[42] N. R. Raravikar, P. Keblinski, A. M. Rao, M. S. Dresselhaus, L. S. Schadler, P. M. Ajayan, *Phys. Rev. B* **2002**, *66*, 235424.

[43] A. Nish, J.-Y. Hwang, J. Doig, R. J. Nicholas, *Nat. Nanotechnol.* **2007**, *2*, 640–646.

[44] "Circular Dichroism", *Wikipedia*, Wikipedia Foundation, 08 Sept. 2020, https://en.wikipedia.org/wiki/Circular_dichroism.

[45] L. D. Barron, *Molecular Light Scattering and Optical Activity*, Cambridge University Press, Cambridge, **2009**.

[46] A. Sánchez-Castillo, C. E. Román-Velázquez, C. Noguez, *Phys. Rev. B* **2006**, *73*, 045401.

[47] A. Sánchez-Castillo, C. Noguez, *J. Phys. Chem. C* **2010**, *114*, 9640–9644.

[48] N. Sato, Y. Tatsumi, R. Saito, *Phys. Rev. B* **2017**, *95*, 155436.

[49] X. Wei, T. Tanaka, Y. Yomogida, N. Sato, R. Saito, H. Kataura, *Nat. Commun.* **2016**, *7*, 12899.

[50] F. Wang, K. Matsuda, A. F. M. M. Rahman, X. Peng, T. Kimura, N. Komatsu, *J. Am. Chem. Soc.* **2010**, *132*, 10876–10881.

[51] A. Grüneis, R. Saito, Ge. G. Samsonidze, T. Kimura, M. A. Pimenta, A. Jorio, A. G. S. Filho, G. Dresselhaus, M. S. Dresselhaus, *Phys. Rev. B* **2003**, *67*, 165402.

[52] Y. Segawa, A. Yagi, K. Matsui, K. Itami, *Angew. Chem. Int. Ed.* **2016**, *55*, 5136–5158.

[53] H. Omachi, T. Nakayama, E. Takahashi, Y. Segawa, K. Itami, *Nat. Chem.* **2013**, *5*, 572–576.

[54] J. R. Sanchez-Valencia, T. Dienel, O. Gröning, I. Shorubalko, A. Mueller, M. Jansen, K. Amsharov, P. Ruffieux, R. Fasel, *Nature* **2014**, *512*, 61–64.

[55] Y. A. Kim, H. Muramatsu, T. Hayashi, M. Endo, *Carbon* **2012**, *50*, 4588–4595.

[56] D. S. Bethune, C. H. Kiang, M. S. de Vries, G. Gorman, R. Savoy, J. Vazquez, R. Beyers, *Nature* **1993**, *363*, 605–607.

[57] M. E. Itkis, D. E. Perea, S. Niyogi, J. Love, J. Tang, A. Yu, C. Kang, R. Jung, R. C. Haddon, *J. Phys. Chem. B* **2004**, *108*, 12770–12775.

[58] N. Arora, N. N. Sharma, *Diam. Relat. Mater.* **2014**, *50*, 135–150.

[59] T. Guo, P. Nikolaev, A. G. Rinzler, D. Tomanek, D. T. Colbert, R. E. Smalley, *J. Phys. Chem.* **1995**, *99*, 10694–10697.

[60] M. Yudasaka, T. Komatsu, T. Ichihashi, S. Iijima, *Chem. Phys. Lett.* **1997**, *278*, 102–106.

[61] M. Yudasaka, R. Yamada, N. Sensui, T. Wilkins, T. Ichihashi, S. Iijima, *J. Phys. Chem. B* **1999**, *103*, 6224–6229.

[62] C. D. Scott, S. Arepalli, P. Nikolaev, R. E. Smalley, *Appl. Phys. A* **2001**, *72*, 573–580.

[63] R. Das, Z. Shahnavaz, Md. E. Ali, M. M. Islam, S. B. Abd Hamid, *Nanoscale. Res. Lett.* **2016**, *11*, 510.

[64] A. M. Cassell, J. A. Raymakers, J. Kong, H. Dai, *J. Phys. Chem. B* **1999**, *103*, 6484–6492.

[65] A. R. Harutyunyan, B. K. Pradhan, U. J. Kim, G. Chen, P. C. Eklund, *Nano Lett.* **2002**, *2*, 525–530.

[66] B. Zheng, C. Lu, G. Gu, A. Makarovski, G. Finkelstein, J. Liu, *Nano Lett.* **2002**, *2*, 895–898.

[67] Y. Li, D. Mann, M. Rolandi, W. Kim, A. Ural, S. Hung, A. Javey, J. Cao, D. Wang, E. Yenilmez, Q. Wang, J. F. Gibbons, Y. Nishi, H. Dai, *Nano Lett.* **2004**, *4*, 317–321.

[68] P. Nikolaev, M. J. Bronikowski, R. K. Bradley, F. Rohmund, D. T. Colbert, K. A. Smith, R. E. Smalley, *Chem. Phys. Lett.* **1999**, *313*, 91–97.

[69] I. W. Chiang, B. E. Brinson, A. Y. Huang, P. A. Willis, M. J. Bronikowski, J. L. Margrave, R. E. Smalley, R. H. Hauge, *J. Phys. Chem. B* **2001**, *105*, 8297–8301.

[70] T. Guo, P. Nikolaev, A. Thess, D. T. Colbert, R. E. Smalley, *Chem. Phys. Lett.* **1995**, *243*, 49–54.

[71] T. Lei, X. Chen, G. Pitner, H.-S. P. Wong, Z. Bao, *J. Am. Chem. Soc.* **2016**, *138*, 802–805.

[72] B. Kitiyanan, W. E. Alvarez, J. H. Harwell, D. E. Resasco, *Chem. Phys. Lett.* **2000**, *317*, 497–503.

[73] T. Lei, I. Pochorovski, Z. Bao, *Acc. Chem. Res.* **2017**, *50*, 1096–1104.

[74] S. M. Bachilo, L. Balzano, J. E. Herrera, F. Pompeo, D. E. Resasco, R. B. Weisman, *J. Am. Chem. Soc.* **2003**, *125*, 11186–11187.

[75] W. A. G. Rojas, M. C. Hersam, *Adv. Mater.* **2020**, *32*, 1905654.

[76] J. L. Blackburn, T. M. Barnes, M. C. Beard, Y.-H. Kim, R. C. Tenent, T. J. McDonald, B. To, T. J. Coutts, M. J. Heben, *ACS Nano* **2008**, *2*, 1266–1274.

[77] W. Wang, K. A. S. Fernando, Y. Lin, M. J. Meziani, L. M. Veca, L. Cao, P. Zhang, M. M. Kimani, Y.-P. Sun, *J. Am. Chem. Soc.* **2008**, *130*, 1415–1419.

[78] S. Paul, D.-W. Kim, *Carbon* **2009**, *47*, 2436–2441.

[79] D. S. Hecht, L. Hu, G. Irvin, *Adv. Mater.* **2011**, *23*, 1482–1513.

[80] A. Javey, J. Guo, Q. Wang, M. Lundstrom, H. Dai, *Nature* **2003**, *424*, 654–657.

[81] T. Dürkop, S. A. Getty, E. Cobas, M. S. Fuhrer, *Nano Lett.* **2004**, *4*, 35–39.

[82] L. Nougaret, H. Happy, G. Dambrine, V. Derycke, J.-P. Bourgoin, A. A. Green, M. C. Hersam, *Appl. Phys. Lett.* **2009**, *94*, 243505.

[83] Q. Cao, S. Han, G. S. Tulevski, Y. Zhu, D. D. Lu, W. Haensch, *Nat. Nanotechnol.* **2013**, *8*, 180–186.

[84] C. Wang, K. Takei, T. Takahashi, A. Javey, *Chem. Soc. Rev.* **2013**, *42*, 2592–2609.

[85] F. Hennrich, S. Lebedkin, S. Malik, J. Tracy, M. Barczewski, H. Rösner, M. Kappes, *Phys. Chem. Chem. Phys.* **2002**, *4*, 2273–2277.

[86] Q. Cao, J. A. Rogers, *Adv. Mater.* **2009**, *21*, 29–53.

[87] L. Hu, D. S. Hecht, G. Grüner, *Chem. Rev.* **2010**, *110*, 5790–5844.

[88] P. Avouris, M. Freitag, V. Perebeinos, *Nat. Photonics* **2008**, *2*, 341–350.

[89] T. Hasan, Z. Sun, F. Wang, F. Bonaccorso, P. H. Tan, A. G. Rozhin, A. C. Ferrari, *Adv. Mater.* **2009**, *21*, 3874–3899.

[90] H. Wang, Z. Bao, *Nano Today* **2015**, *10*, 737–758.

[91] J. Kong, N. R. Franklin, C. Zhou, M. G. Chapline, S. Peng, K. Cho, H. Dai, *Science* **2000**, *287*, 622–625.

[92] K. Chen, W. Gao, S. Emaminejad, D. Kiriya, H. Ota, H. Y. Y. Nyein, K. Takei, A. Javey, *Adv. Mater.* **2016**, *28*, 4397–4414.

[93] M. M. Shulaker, G. Hills, N. Patil, H. Wei, H.-Y. Chen, H.-S. P. Wong, S. Mitra, *Nature* **2013**, *501*, 526–530.

[94] G. Hills, C. Lau, A. Wright, S. Fuller, M. D. Bishop, T. Srimani, P. Kanhaiya, R. Ho, A. Amer, Y. Stein, D. Murphy, Arvind, A. Chandrakasan, M. M. Shulaker, *Nature* **2019**, *572*, 595–602.

[95] S. J. Tans, A. R. M. Verschueren, C. Dekker, *Nature* **1998**, *393*, 49–52.

[96] P. Prakash, K. Mohana Sundaram, M. Anto Bennet, *Renew. Sustain. Energy Rev.* **2018**, *89*, 194–203.

[97] C. Pu, Y. Xu, Q. Liu, A. Zhu, G. Shi, *Anal. Chem.* **2019**, *91*, 3015–3020.

[98] M. C. Hersam, *Nat. Nanotechnol.* **2008**, *3*, 387–394.

[99] N. Rouhi, D. Jain, P. J. Burke, *ACS Nano* **2011**, *5*, 8471–8487.

[100] M. Holzinger, O. Vostrowsky, A. Hirsch, F. Hennrich, M. Kappes, R. Weiss, F. Jellen, *Angew. Chem. Int. Ed.* **2001**, *40*, 4002–4005.

[101] A. Hirsch, *Angew. Chem. Int. Ed.* **2002**, *41*, 1853–1859.

[102] V. Georgakilas, K. Kordatos, M. Prato, D. M. Guldi, M. Holzinger, A. Hirsch, *J. Am. Chem. Soc.* **2002**, *124*, 760–761.

[103] F. J. Berger, J. Lüttgens, T. Nowack, T. Kutsch, S. Lindenthal, L. Kistner, C. C. Müller, L. M. Bongartz, V. A. Lumsargis, Y. Zakharko, J. Zaumseil, *ACS Nano* **2019**, *13*, 9259–9269.

[104] D. Janas, *Mater. Chem. Front.* **2018**, *2*, 36–63.

[105] S. Qiu, K. Wu, B. Gao, L. Li, H. Jin, Q. Li, *Adv. Mater.* **2019**, *31*, 1800750.

[106] M. S. Arnold, S. I. Stupp, M. C. Hersam, *Nano Lett.* **2005**, *5*, 713–718.

[107] A. A. Green, M. C. Hersam, *Adv. Mater.* **2011**, *23*, 2185–2190.

[108] S. Ghosh, S. M. Bachilo, R. B. Weisman, *Nat. Nanotechnol.* **2010**, *5*, 443–450.

[109] T. Tanaka, Y. Urabe, D. Nishide, H. Kataura, *Appl. Phys. Express* **2009**, *2*, 125002.

[110] H. Liu, D. Nishide, T. Tanaka, H. Kataura, *Nat. Commun.* **2011**, *2*, 309.

[111] M. Rito-Palomares, J. Benavides, *Aqueous Two-Phase Systems for Bioprocess Development for the Recovery of Biological Products*, Springer International Publishing, Cham, **2017**.

[112] C. Y. Khripin, J. A. Fagan, M. Zheng, *J. Am. Chem. Soc.* **2013**, *135*, 6822–6825.

[113] G. Ao, C. Y. Khripin, M. Zheng, *J. Am. Chem. Soc.* **2014**, *136*, 10383–10392.

[114] J. A. Fagan, E. H. Hároz, R. Ihly, H. Gui, J. L. Blackburn, J. R. Simpson, S. Lam, A. R. Hight Walker, S. K. Doorn, M. Zheng, *ACS Nano* **2015**, *9*, 5377–5390.

[115] H. Li, G. Gordeev, O. Garrity, S. Reich, B. S. Flavel, *ACS Nano* **2019**, *13*, 2567–2578.

[116] B. Koh, G. Kim, H. K. Yoon, J. B. Park, R. Kopelman, W. Cheng, *Langmuir* **2012**, *28*, 11676–11686.

[117] R. J. Chen, Y. Zhang, D. Wang, H. Dai, *J. Am. Chem. Soc.* **2001**, *123*, 3838–3839.

[118] N. Nakashima, Y. Tomonari, H. Murakami, *Chem. Lett.* **2002**, *31*, 638–639.

[119] C. Ehli, G. M. A. Rahman, N. Jux, D. Balbinot, D. M. Guldi, F. Paolucci, M. Marcaccio, D. Paolucci, M. Melle-Franco, F. Zerbetto, S. Campidelli, M. Prato, *J. Am. Chem. Soc.* **2006**, *128*, 11222–11231.

[120] R. M. Tromp, A. Afzali, M. Freitag, D. B. Mitzi, Zh. Chen, *Nano Lett.* **2008**, *8*, 469–472.

[121] Z. Dai, L. Yan, Sk. M. Alam, J. Feng, P. R. D. Mariathomas, Y. Chen, C. M. Li, Q. Zhang, L.-J. Li, K. H. Lim, M. B. Chan-Park, *J. Phys. Chem. C* **2010**, *114*, 21035–21041.

[122] A. K. Sundramoorthy, S. Mesgari, J. Wang, R. Kumar, M. A. Sk., S. H. Yeap, Q. Zhang, S. K. Sze, K. H. Lim, M. B. Chan-Park, *J. Am. Chem. Soc.* **2013**, *135*, 5569–5581.

[123] J. Han, Q. Ji, H. Li, G. Li, S. Qiu, H.-B. Li, Q. Zhang, H. Jin, Q. Li, J. Zhang, *Chem. Commun.* **2016**, *52*, 7683–7686.

[124] H. Li, B. Zhou, Y. Lin, L. Gu, W. Wang, K. A. S. Fernando, S. Kumar, L. F. Allard, Y.-P. Sun, *J. Am. Chem. Soc.* **2004**, *126*, 1014–1015.

[125] X. Peng, N. Komatsu, S. Bhattacharya, T. Shimawaki, S. Aonuma, T. Kimura, A. Osuka, *Nat. Nanotechnol.* **2007**, *2*, 361–365.

[126] S. K. Samanta, M. Fritsch, U. Scherf, W. Gomulya, S. Z. Bisri, M. A. Loi, *Acc. Chem. Res.* **2014**, *47*, 2446–2456.

[127] D. Tuncel, *Nanoscale* **2011**, *3*, 3545–3554.

[128] T. Fujigaya, N. Nakashima, *Sci. Technol. Adv. Mater.* **2015**, *16*, 024802.

[129] W. Gomulya, G. D. Costanzo, E. J. F. de Carvalho, S. Z. Bisri, V. Derenskyi, M. Fritsch, N. Fröhlich, S. Allard, P. Gordiichuk, A. Herrmann, S. J. Marrink, M. C. dos Santos, U. Scherf, M. A. Loi, *Adv. Mater.* **2013**, *25*, 2948–2956.

[130] M. Tange, T. Okazaki, S. Iijima, *J. Am. Chem. Soc.* **2011**, *133*, 11908–11911.

[131] N. Berton, F. Lemasson, J. Tittmann, N. Stürzl, F. Hennrich, M. M. Kappes, M. Mayor, *Chem. Mater.* **2011**, *23*, 2237–2249.

[132] N. Berton, F. Lemasson, A. Poschlad, V. Meded, F. Tristram, W. Wenzel, F. Hennrich, M. M. Kappes, M. Mayor, *Small* **2014**, *10*, 360–367.

[133] H. Ozawa, N. Ide, T. Fujigaya, Y. Niidome, N. Nakashima, *Chem. Lett.* **2011**, *40*, 239–241.

[134] N. A. Rice, A. V. Subrahmanyam, B. R. Coleman, A. Adronov, *Macromolecules* **2015**, *48*, 5155–5161.

[135] F. A. Lemasson, T. Strunk, P. Gerstel, F. Hennrich, S. Lebedkin, C. Barner-Kowollik, W. Wenzel, M. M. Kappes, M. Mayor, *J. Am. Chem. Soc.* **2011**, *133*, 652–655.

[136] F. Lemasson, N. Berton, J. Tittmann, F. Hennrich, M. M. Kappes, M. Mayor, *Macromolecules* **2012**, *45*, 713–722.

[137] A. Chortos, I. Pochorovski, P. Lin, G. Pitner, X. Yan, T. Z. Gao, J. W. F. To, T. Lei, J. W. Will, H.-S. P. Wong, Z. Bao, *ACS Nano* **2017**, *11*, 5660–5669.

[138] B. Norton-Baker, R. Ihly, I. E. Gould, A. D. Avery, Z. R. Owczarczyk, A. J. Ferguson, J. L. Blackburn, *ACS Energy Lett.* **2016**, *1*, 1212–1220.

[139] W. Z. Wang, W. F. Li, X. Y. Pan, C. M. Li, L.-J. Li, Y. G. Mu, J. A. Rogers, M. B. Chan-Park, *Adv. Funct. Mater.* **2011**, *21*, 1643–1651.

[140] F. Lemasson, J. Tittmann, F. Hennrich, N. Stürzl, S. Malik, M. M. Kappes, M. Mayor, *Chem. Commun.* **2011**, *47*, 7428–7430.

[141] S. Liang, Y. Zhao, A. Adronov, *J. Am. Chem. Soc.* **2014**, *136*, 970–977.

[142] F. Toshimitsu, N. Nakashima, *Nat. Commun.* **2014**, *5*, 5041.

[143] I. Pochorovski, H. Wang, J. I. Feldblyum, X. Zhang, A. L. Antaris, Z. Bao, *J. Am. Chem. Soc.* **2015**, *137*, 4328–4331.

[144] T. Z. Gao, Z. Sun, X. Yan, H.-C. Wu, H. Yan, Z. Bao, *Small* **2020**, *16*, 2000923.

[145] P. Gerstel, S. Klumpp, F. Hennrich, A. Poschlad, V. Meded, E. Blasco, W. Wenzel, M. M. Kappes, C. Barner-Kowollik, *ACS Macro Lett.* **2014**, *3*, 10–15.

[146] W. Gomulya, V. Derenskyi, E. Kozma, M. Pasini, M. A. Loi, *Adv. Funct. Mater.* **2015**, *25*, 5858–5864.

[147] C. Kanimozhi, G. J. Brady, M. J. Shea, P. Huang, Y. Joo, M. S. Arnold, P. Gopalan, *ACS Appl. Mater. Interfaces* **2017**, *9*, 40734–40742.

[148] M. J. Shea, R. D. Mehlenbacher, M. T. Zanni, M. S. Arnold, *J. Phys. Chem. Lett.* **2014**, *5*, 3742–3749.

[149] P. Deria, C. D. Von Bargen, J.-H. Olivier, A. S. Kumbhar, J. G. Saven, M. J. Therien, *J. Am. Chem. Soc.* **2013**, *135*, 16220–16234.

[150] D. Fong, A. Adronov, *Chem. Sci.* **2017**, *8*, 7292–7305.

[151] Y. Kanai, J. C. Grossman, *Nano Lett.* **2008**, *8*, 908–912.

[152] X. Peng, N. Komatsu, T. Kimura, A. Osuka, *J. Am. Chem. Soc.* **2007**, *129*, 15947–15953.

[153] X. Peng, N. Komatsu, T. Kimura, A. Osuka, *ACS Nano* **2008**, *2*, 2045–2050.

[154] S.-Y. Ju, D. C. Abanulo, C. A. Badalucco, J. A. Gascón, F. Papadimitrakopoulos, *J. Am. Chem. Soc.* **2012**, *134*, 13196–13199.

[155] X. Wei, T. Tanaka, T. Hirakawa, Y. Yomogida, H. Kataura, *J. Am. Chem. Soc.* **2017**, *139*, 16068–16071.

[156] A. A. Green, M. C. Duch, M. C. Hersam, *Nano Res.* **2009**, *2*, 69–77.

[157] H. Liu, T. Tanaka, H. Kataura, *Nano Lett.* **2014**, *14*, 6237–6243.

[158] T. Tanaka, Y. Urabe, T. Hirakawa, H. Kataura, *Anal. Chem.* **2015**, *87*, 9467–9472.

[159] G. Dukovic, M. Balaz, P. Doak, N. D. Berova, M. Zheng, R. S. Mclean, L. E. Brus, *J. Am. Chem. Soc.* **2006**, *128*, 9004–9005.

[160] G. Ao, J. K. Streit, J. A. Fagan, M. Zheng, *J. Am. Chem. Soc.* **2016**, *138*, 16677–16685.

[161] K. Akazaki, F. Toshimitsu, H. Ozawa, T. Fujigaya, N. Nakashima, *J. Am. Chem. Soc.* **2012**, *134*, 12700–12707.

[162] X. Li, X. Zhang, W. Li, Y. Wang, T. Liu, B. Zhang, W. Yang, *J. Mater. Chem.* **2011**, *21*, 3916–3924.

[163] J. Rotzler, D. Vonlanthen, A. Barsella, A. Boeglin, A. Fort, M. Mayor, *Eur. J. Org. Chem.* **2010**, *2010*, 1096–1110.

[164] J. P. Wolfe, J. Åhman, J. P. Sadighi, R. A. Singer, S. L. Buchwald, *Tetrahedron Lett.* **1997**, *38*, 6367–6370.

[165] S. Hossain, P. K. Roy, C. Zakaria, *Int. J. Chem. Stud.* **2018**, *6*, 19-31.

[166] J. Ding, Z. Li, J. Lefebvre, F. Cheng, G. Dubey, S. Zou, P. Finnie, A. Hrdina, L. Scoles, G. P. Lopinski, C. T. Kingston, B. Simard, P. R. L. Malenfant, *Nanoscale* **2014**, *6*, 2328–2339.

[167] K. Mulla, S. Liang, H. Shaik, E. A. Younes, A. Adronov, Y. Zhao, *Chem. Comm.* **2015**, *51*, 149–152.

[168] M. S. Strano, M. Zheng, A. Jagota, G. B. Onoa, D. A. Heller, P. W. Barone, M. L. Usrey, *Nano Lett.* **2004**, *4*, 543–550.

[169] A. Nish, J.-Y. Hwang, J. Doig, R. J. Nicholas, *Nat. Nanotechnol.* **2007**, *2*, 640-646.

[170] D. Fong, A. Adronov, *Macromolecules* **2017**, *50*, 8002–8009.

[171] D. A. Tsyboulski, J.-D. R. Rocha, S. M. Bachilo, L. Cognet, R. B. Weisman, *Nano Lett.* **2007**, *7*, 3080–3085.

[172] S. van Bezouw, D. H. Arias, R. Ihly, S. Cambré, A. J. Ferguson, J. Campo, J. C. Johnson, J. Defillet, W. Wenseleers, J. L. Blackburn, *ACS Nano* **2018**, *12*, 6881–6894.

[173] J. Ding, M. Day, G. Robertson, J. Roovers, *Macromolecules* **2002**, *35*, 3474–3483.

[174] N. Sakai, S. Matile, *J. Am. Chem. Soc.* **2018**, *140*, 11438–11443.

[175] J. M. Seco, E. Quiñoá, R. Riguera, *Chem. Rev.* **2012**, *112*, 4603–4641.

[176] N. H. Oberlies, J. Rivera-Chávez, *J. Nat. Prod.* **2017**, *80*, 1231–1231.

[177] J. A. Dale, D. L. Dull, H. S. Mosher, *J. Org. Chem.* **1969**, *34*, 2543–2549.

[178] J. A. Dale, H. S. Mosher, *J. Am. Chem. Soc.* **1973**, *95*, 512–519.

[179] A. Cimmino, M. Masi, M. Evidente, S. Superchi, A. Evidente, *J. Pharm. Biomed. Anal.* **2017**, *144*, 59–89.

[180] D. A. Allen, A. E. Tomaso, O. P. Priest, D. F. Hindson, J. L. Hurlburt, *J. Chem. Educ.* **2008**, *85*, 698.

[181] J. Tomasi, B. Mennucci, R. Cammi, *Chem. Rev.* **2005**, *105*, 2999–3094.

[182] R. E. Stratmann, G. E. Scuseria, M. J. Frisch, *J. Chem. Phys.* **1998**, *109*, 8218–8224.

[183] J. Llano, L. A. Eriksson, *Phys. Chem. Chem. Phys.* **2004**, *6*, 4707–4713.

[184] L. Goerigk, S. Grimme, *J. Phys. Chem. A* **2009**, *113*, 767–776.

[185] T. Miyahara, H. Nakatsuji, *J. Phys. Chem. A* **2018**, *122*, 100–118.

[186] M. J. Frisch, G. W. Trucks, H. B. Schlegel, G. E. Scuseria, M. A. Robb, J. R. Cheeseman, G. Scalmani, V. Barone, B. Mennucci, G. A. Petersson, H. Nakatsuji, M. Caricato, X. Li, H. P. Hratchian, A. F. Izmaylov, J. Bloino, G. Zheng, J. L. Sonnenberg, M. Hada, M. Ehara, K. Toyota, R. Fukuda, J. Hasegawa, M. Ishida, T. Nakajima, Y. Honda, O. Kitao, H. Nakai, T. Vreven, J. A. Montgomery Jr, J. E. Peralta, F. Ogliaro, M. Bearpark, J. J. Heyd, E. Brothers, K. N. Kudin, V. N. Staroverov, T. Keith, R. Kobayashi, J. Normand, K. Raghavachari, A. Rendell, J. C. Burant, S. S. Iyengar, J. Tomasi, M. Cossi, N. Rega, J. M. Millam, M. Klene, J. E. Knox, J. B. Cross, V. Bakken, C. Adamo, J. Jaramillo, R. Gomperts, R. E. Stratmann, O. Yazyev, A. J. Austin, R. Cammi, C. Pomelli, J. W. Ochterski, R. L. Martin, K. Morokuma, V. G. Zakrzewski, G. A. Voth, P. Salvador, J. J. Dannenberg, S. Dapprich, A. D. Daniels, O. Farkas, J. B. Foresman, J. V. Ortiz, J. Ioslowski, D. J. Fox, Gaussian 09, RevisionB.01, Gaussian, Inc., Wallingford CT, **2010**.

[187] N. M. O'boyle, A. L. Tenderholt, K. M. Langner, *J. Comput. Chem.* **2008**, *29*, 839–845.

[188] T. Yamada, K. Nomura, M. Fujiki, *Macromolecules* **2018**, *51*, 2377–2387.

[189] H. Telg, J. G. Duque, M. Staiger, X. Tu, F. Hennrich, M. M. Kappes, M. Zheng, J. Maultzsch, C. Thomsen, S. K. Doorn, *ACS Nano* **2012**, *6*, 904–911.

[190] K.-C. Chuang, A. Nish, J.-Y. Hwang, G. W. Evans, R. J. Nicholas, *Phys. Rev. B* **2008**, *78*, 085411.

[191] G. Ao, J. K. Streit, J. A. Fagan, M. Zheng, *J. Am. Chem. Soc.* **2016**, *138*, 16677–16685.

[192] T. Lei, X. Chen, G. Pitner, H.-S. P. Wong, Z. Bao, *J. Am. Chem. Soc.* **2016**, *138*, 802–805.

[193] S. Lebedkin, P. Schweiss, B. Renker, S. Malik, F. Hennrich, M. Neumaier, C. Stoermer, M. M. Kappes, *Carbon* **2002**, *40*, 417–423.

[194] A. Sarkar, Q. Wang, A. Schiele, M. R. Chellali, S. S. Bhattacharya, D. Wang, T. Brezesinski, H. Hahn, L. Velasco, B. Breitung, *Adv. Mater.* **2019**, *31*, 1806236.

[195] W. Humphrey, A. Dalke, K. Schulten, *J. Mol. Graph.* **1996**, *14*, 33–38.

[196] TURBOMOLE V7.0 2015, a development of University of Karlsruhe and Forschungszentrum Karlsruhe GmbH, 1989-2007, TURBOMOLE GmbH, since 2007, available from http://www.turbomole.com.

[197] D. A. Case, K. Belfon, I. Y. Ben-Shalom, S. R. Brozell, D. S. Cerutti, T. E. Cheatham, V. W. D. Cruzeiro, T. A. Darden, R. E. Duke, G. Giambasu, M. K. Gilson, H. Gohlke, A. W. Goetz, R. Harris, S. Izadi, S. A. Izmailov, K. Kasavajhala, A. Kovalenko, R. Krasny, T. Kurtzman, T. S. Lee, S. LeGrand, P. Li, C. Lin, J. Liu, T. Luchko, R. Luo, V. Man, K. M. Merz, Y. Miao, O. Mikhailovskii, G. Monard, H. Nguyen, A. Onufriev, F. Pan, S. Pantano, R. Qi, D. R. Roe, A. Roitberg, C. Sagui, S. Schott-Verdugo, J. Shen, C. L. Simmerling, N. R. Skrynnikov, J. Smith, J. Swails, R. C. Walker, J. Wang, L. Wilson, R. M. Wolf, X. Wu, Y. Xiong, Y. Xue, D. M. York, P. A. Kollman, **2020**. AMBER 2020. University of California, San Francisco.

[198] T. Strunk, M. Wolf, M. Brieg, K. Klenin, A. Biewer, F. Tristram, M. Ernst, P. J. Kleine, N. Heilmann, I. Kondov, W. Wenzel, *J. Comput. Chem.* **2012**, *33*, 2602–2613.

[199] L. Martínez, R. Andrade, E. G. Birgin, J. M. Martínez, *J. Comput. Chem.* **2009**, *30*, 2157–2164.

[200] S. Plimpton, *J. Comput. Phys.* **1995**, *117*, 1–19.

[201] H. Sun, *J. Phys. Chem. B* **1998**, *102*, 7338–7364.

[202] H. Sun, Z. Jin, C. Yang, R. L. C. Akkermans, S. H. Robertson, N. A. Spenley, S. Miller, S. M. Todd, *J. Mol. Model* **2016**, *22*, 47.

[203] M. Deserno, C. Holm, *J. Chem. Phys.* **1998**, *109*, 7694–7701.

8 Appendix

8.1 NMR spectra for Mosher analysis

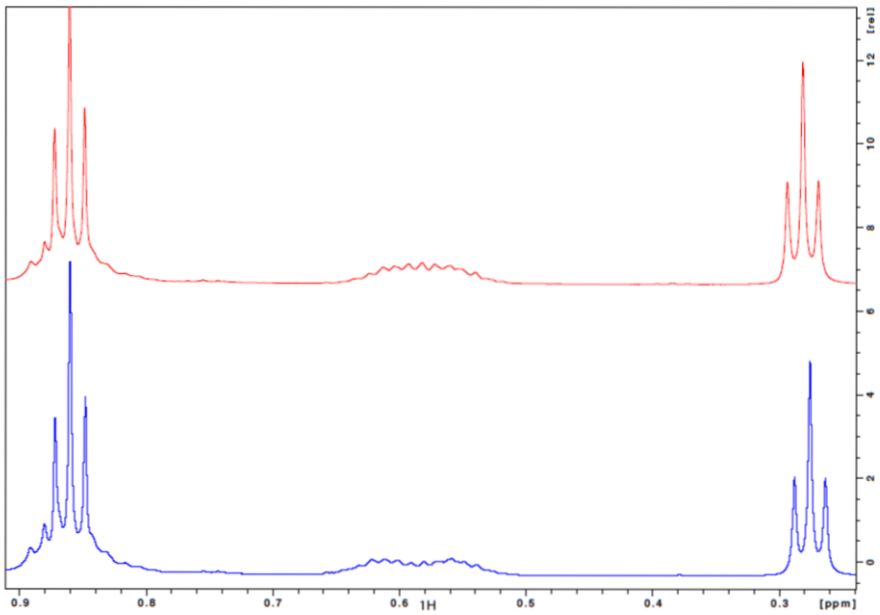

Figure 8.1. High field part of the ^{1}H-NMR spectra (600 MHz, $CDCl_3$) of (*R*)-Mosher-**M3-1** (red) and (*R*)-Mosher-**M3-2** (blue).

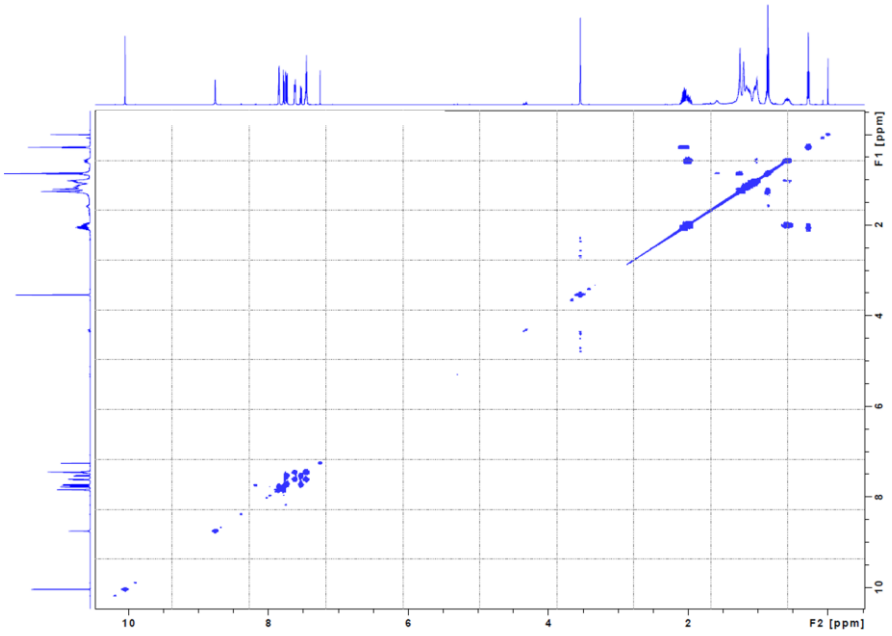

Figure 8.2. COSY spectrum (600 MHz, $CDCl_3$) of (*R*)-Mosher-**M3-1**.

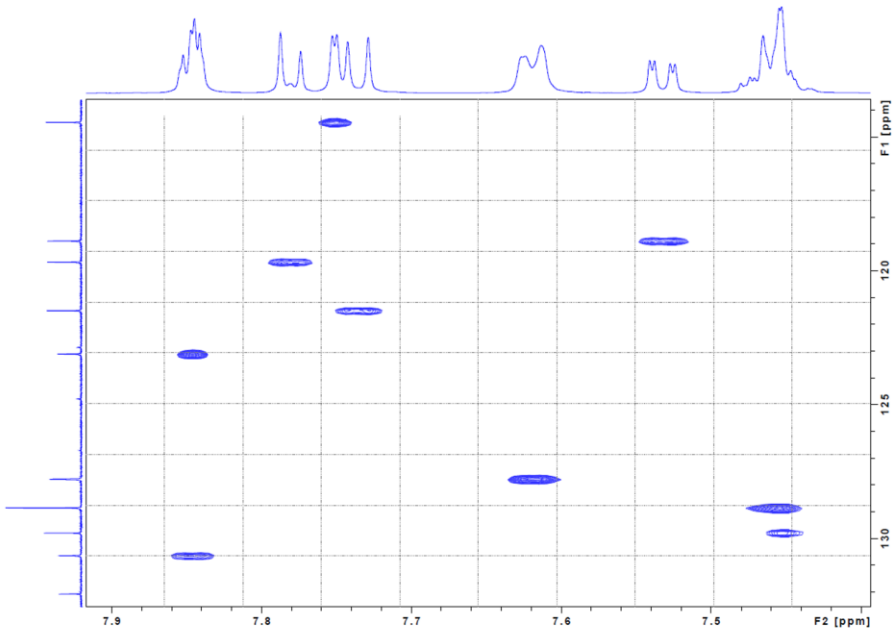

Figure 8.3. Aromatic region of the HSQC spectrum (600 MHz, $CDCl_3$) of (*R*)-Mosher-**M3-1**.

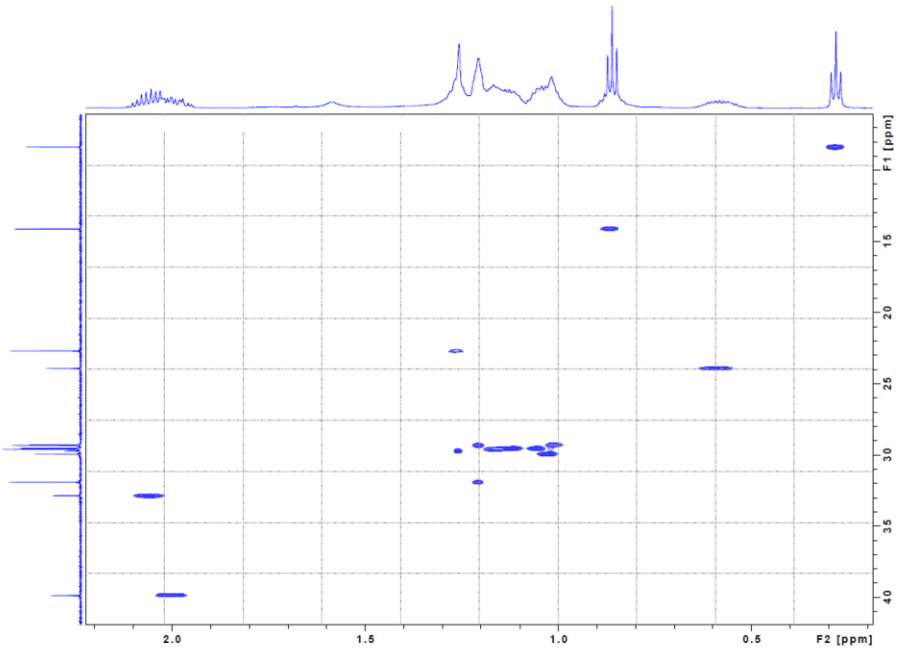

Figure 8.4. Aliphatic region of the HSQC spectrum (600 MHz, $CDCl_3$) of (*R*)-Mosher-**M3-1**.

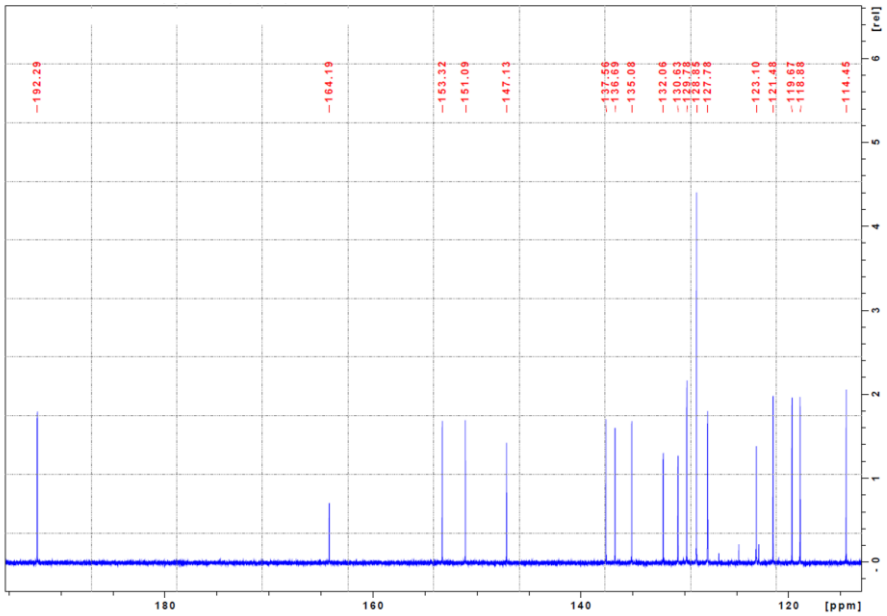

Figure 8.5. Aromatic region of the $^{13}C\{^1H\}$ spectrum (151 MHz, $CDCl_3$) of (*R*)-Mosher-**M3-1**.

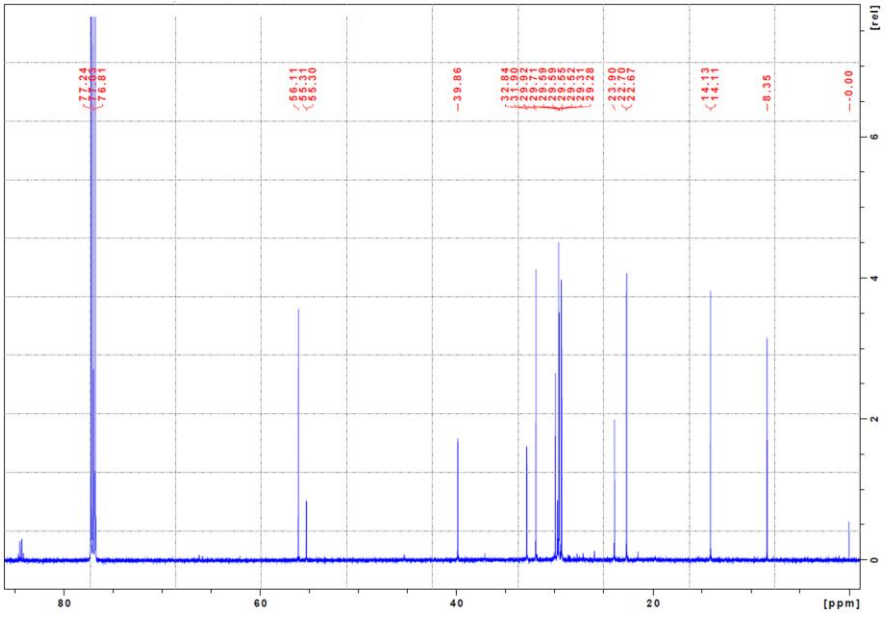

Figure 8.6. Aliphatic region of the $^{13}C\{^{1}H\}$ spectrum (151 MHz, $CDCl_3$) of (*R*)-Mosher-**M3-1**.

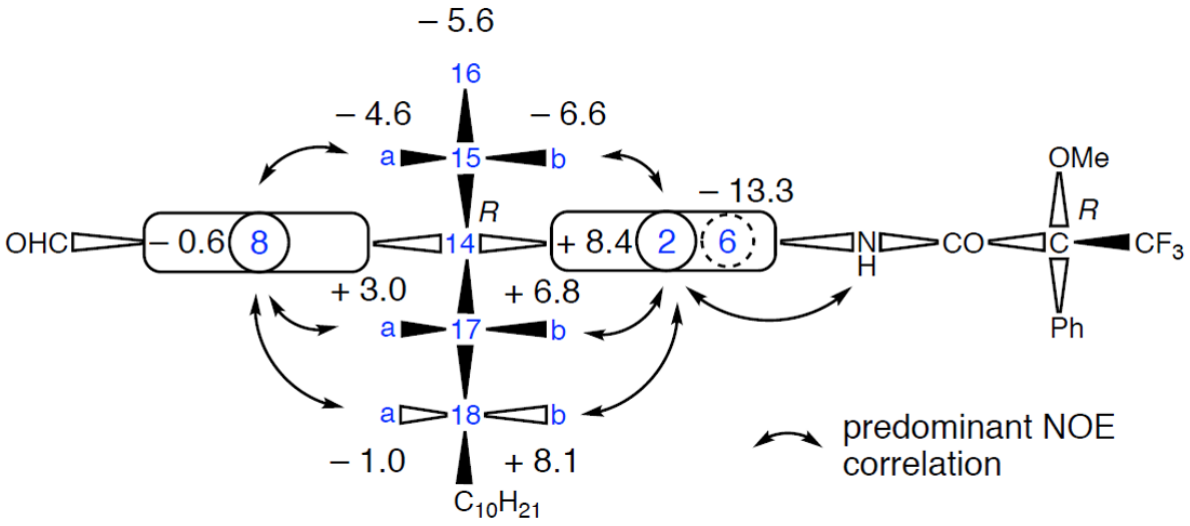

Figure 8.7. Schematic view on (*R*)-Mosher-**M3-1** amide from above C-14. $\Delta\delta^{S-R}$ values are indicated in black, atom numbering in blue.

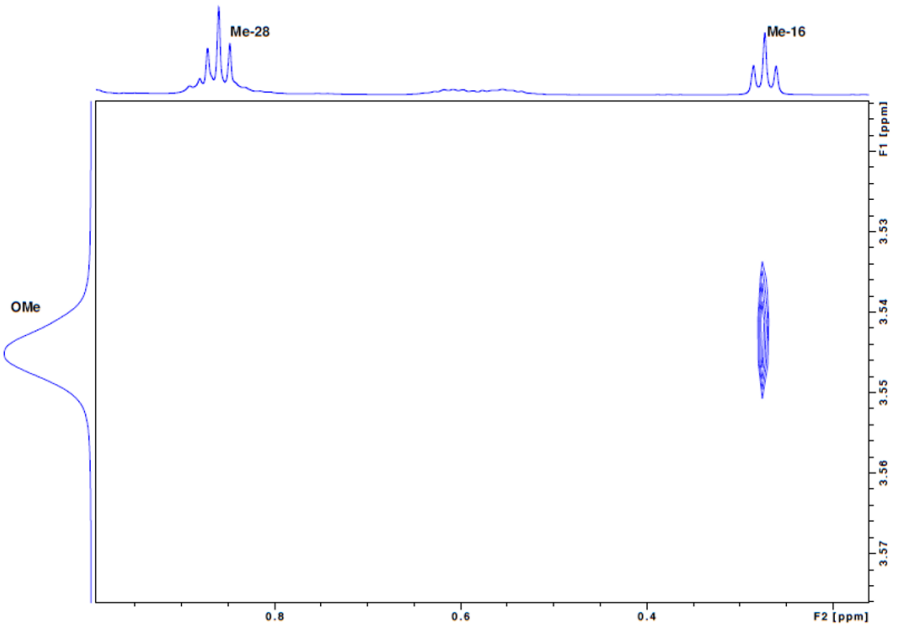

Figure 8.8. Selected region of the NOESY spectrum (600 MHz, $CDCl_3$) of (*R*)-Mosher-**M3-1**.

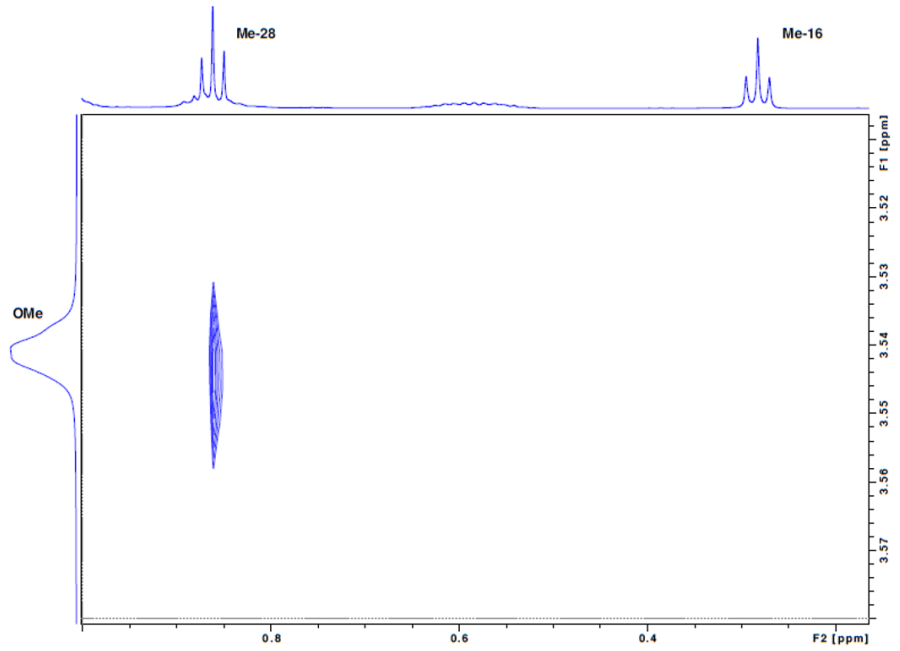

Figure 8.9. Selected region of the NOESY spectrum (600 MHz, $CDCl_3$) of (*R*)-Mosher-**M3-2**.

8.2 Characterization of enantiomerically separated CoMoCAT SWCNTs

The pristine CoMoCAT SWCNTs were dispersed in toluene and vigorously sonicated before the measurement.

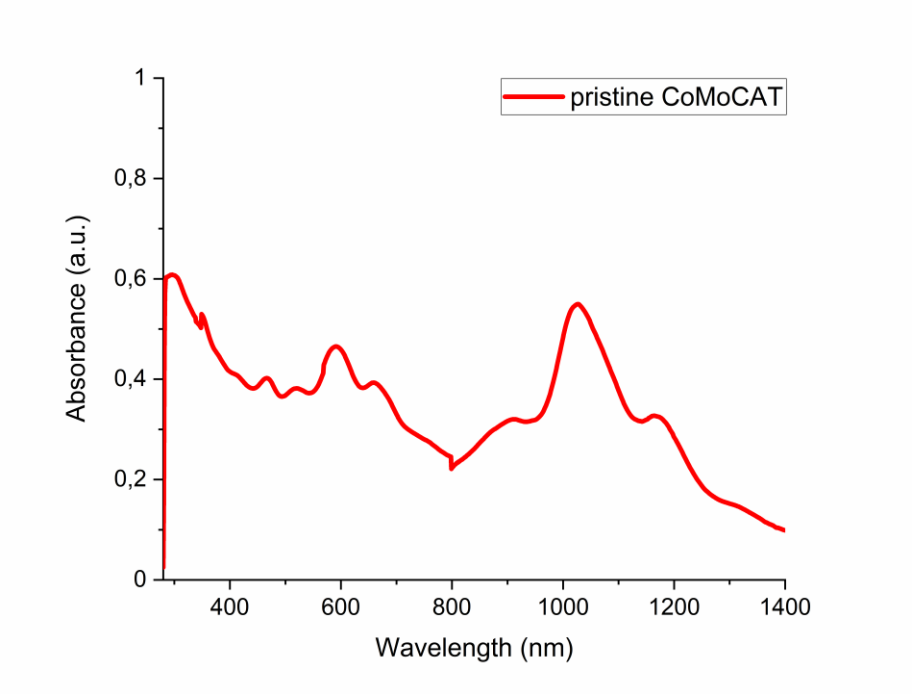

Figure 8.10. Absorption spectrum of pristine CoMoCAT SWCNTs. The sample was measured in toluene at room temperature.

Absorption spectra of neat **ACP** polymer and **ACP** wrapped CoMoCAT SWCNTs for better clarification of the overlapped area. The peak at 345 nm belongs to E_{33} of (6,5) SWCNT.

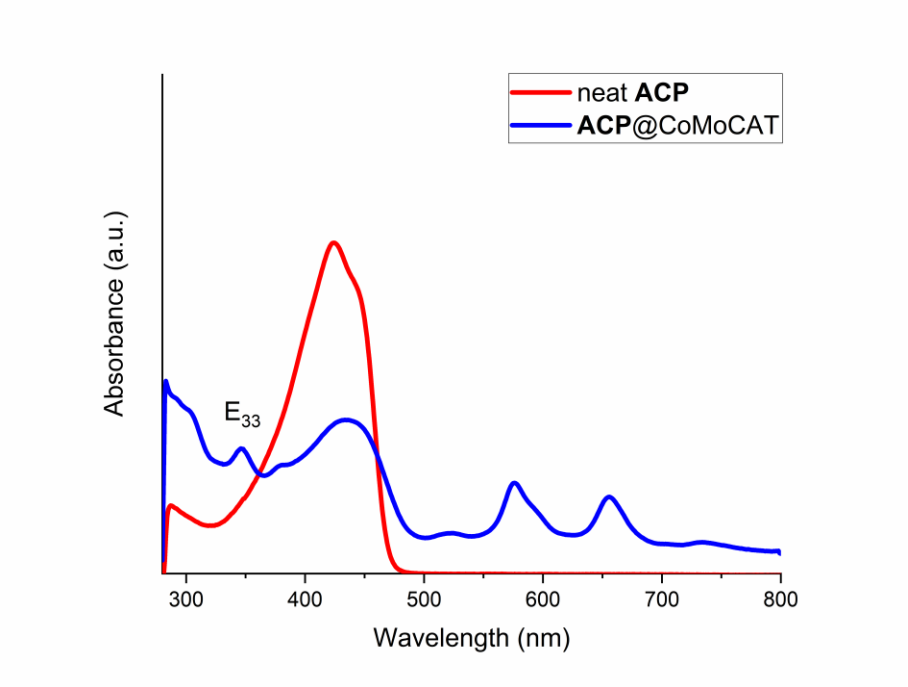

Figure 8.11. Absorption spectra of neat **ACP** polymer and **ACP** wrapped CoMoCAT SWCNTs. All samples were measured in toluene at room temperature.

8.3 ^{1}H and ^{13}C NMR spectra of all new compounds

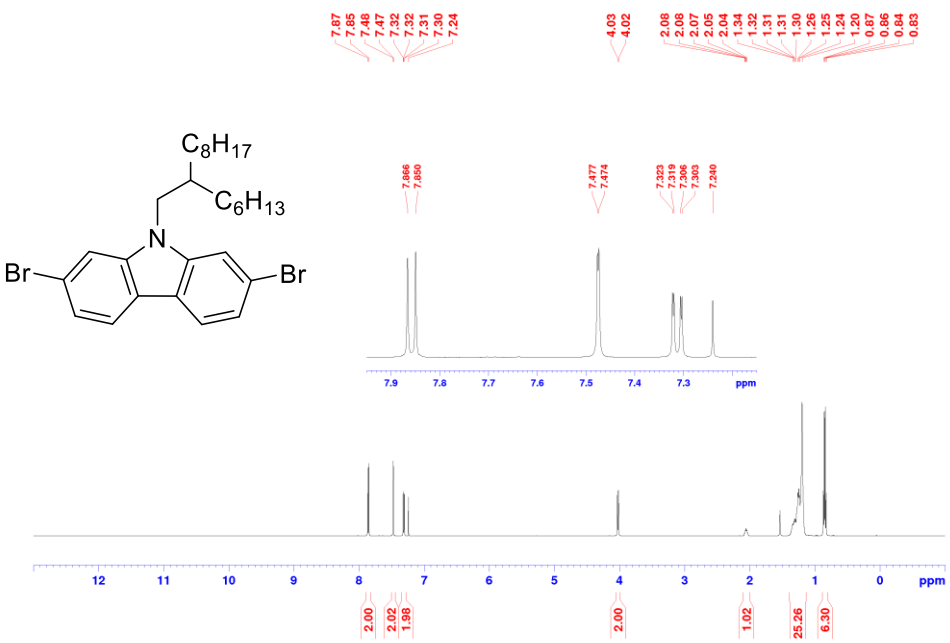

Figure 8.12. ^{1}H NMR spectrum (500 MHz, $CDCl_3$) of **2**.

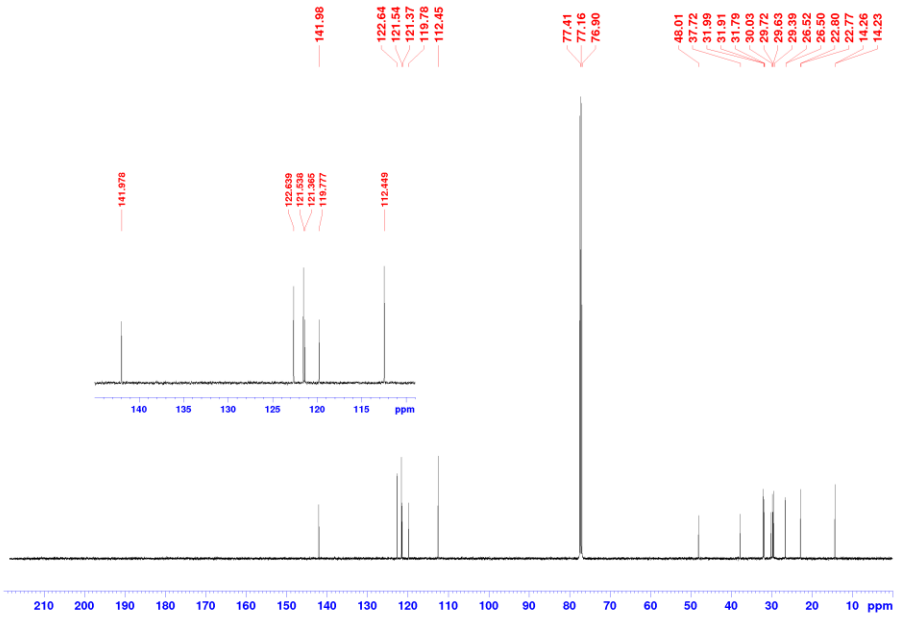

Figure 8.13. ^{13}C NMR spectrum (125 MHz, $CDCl_3$) of **2**.

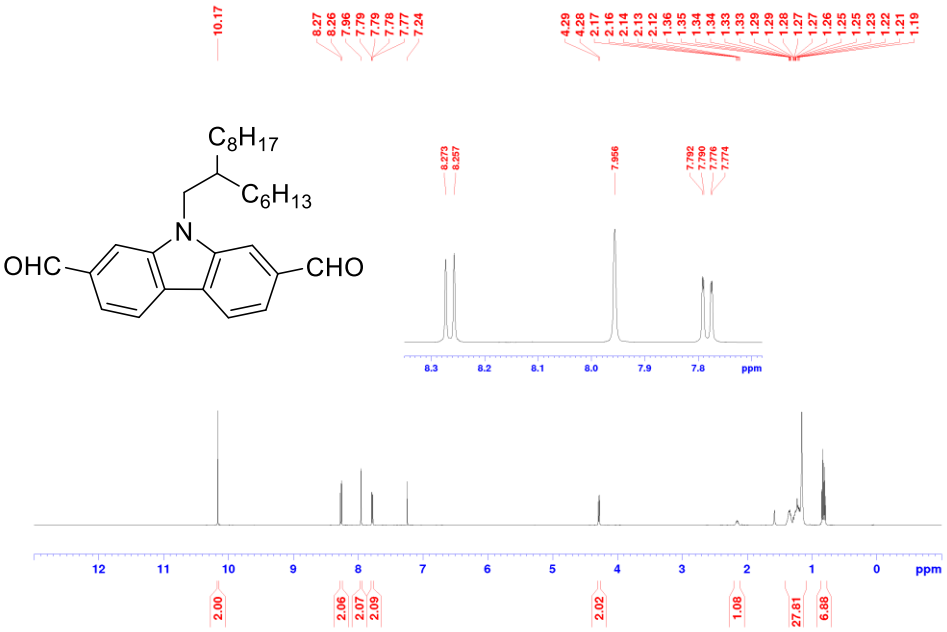

Figure 8.14. ^{1}H NMR spectrum (500 MHz, $CDCl_3$) of **M1**.

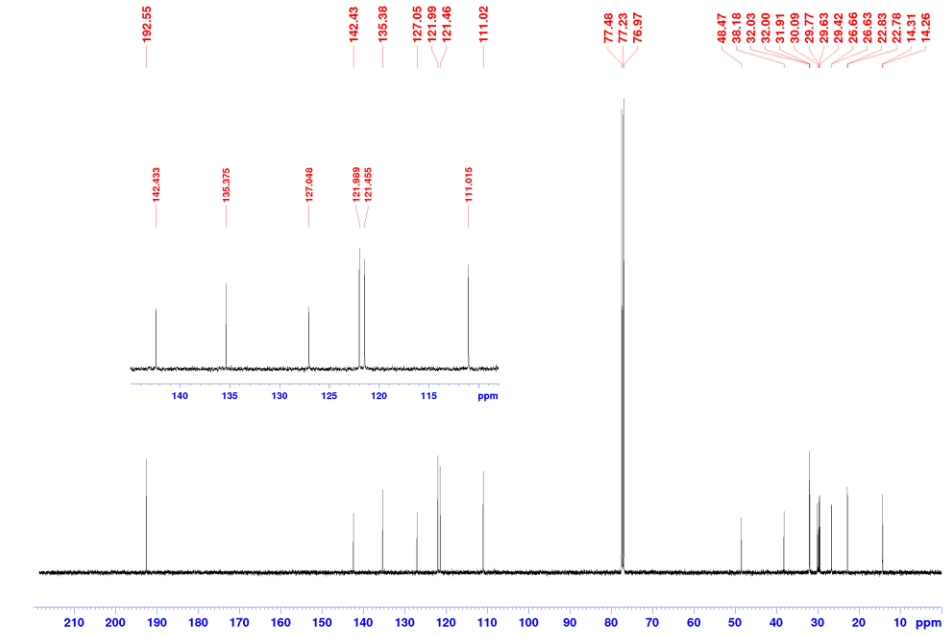

Figure 8.15. ^{13}C NMR spectrum (125 MHz, $CDCl_3$) of **M1**.

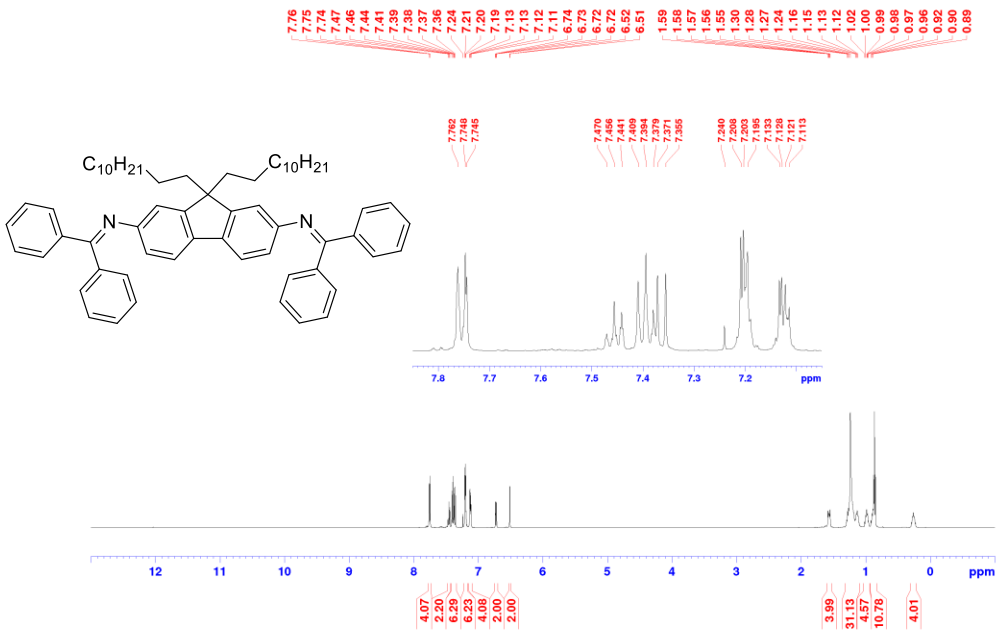

Figure 8.16. ^{1}H NMR spectrum (500 MHz, $CDCl_3$) of **4**.

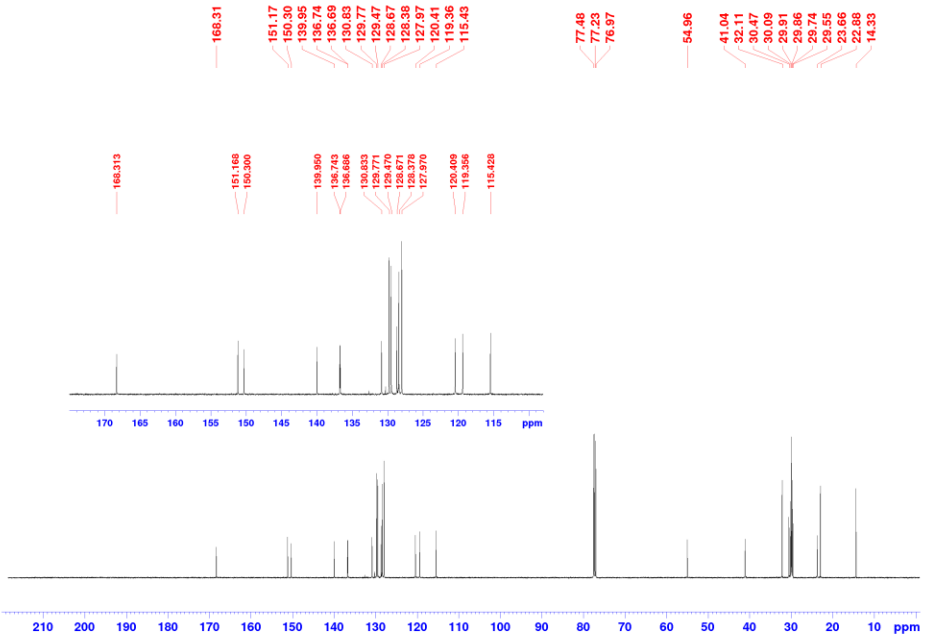

Figure 8.17. ^{13}C NMR spectrum (125 MHz, $CDCl_3$) of **4**.

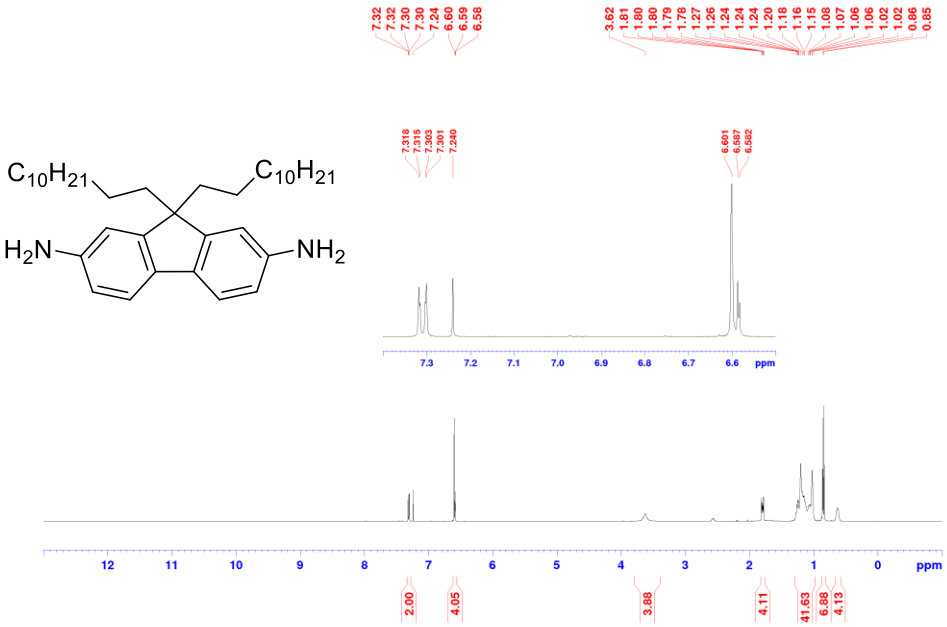

Figure 8.18. ^{1}H NMR spectrum (500 MHz, $CDCl_3$) of **M2**.

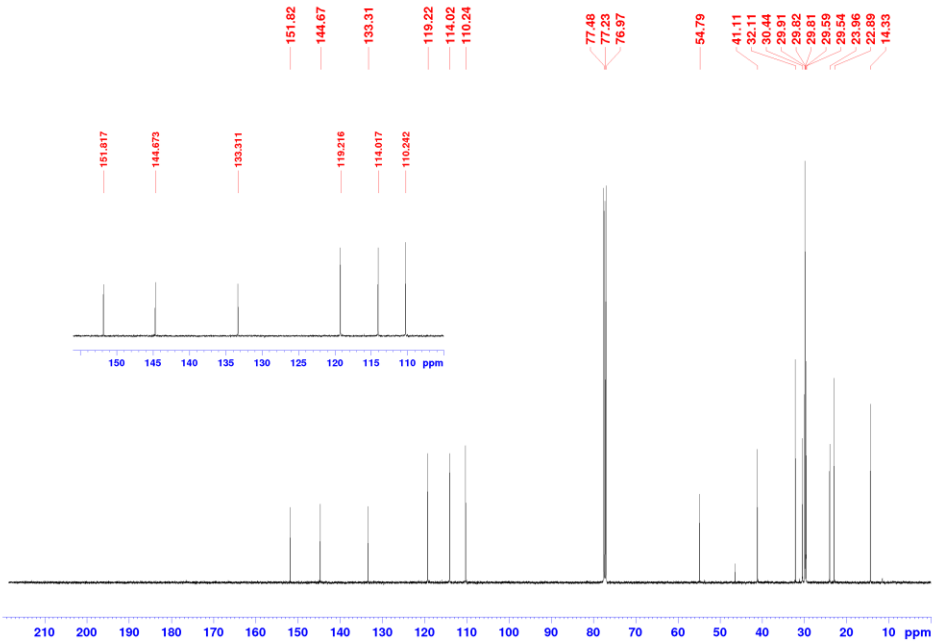

Figure 8.19. ^{13}C NMR spectrum (125 MHz, $CDCl_3$) of **M2**.

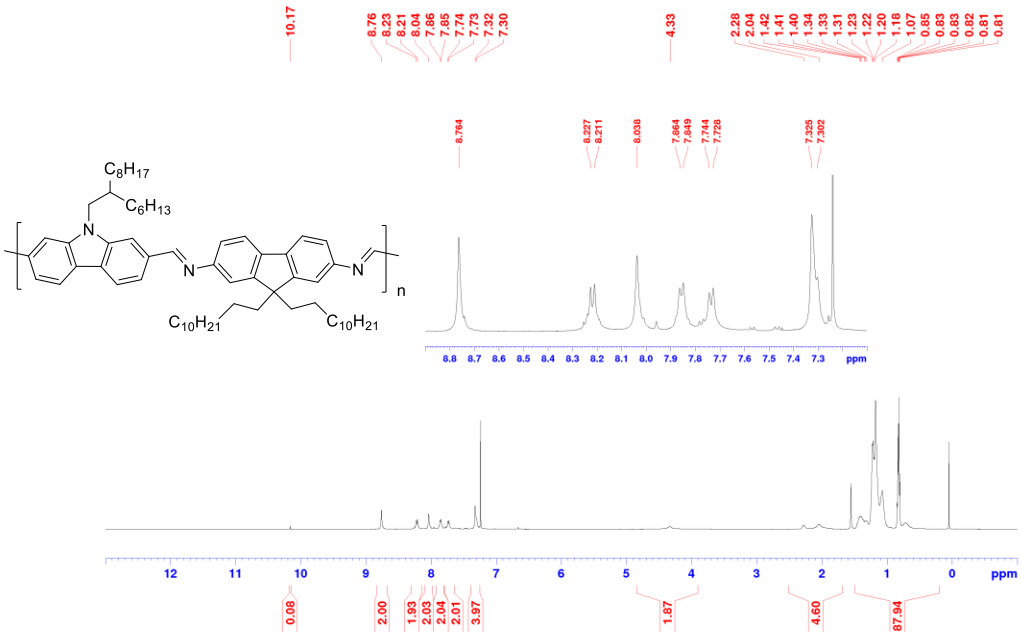

Figure 8.20. ^{1}H NMR spectrum (500 MHz, $CDCl_3$) of **P1**.

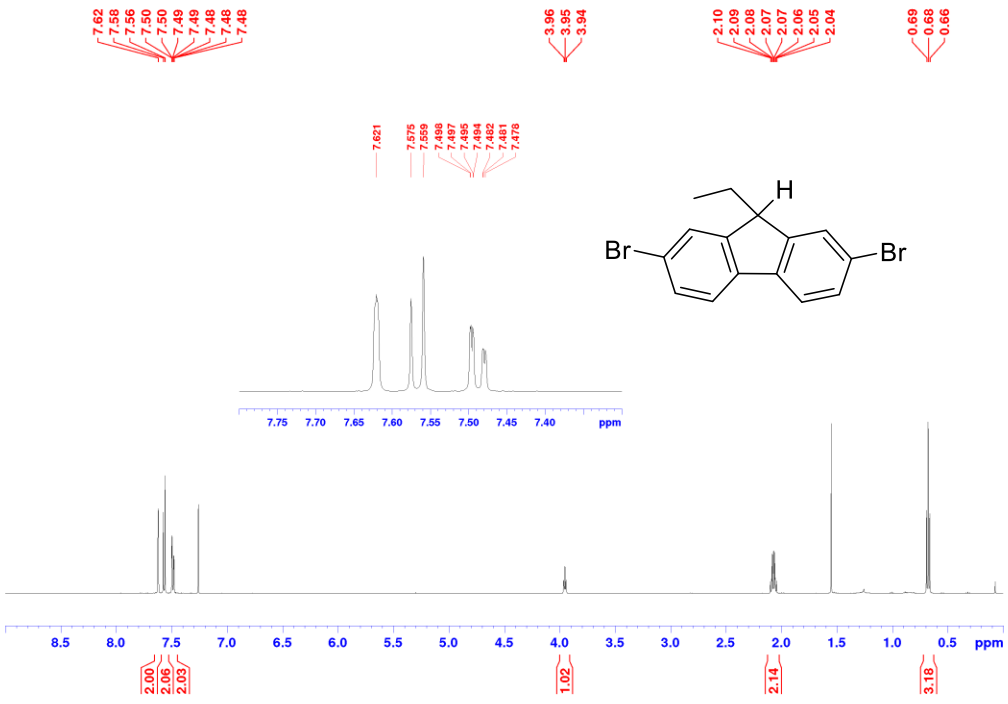

Figure 8.21. ^{1}H NMR spectrum (500 MHz, $CDCl_3$) of **6**.

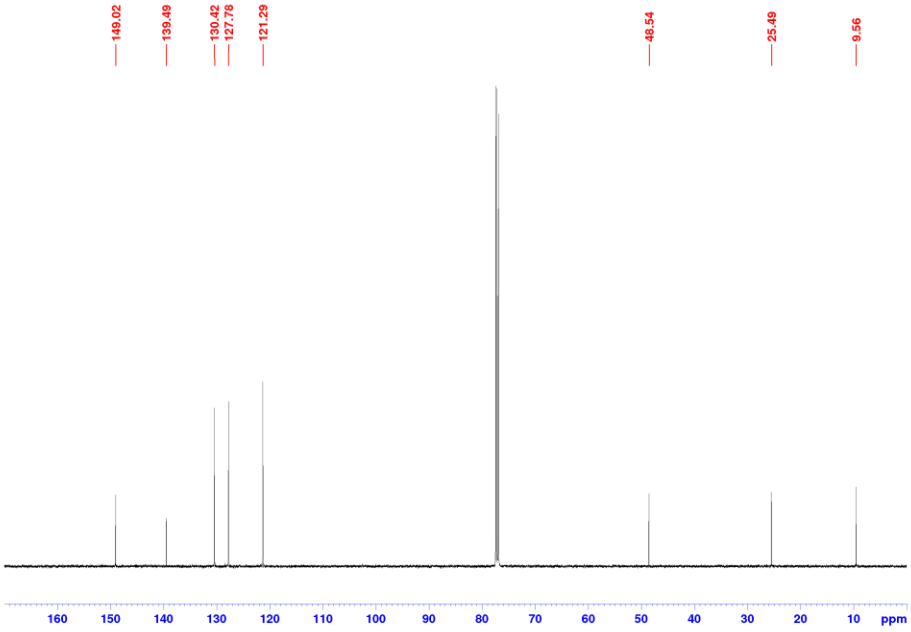

Figure 8.22. ^{13}C NMR spectrum (125 MHz, $CDCl_3$) of **6**.

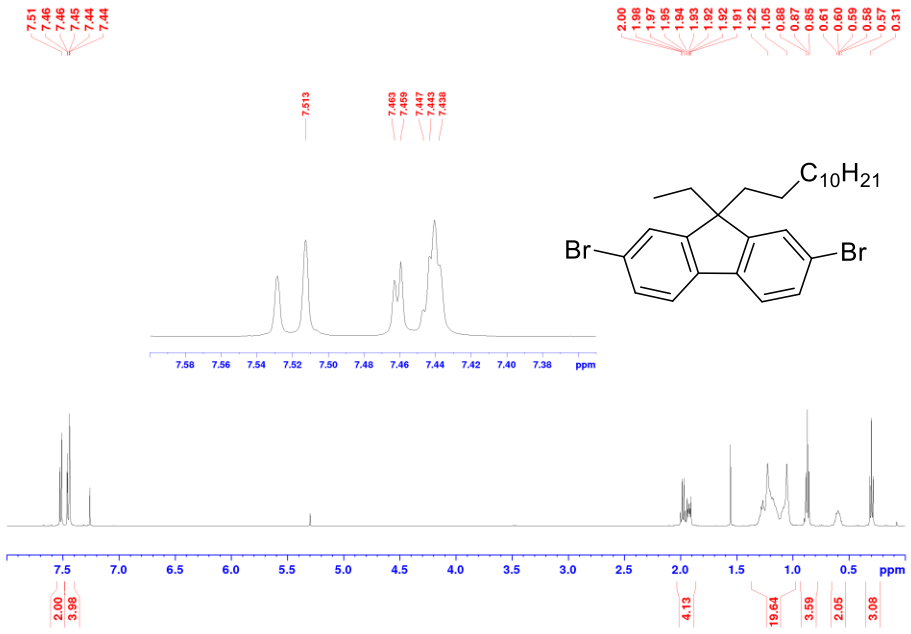

Figure 8.23. ^{1}H NMR spectrum (500 MHz, $CDCl_3$) of **7**.

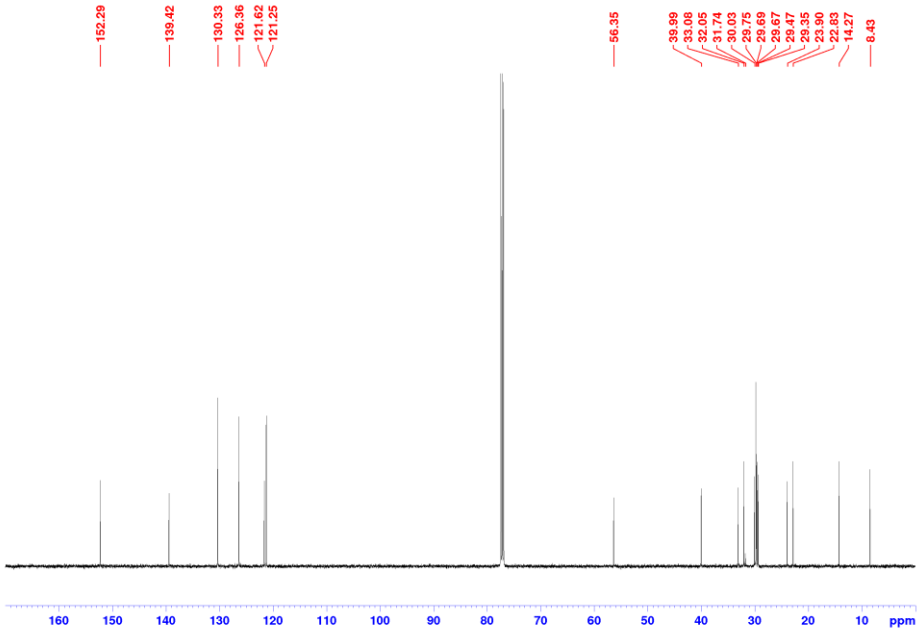

Figure 8.24. ^{13}C NMR spectrum (125 MHz, $CDCl_3$) of **7**.

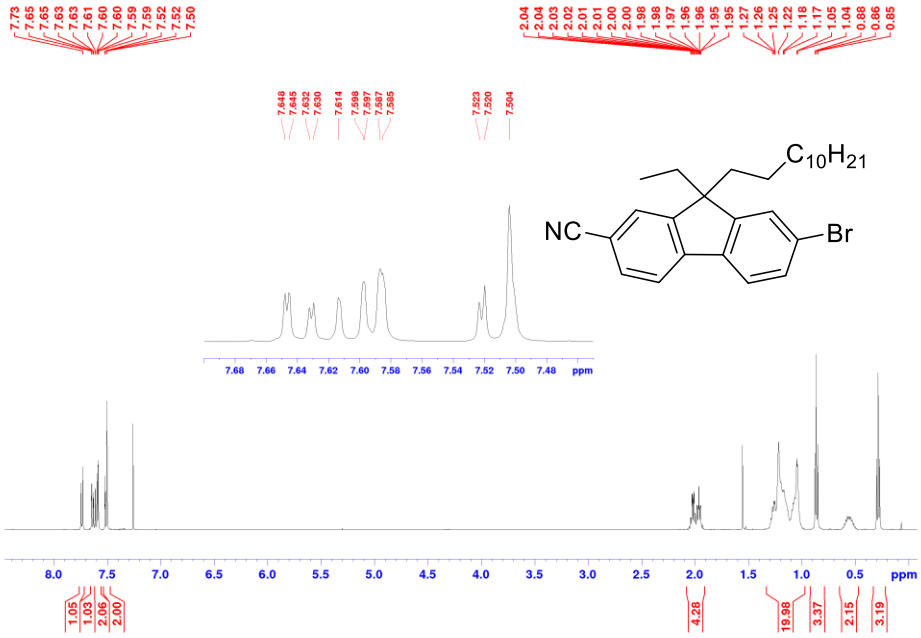

Figure 8.25. ^{1}H NMR spectrum (500 MHz, $CDCl_3$) of **8**.

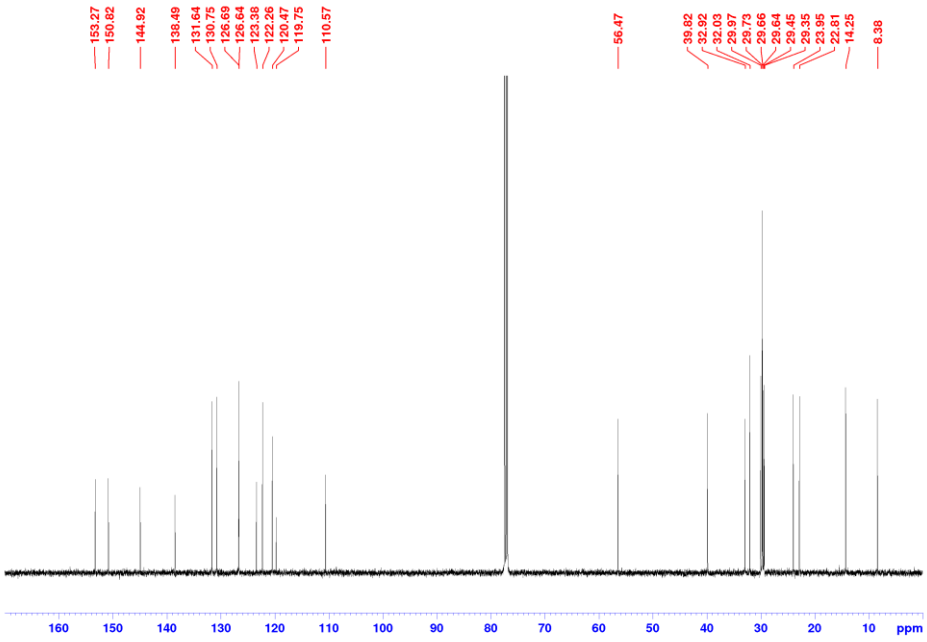

Figure 8.26. ^{13}C NMR spectrum (125 MHz, $CDCl_3$) of **8**.

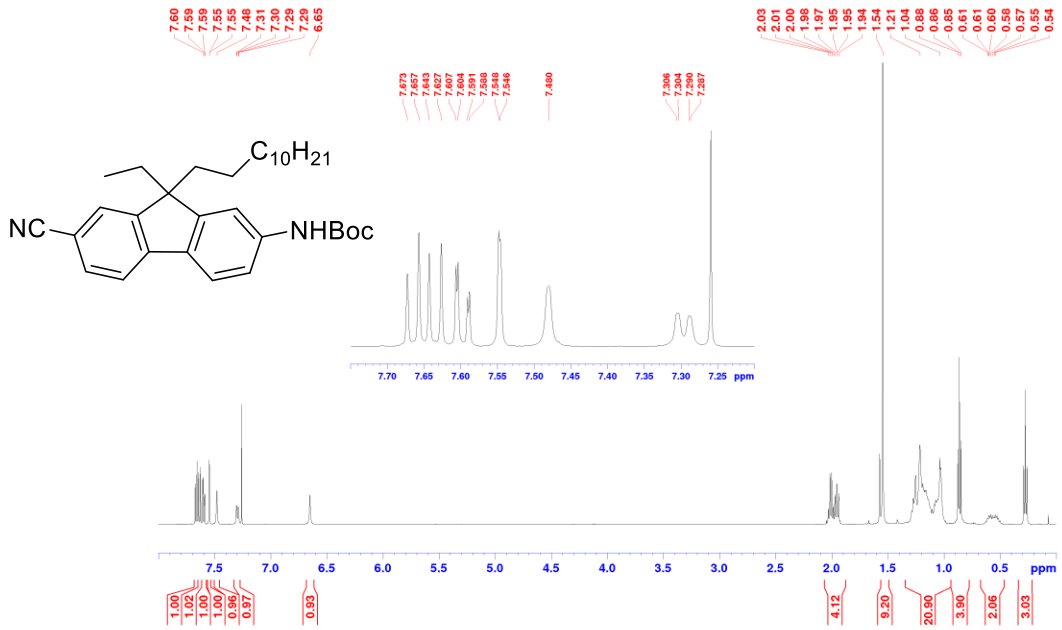

Figure 8.27. ^{1}H NMR spectrum (500 MHz, $CDCl_3$) of **9**.

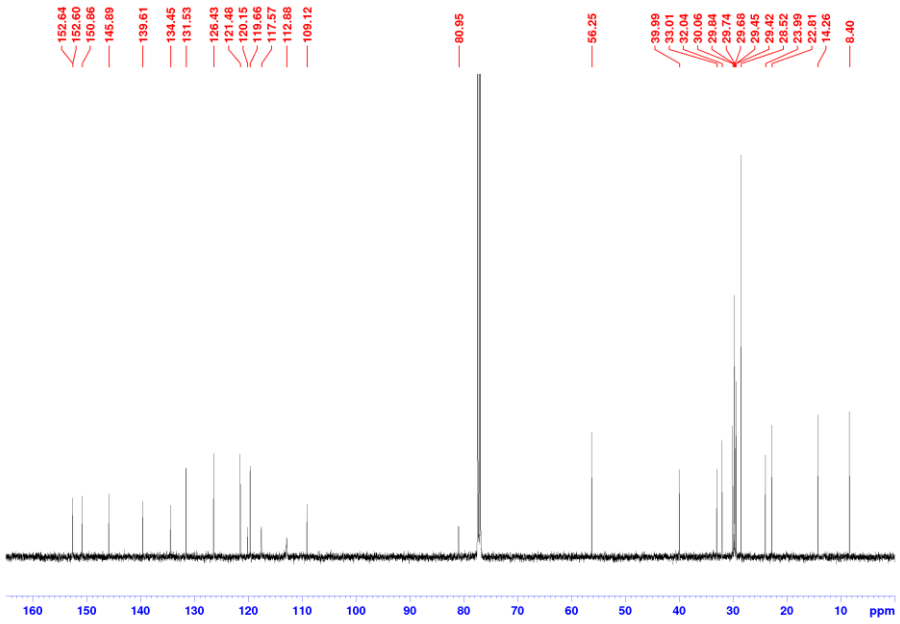

Figure 8.28. ^{13}C NMR spectrum (125 MHz, $CDCl_3$) of **9**.

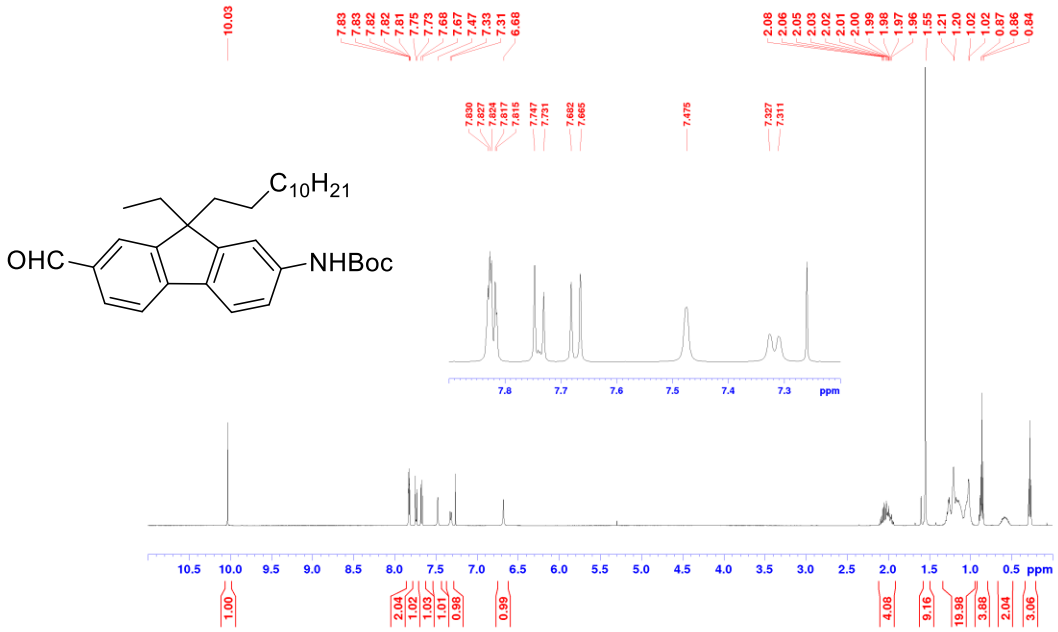

Figure 8.29. ^{1}H NMR spectrum (500 MHz, $CDCl_3$) of **M3**.

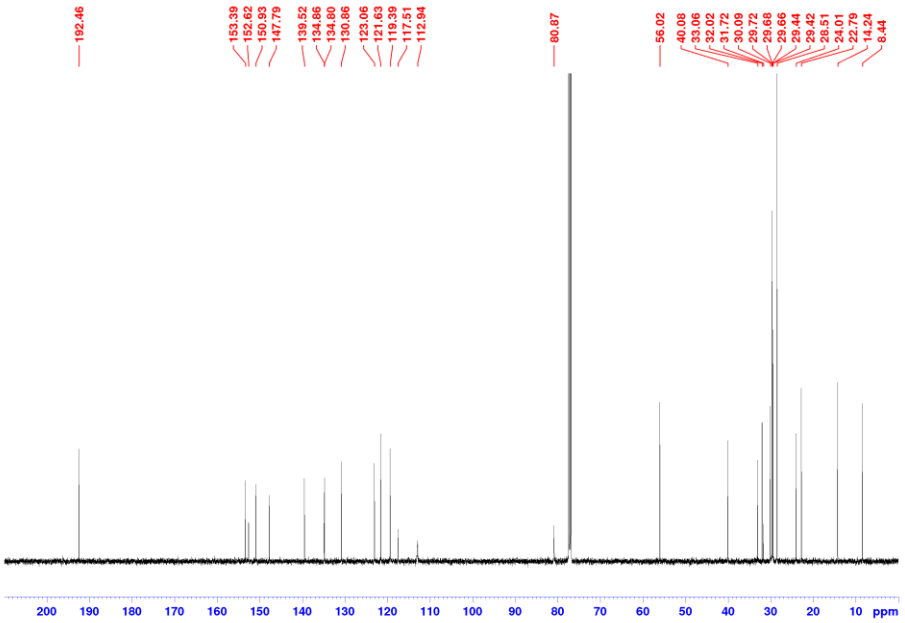

Figure 8.30. ^{13}C NMR spectrum (125 MHz, $CDCl_3$) of **M3**.

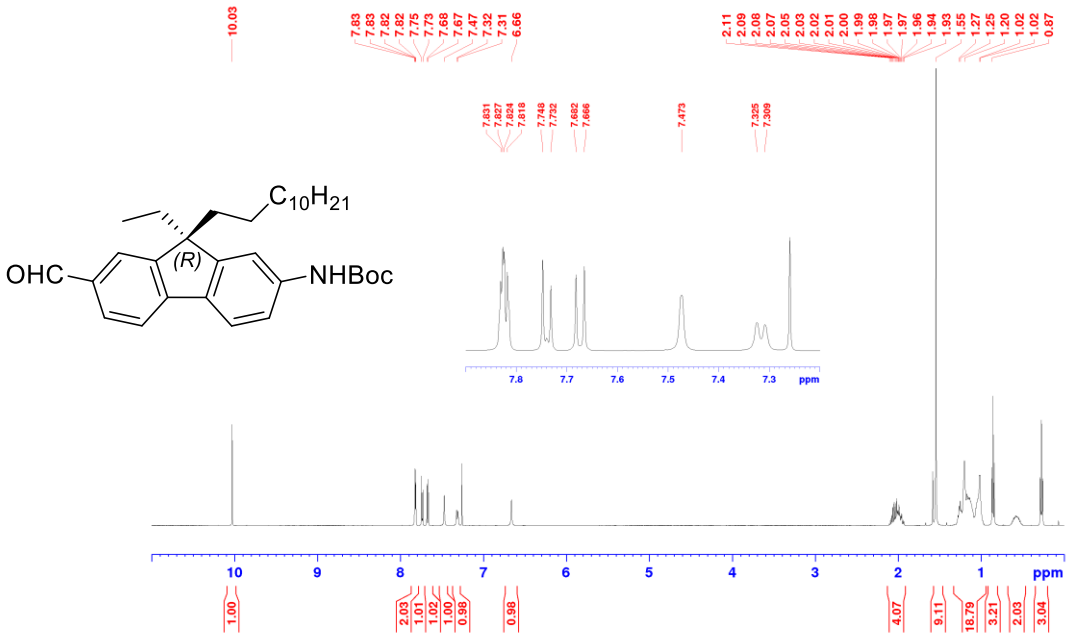

Figure 8.31. ^{1}H NMR spectrum (500 MHz, $CDCl_3$) of **(*R*)-M3**.

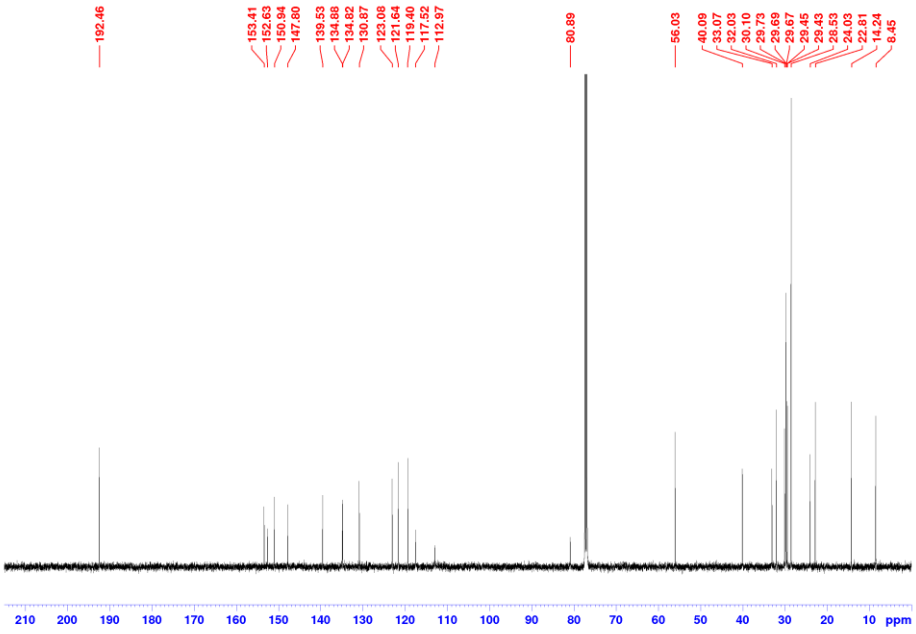

Figure 8.32. ^{13}C NMR spectrum (125 MHz, $CDCl_3$) of **(*R*)-M3**.

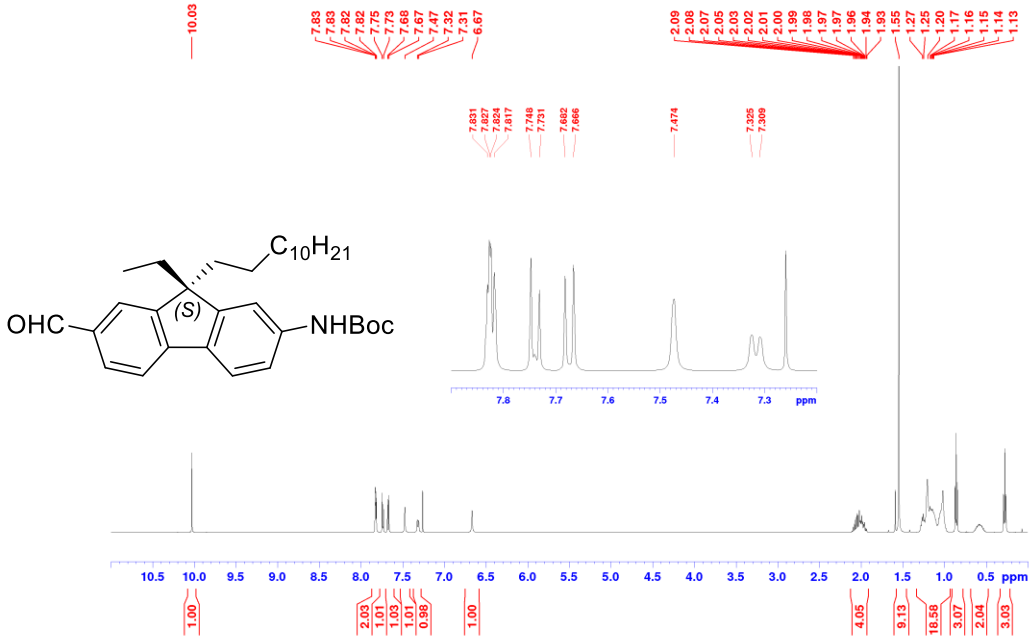

Figure 8.33. ^{1}H NMR spectrum (500 MHz, $CDCl_3$) of **(*S*)-M3**.

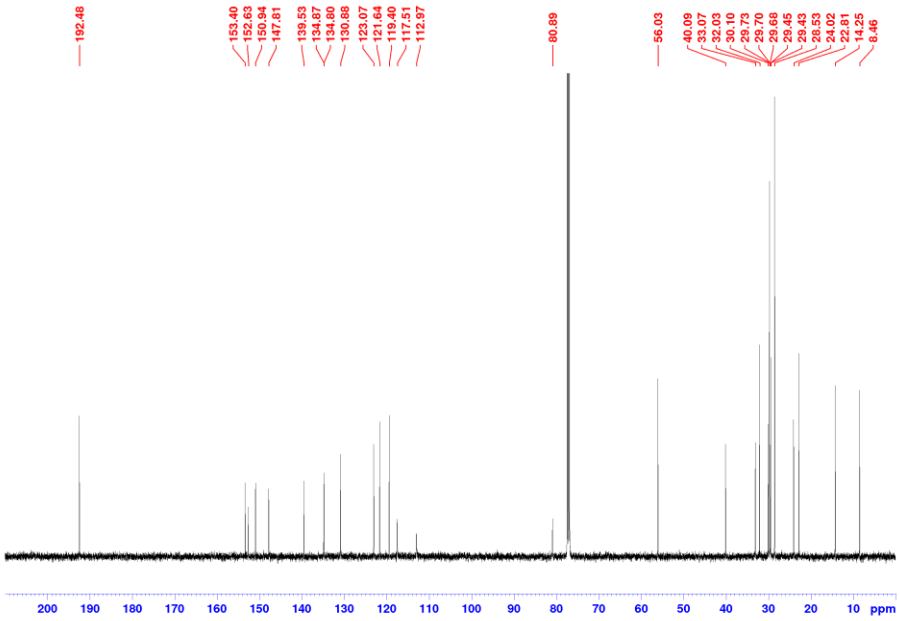

Figure 8.34. ^{13}C NMR spectrum (125 MHz, $CDCl_3$) of **(*S*)-M3**.

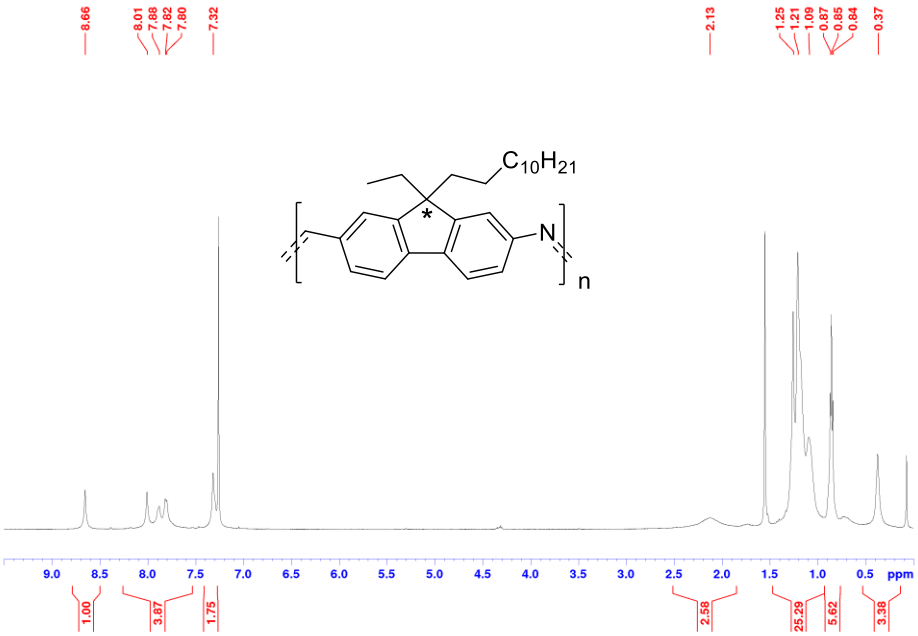

Figure 8.35. ^{1}H NMR spectrum (500 MHz, $CDCl_3$) of **ACP**.

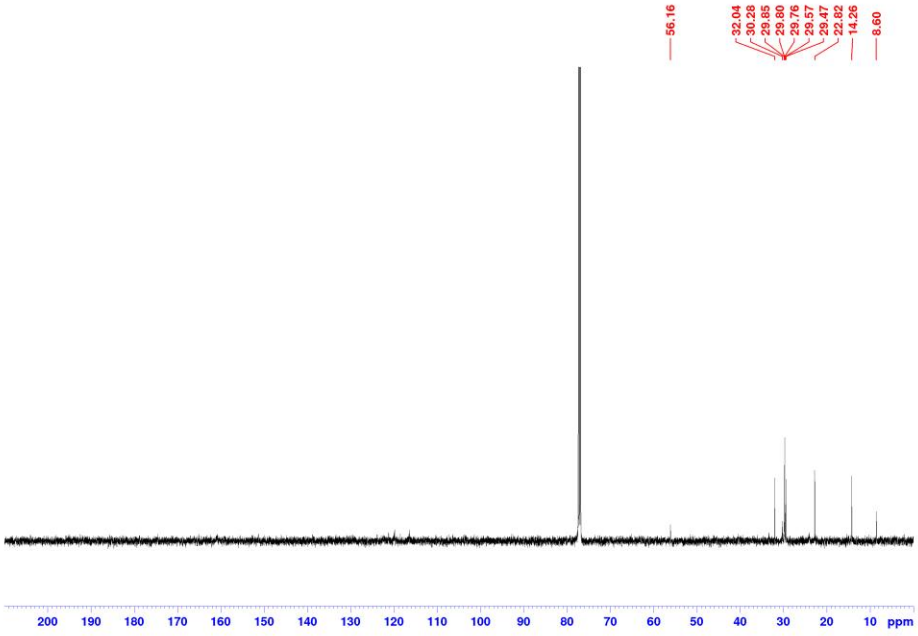

Figure 8.36. ^{13}C NMR spectrum (125 MHz, $CDCl_3$) of **ACP**.

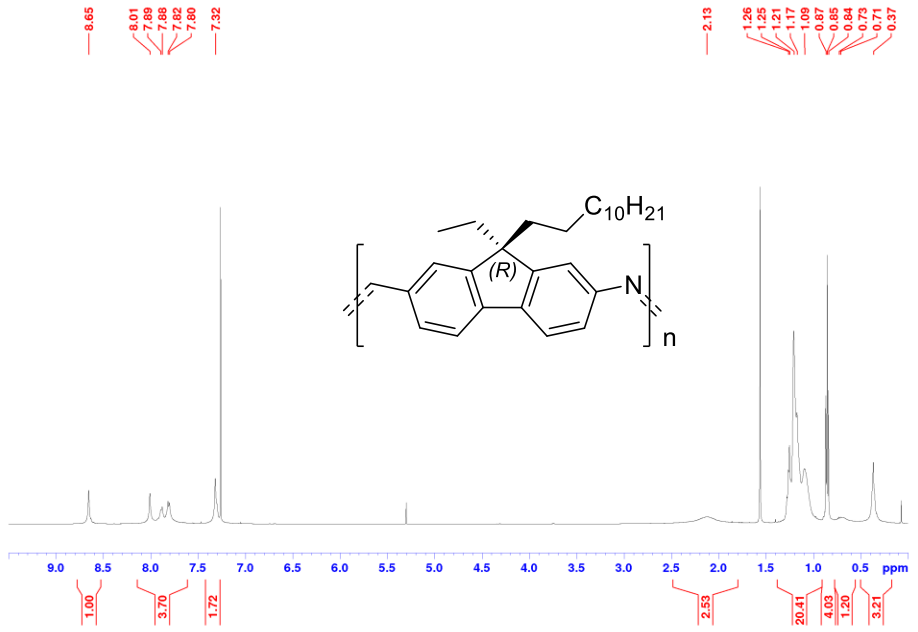

Figure 8.37. ^{1}H NMR spectrum (500 MHz, $CDCl_3$) of **(*R*)-CP**.

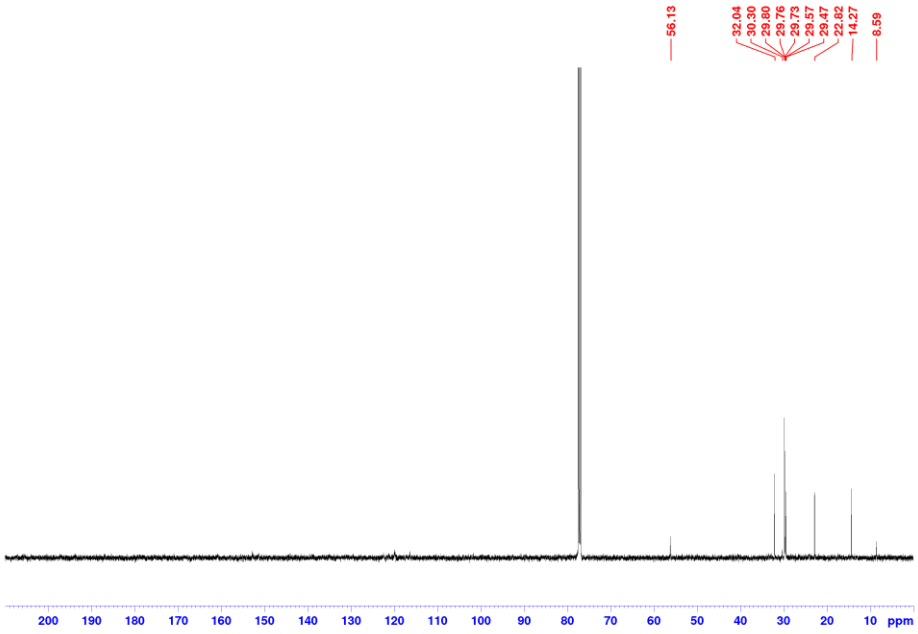

Figure 8.38. ^{13}C NMR spectrum (125 MHz, $CDCl_3$) of **(*R*)-CP**.

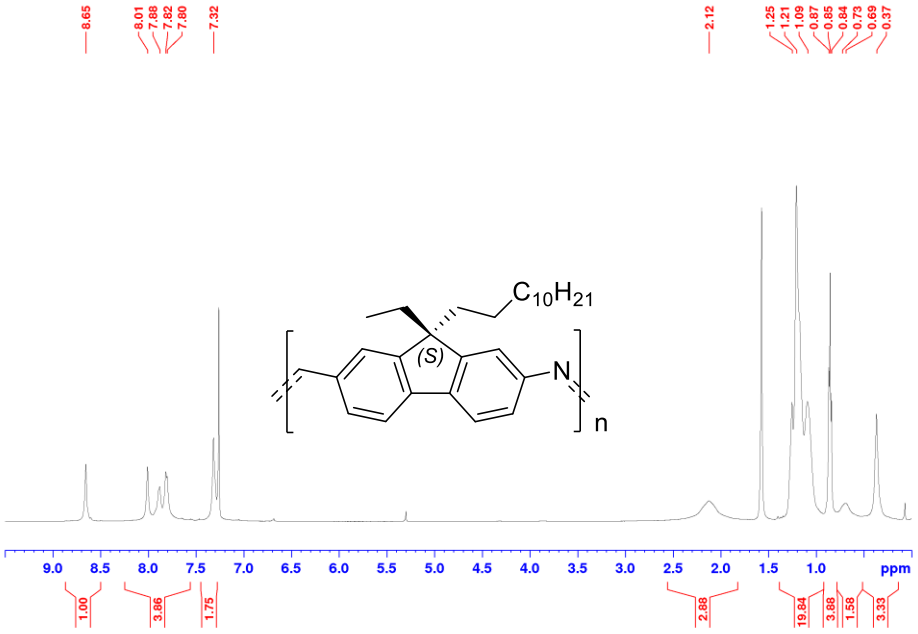

Figure 8.39. ^{1}H NMR spectrum (500 MHz, $CDCl_3$) of **(*S*)-CP**.

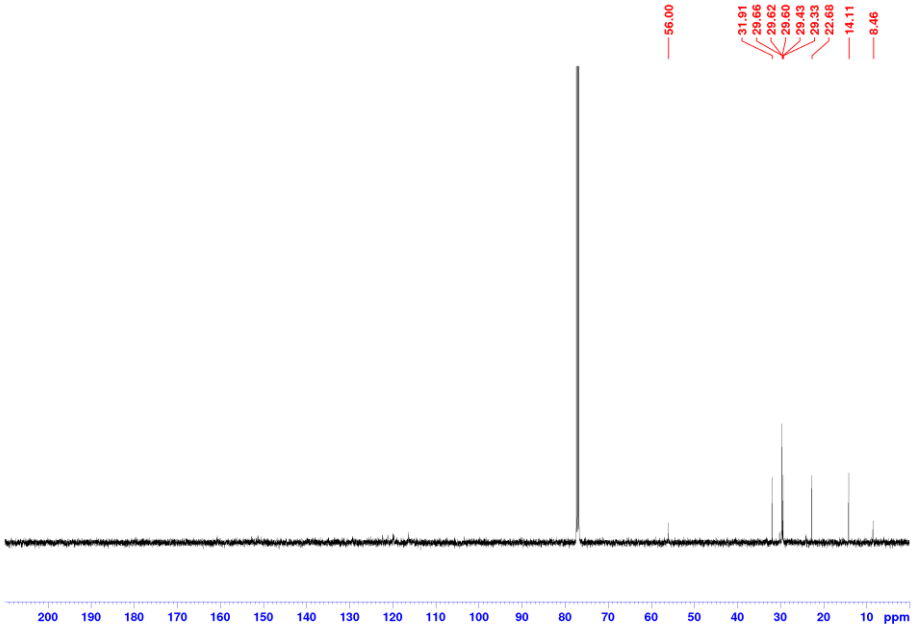

Figure 8.40. ^{13}C NMR spectrum (125 MHz, $CDCl_3$) of **(*S*)-CP**.

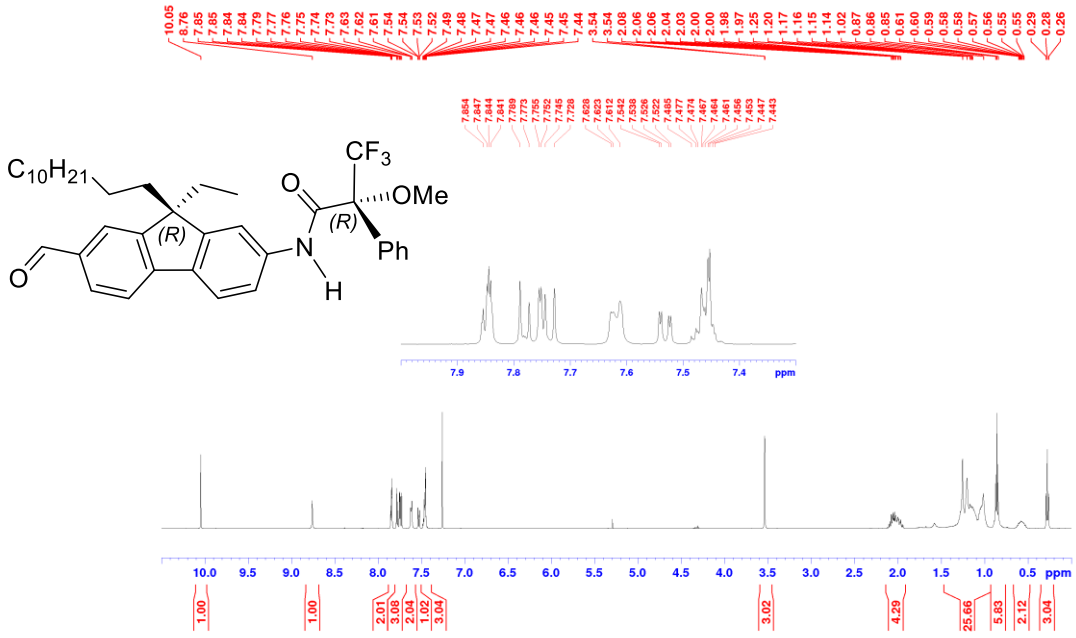

Figure 8.41. ^{1}H NMR spectrum (500 MHz, $CDCl_3$) of (*R*)-Mosher-**(*R*)-M3** (equal to (*R*)-Mosher-**M3-1**).

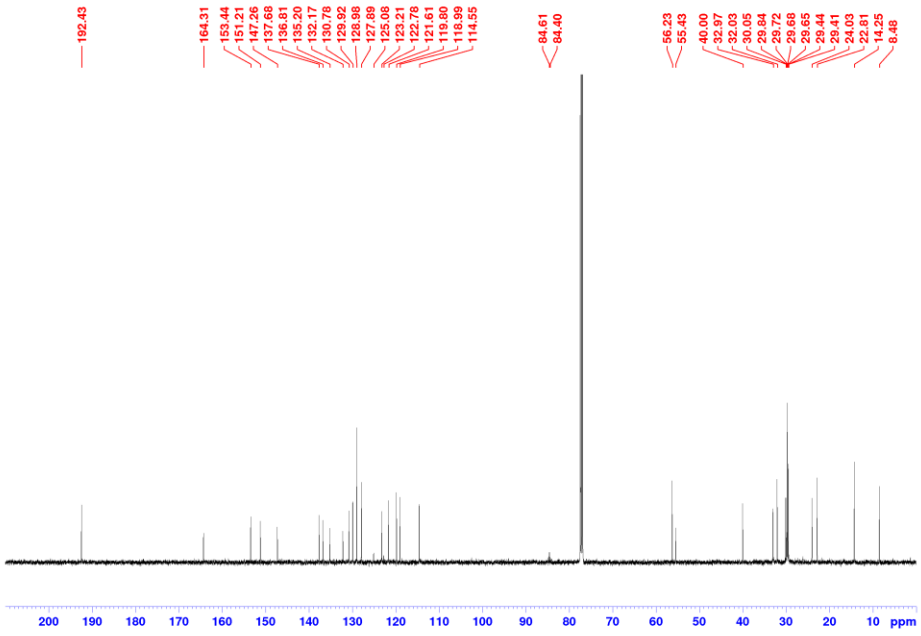

Figure 8.42. ^{13}C NMR spectrum (125 MHz, $CDCl_3$) of (*R*)-Mosher-**(*R*)-M3** (equal to (*R*)-Mosher-**M3-1**).

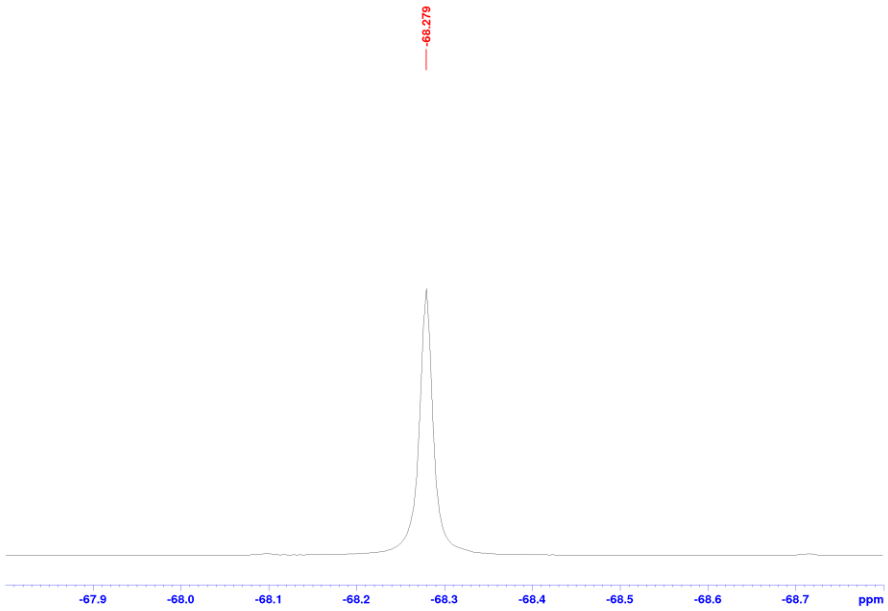

Figure 8.43. ^{19}F NMR spectrum (470 MHz, $CDCl_3$) of (*R*)-Mosher-**(*R*)-M3** (equal to (*R*)-Mosher-**M3-1**).

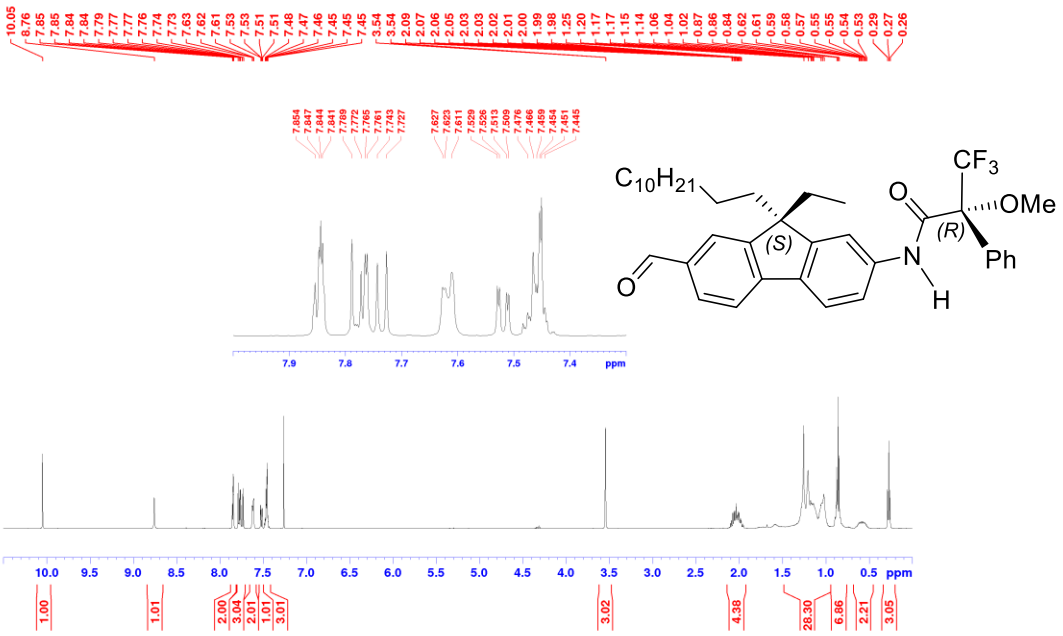

Figure 8.44. ^{1}H NMR spectrum (500 MHz, $CDCl_3$) of (*R*)-Mosher-**(*S*)-M3** (equal to (*R*)-Mosher-**M3-2**).

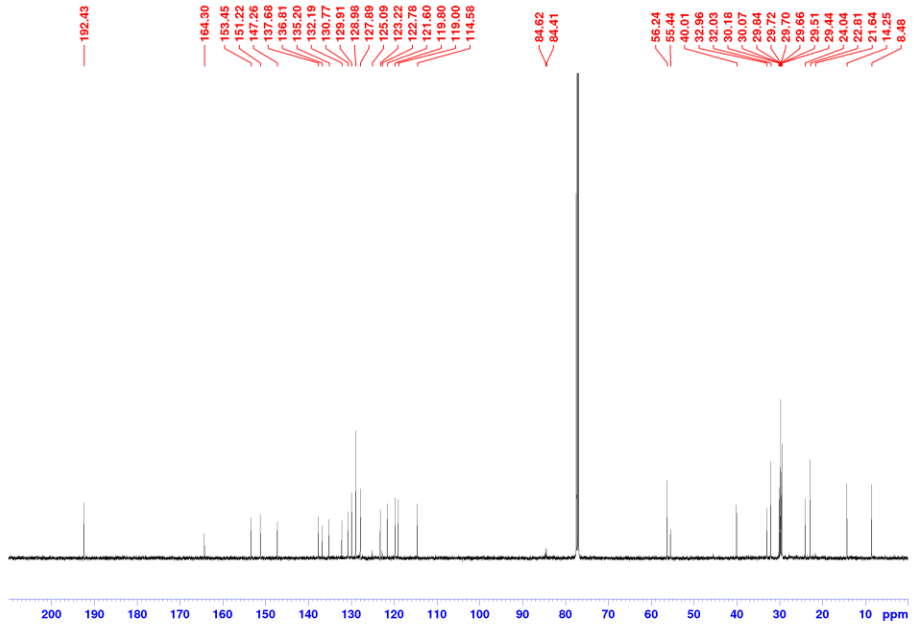

Figure 8.45. ^{13}C NMR spectrum (125 MHz, $CDCl_3$) of (*R*)-Mosher-**(*S*)-M3** (equal to (*R*)-Mosher-**M3-2**).

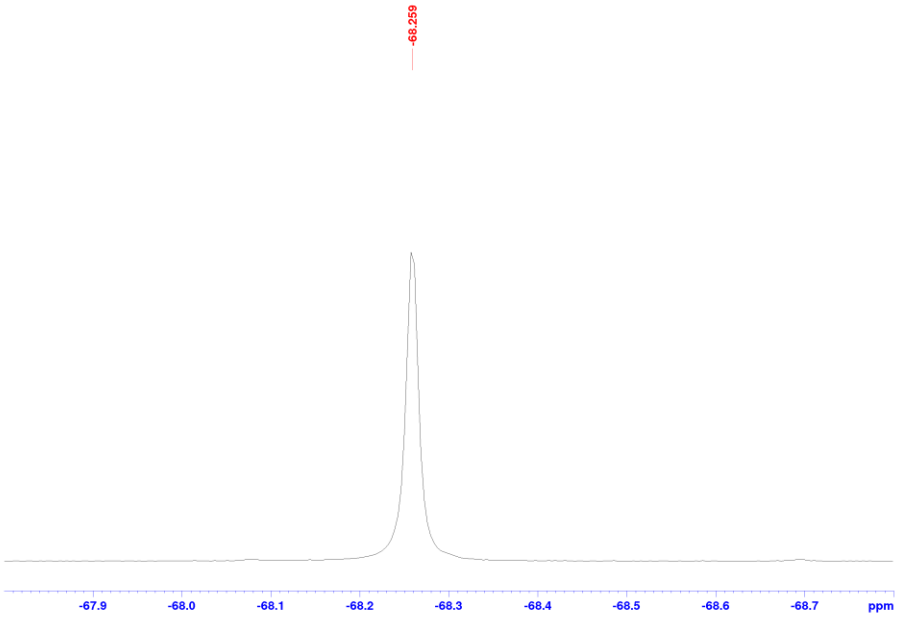

Figure 8.46. ^{19}F NMR spectrum (470 MHz, $CDCl_3$) of (*R*)-Mosher-**(*S*)-M3** (equal to (*R*)-Mosher-**M3-2**).

8.4 Curriculum Vitae

Personal Information

Name	Liang Xu
Date of birth	08.10.1987
Place of birth	Shanghai
Nationality	Chinese
E-Mail	liangxush@yahoo.com

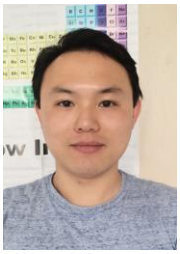

Educational Background

04/2017–02/2021	**Ph.D Chemistry**, Universität Basel, Switzerland Supervisor: Prof. Dr. Marcel Mayor *"Degradable Fluorene-based Polymers for Highly Selective Sorting of Semiconducting Single-walled Carbon Nanotubes"*
10/2011–10/2016	**M.Sc Chemistry**, Albert-Ludwigs-Universität Freiburg, Germany Supervisor: Prof. Dr. Michael Sommer *"Functionalization of Perylene and Terrylene with NDI Bromides via Palladium-catalyzed Direct C-H Arylation as Model Reactions for the Edge Functionalization of Graphene"*
09/2006–07/2011	**B.Sc Applied Chemistry**, Tongji University, China Supervisor: Prof. Dr. Li-Hua Gan *"Preparation of Sulfur-functionalized Mesoporous Carbon Foams and their Characteristics"*

Professional Skills

Experienced and trained with techniques in organic chemistry, including Schlenk-line techniques for the air- and moisture-free reactions, purification and characterization of organic compounds. Experienced with techniques in material science for processing carbon materials such as graphene composites and carbon nanotubes. Good knowledge of analytical techniques including NMR spectroscopy, mass spectrometry (GC/MS, MALDI-TOF), HPLC, GPC, IR spectroscopy, UV-

Vis-NIR absorption spectroscopy, Raman spectroscopy, PLE spectroscopy, CD spectroscopy, AFM, and isothermal titration calorimetry. Experienced in scientific work and team-work.

Language

Chinese	native language
English	fluent
German	conversational

Scientific activity and publication

Conference 21–26 July 2019	19th International Conference on the Science and Application of Nanotubes and Low-Dimensional Materials, Würzburg, Germany, with poster presentation
Publication	"Enantiomeric Separation of Semiconducting Single-Walled Carbon Nanotubes by Acid Cleavable Chiral Polyfluorene", submitted to *ACS Nano*.